



# Construction of the Inner Tracker and Sensitivity to the $B_s^0 \rightarrow \mu\mu$ Decay at LHCb

Thèse de Doctorat

présentée à la Section de Physique de la Faculté des Sciences de Base  
de l'École Polytechnique Fédérale de Lausanne  
pour l'obtention du grade de Docteur ès Sciences

par

**Marc-Olivier Bettler**

Ingénieur Physicien diplômé de l'École Polytechnique Fédérale de Lausanne, Suisse

Jury

**Prof. Quang Minh Tran**, Président du jury

**Prof. Olivier Schneider**, Directeur de thèse

**Dr Antonio Pellegrino**, Rapporteur

**Dr Frederic Teubert**, Rapporteur

**Dr Urs Langenegger**, Rapporteur



# Résumé

LHCb est l'une des quatre principales expériences au Grand Collisionneur de Hadrons (LHC) du CERN. Le LHC a démarré en septembre 2008, puis après une panne d'un an, a redémarré avec succès en novembre 2009. Durant trois semaines, la communauté des physiciens des particules a eu l'occasion d'observer les premières collisions proton-proton dans le LHC, puis très vite, d'assister au nouveau record du faisceau le plus énergétique. L'aisance dont font preuve les opérateurs de la complexe machinerie du LHC est d'excellent augure pour la prochaine période de prise de données débutant fin février 2010.

LHCb est l'expérience du LHC dédiée à la physique du quark  $b$ , au travers de l'étude de la violation  $\mathcal{CP}$  et de désintégrations rares. Les ambitions scientifiques de LHCb sont importantes : elle a en effet pour but la recherche indirecte de Nouvelle Physique (NP), ainsi que la mesure précise des paramètres de la violation  $\mathcal{CP}$ . Le détecteur LHCb se présente sous la forme d'un spectromètre à un bras.

La mesure du rapport d'embranchement de la désintégration  $B_s^0 \rightarrow \mu^+ \mu^-$ , encore jamais observée, est considérée à l'heure actuelle comme l'un des tests les plus décisifs quant à l'existence de phénomènes, dont la description échappe au Modèle Standard (MS). En effet, il existe une plage inexplorée considérable entre la limite supérieure expérimentale actuelle et la prédition de ce rapport d'embranchement par le MS, ce qui rend une mesure incompatible avec le MS possible. De plus, il existe des prédictions pour ce rapport d'embranchement dans le cadre de nombreuses théories, prétendant à une description plus précise de la matière que celle offerte par le MS. Certaines de ces prédictions diffèrent significativement de celle du MS, offrant le potentiel d'une découverte indirecte de Nouvelle Physique. Dans cette thèse, j'ai étudié la sensibilité de LHCb à la mesure du rapport d'embranchement de  $B_s^0 \rightarrow \mu^+ \mu^-$  en utilisant des simulations Monte Carlo. Je montre que LHCb peut concurrencer le Tevatron sur la limite supérieure d'exclusion du rapport d'embranchement de  $B_s^0 \rightarrow \mu^+ \mu^-$  en 2010 déjà et qu'environ  $3 \text{ fb}^{-1}$  collectés à  $\sqrt{s} = 14 \text{ TeV}$  sont suffisants pour mesurer un signal compatible avec le MS à  $3\sigma$ .

La mesure de la trajectoire des particules chargées est essentielle dans une expérience de physique des particules. Elle permet en effet d'accéder à leur quantité de mouvement et de reconstruire les propriétés physiques de particules à court temps de vie dont elles sont le produit de désintégration. Le trajectographe interne (IT) est le détecteur qui fournit ces informations pour les particules volant dans la partie interne de l'expérience LHCb. Du fait de sa position centrale, l'IT requiert l'utilisation de matériaux légers, tout en offrant la précision et la rigidité nécessaires.

Durant mon travail de thèse, j'ai participé à la construction de l'IT à travers l'établissement d'une procédure détaillée pour son assemblage. A cette occasion, j'ai mis en évidence plusieurs problèmes que j'ai contribué à résoudre de manière pragmatique. J'ai également défini des critères de qualité requis aux points-clés de l'assemblage, ainsi que les modalités de leur évaluation. J'ai ensuite conduit l'assemblage des douze boîtes composant l'IT, qui ont été intégrées à l'expérience LHCb en été 2008. Après alignement, la précision globale sur la position des modules de l'IT est en moyenne de  $19 \mu\text{m}$ . La rigueur et les tests systématiques entourant l'assemblage de l'IT ont permis de garder la fraction des pistes inutilisables au-dessous de 1 %. Finalement, les premières collisions dans le LHC ont été observées !

**Mots-clés :** CERN, LHC, LHCb, détecteur de traces au silicium, désintégration rare, nouvelle physique,  $B_s^0 \rightarrow \mu^+ \mu^-$ .



# Abstract

LHCb is one of the four main experiments hosted at the Large Hadron Collider (LHC) at CERN. The LHC first started in September 2008 and, after a one-year hiccup, restarted in November 2009. In the course of three weeks, the HEP community witnessed the first LHC proton-proton collisions and a new record of the most energetic particle beam. The ease shown by the operators of the complex LHC machine augurs very well for the extended period of data-taking scheduled to start at the end of February 2010.

LHCb is the LHC experiment primarily dedicated to the  $b$  realm, through the study of  $\mathcal{CP}$  violation and rare decays. Its physics goals are ambitious: it aims at the indirect search of New Physics and at the precise measurements of  $\mathcal{CP}$  violation parameters. The LHCb detector was designed as a single-arm forward spectrometer.

The branching fraction of the yet-unobserved  $B_s^0 \rightarrow \mu^+ \mu^-$  decay is currently considered as one of the most stringent tests for the existence of physics beyond the Standard Model (SM) of particle physics. There exists indeed a large unexplored range between the current experimental upper limit and the SM prediction about this branching fraction, making a measurement incompatible with the SM possible. Furthermore, there exist predictions for this branching fraction in the frame of numerous theoretical models that aim at a more accurate description of matter than that offered by the Standard Model. Some of those predictions significantly differ from the SM one, opening the possibility of an indirect discovery of New Physics. In this thesis, I present the study of the sensitivity of the LHCb experiment to this branching fraction with Monte Carlo simulations. I show that LHCb will compete with the Tevatron for the exclusion limit of the  $B_s^0 \rightarrow \mu^+ \mu^-$  branching fraction already in 2010 and that approximately  $3 \text{ fb}^{-1}$  at  $\sqrt{s} = 14 \text{ TeV}$  are enough for a  $3\sigma$  evidence of a SM signal.

In a particle physics experiment, the precise measurement of the charged particle trajectories is essential. Indeed tracking gives experimental access to their momentum and allows the reconstruction of the physical properties of the short-lived particle of which they are the decay products. The Inner Tracker is the detector that provides tracking information for the particles flying in the innermost part of LHCb. Because of its central position, the Inner Tracker calls for the use of very light-weighted material which compete with the precision and rigidity required by such a detector.

During my thesis work, I contributed to the construction of the Inner Tracker through the set up of an assembly procedure for the detector boxes, uncovering several design flaws and contributed to solve them pragmatically. I defined quality requirements at key steps of the assembly and implemented tests to assess them. I conducted the assembly of the twelve Inner Tracker detectors boxes that were installed in the LHCb cavern in Summer 2008. After software alignment, the overall precision of the Inner Tracker modules position is on average  $19 \mu\text{m}$  along the relevant direction. The careful box assembly and the quality tests along the procedure allowed to keep the dead strips fraction below 1%. Finally, tracks from the LHC collisions have been seen !

**Keywords:** CERN, LHC, LHCb, Silicon Tracker, Rare Decay, New Physics,  $B_s^0 \rightarrow \mu^+ \mu^-$ .



# Acknowledgements

J'aimerais remercier tous les membres du LPHE qui en font un endroit où on ne s'ennuie pas! Plus particulièrement, merci à Esther et à Erika pour leur efficace bonne humeur et à Aurelio, Tatsuya et Olivier pour leurs conseils avertis.

Merci à mes cousins Cédric et Louis, le premier même s'il court plus vite que moi, et le second pour avoir réussi à sauver la baraque en alignant mes boîtes, merci à Guido qui m'appelle 'cheri' quand il me trouve trop naïf, merci à Fred, mon modèle en matière de pilosité faciale, à Vincent pour son oeuvre picturale, à Japhet le vigilant and to Lucky Paul who can fix the cluster faster than his shadow.

Pour la patience et l'infine tolérance qu'ils m'ont témoigné, j'aimerais saluer mes collègues de bureau: Géraldine, Neus, Ralucca, Anne, Jérémie, Hubert and Matt.

Merci aussi aux professeurs Gailloud et Weil de prouver quotidiennement que la joie de vivre et la curiosité ne sont pas liées à l'âge. Marco est particulièrement reconnaissant au professeur Gailloud d'avoir relu la partie théorique de ce document et de lui avoir fait découvrir les joies du discours à la troisième personne.

Ma gratitude va surtout à mon directeur de thèse, Olivier Schneider, qui est à l'origine de mon intérêt pour la physique des particules, qui m'a judicieusement guidé vers une analyse extrêmement intéressante et qui a corrigé ce document jusqu'à épuisement.

Pour leur aide durant la construction de l'Innner Tracker, j'aimerais remercier Jeroen van Hunen et Helge Voss pour m'avoir fait confiance, Alain Pinard qui a 'débugué' la première boîte avec moi, Raymond Frei et Jean-Philippe Hertig pour leur souplesse dans la recherche de solutions, Géraldine et Neal pour leurs petites mains, Eliseo, l'homme aux deux téléphones, ainsi que Rodolfo Gonzalez, Bernard Howald, Jean-Marc Repond, Manuel Santos et Jean-René Moser à l'atelier mécanique et encore Guy Masson et Pierre-Alain Baehler à l'atelier électronique.

I want to thank the  $B_s^0 \rightarrow \mu^+ \mu^-$  people, Gaia, Frederic, Jose Angel and Hugo for their insight. Frederic, thank you also for the extensive reading of this document. Most particularly, I want to thank my friend Diego, who as my postdoc-without-a-Ph. D. answered all my questions.

I would also like to acknowledge the galician horde, Abe, Xavier, Daniel and Diego, who make CERN building 13 such a lively<sup>1</sup> place.

Merci à mes parents pour leur amour et leur soutien, mais surtout pour avoir nourri notre enfance, celle de mes petits frères et la mienne, d'aventures extraordinaires. Merci à ces derniers d'être mes compagnons dans ces aventures. Merci aussi à la famille de ma belle, dont le petit qui a tapé l'introduction. Et à Sébastien du Ciel.

Enfin, ma toute belle Camille, j'aimerais te remercier pour ta patience et ton amour.

IMVWO GCNNS SNDUM ODXEN UINVF INAXM ROUG AIFUT PMUEP DMYSO REGIW OEORM OEVRO  
DGNVN ARFUN VPMNV CTFDR NOEVZ NVFOO HVFAN PORED ODNIF UTAVO KETOE WYXVR MEZIF  
UTAVO KEVRM CTOPG AFOVA OGAOQ YOWAG IGUIC OUPSA UMSOA DAVVK IDEVN VIDGA NRDYT  
UOFSA OUDNA SUQCO POGAI FUTTS EUXVA VIPAV OKETV AOGWT UQDXS NMURN VENRD NMKVA  
NSDPN DONVK ENIPT CXMOA OCENG AIUFO NIENI FUT ENQO CTVUMX NVCTDY

Merci à tous,  
Marco

<sup>1</sup>A typical dialogue taking place in front of the Santiago's office:  
— I fear someone is being butchered in there.  
— Don't worry, they are just having a civilised conversation.



# Contents

<b>Résumé</b>	iii
<b>Abstract</b>	v
<b>Acknowledgements</b>	vii
<b>Introduction</b>	1
<b>1 The Standard Model of Particle Physics and its Extensions</b>	3
1.1 The Standard Model of Particles Physics . . . . .	3
1.1.1 The Leptonic Sector of the Electroweak Theory . . . . .	5
1.1.2 Extension to the Quark Sector . . . . .	8
1.1.3 The Strong Interaction Lagrangian . . . . .	10
1.2 Beyond the Standard Model . . . . .	10
1.2.1 Motivations . . . . .	10
1.2.2 Models Beyond the Standard Model . . . . .	12
1.3 Flavour-Changing Neutral Current FCNC . . . . .	15
1.4 $B_s^0 \rightarrow \mu^+ \mu^-$ from a theoretical point of view . . . . .	17
1.4.1 Standard Model Prediction . . . . .	18
1.4.2 Two Higgs Doublet Model . . . . .	21
1.4.3 Minimal Flavour Violation . . . . .	23
1.4.4 MSSM with Anomaly Mediated Symmetry Breaking . . . . .	24
1.4.5 Constrained MSSM . . . . .	26
1.4.6 MSSM with Non-Universal Higgs Masses . . . . .	27
1.4.7 Maximally $\mathcal{CP}$ -Violating MSSM with Minimal Flavour Violation . . . . .	29
1.4.8 $\mathcal{R}$ -Parity Violating MSSM . . . . .	29
1.4.9 $Z'$ Models . . . . .	31
<b>2 CERN, the LHC Machine and its Experiments</b>	33
2.1 The European Organisation for Nuclear Research CERN . . . . .	33
2.2 The Large Hadron Collider . . . . .	34
2.2.1 Luminosity . . . . .	34
2.2.2 Centre-of-Mass Energy . . . . .	35
2.2.3 LHC Accelerator Chain and Experiments . . . . .	36

<b>3 The LHC beauty Experiment</b>	<b>39</b>
3.1 The Tracking System . . . . .	39
3.1.1 The Vertex Locator . . . . .	40
3.1.2 The Trackers . . . . .	43
3.1.2.1 The Tracker Turicensis . . . . .	43
3.1.2.2 The Inner Tracker . . . . .	43
3.1.2.3 The Outer Tracker . . . . .	45
3.1.3 The Magnet . . . . .	45
3.1.4 The Track Reconstruction . . . . .	46
3.2 The Particle Identification Devices . . . . .	48
3.2.1 The Čerenkov Detectors . . . . .	49
3.2.2 The Calorimeters . . . . .	51
3.2.3 The Muon Detectors . . . . .	51
3.2.4 Particle Identification . . . . .	53
3.3 The Trigger System . . . . .	54
3.3.1 First Level Trigger L0 . . . . .	54
3.3.2 The High Level Trigger HLT . . . . .	55
3.4 The LHCb Software . . . . .	57
<b>4 Production and Assembly of the Inner Tracker</b>	<b>59</b>
4.1 Origin of the Elements Composing the Inner Tracker . . . . .	62
4.2 Production of the Detector Modules . . . . .	63
4.3 Detector Box Components . . . . .	66
4.3.1 The Cover . . . . .	66
4.3.2 The Box Container . . . . .	70
4.3.3 The Cooling Rod . . . . .	71
4.3.4 The Detector Modules . . . . .	72
4.3.5 The Assembly Set-ups . . . . .	74
4.4 Assembly Procedure of an Inner Tracker Detector Box . . . . .	77
4.4.1 Mounting of the Cover on the Sliding Set-up . . . . .	77
4.4.2 Adjustment of the Detector Box Position . . . . .	77
4.4.3 Mounting the First Cooling Rod . . . . .	78
4.4.4 Fixation of the First Cooling Rod under the Cover . . . . .	79
4.4.5 Mounting of the Second Cooling Rod . . . . .	79
4.4.6 HV Test of the Modules . . . . .	79
4.4.7 Cooling Circuit Closure . . . . .	80
4.4.8 Cooling Circuit Leak Test . . . . .	80
4.4.9 Survey of the Visible Layers . . . . .	81
4.4.10 Full Electrical Tests . . . . .	82
4.4.11 Test of the Height of the Modules . . . . .	83
4.4.12 Final Insertion of the Detector into the Container . . . . .	86
4.5 Commissioning and Performance of the Inner Tracker . . . . .	86

<b>5 Analysis for the <math>B_s^0 \rightarrow \mu^+\mu^-</math> Decay Search</b>	<b>91</b>
5.1 Strategy for the $B_s^0 \rightarrow \mu^+\mu^-$ Decay Search . . . . .	92
5.2 Fully Simulated Monte Carlo Samples . . . . .	93
5.3 Event Selection . . . . .	94
5.3.1 $B_s^0 \rightarrow \mu^+\mu^-$ Selection . . . . .	95
5.3.2 $B_{(s)}^0 \rightarrow h^+h^-$ Selection . . . . .	101
5.3.3 $B^+ \rightarrow J/\psi(\mu\mu)K^+$ Selection . . . . .	102
5.3.4 Interchannel Comparison of the $B$ Phase Space . . . . .	102
5.4 Geometrical Likelihood . . . . .	105
5.4.1 Gaussianisation and Decorrelation of the Input Distributions . . . . .	106
5.4.2 Construction of the Geometrical Likelihood . . . . .	107
5.4.3 Calibration of the Geometrical Likelihood . . . . .	110
5.5 Invariant Mass . . . . .	110
5.6 Muon Identification . . . . .	111
5.7 Sensitivity to the $B_s^0 \rightarrow \mu^+\mu^-$ Branching Fraction . . . . .	112
5.7.1 The Modified Frequentist Approach: $\text{CL}_s$ . . . . .	112
5.7.2 Input and Assumptions . . . . .	115
5.7.3 Toy Monte Carlo Method . . . . .	116
5.7.4 Results . . . . .	117
<b>Conclusion</b>	<b>123</b>
<b>A Normalisation, Trigger and Reconstruction Efficiencies</b>	<b>125</b>
A.1 Normalisation . . . . .	125
A.2 Reconstruction Efficiency . . . . .	127
A.3 Trigger Efficiency . . . . .	129
<b>B More on Event Selection</b>	<b>131</b>
<b>C More on the Geometry Likelihood</b>	<b>145</b>
<b>References</b>	<b>153</b>



# List of Figures

1.1	Gauge couplings <i>vs</i> energy scale $Q$ in the SM and in the MSSM. . . . .	14
1.2	Lepton pair creation. . . . .	16
1.3	FCNC in the $B_s^0 \rightarrow \phi\gamma$ radiative decay. . . . .	16
1.4	$A_{FB}$ in the $B^0 \rightarrow K^{(*)}\ell^+\ell^-$ channel at Belle. . . . .	17
1.5	SM Feynman diagrams for $\bar{B}_s^0 \rightarrow \mu^+\mu^-$ . . . . .	19
1.6	2HDM Feynman diagrams for $\bar{B}_s^0 \rightarrow \mu^+\mu^-$ . . . . .	22
1.7	$\mathcal{B}(B_s^0 \rightarrow \mu^+\mu^-)$ in 2HDM. . . . .	23
1.8	$\mathcal{B}(B_s^0 \rightarrow \mu^+\mu^-)$ and $\mathcal{B}(B^0 \rightarrow \mu^+\mu^-)$ correlation in MFV. . . . .	24
1.9	$\mathcal{B}(B_s^0 \rightarrow \mu^+\mu^-)$ vs $\tan\beta$ in AMSB. . . . .	25
1.10	$\mathcal{B}(B_s^0 \rightarrow \mu^+\mu^-)$ in the $\tan\beta-m_{3/2}$ plane in AMSB. . . . .	25
1.11	$\mathcal{B}(B_s^0 \rightarrow \mu^+\mu^-)$ in CMSSM. . . . .	26
1.12	$\mathcal{B}(B_s^0 \rightarrow \mu^+\mu^-)$ in NUHM. . . . .	27
1.13	$\mathcal{B}(B_s^0 \rightarrow \mu^+\mu^-)$ in NUHM. . . . .	28
1.14	$\mathcal{B}(B_s^0 \rightarrow \mu^+\mu^-)$ in MCPMFV. . . . .	29
1.15	$\mathcal{B}(B_s^0 \rightarrow \mu^+\mu^-)$ in mSUGRA with $\mathcal{R}$ -parity violation. . . . .	30
1.16	$\mathcal{B}(B_s^0 \rightarrow \mu^+\mu^-)$ with $Z'$ . . . . .	31
2.1	Cross section of a LHC dipole. . . . .	35
2.2	The LHC accelerator chain. . . . .	36
2.3	The ATLAS apparatus. . . . .	37
2.4	The CMS apparatus. . . . .	37
2.5	The ALICE apparatus. . . . .	37
3.1	Angular distribution of $b\bar{b}$ pairs produced at LHC . . . . .	40
3.2	Number of interactions per bunch crossing vs $\mathcal{L}$ . . . . .	40
3.3	LHCb tracking system. . . . .	41
3.4	VeLo modules layout. . . . .	42
3.5	Sketch of two VeLo sensors. . . . .	42
3.6	Layout of a TT plane. . . . .	44
3.7	TT module. . . . .	44
3.8	Cross-section of an OT module. . . . .	44

3.9	Outer Tracker straw-tube modules.	44
3.10	Measurement of the LHCb magnetic field main component $B_y$ .	46
3.11	Track categorisation.	47
3.12	Momentum resolution <i>vs</i> track momentum and IP resolution <i>vs</i> $1/p_T$ .	48
3.13	LHCb particle identification devices.	49
3.14	Simulation of a typical event in RICH1.	50
3.15	Čerenkov angle vs particle momentum for different radiators and different particle types.	50
3.16	Layout of the muon system.	52
3.17	Detail of a MWPC muon detector.	52
3.18	Detail of a GEM muon detector.	52
3.19	LHCb trigger flow.	55
4.1	Inner Tracker detector boxes layout.	62
4.2	Detector module composition and hybrid gluing jig.	64
4.3	Sensor gluing procedure.	65
4.4	Daily production of Inner Tracker detector modules.	66
4.5	Schematic view of a cover.	67
4.6	A box container and a cover showing a thermoswitch.	68
4.7	Mini patch-panel for the BEAMS and thermoswitch circuit.	69
4.8	A cover mounted on the set-up.	69
4.9	Column, fork, and colonnettes.	69
4.10	BEAMS device.	71
4.11	Crenels on a cooling rod.	73
4.12	A cooling rod under pressure test.	73
4.13	A cooling rod mounted on the mounting set-up.	73
4.14	Foam protection on sensors.	74
4.15	Module identification sticker.	75
4.16	Sketches of the cooling rod station and sliding set-up.	75
4.17	Cover positioned on the set-up.	76
4.18	Application of the conductive grease on a cooling rod.	78
4.19	Fixation of the modules on a cooling rod.	79
4.20	Closure of the cooling circuit.	81
4.21	Will the modules fit into the container?	84
4.22	Measurement of the height.	85
4.23	Glass frame for height adjustment and a detector box being closed.	85
4.24	Schematic view of the TED dumped injection test.	87
4.25	General status of the Inner Tracker.	88
4.26	Alignment of the Inner Tracker.	89
4.27	Alignment of the Inner Tracker.	89

5.1	$B_s^0$ mass, $\mu$ DOCA and $B_s^0$ IP distributions for $B_s^0 \rightarrow \mu^+\mu^-$ events passing the alternate and the standard selections. . . . .	98
5.2	$B_s^0 p_T$ , $B_s^0$ FD and smallest $\mu$ IP distributions for $B_s^0 \rightarrow \mu^+\mu^-$ events passing the alternate and the standard selections. . . . .	99
5.3	$B_s^0$ pseudorapidity and $B_s^0$ momentum distributions for $B_s^0 \rightarrow \mu^+\mu^-$ events passing the alternate and the standard selections. . . . .	100
5.4	$B$ pseudorapidity, $B p_T$ and $B p$ distributions for events passing the alternate and standard selections for the three channels. . . . .	104
5.5	GL input variables distributions before and after their gaussianisation and decorrelation for the $B_s^0 \rightarrow \mu^+\mu^-$ signal. . . . .	108
5.6	GL input variables distributions before and after their gaussianisation and decorrelation for the dimuon background. . . . .	109
5.7	Distributions of the GL for $B_s^0 \rightarrow \mu^+\mu^-$ and dimuon background. . . . .	110
5.8	Invariant mass calibration. . . . .	111
5.9	Muon identification DLL. . . . .	112
5.10	Illustration of the test-statistic $Q$ in a bin. . . . .	113
5.11	Illustration of the $CL_{s+b}$ and $CL_b$ quantities. . . . .	114
5.12	Flow-chart of the sensitivity study. . . . .	118
5.13	Expected 90% C.L. upper limit on $\mathcal{B}(B_s^0 \rightarrow \mu^+\mu^-)$ in absence of signal for 7 TeV collisions. . . . .	120
5.14	Expected 90% C.L. upper limit on $\mathcal{B}(B_s^0 \rightarrow \mu^+\mu^-)$ in absence of signal at 14 TeV. . . . .	121
5.15	$\mathcal{B}(B_s^0 \rightarrow \mu^+\mu^-)$ at which a $5\sigma$ discovery is expected at 14 TeV. . . . .	121
A.1	Ratio of reconstruction efficiency between 4- and 3-body decays, and 3- and 2-body decays. . . . .	128
B.1	SV $\chi^2$ , $B_s^0$ IPS, $B_s^0$ FDS and smallest $\mu$ IPS distributions for $B_s^0 \rightarrow \mu^+\mu^-$ events passing the alternate and the standard selections. . . . .	132
B.2	$B_s^0$ proper time, $\mu^+$ and $\mu^-$ isolations distributions for $B_s^0 \rightarrow \mu^+\mu^-$ events passing the alternate and the standard selections. . . . .	133
B.3	$B_{(s)}^0$ mass, $\mu$ DOCA and $B_{(s)}^0$ IP distributions for $B_{(s)}^0 \rightarrow h^+h^-$ events passing the alternate and the standard selections. . . . .	135
B.4	$B_{(s)}^0 p_T$ , $B_{(s)}^0$ FD and smallest $h$ IP distributions for $B_{(s)}^0 \rightarrow h^+h^-$ events passing the alternate and the standard selections. . . . .	136
B.5	SV $\chi^2$ , $B_{(s)}^0$ IPS, $B_{(s)}^0$ FDS and smallest $h$ IPS distributions for $B_{(s)}^0 \rightarrow h^+h^-$ events passing the alternate and the standard selections. . . . .	137
B.6	$B_{(s)}^0$ pseudorapidity and $B_{(s)}^0$ momentum distributions for $B_{(s)}^0 \rightarrow h^+h^-$ events passing the alternate and the standard selections. . . . .	138
B.7	$B_s^0$ proper time, $\mu^-$ and $\mu^+$ isolations distributions for $B_{(s)}^0 \rightarrow h^+h^-$ events passing the alternate and the standard selections. . . . .	139
B.8	$B^+$ mass, $\mu$ DOCA and $B^+$ IP distributions for $B^+ \rightarrow J/\psi K^+$ events passing the alternate and the standard selections. . . . .	141
B.9	$B^+ p_T$ , $J/\psi$ FD and $K^+$ IP distributions for $B^+ \rightarrow J/\psi K^+$ events passing the alternate and the standard selections. . . . .	142

B.10 $J/\psi$ vertex $\chi^2$ , $B^+$ IPS, $J/\psi$ FDS and $K^+$ IPS distributions for $B^+ \rightarrow J/\psi K^+$ events passing the alternate and the standard selections. . . . .	143
B.11 $B^+$ pseudorapidity and $B^+$ momentum distributions for $B^+ \rightarrow J/\psi K^+$ events passing the alternate and the standard selections. . . . .	144
C.1 2D distributions of the GL input variables for the $B_s^0 \rightarrow \mu^+ \mu^-$ signal. . . . .	146
C.2 2D distributions of the GL input variables for the dimuon background. . . . .	147
C.3 Distributions of the GL input variables (without the muon isolations) before and after their gaussianisation and decorrelation for the $B_s^0 \rightarrow \mu^+ \mu^-$ signal. . . . .	149
C.4 Distributions of the GL input variables (without the muon isolations) before and after their gaussianisation and decorrelation for the dimuon background. . . . .	150
C.5 2D distributions of the GL input variables (defined without the muons isolations information) for the $B_s^0 \rightarrow \mu^+ \mu^-$ signal. . . . .	151
C.6 2D distributions of the GL input variables (defined without the muons isolations information) for the dimuon background. . . . .	152

# List of Tables

1.1	Leptons.	5
1.2	Weak hypercharge of scalars, left-handed doublet and right-handed singlet of lepton.	6
1.3	Bosons.	7
1.4	Quarks.	9
1.5	Current content of the Universe.	11
1.6	MSSM particle contents.	13
1.7	SM predictions and experimental limits on the $B^0 \rightarrow \ell^+ \ell^-$ branching fractions.	21
1.8	SM predictions and experimental limits on the $B_s^0 \rightarrow \ell^+ \ell^-$ branching fractions.	21
4.1	Inner Tracker silicon sensors specifications.	61
5.1	Monte Carlo samples.	94
5.2	$B_s^0 \rightarrow \mu^+ \mu^-$ selection efficiency.	96
5.3	$B_{(s)}^0 \rightarrow h^+ h^-$ selection efficiency.	101
5.4	$B^+ \rightarrow J/\psi K^+$ selection efficiency.	103
5.5	Summary table for the selection efficiency for the $B_s^0 \rightarrow \mu^+ \mu^-$ , $B_{(s)}^0 \rightarrow h^+ h^-$ and $B^+ \rightarrow J/\psi K^+$ channels.	103
A.1	Normalisation channels.	126



# Introduction

The topicality of the construction of CERN's latest accelerator, the LHC, and of the associated experiments directed me towards particle physics. Furthermore, I enjoy the diversity of the tasks a particle physicist is bound to be confronted with. In the course of my PhD work I had the opportunity to tackle the daily challenges arising from R&D and prototyping as well as to prepare an analysis using sophisticated methods. Indeed, I accompanied the LHCb Inner Tracker from the production of the detector modules to the integration of the detector boxes in the experiment. And I was particularly interested in the branching fraction measurement of the yet unobserved  $B_s^0 \rightarrow \mu^+ \mu^-$  decay, which is of great interest in the indirect search for Physics beyond the Standard Model. It is considerably enhanced for large  $\tan \beta$  values, which makes it a double-edged result. Either the branching fraction is measured at a level incompatible with the SM and New Physics is discovered, or no enhancement is seen and models with large  $\tan \beta$  are ruled out.

The LHC first started in September 2008 and, after a one-year delay, it restarted when the first proton beams were injected into the LHC ring on November 20, 2009. Only three days later, two counter circulating proton beams were orbiting simultaneously at the injection energy of 450 GeV in the ring, and the first collisions were seen in the LHC detectors. Seven days later the machine was tamed enough to accelerate beams, so that collisions at the energy of  $\sqrt{s} = 2.36$  TeV were recorded, setting a new record of the most energetic collision in a collider.

Chapter 1 sets this thesis in the context of current theoretical research in particle physics. The theoretical framework required to understand the stakes of the  $B_s^0 \rightarrow \mu^+ \mu^-$  branching fraction measurement is presented. The standard Model (SM) which is successful at describing almost every single ever observed aspect of matter is first introduced. The reasons not to be fully satisfied are given, which opens the world of the extensions to the SM. The particular case of the flavour-changing neutral current process  $B_s^0 \rightarrow \mu^+ \mu^-$  is detailed and the prediction of its branching fraction within the SM is derived. Then alternate models explicitly proposing a prediction for this branching fraction are reviewed and their prediction quoted.

The LHC machine, whose successful (re-)start in late autumn 2009 augurs very well for the future, is described in Chapter 2. Chapter 3 details the LHCb experimental setup. The various subdetectors and subsystems are reviewed. The production of the Inner Tracker detector modules and the assembly of its detector boxes constitute Chapter 4. The assembly procedure is detailed and the current state of the Inner Tracker is given.

Chapter 5 assesses the LHCb sensitivity to the  $B_s^0 \rightarrow \mu^+ \mu^-$  branching fraction measurement. An alternative to the analysis developed within LHCb is presented and its sensitivity compared to that of the standard analysis. Finally, the LHCb potential to exclude and measure the  $B_s^0 \rightarrow \mu^+ \mu^-$  branching fraction is given.



# Chapter 1

## The Standard Model of Particle Physics and its Extensions



USEFULNESS OF A MEXICAN HAT...

The Standard Model is the theory that describes matter components and their interactions. It was built over 50 years and evolved with successive observations. Although the Standard Model is probably one of the most predictive and tested theory, it suffers from a few issues that hint for a more complete underlying theory.

This chapter aims at the theoretical motivation of the analysis described in Chapter 5. To that end, the theory known as the Standard Model of High Energy Physics is introduced in Section 1.1. Motivations for the hypothesis of the existence of a more comprehensive theory, together with possible realisations are presented in Section 1.2. Flavour-Changing Neutral Current (FCNC) processes are presented in Section 1.3, whereas Section 1.4 lists the prediction of the Standard Model, as well as most interesting predictions of models beyond the Standard Model, for the branching fraction of the  $B_s^0 \rightarrow \mu^+ \mu^-$  decay.

### 1.1 The Standard Model of Particles Physics

The Standard Model (SM) aims at the description of the known elementary and composed particles as well as their interactions. The matter we are familiar with is built of atoms. Physicists in the past century discovered that atoms are, contrary to the etymology of the name, composed of smaller particles identified as the electron, the proton, and the neutron.

In 1930, to explain the energy spectrum of the electron observed in  $\beta$  decays, Pauli postulated the existence of the electronic neutrino [1], which was observed<sup>1</sup> much later in 1956 [2]. In the 1960s, experiments showed that the proton and the neutron are also made of smaller particles, the  $u$  and  $d$  quarks. Those four particles form the first family of elementary particles: the leptons  $e^-$  and the quarks  $u$  and  $d$  and their respective antiparticles<sup>2</sup>.

<sup>1</sup>The electronic neutrino was discovered at the Savannah nuclear power plant. Frederick Reines was honoured with the 1995 Nobel Prize in Physics “for the detection of the neutrino”.

<sup>2</sup>Unless specified otherwise, charge conjugate modes are implied throughout this document.

Actually, similar families, consisting of more massive particles exist. Currently, three families of leptons as well as three families of quarks along with their antiparticles have been discovered. Moreover experiments at the LEP collider proved there exist only three fermion families with light neutrino ( $m_\nu < M_Z$ ) [3]. Non-elementary particles, called hadrons, are composed of either a quark-antiquark pair(mesons) or of three quarks (baryons) or three antiquarks (antibaryons).

These elementary particles are fermions, and their interactions are mediated by bosons. There are four interactions:

- **The electromagnetic interaction** occurs between electrically charged particles. It is mediated by the photon  $\gamma$ . Since the photon is massless, the electromagnetic interaction has an infinite range.
- **The weak interaction** takes place between all quarks and leptons. Its mediators are the massive bosons  $W^-$ ,  $W^+$  ( $80.4 \text{ GeV}/c^2$ ) and  $Z^0$  ( $91.2 \text{ GeV}/c^2$ ). Due to the large mass of these bosons, the weak interaction is of very short range. Consequently, it happens very rarely in usual decays. However, the weak interaction has the peculiarity to allow processes that violate some conservations laws. It tolerates indeed flavour-changing, and  $\mathcal{C}$ ,  $\mathcal{P}$ ,  $\mathcal{T}$ ,  $\mathcal{CP}$  violating processes. Hence it allows decays that are forbidden by the electromagnetic or the strong interaction.
- **The strong interaction** occurs between colour-charged particles. There are six types of strong charges: three colours and three anticolours ( $r, g, b, \bar{r}, \bar{g}, \bar{b}$ ). The strong interaction is mediated by eight electrically neutral and massless gluons. This interaction is the one that holds quarks together to build neutrons and protons. Contrarily to the other interactions, the strong interaction does not decrease with distance. As a consequence, free quarks have never been observed: we only see them confined in hadrons.
- **The gravitational interaction** affects all massive particles. It is thought to be mediated by a massless boson, the graviton. Although the range of the gravity force is infinite, its strength is negligible compared to other interactions. Hence, at the energy and distance scales reached so far in accelerator experiments, it does not play any role. Gravity is not described in the SM.

The relative strengths of the four fundamental interactions differ enormously. Questioning this fact is a motivation for more complex theories, as explained in Section 1.2. In a coarse approximation, where dependencies on the energy and particle type are ignored, one can rank the interaction strengths. Setting the gravitational strength to 1, the relative strength of the weak interaction would be of the order of  $10^{25}$ , the electromagnetic interaction would reaches  $10^{36}$  and the strong interaction  $10^{38}$ .

The SM theory is the result of an evolutionary process. It is the step by step unification of different simpler theories.

Quantum Electrodynamics (QED) is the first quantum field theory. It follows from the quantification of the electrodynamics theory. The electromagnetic and the weak interaction descriptions were unified in the electroweak GSW<sup>3</sup> theory by Glashow [4], Salam [5], and Weinberg [6]. The spontaneous symmetry breaking gives masses to the weak bosons. This happens through the so-called Higgs mechanism, proposed by three independent and almost simultaneous papers in 1964 [7–9]. Quantum Chromodynamics (QCD) deals with the strong interaction. It

---

<sup>3</sup>Glashow, Salam, and Weinberg were awarded the 1979 Nobel Prize in Physics “for their contributions to the theory of the unified weak and electromagnetic interaction between elementary particles, including, *inter alia*, the prediction of the weak neutral current”.

Table 1.1: Leptons after electroweak SSB. Neutrinos are massless in the SM, however, they do have a non-zero mass. Their 95 % C.L. mass upper limit [10] is quoted.

Name	Symbol	Mass [ MeV/c <sup>2</sup> ]	Charge [e]	lifetime
Electron	$e^-$	0.511	-1	$> 4.6 \times 10^{26}$ yr
Electron Neutrino	$\nu_e$	$< 2.25 \times 10^{-8}$	0	
Muon	$\mu^-$	105.7	-1	$2.2 \times 10^{-6}$ s
Muon Neutrino	$\nu_\mu$	$< 0.19$	0	
Tau	$\tau^-$	1776.9	-1	$2.9 \times 10^{-13}$ s
Tau Neutrino	$\nu_\tau$	$< 18.2$	0	

explains the confinement of the quarks. The quarks can only occur in colourless bound states. Therefore they are confined into hadrons, either mesons or baryons. This also implies that an infinite energy is required to split hadrons into free quarks. Another feature of the QCD theory is the asymptotic freedom of the quarks. It means that the strength of the strong interaction decreases with increasing energy.

In the next section, the lepton sector of the SM in the GSW theory is derived. The quark sector will then be introduced by analogy.

### 1.1.1 The Leptonic Sector of the Electroweak Theory

Leptons are elementary particles; they are spin  $-\frac{1}{2}$  fermions, subjected to gravity, electromagnetic and weak interactions. The three families of leptons are listed in Table 1.1. The derivation of the formalism mainly follows the approach of Ref. [11], with contributions from Refs. [12–14].

We want to construct a theory describing both charged and neutral currents. The simplest group containing the three vector gauge bosons  $W_\mu^j$  ( $j = 1, 2, 3$ ) — at this stage still massless — is the symmetry group  $SU(2)$ . But as the electromagnetic interaction involves both left- and right-handed leptons, whereas the  $W_\mu^j$  couple only with the left-handed ones, we need a further gauge vector boson  $B$  associated to the  $U(1)$  symmetry group. The total gauge group is therefore  $SU(2) \otimes U(1)$ .

Since we want to end up with three massive bosons, we require four independent scalar fields. The simplest choice, called minimal SM, is one doublet of complex scalar fields, one electrically charged and the other neutral:

$$\phi = \begin{pmatrix} \phi^+ \\ \phi^0 \end{pmatrix}.$$

The transformations of  $\phi$  under  $SU(2)$  and  $U(1)$  are

$$SU(2) \quad \phi \rightarrow \phi' = e^{-i\mathbf{I}_w \cdot \boldsymbol{\theta}(x)} \phi \quad (1.1)$$

$$U(1) \quad \phi \rightarrow \phi' = e^{-i\frac{Y_w}{2}\theta(x)} \phi. \quad (1.2)$$

where  $\mathbf{I}_w = \frac{\sigma_w}{2}$  is the weak isospin and  $Y_w$  the weak hypercharge. It is related to the electric charge  $Q$  and to the third component of the weak isospin  $I_{w3}$  through  $Y_w = 2(Q - I_{w3})$ . In the following lines, the transformation (1.2) will be applied successively to scalar fields in Eq. (1.5), to left-handed lepton doublets and right-handed lepton singlets in Eq. (1.10). The resulting  $Y_w$

Table 1.2: Half weak hypercharge  $\frac{Y_w}{2}$  for scalar fields, left-handed lepton doublet and right-handed lepton singlet.

	$Q$	$I_{w3}$	$\frac{Y_w}{2}$
$\phi = \begin{pmatrix} \phi^+ \\ \phi^0 \end{pmatrix}$	+1 0	$+\frac{1}{2}$ $-\frac{1}{2}$	$+\frac{1}{2}$ $+\frac{1}{2}$
$\mathbf{L} \propto \begin{pmatrix} \nu_\ell \\ \ell \end{pmatrix}$	0 -1	$+\frac{1}{2}$ $-\frac{1}{2}$	$-\frac{1}{2}$ $-\frac{1}{2}$
R	-1	0	-1

values, for each of these cases are computed in Table 1.2 and help to understand Eqs (1.5) and (1.10). The Lagrangian density  $\mathcal{L}$ , which takes into account the fermions (F), the Higgs scalars (S) and the gauge bosons (B) is

$$\mathcal{L} = \mathcal{L}_{\text{SB}} + \mathcal{L}_{\text{FB}} + \mathcal{L}_{\text{FS}} + \mathcal{L}_{\text{BB}}. \quad (1.3)$$

The first term of the Lagrangian (1.3),  $\mathcal{L}_{\text{SB}}$ , is the coupling of the scalar fields to the gauge bosons. It is given by

$$\mathcal{L}_{\text{SB}} = |D_\mu \phi|^2 - V(\phi^\dagger \phi), \quad (1.4)$$

in which the term  $|D_\mu \phi|^2$  yields masses to the intermediate bosons. Explicitly,

$$D_\mu = (\partial_\mu + \frac{i}{2}g \mathbf{W}_\mu \cdot \boldsymbol{\sigma} + \frac{i}{2}g' B_\mu) \quad (1.5)$$

is the covariant derivative introduced to ensure the local invariance,  $g$  and  $g'$  being the weak coupling constants, respectively. The potential,  $V(\phi^\dagger \phi) = \mu^2 \phi^\dagger \phi + \lambda(\phi^\dagger \phi)^2$ , is adjusted in order to produce spontaneous symmetry breaking (SSB)<sup>4</sup>. One way to get such a breaking is to impose  $\mu^2$  smaller than zero. The SSB gives then masses to our three vector bosons. We may choose  $\phi^0$  to have the following value in the vacuum state:

$$\langle \phi^0 \rangle = \begin{pmatrix} 0 \\ \frac{v}{\sqrt{2}} \end{pmatrix}.$$

We have to ensure that the gauge boson that remains massless is the one associated with the photon. To that end, we introduce the following rotation by an angle  $\theta_W$  (Weinberg angle):

$$\begin{pmatrix} B_\mu \\ W_\mu^3 \end{pmatrix} = \begin{pmatrix} \cos \theta_W & -\sin \theta_W \\ \sin \theta_W & \cos \theta_W \end{pmatrix} \begin{pmatrix} A_\mu \\ Z_\mu \end{pmatrix}. \quad (1.6)$$

Since this transformation is orthogonal, the new free fields are independent.  $A_\mu$  represents the photon field and  $Z_\mu$  the massive neutral boson field. Hence, the relation (1.6) provides the value of  $\theta_W$  we need in order for  $A_\mu$  to be the massless photon field:  $\tan \theta_W = \frac{g'}{g}$ . Furthermore, in order to obtain the correct strength of the electromagnetic coupling we want

$$e = g \sin \theta_W = g' \cos \theta_W = \frac{gg'}{\sqrt{g^2 + (g')^2}}, \quad (1.7)$$

<sup>4</sup>The SSB framework was developed by Yoichiro Nambu in 1960 [15]. He was awarded the 2008 Nobel Prize in Physics for “for the discovery of the mechanism of spontaneous broken symmetry in subatomic physics”.

Table 1.3: Vector bosons and the SM Higgs boson after electroweak SSB. Note that, similarly to the photon, gluons, by construction, do not couple to Higgs fields and as such do not have a mass. The Higgs mass limit is given at 95 % C.L. [10].

Interaction	Name	Symbol	Mass [ GeV/c <sup>2</sup> ]	Charge [e]
Electromagnetic	photon	$\gamma$	0	0
		$W^+$	80.4	+1
	Weak	$W^-$	80.4	-1
Strong	gluons	$Z^0$	91.2	0
		$g$	0	0
Higgs	$H$		> 114.4	0

where  $e$  is the absolute value of the electric charge of the electron. Since  $g$  is the weak coupling, the relation (1.7) somehow unifies the weak and the electromagnetic interactions.

We define then the following combination in order to obtain the correct charged states for the vector bosons

$$W_\mu^\pm = \frac{1}{\sqrt{2}}(W_\mu^1 \mp iW_\mu^2).$$

Considering Eq. (1.4) applied to the minimal SM doublet  $\phi$  (Higgs mechanism) we get the masses of the vector bosons:

$$m_W = \frac{gv}{2}, \quad m_Z = \frac{gv}{2\cos\theta_W} = \frac{m_W}{\cos\theta_W} \quad \text{and} \quad m_\gamma = 0. \quad (1.8)$$

The mass of the Higgs scalar,  $m_H = \sqrt{-2\mu^2}$ , is a free parameter in the theory. Experimental measurements of the vector bosons and the Higgs scalar are grouped in Table 1.3.

The second term of the Lagrangian (1.3),  $\mathcal{L}_{FB}$ , which describes the coupling between the fermions and the gauge bosons has two parts. Left-handed leptons interact with both the weak bosons and the photon, whereas right-handed leptons only couple with the photon. Thus, we can split the leptons according to their helicity. The left-handed part is represented by the doublets

$$\mathbf{L} = \frac{1}{2}(1 - \gamma^5) \begin{pmatrix} \nu_\ell \\ \ell \end{pmatrix} = \begin{pmatrix} \nu_e \\ e \end{pmatrix}_L, \begin{pmatrix} \nu_\mu \\ \mu \end{pmatrix}_L, \begin{pmatrix} \nu_\tau \\ \tau \end{pmatrix}_L$$

and the right-handed part is represented by the singlet

$$\mathbf{R} = \frac{1}{2}(1 + \gamma^5)\ell = e_R, \mu_R, \tau_R. \quad (1.9)$$

Right-handed neutrinos were never observed and are therefore not included in the SM.

We define therefore the following Lagrangian:

$$\mathcal{L}_{FB} = \bar{\mathbf{L}} i\gamma^\mu (\partial_\mu + \frac{i}{2}g\mathbf{W}_\mu \cdot \boldsymbol{\sigma} - \frac{i}{2}g'B_\mu)\mathbf{L} + \bar{\mathbf{R}} i\gamma(\partial_\mu - ig'B_\mu)\mathbf{R}. \quad (1.10)$$

The structure involving  $B_\mu$  and  $W_\mu$  is similar to what we had in Eq. (1.5). The only difference lies in the minus sign in front of  $g'$ .

The right-handed part of  $\mathcal{L}_{FB}$  is then chosen such that the sum with the left-handed part gives the correct electromagnetic coupling. Since the left- and the right-handed electrons transform differently, we cannot simply add a gauge invariant electron mass term of the form  $m_e \bar{e}e$  in the Lagrangian. Therefore, in order to give a mass to the electron, we add an interaction term in the Lagrangian and we use the SSB mechanism. The term coupling the fermions ( $\ell = e, \mu, \tau$ ) and the Higgs scalars is:

$$\mathcal{L}_{FS} = -G_\ell \left[ (\bar{\mathbf{L}}\phi)\mathbf{R} + \bar{\mathbf{R}}(\phi^\dagger\mathbf{L}) \right]$$

Using  $\langle \phi^0 \rangle = \begin{pmatrix} 0 \\ \frac{v}{\sqrt{2}} \end{pmatrix}$  we obtain for the electron  $\ell = e$ :

$$\mathcal{L}_{FS} = -G_e \frac{v}{\sqrt{2}} [(\bar{\nu}_e, \bar{e})_L \begin{pmatrix} 0 \\ 1 \end{pmatrix} e_R + \bar{e}_R (0, 1) \begin{pmatrix} \nu_e \\ e \end{pmatrix}] \quad (1.11)$$

$$= -G_e \frac{v}{\sqrt{2}} (\bar{e}_L e_R + \bar{e}_R e_L) \quad (1.12)$$

$$= -G_e \frac{v}{\sqrt{2}} \bar{e}e \quad (1.13)$$

Hence, the mass of the electron is  $m_{e^\pm} = G_e \frac{v}{\sqrt{2}}$ . The same process yields to mass to the  $\mu^\mp$  and the  $\tau^\mp$ . Since there are no right-handed neutrinos, the neutrinos do not acquire mass in this approach of the SM.

'T Hooft and Veltman<sup>5</sup> have proved that the electroweak theory was normalisable in 1971 [16]. Before this date, this theory was of little interest.

### 1.1.2 Extension to the Quark Sector

In this section, we enlarge the SM in order to include the hadrons. We want to use the similarity between the leptons families and the quarks families, as listed in Table 1.4. However, fundamental differences exist between them:

- While the weak interaction respects the conservation of the leptonic charge, weak charged currents violate the flavour conservation.
- Furthermore, whereas the neutrinos are considered massless in the SM, all the quarks are massive.

To cope with these differences, we introduce *bare* quarks  $d_i^0$  and  $u_i^0$  ( $i = 1, 2, 3$ ), that are not mass eigenstates, but couple to the electroweak bosons exactly in the same way the lepton doublets and singlets do.

We can then construct a Lagrangian for the bare quarks similarly to Eq. (1.11):

$$\mathcal{L}_{QS} \sim \frac{v}{\sqrt{2}} [\bar{\mathbf{d}}_L^0 \mathbf{D} \mathbf{d}_R^0 + \bar{\mathbf{u}}_L^0 \mathbf{U} \mathbf{u}_R^0], \quad (1.14)$$

---

<sup>5</sup>Together, they were awarded the 1999 Nobel Prize in Physics “for elucidating the quantum structure of electroweak interactions in physics”.

Table 1.4: Quarks after electroweak SSB [10].

Name	Symbol	Mass [ MeV/c <sup>2</sup> ]	Charge [ e ]
Up	$u$	$2.55^{+0.75}_{-1.05}$	$+\frac{2}{3}$
Down	$d$	$5.04^{+0.96}_{-1.54}$	$-\frac{1}{3}$
Charm	$c$	$1270^{+70}_{-110}$	$+\frac{2}{3}$
Strange	$s$	$105^{+25}_{-35}$	$-\frac{1}{3}$
Top	$t$	$171300 \pm 1200$	$+\frac{2}{3}$
Bottom	$b$	$4200^{+170}_{-70}$	$-\frac{1}{3}$

where  $\mathbf{U}$  and  $\mathbf{D}$  are arbitrary  $3 \times 3$  matrices. Two pairs of unitary matrices are needed in order to diagonalise  $\mathbf{U}$  and  $\mathbf{D}$ , so that

$$\frac{v}{\sqrt{2}} \mathbf{V}_L^D \mathbf{D} \mathbf{V}_R^{D\dagger} = \begin{pmatrix} m_d & & \\ & m_s & \\ & & m_b \end{pmatrix}, \quad (1.15)$$

$$\text{and } \frac{v}{\sqrt{2}} \mathbf{V}_L^U \mathbf{U} \mathbf{V}_R^{U\dagger} = \begin{pmatrix} m_u & & \\ & m_c & \\ & & m_t \end{pmatrix}. \quad (1.16)$$

The new quark fields — the mass eigenstates — are

$$\mathbf{u}_L \equiv \mathbf{V}_L^U \mathbf{u}_L^0, \quad \mathbf{u}_R \equiv \mathbf{V}_R^U \mathbf{u}_R^0, \quad \mathbf{d}_L \equiv \mathbf{V}_L^D \mathbf{d}_L^0 \quad \text{and} \quad \mathbf{d}_R \equiv \mathbf{V}_R^D \mathbf{d}_R^0.$$

Using these new fields, Eq. (1.14) can be written as a sum of mass-like terms of the form  $m\bar{\psi}\psi$  for each quark.

Considering the coupling of the  $W^\pm$  to the quarks, we can see that the weak charged current for the quarks is diagonal in flavour for the bare quarks. However, when expressed in the new quark fields it becomes non diagonal in flavour:

$$J_{+, \text{hadrons}}^\mu = \overline{\mathbf{u}}_L^0 \gamma_\mu \mathbf{d}_L^0 W^\mu = \overline{\mathbf{u}}_L \gamma_\mu \underbrace{\mathbf{V}_L^U \mathbf{V}_L^{D\dagger}}_{\mathbf{V}_{\text{CKM}}} \mathbf{d}_L W^\mu. \quad (1.17)$$

Thus, the weak mixing matrix<sup>6</sup>  $\mathbf{V}_{\text{CKM}}$  allows charged weak interaction to mix flavour. One usually defines the CKM matrix as:

$$\begin{pmatrix} d' \\ s' \\ b' \end{pmatrix} = \begin{pmatrix} V_{ud} & V_{us} & V_{ub} \\ V_{cd} & V_{cs} & V_{cb} \\ V_{td} & V_{ts} & V_{tb} \end{pmatrix} \begin{pmatrix} d \\ s \\ b \end{pmatrix}. \quad (1.18)$$

In this approach, the CKM matrix appears as a consequence of the transformation from flavour eigenstates to mass eigenstates.

<sup>6</sup>The CKM matrix is named after the initial of three people, Nicola Cabibbo, Makoto Kobayashi, and Toshihide Maskawa. Cabibbo introduced quark mixing under the form of a  $2 \times 2$  rotation matrix — only 2 families were known at the time — to preserve the universality of the weak interaction in 1963 [17]. Makoto Kobayashi and Toshihide Maskawa generalised the Cabibbo matrix into the CKM matrix and related it to the  $\mathcal{CP}$  violation [18]. They were awarded the 2008 Nobel Prize in Physics for “the discovery of the origin of the broken symmetry which predicts the existence of at least three families of quarks in nature”.

The current experimental values of the modulus of the CKM matrix read [19]:

$$\mathbf{V}_{\text{CKM}} \approx \begin{pmatrix} 0.97433^{+0.00017}_{-0.00017} & 0.22512^{+0.00075}_{-0.00075} & 0.00351^{+0.00014}_{-0.00016} \\ 0.22498^{+0.00075}_{-0.00075} & 0.97349^{+0.00018}_{-0.00017} & 0.04117^{+0.00038}_{-0.00117} \\ 0.00859^{+0.00028}_{-0.00029} & 0.04042^{+0.00037}_{-0.00118} & 0.999146^{+0.000048}_{-0.000016} \end{pmatrix}. \quad (1.19)$$

### 1.1.3 The Strong Interaction Lagrangian

Up to now, we have encountered six different quarks,  $u, d, c, s, t, b$ , that refer to different flavour states. However, an additional degree of freedom, associated to another quantum number, exists: the colour. Each quark can exist in three colour states: red, green, or blue. The strong interaction is colour blind, which means that it is invariant under transformations of a  $SU(3)$  group that mixes up the colours. Including this new feature, the total SM gauge group becomes  $SU(3) \otimes SU(2) \otimes U(1)$ .

## 1.2 Beyond the Standard Model

The SM is probably one of the most thoroughly tested theory after Newton's laws. In the past decades, almost all the experimental results were found in agreement with the SM predictions. Only a few observations show tension with respect to SM predictions, such as the measurement of the Weinberg angle at NuTeV [21] or that of the anomalous magnetic moment of the muon by the  $g - 2$  collaboration [22]. The CKM matrix elements are being measured with great precision, and the electroweak observables are also in good agreement with the SM expectations. Despite this success, the SM is not completely satisfactory.

### 1.2.1 Motivations

Several reasons are invoked not to be satisfied with the SM:

- The concept used to explain the mass of the particles relies on the existence of the Higgs boson. This boson has never been observed. Previous direct and indirect searches have set lower and upper limits for the Higgs mass, so that if it exists it will be observed by the ATLAS and CMS experiments at CERN — see Section 2.2.3 — within a few years. If these experiments do not observe the Higgs, the SM would need to be revised. In that prospect, it is interesting to investigate other models.
- Neutrinos are massless in the SM. If neutrinos oscillate they are bound to be massive, and the fact is, they do. The first hint of such an oscillation was the observation of a deficit in the solar neutrino flux measured at the Homestake<sup>7</sup> mine experiment in the late sixties [23]. This deficit was not understood at the time and raised quite a controversy. The experimental validation first came in 1998 with SuperKamiokande's strong evidence for cosmic neutrino<sup>8</sup> oscillations [24]. Since then, cosmic neutrino oscillations [25], as well as solar neutrino oscillations [26] were confirmed. Hence, neutrinos do have a mass and the SM has to be modified.

<sup>7</sup>The 2002 Nobel Prize in Physics was awarded to Raymond Davis Jr., the head of the Homestake experiment, "for pioneering contributions to astrophysics, in particular for the detection of cosmic neutrinos".

<sup>8</sup>Cosmic neutrinos are produced when Supernova explode, or in the turbulent gaseous environment left over by Supernova explosion. Solar neutrinos are produced in the nuclear fusion processes occurring in the Sun; they are by far the dominant fraction of the neutrinos passing through the Earth.

Table 1.5: Current content of the Universe. Values comes from the observation of the CMB by the WMAP satellite, combined with the measurement of the current value of the Hubble parameter, by the Hubble Space Telescope [33]. Data taken from Ref. [34].

Constituents of the Universe	
Dark Energy	74.2 %
Dark Matter	21.4 %
Baryons (SM matter)	4.4 %

- In 1998, astronomers observing supernovae concluded that the Universe is presently undergoing an *accelerated* expansion [27, 28]. This came as a complete surprise. Indeed, the gravitational interaction between the constituents of the Universe was expected to slow down its expansion. Since that observation, the analysis of the Cosmic Microwave Background (CMB) strongly corroborated the acceleration [29]. One of the few possible explanations for the acceleration of the Universe expansion is to invoke the presence of an exotic form of energy that drives the acceleration: the Dark Energy.

Another cosmological puzzle is related to the incompatibility of the matter density distribution and its speed distribution in galaxies. This incoherence was first spotted by Zwicky in 1933 [30, 31], and rediscovered in the seventies [32]. If General Relativity is correct, an important fraction of the Universe mass is invisible to us. It only interacts gravitationally with the known matter. This additional mass is called Dark Matter and the SM does not provide any particle that suits its properties.

Together, those two facts lead to quite a setback for the SM model. Indeed, if one assumes the existence of Dark Energy and Dark Matter, whatever their exact nature, to explain these cosmological puzzles, then one gets precise proportions for the constituents of the Universe, as shown in Table 1.5. The Baryonic Matter, which is described by the SM, only accounts for 4.4 % of our Universe content.

- The Big Bang should have produced matter and anti-matter in equal amounts. During the cool-down, they would have annihilated, resulting in photons exclusively. On the contrary, the Universe appears to be made of what we call Matter, which is considered as a left-over of the annihilation, because matter was produced in excess with respect to antimatter at start. This is called the Baryon asymmetry. Even though the  $\mathcal{CP}$  violation explains a matter-antimatter asymmetry, the SM fails to account for the extent of the observed asymmetry.
- The electroweak parameter  $\sin^2 \theta_W$  has been extracted from the ratios of the neutral-current interaction cross section to the charged-current interaction cross section, for neutrinos and antineutrinos by the NuTeV collaboration [21]. The result  $\sin^2 \theta_W = 0.2277 \pm 0.0016$  is  $3\sigma$  above the SM prediction.
- The muon anomalous magnetic moment,  $a_\mu = \frac{g_\mu - 2}{2}$ , is one of the most precisely measured quantities in Physics, as well as one of the most precisely theoretically predicted [35]. The latest experimental result, from the  $g - 2$  collaboration [22], shows a discrepancy between theory and experiment of about 3 standard deviations. The difference between the experimental measurement and the SM prediction,  $\Delta a_\mu \equiv a_\mu^{\text{exp}} - a_\mu^{\text{SM}} = (290 \pm 90) \times 10^{-11}$  is often used to constrain NP candidate models.
- Concerns about the naturalness of a theory occur when some parameters of this model must be adjusted very precisely, tuned finely, to agree with observations. In today's

Physics, naturalness is an issue in the value of the cosmological constant and in the strong  $\mathcal{CP}$ -violation and hierarchy problems.

The hierarchy problem can be formulated as the following question : Why are the strengths of the gravitational, electromagnetic, weak and strong couplings so different? The SM provides no explanation for this fact.

The SM does not predict the mass of the Higgs and, experimentally, the Higgs boson is still unobserved. However, there are experimental bounds on its mass. Direct searches set a lower bound at  $114.4 \text{ GeV}/c^2$  [36], whereas indirect searches resulted in a mass of  $87^{+35}_{-26} \text{ GeV}/c^2$  [37]. By searching for Higgs decaying into a  $W$ -pair, Tevatron experiments are sensitive to Higgs with a mass greater than  $130 \text{ GeV}/c^2$ . The combination of CDF and DØ results allows to exclude at 95 % C.L. the  $163 < m_H < 166 \text{ GeV}/c^2$  mass range for a SM Higgs boson [38]. Theoretically, quantum fluctuations are expected to produce corrections to the Higgs mass that would lift it to high values, much larger than the experimentally allowed region. The only way to keep the mass low is by delicate fine-tuning of parameters.

- Finally, the gravity is not included in the SM.

Actually, among the reasons invoked above only the hierarchy problem is the historical motivation for the theorists to imagine further theories. Their deep motivation to investigate beyond the SM is curiosity and aesthetics. It is attracting to see the SM as a low energy scale effective theory which would be an approximation of a more fundamental theory. In a similar way Newton's law is the effective realisation at human scale of Einstein's General Relativity.

### 1.2.2 Models Beyond the Standard Model

We describe here some of the extensions or alternatives to the SM that theorists have developed.

#### SuperSymmetry

Supersymmetry (SUSY) [39] is the transformation that turns a bosonic state into a fermionic state, and *vice versa*:

$$Q|\text{Boson}\rangle = |\text{Fermion}\rangle, \quad \text{and} \quad Q^\dagger|\text{Fermion}\rangle = |\text{Boson}\rangle,$$

where  $Q$  is an anticommuting spinor, and  $Q^\dagger$  its conjugate.

The irreducible representation of a supersymmetric algebra is called a supermultiplet. It contains both fermion and boson states, that are called superpartners of each other. Superpartners have the same mass, electric charge, weak isospin and colour degrees of freedom.

The names of the superpartners of the SM fermions are constructed by prepending a *s*, for scalar, to the SM names. So one gets, for example, *sbottom* quark or *smuon*. The superpartners of the SM bosons are fermions whose names are formed by appending *ino* to their SM names. So one has *winos*, *gluinos* and *photinos*. A direct consequence of this formalism is that the number of fermions is equal to the number of bosons.

The minimal contents of a supersymmetric model appear in Table 1.6, and form the Minimal Supersymmetric Standard Model (MSSM).

In the SM, baryon and lepton numbers,  $B$  and  $L$  respectively, appear as accidental global symmetries which are not violated at any order of perturbation theory. One defines the  $\mathcal{R}$ -parity as

$$\mathcal{R} = (-1)^{3B+L+2S},$$

Table 1.6: MSSM particle contents. Modified from Ref. [39].

Names	bosons, spin 0	fermions, spin $\frac{1}{2}$
squarks, quarks ( $\times$ 3 families)	$(\tilde{u}_L, \tilde{d}_L)$ $\tilde{u}_R$ $\tilde{d}_R$	$(u_L, d_L)$ $u_R$ $d_R$
sleptons, leptons ( $\times$ 3 families)	$(\tilde{\nu}, \tilde{e}_L)$ $\tilde{e}_R$	$(\nu, e_L)$ $e_R$
Higgs, Higgsinos	$(H_u^+, H_u^0)$ $(H_d^0, H_d^-)$	$(\tilde{H}_u^+, \tilde{H}_u^0)$ $(\tilde{H}_d^0, \tilde{H}_d^-)$
bosons, spin 1	fermions, spin $\frac{1}{2}$	
gluon, gluino	$g$	$\tilde{g}$
$W$ bosons, winos	$W^\pm$	$\tilde{W}^\pm$
$Z$ boson, zino	$Z^0$	$\tilde{Z}^0$
photon, photino	$\gamma$	$\tilde{\gamma}$

where  $S$  is the spin of the particle; it is a discrete symmetry under which SM particles are even while their superpartners are odd. This symmetry is conserved in the SM, whereas it is naturally violated in the MSSM, unless one assumes conservation for  $B$  and  $L$ . Since no evidence of  $L$  or  $B$  violation has been experimentally observed yet<sup>9</sup>, one can take either of two attitudes. The first is to impose  $\mathcal{R}$ -parity; this constitute the  $\mathcal{R}$ -parity conserving scenario (RPC). The second is to take the view that since there is no good theoretical motivation for applying such a symmetry *a priori*, it is more general to admit all interactions invariant under supersymmetry and gauge symmetry, including *de facto*  $\mathcal{R}$ -parity violating processes, and to examine how they are constrained by experiments. This is the  $\mathcal{R}$ -parity violating scenario (RPV).

In the MSSM with  $\mathcal{R}$ -parity conservation, vertices involving supersymmetric particles always involve them in pairs. This has three consequences:

- supersymmetric particles are produced in pairs from SM particles,
- the decay of a supersymmetric particle always produces a supersymmetric particle, and
- the lightest supersymmetric particle (LSP) is stable and is present in the Universe today as a relic of the Big Bang. The LSP is one of the candidates to explain the nature of Dark Matter.

Figure 1.1 compares the evolution of the gauge couplings with the energy scale. It shows that, unlike in the SM, in the MSSM the gauge couplings can unify at a scale  $\approx 2 \times 10^{16}$  GeV, providing an elegant solution for the hierarchy problem.

The most obvious feature of this theory is that no supersymmetric particles have been observed yet. One should have observed them since their masses are equal to the ones of their SM superpartners if the supersymmetry was unbroken. Therefore, if the supersymmetry exists, it is broken. This symmetry breaking is achieved by the introduction in the Lagrangian

<sup>9</sup>Nucleons are observed to be very stable. The life-time of protons in bound state is  $\tau_p > 10^{34}$  years.

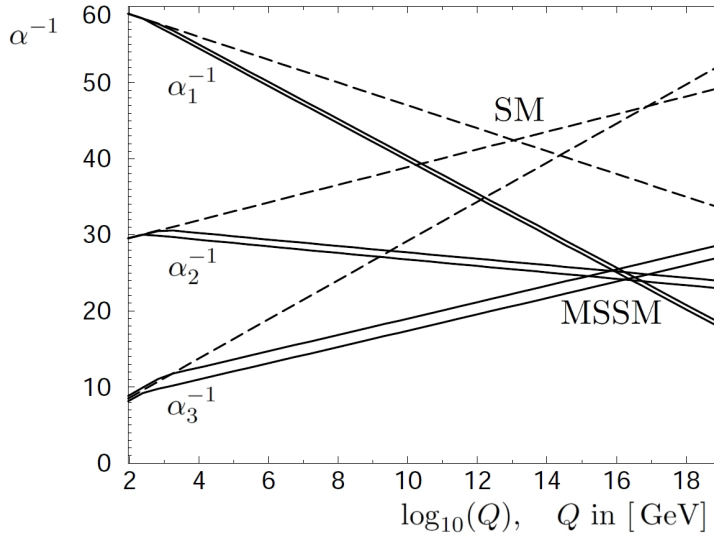


Figure 1.1: Evolution of the inverse of the  $U(1)$ ,  $SU(2)$  and  $SU(3)$  gauge couplings ( $\alpha_1$ ,  $\alpha_2$  and  $\alpha_3$ , respectively) with the energy scale  $Q$ , in the SM (dashed lines) and in the MSSM (solid lines) [39].

of extra interaction terms that respect gauge symmetry while breaking softly — without introducing quadratic divergences — the supersymmetry. This is the soft-supersymmetry-breaking mechanism.

When considering the most general symmetry breaking mechanism — without choosing a specific nature for the symmetry breaking — one gets a very large number of free parameters, more than 100, in the Lagrangian<sup>10</sup>. However, when one considers a specific explanation for the symmetry breaking mechanism, the number of parameters drops to a few. The source of the symmetry breaking is an auxiliary field, which is hidden, *i.e.* which couples to a messenger, a mediator particle, and whose only observable effect is the mass difference between particles and their hypothesised superpartners. The most popular mediation scenarios are the following [39]:

- The **Gravity Mediated Symmetry Breaking** scenario assumes gravity is the mediator for the supersymmetry breaking [42, 43]. Its minimal realisation, called mSUGRA, is particularly popular.
- The **Gauge Mediated Symmetry Breaking (GMSB)** scenario [44] introduces new chiral supermultiplets, called messengers, that couple to the SUSY breaking source and also to the MSSM content through the ordinary gauge interactions, *i.e.* through the gauge bosons and the gauginos. The gravitational interaction with the hidden field still exists, but its effects are negligible with respect to the gauge interaction effects.
- The **Anomaly Mediated Symmetry Breaking (AMSB)** scenario uses the conformal anomalies that always arise when one tries to eliminate auxiliary background field from a softly broken Lagrangian, by making a Weyl rescaling [45] as mediator for the hidden field, the source of the SUSY breaking. Such anomalies are always present in a broken supersymmetric theory, whatever the nature of the breaking. In the AMSB, the effect of the anomaly mediation is predominant with respect to the gravity or gauge mediation.

<sup>10</sup>This number varies among authors, from 110 [40] to 124 [41]. We think that the exact number is irrelevant; the fact that this number is huge with respect to the number of parameters in the SM is, tough.

### Extra dimensions

The idea of the existence of more than three spatial dimensions goes back to early the 1920s. Kaluza [46] and Klein [47] discovered that the four-dimensional gravitational and electromagnetic fields can be understood as components of a five-dimensional space, with a compact fifth dimension.

If extra dimensions are too tightly compactified, to a radius of the order of the Planck length ( $\sim 10^{-35}$  m), they would be completely inaccessible to any experiment [48]. Their existence would be unverifiable. But if the compactness of the extra dimension is larger, it would affect observable variables, and processes unknown in the SM are predicted. Such new particles were not yet observed, setting an upper limit on the compactification radius at  $\sim 10^{-15}$  m [49].

Models with extra dimensions provide a natural explanation to the hierarchy between the electroweak scale and the Planck scale. When something moves in the bulk from the gravity brane<sup>11</sup> to the electroweak brane — where we live — its mass and energy decreases whereas distance and time expand. This results in the hierarchy.

Of course, if some of the various implementations does explain the experimental observations better than the SM it becomes much more interesting.

## 1.3 Flavour-Changing Neutral Current FCNC

The CKM matrix elements explain how quarks can change flavour via charged current interactions, thus involving a  $W^+$  or a  $W^-$  boson. In a flavour-changing neutral current (FCNC) process a quark changes flavour without changing its electric charge. FCNC processes are experimentally observed to be highly suppressed, *i.e.* they occur with a tiny probability. This fact is at the origin of a key feature of the SM. In the early seventies, only the three lightest quarks were known. The theory based on these three quarks did predict the existence of unsuppressed FCNC processes, flatly contradicting the experimental results.

Glashow, Iliopoulos and Maiani [50] showed that if there existed a fourth quark, all quarks would have a partner, and would form two families (with all left-handed quarks described as doublets and all right-handed quarks as singlets). This is known as the GIM mechanism. The GIM mechanism, associated with the non-observation of FCNC, allowed the prediction of the existence of a fourth quark. The charm quark was eventually observed in 1974<sup>12</sup>, simultaneously at SLAC (Stanford Linear Accelerator Center) [51] and at BNL (Brookhaven National Laboratory) [52]. The same scenario did occur for the third family, when the bottom quark was observed, leading to the prediction of the existence of the top quark. Its observation followed in 1995 at Fermilab (Fermi National Accelerator Laboratory) [53, 54].

The impossibility to have a FCNC process at tree level can be illustrated with Feynman diagrams. In the SM, the only ones that can produce a lepton pair are those shown in Fig. 1.2 and proceed through  $\gamma$ ,  $Z^0$  or  $H^0$ . However, it is not possible to produce either of those directly from a  $\bar{b}s$  or  $\bar{b}d$  quark pair. They can only occur through higher-level contributions, involving loops, such as  $Z^0$ -penguins or box-diagrams. In the  $b$ -sector, the dominant diagram is the one involving a virtual top quark, because of its large mass and because of the large  $V_{tb}$  value.

<sup>11</sup>A brane is a space of dimension  $N - 1$  in a  $N$ -dimensional space. A brane occurs when one dimension is warped out.

<sup>12</sup>Burton Richter and Samuel Chao Chung Ting were awarded the 1976 Nobel Prize in Physics “for their pioneering work in the discovery of a heavy elementary particle of a new kind”.

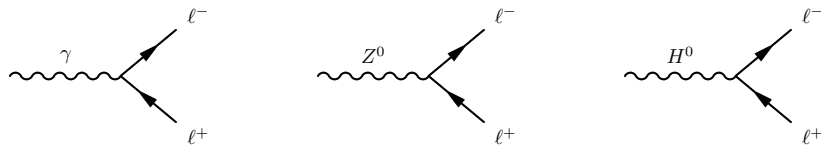


Figure 1.2: Lepton pair creation.

The study of FCNC processes plays an important role in the search for NP. There are two ways to discover NP. Either one looks for NP particles directly, as will be done at general-purpose experiments such as ATLAS and CMS (see Section 2.2.3), or one can look for the effects of NP particles on observables quantities, through their virtual existence in loops. LHCb (see Section 3) is well suited for this indirect approach.

The NP discovery potential of the indirect search is related to the degree of fulfilment of the following criteria for a given process:

- the amplitude of the process has to be suppressed in the SM, at least to the level at which NP contributions could appear, and ideally below;
- the theoretical errors on the SM observable predictions should be smaller than the variations of the prediction amongst concurrent models;
- and finally, the SM prediction should differ significantly from the NP ones, so that a conclusive result can be reached with a reasonable amount of data.

FCNC processes are among the best ones to look for NP. At LHCb, preparation work for the study of three of them is well advanced [55]:

- The  $B_s^0 \rightarrow \phi\gamma$  radiative decay was recently observed in agreement with the SM at Belle [56]. It dominantly proceeds through the Feynman diagram shown in Fig. 1.3. The polarisation of the final state photon is an observable sensitive to NP contribution. In the SM the polarisation of the photon is precisely predicted.  $\bar{B}_s^0 \rightarrow X_s \gamma_L$  and  $B_s^0 \rightarrow X_s \gamma_R$  are allowed transitions under helicity conservation, whereas the crossed transitions are suppressed by a factor  $\frac{m_s}{m_b}$ . However, in extensions of the SM, such as the Left-Right Symmetric Model [57] and the unconstrained MSSM [58], this polarisation can be free. LHCb is planning to measure the polarisation of the final state photon [60–62].

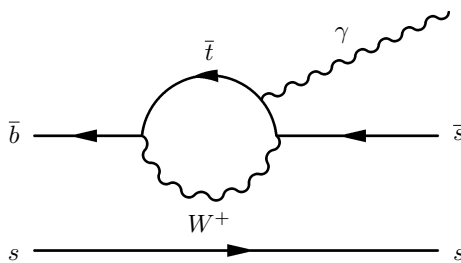


Figure 1.3: FCNC in the  $B_s^0 \rightarrow \phi\gamma$  radiative decay.

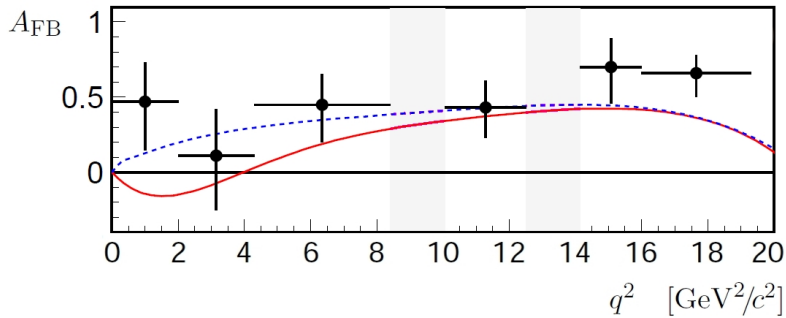


Figure 1.4: Belle measurement of the forward-backward asymmetry  $A_{FB}$  as a function of the dilepton squared mass  $q^2$ , in the  $B^0 \rightarrow K^{(*)}\ell^+\ell^-$  channel [63]. The solid and dashed curves show the SM prediction and prediction with  $\mathcal{C}_7 = -\mathcal{C}_7^{\text{SM}}$ , respectively.

- Another FCNC decay that will be studied at LHCb is  $B^0 \rightarrow K^{*0}\mu^+\mu^-$  [64–66]. In this case, the observables are angular distributions, and more specifically ratio of angular distributions. Some observables have NP predictions that differ significantly from the SM ones [67, 68]. A thorough study has identified additional observable asymmetries which presents considerable NP sensitivities [69]. The muon forward-backward asymmetry,  $A_{FB}$ , as a function of the dimuon mass squared,  $q^2 = M_{\ell\ell}^2 c^2$ , was already measured at BABAR [70], Belle [63] and CDF [71] and exhibits some tension with respect to the SM prediction. However, the statistics is very low: the Belle analysis, the most sensitive so far, is based on  $246.7^{+22.6}_{-20.3}$  events only (see Fig. 1.4).
- Finally, the  $B_s^0 \rightarrow \mu^+\mu^-$  decay [72, 73], through the value of its branching fraction is probably the most interesting on the short term. The LHCb sensitivity to this decay is presented in Chapter 5, while in the next section it is discussed from a phenomenological point of view.

## 1.4 $B_s^0 \rightarrow \mu^+\mu^-$ from a theoretical point of view

The leptonic FCNC  $B^0 \rightarrow \ell^+\ell^-$  and  $B_s^0 \rightarrow \ell^+\ell^-$  decays are particularly interesting to constrain theoretical models. Indeed, in addition to the electroweak loop suppression discussed in Section 1.3, within the SM, those decay rates are helicity suppressed by a factor

$$\left( \frac{m_\ell}{m_{B_{(s)}^0}} \right)^2, \quad (1.20)$$

where  $m_\ell$  and  $m_{B_{(s)}^0}$  are the charged lepton and  $B_{(s)}^0$  meson masses.

From a theoretical point of view, all six  $B_{(s)}^0 \rightarrow \ell^+\ell^-$  decay amplitudes, with  $\ell = e, \mu, \tau$ , are interesting. In the SM, the branching fraction values of these six decays are related to each other in a simple way, which is not necessarily the case in NP models, providing a good motivation for the branching fraction measurement of the six decays. However, all of those decays are not equally experimentally accessible. The branching fractions are indeed proportional to the mass squared of the leptons. Thus, decays into electrons have much smaller branching fractions than the others, making them less accessible. The two decays with  $\tau$  final states are difficult to measure because  $\tau$  leptons are short-lived (see Table 1.1) and their decays produce neutrinos,

which are difficult to measure. For these reasons, the muonic decays are the most accessible experimentally. While the  $B^0$  production is expected to be 4 times larger than the  $B_s^0$  production, the  $B^0$  muonic decay is suppressed relatively to the  $B_s^0$  decay by a factor  $|V_{td}/V_{ts}|^2 \sim \mathcal{O}(10^{-2})$  in the SM, so that  $B^0 \rightarrow \mu^+ \mu^-$  is much less probable than  $B_s^0 \rightarrow \mu^+ \mu^-$ . For all these reasons, LHCb is currently focusing on the latter decay only.

In the following sections we will present predictions for the  $B_s^0 \rightarrow \mu^+ \mu^-$  branching fraction for different theoretical frameworks. The SM prediction will be treated in Section 1.4.1, while predictions of frameworks beyond the SM constitute Sections 1.4.2 to 1.4.9. Some more exotic theoretical scenarios, such as the topcolour-assisted technicolour (TC2) [74, 75], are not presented even though they provide prediction for this branching fraction [76].

#### 1.4.1 Standard Model Prediction

The decays  $B_{(s)}^0 \rightarrow \ell^+ \ell^-$  are FCNC processes. As explained in the Section 1.3, such processes are forbidden at tree level in the SM, and this by construction.

To describe the behaviour of those decays, one employs a tool of QFT, the Operator Product Expansion (OPE) [77, 78], to express an effective Hamiltonian [79]. In that framework, the amplitude  $A$  for a process, such as a weak decay, can be written as [80]

$$A \propto \langle H_{\text{eff}} \rangle = \sum_i C_i(\mu) \langle \mathcal{O}_i(\mu) \rangle, \quad (1.21)$$

where  $\mathcal{O}_i$  are local operators and  $C_i$  are so-called Wilson coefficients. Both depend on the QCD renormalisation scale  $\mu$ , and the Wilson coefficients also depend on the  $W$  and top quark masses. Intuitively, this sum can be viewed as the effective Hamiltonian of the process considered, with  $\mathcal{O}_i$  the effective vertices and  $C_i$  their coupling constants. The goal of the OPE is to separate the full problem into two parts: the long-distance contributions contained in the operator matrix elements  $\mathcal{O}_i$  and the short-distance physics described by the Wilson coefficients. The renormalisation scale  $\mu$  separates the two regimes and its value can be chosen depending on the particular process studied. The  $\mathcal{O}_i$  deal with the low-energy strong interaction and their estimation represents a difficult problem for theorists. They usually constitute the main theoretical uncertainty in weak decays, but for a few particular cases, such as the  $B_s^0 \rightarrow \mu^+ \mu^-$  decay. In this case, the matrix elements can be expressed completely in terms of the meson decay constant, avoiding the problem of long distance QCD. Oppositely, short-distance QCD interactions can be computed perturbatively, leading to a good theoretical prediction for the Wilson coefficients.

Using the unitarity of the CKM matrix and omitting terms proportional to  $V_{ub}V_{us}^*/V_{tb}V_{ts}^* \sim \mathcal{O}(10^{-2})$ , one can write [81]

$$H_{\text{eff}} = -\frac{4G_F}{\sqrt{2}} V_{tb}V_{ts}^* \left\{ \sum_i C_i^{(\prime)} \mathcal{O}_i^{(\prime)} + C_P^{(\prime)} \mathcal{O}_P^{(\prime)} + C_S^{(\prime)} \mathcal{O}_S^{(\prime)} \right\}, \quad (1.22)$$

where  $G_F$  is the Fermi constant. The operators  $\mathcal{O}_x^{(\prime)}$  ( $x = i, P, S$ ) are conventionally defined, with the prime referring to chirality flip of the quark current.

Most of the operators in Eq. (1.22) vanish when one considers the purely leptonic  $B_{(s)}^0 \rightarrow \ell^+ \ell^-$

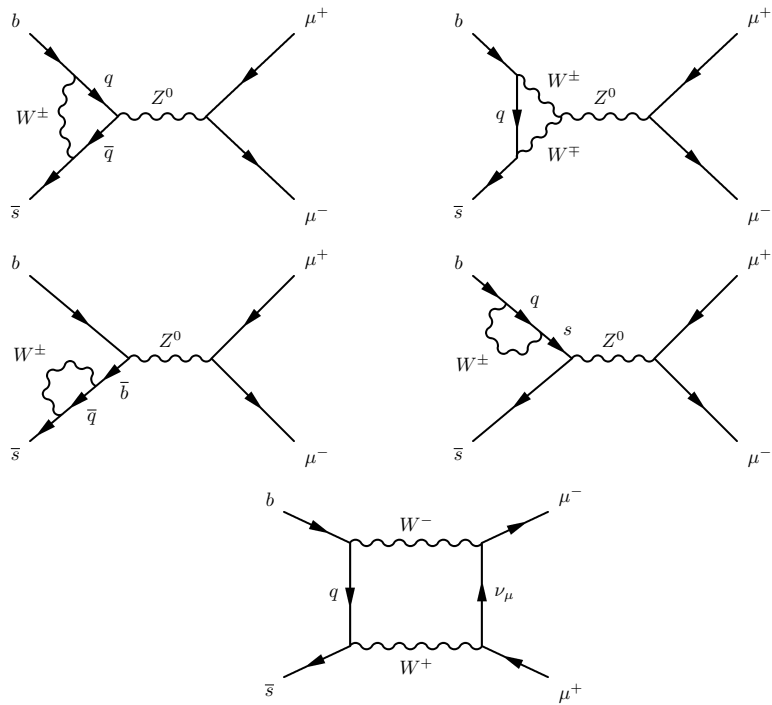


Figure 1.5: Dominant Feynman diagrams for  $\bar{B}_s^0 \rightarrow \mu^+ \mu^-$  in the SM.

decays<sup>13</sup>, and only three operators remain:

$$\begin{aligned} \mathcal{O}_{10} &\equiv \mathcal{O}_A = \frac{e^2}{16\pi^2} (\bar{s}\gamma^\mu P_L b)(\bar{\ell}\gamma_\mu\gamma_5\ell), \\ \mathcal{O}_P &= \frac{e^2}{16\pi^2} m_b(\bar{s}P_R b)(\bar{\ell}\gamma_5\ell), \\ \mathcal{O}_S &= \frac{e^2}{16\pi^2} m_b(\bar{s}P_R b)(\bar{\ell}\ell). \end{aligned} \quad (1.23)$$

The self-energy,  $Z^0$ -penguins and  $W$ -box diagrams shown in Fig. 1.5 form the dominant contributions to these decays, and contribute only to the  $\mathcal{C}_{10}$  Wilson coefficient [82, 83]. There exist contributions from Higgs penguin to  $\mathcal{C}_S$  [84] and from would-be neutral pseudo-scalar Goldstone boson to  $\mathcal{C}_P$  [85]. However, because the Higgs-muon Yukawa coupling is so small ( $\propto \frac{m_\ell}{M_W}$ ), those two Higgs penguin contributions to the decay amplitude can be safely neglected in the SM. This is not necessarily true in extensions of the SM where  $\mathcal{C}_S$  and  $\mathcal{C}_P$  can become very important as

<sup>13</sup> $\mathcal{O}_1$ – $\mathcal{O}_6$  are four-quark operators, and as such do not contribute.  $\mathcal{O}_7$  and  $\mathcal{O}_8$  are tensor operators, which vanish when taken between the  $B_{(s)}^0$  and vacuum state:

$$\langle 0 | \bar{b} \sigma_{\mu\nu} s | B_{(s)}^0 \rangle = 0.$$

$\mathcal{O}_9$  does not contributes because it vanishes when contracted with the  $B_{(s)}^0$  momentum:

$$p^\mu(\bar{\ell}\gamma^\mu\ell) = (p_\ell^\mu + p_{\bar{\ell}}^\mu)(\bar{\ell}\gamma^\mu\ell) = m_\ell(\bar{\ell}\ell) - m_{\bar{\ell}}(\bar{\ell}\ell) = 0.$$

Finally, right-handed operators, in particular  $\mathcal{O}'_S$  and  $\mathcal{O}'_P$ , do not contribute either, because their contribution, proportional to  $m_s$ , is negligible compared to the left-handed operator contributions proportional to  $m_b$ .

discussed in the following sections. Thus, one gets in the SM:

$$\mathcal{B}(B_{(s)}^0 \rightarrow \ell^+ \ell^-) = \frac{G_F^2 \alpha^2}{16\pi^3 \sin^4 \theta_W} |V_{tb} V_{ts}^*|^2 \tau_{B_{(s)}^0} m_{B_{(s)}^0} f_{B_{(s)}^0}^2 m_\ell^2 \sqrt{1 - \frac{4m_\ell^2}{m_{B_{(s)}^0}^2}} \mathcal{C}_{10}^2 \quad (1.24)$$

where  $\tau_{B_{(s)}^0}$ ,  $m_{B_{(s)}^0}$  and  $f_{B_{(s)}^0}$  are respectively the lifetime, mass and decay constant of the  $B_{(s)}^0$  and  $m_\ell$  is the lepton mass.

Numerically, with the 0.5 % accurate NLO prediction

$$\mathcal{C}_{10} = 0.9636 \left[ \frac{80.4 \text{ GeV}/c^2}{M_W} \frac{\bar{m}_t}{164 \text{ GeV}/c^2} \right]^{1.52}, \quad (1.25)$$

one gets the following SM prediction for the  $B_s^0 \rightarrow \mu^+ \mu^-$  branching fraction [86]

$$\mathcal{B}(B_s^0 \rightarrow \mu^+ \mu^-) = (3.86 \pm 0.15) \times 10^{-9} \times \frac{\tau_{B_s^0}}{1.527 \text{ ps}} \left[ \frac{|V_{ts}|}{0.0408} \right]^2 \left[ \frac{f_{B_s^0}}{240 \text{ MeV}} \right]^2. \quad (1.26)$$

In the latter equation, the less known factors have been factored out; in particular, the hadronic uncertainties are included in the decay constant.

Alternatively, the CKM dependencies and hadronic uncertainties can be eliminated by expressing the branching fraction as a function of  $\Delta M_{B_{(s)}^0}$ , the  $B_{(s)}^0 - \bar{B}_{(s)}^0$  meson mass difference.

In the process, ones trades  $f_{B_{(s)}^0}$  for a less uncertain bag parameter  $\hat{B}_{B_{(s)}^0}$  and one gets [87, 88]

$$\mathcal{B}(B_{(s)}^0 \rightarrow \mu^+ \mu^-) = (1.70 \pm 0.09) \times 10^{-10} \frac{\tau_{B_{(s)}^0}}{\hat{B}_{B_{(s)}^0}} \Delta M_{B_{(s)}^0}, \quad (1.27)$$

which gives<sup>14</sup>

$$\mathcal{B}(B_s^0 \rightarrow \mu^+ \mu^-) = (3.35 \pm 0.32) \times 10^{-9}. \quad (1.28)$$

We use the latter value as the SM prediction in this document.

The SM predictions and the most stringent experimental upper limits for the three  $B^0 \rightarrow \ell^+ \ell^-$  decays and the three  $B_s^0 \rightarrow \ell^+ \ell^-$  decays are gathered in Table 1.7 and Table 1.8, respectively.

---

<sup>14</sup>The prediction (1.28) is computed with  $\hat{B}_{B_s^0} = 1.30 \pm 0.10$ ,  $\tau_{B_s^0} = (1.466 \pm 0.059) \times 10^{-12} \text{ s}$  and  $\Delta M_{B_s^0} = (17.33 \pm 0.42) \times 10^{12} \text{ s}^{-1}$  as in Ref. [88].

As of beginning 2010, considering the update from lattice QCD computation [89] for  $\hat{B}_{B_s^0} = 1.33 \pm 0.06$  and current values from Ref. [10] for  $\tau_{B_s^0} = (1.425 \pm 0.041) \times 10^{-12} \text{ s}$  and  $\Delta M_{B_s^0} = (17.77 \pm 0.12) \times 10^{12} \text{ s}^{-1}$ , one gets rather [90]

$$\mathcal{B}(B_s^0 \rightarrow \mu^+ \mu^-) = (3.2 \pm 0.2) \times 10^{-9}.$$

Table 1.7: SM predictions and current best experimental 90 % C.L. upper limits on the  $B^0 \rightarrow \ell^+ \ell^-$  branching fractions.

Mode	$B^0 \rightarrow e^+ e^-$	$B^0 \rightarrow \mu^+ \mu^-$	$B^0 \rightarrow \tau^+ \tau^-$
SM prediction	$(2.49 \pm 0.09) \times 10^{-15}$ [86]	$(1.03 \pm 0.09) \times 10^{-10}$ [88]	$(2.23 \pm 0.08) \times 10^{-8}$ [86]
90 % C.L. limit experiment	$< 1.5 \times 10^{-8}$ [91]	$< 6.0 \times 10^{-9}$ [92]	$< 4.1 \times 10^{-3}$ [93]
	CDF	CDF	BABAR

Table 1.8: SM predictions and current best experimental 90 % C.L. upper limits on the  $B_s^0 \rightarrow \ell^+ \ell^-$  branching fractions.

Mode	$B_s^0 \rightarrow e^+ e^-$	$B_s^0 \rightarrow \mu^+ \mu^-$	$B_s^0 \rightarrow \tau^+ \tau^-$
SM prediction	$(9.05 \pm 0.34) \times 10^{-14}$ [86]	$(3.35 \pm 0.32) \times 10^{-9}$ [88]	$(8.2 \pm 0.31) \times 10^{-7}$ [86]
90 % C.L. limit experiment	$< 5.4 \times 10^{-5}$ [94]	$< 3.6 \times 10^{-8}$ [92]	—
	L3	CDF	—

#### 1.4.2 Two Higgs Doublet Model

The Higgs mechanism is introduced to break the symmetry and yield mass to particles. The only experimental evidence of the Higgs sector is the fact that particles have masses. However, there is not yet any experimental support for the particular implementation — one doublet of complex scalar fields — chosen in Section 1.1.1. This choice constitutes the minimal Higgs scenario, *i.e.* the most simple field configuration that achieves what is required. It is however possible that more complicated Higgs scenarios exist instead, both in the context of the SM and beyond, as in the MSSM, actually containing two Higgs doublets.

The minimal extension of the Higgs sector is the SM with two Higgs Doublets Model (2HDM), which we describe here, relying on Ref. [95]. In this model, one introduces two complex doublet scalar fields:

$$\Phi_1 = \begin{pmatrix} \phi_1^+ \\ \phi_1^0 \end{pmatrix} \quad \text{and} \quad \Phi_2 = \begin{pmatrix} \phi_2^+ \\ \phi_2^0 \end{pmatrix} \quad (1.29)$$

with vacuum expectation values

$$\langle \phi_1^0 \rangle = \frac{1}{\sqrt{2}} \begin{pmatrix} 0 \\ v_1 \end{pmatrix} \quad \text{and} \quad \langle \phi_2^0 \rangle = \frac{1}{\sqrt{2}} \begin{pmatrix} 0 \\ v_2 \end{pmatrix} \quad (1.30)$$

which can be rotated by an angle  $\beta$  to get five physical Higgs bosons:

- two charged states, with same masses,

$$H^\pm = -\phi_1^\pm \sin \beta + \phi_2^\pm \cos \beta \quad (1.31)$$

- a  $\mathcal{CP}$ -odd neutral state, pseudo-scalar,

$$A^0 = \sqrt{2}(-Im(\phi_1^0) \sin \beta + Im(\phi_2^0) \cos \beta) \quad (1.32)$$

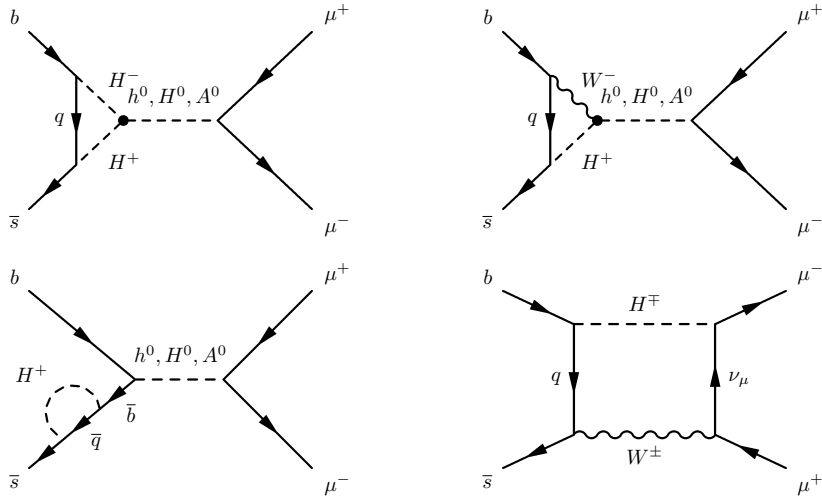


Figure 1.6: Dominant Feynman diagrams for  $\bar{B}_s^0 \rightarrow \mu^+ \mu^-$  in the 2HDM with large  $\tan \beta$  value. Modified from Ref. [101].

- and two  $\mathcal{CP}$ -even neutral states, that mix together with angle  $\alpha$ , conventionally named  $h^0$  and  $H^0$ , so that  $m_{h^0} < m_{H^0}$ ,

$$\begin{aligned} h^0 &= \sqrt{2}(-(Re(\phi_1^0) - v_1) \sin \alpha + (Re(\phi_2^0) - v_2) \cos \alpha) \\ H^0 &= \sqrt{2}((Re(\phi_1^0) - v_1) \cos \alpha + (Re(\phi_2^0) - v_2) \sin \alpha) \end{aligned} \quad (1.33)$$

- Three would-be Goldstone bosons, usually noted  $G^\pm$  and  $G^0$ , are absorbed by the  $W^\pm$  and  $Z^0$  bosons.

The ratio of the vacuum expectation values,  $\tan \beta = \frac{v_1}{v_2}$ , is a key parameter of the model. Instead of the one free parameter in the minimal Higgs, the Higgs mass, one has six free parameters: four Higgs masses,  $\tan \beta$ , and the Higgs mixing angle  $\alpha$ . There are two different models, depending on the Higgs–quarks interaction. In model 2HDM-I, quarks and leptons do not couple to the first Higgs doublet  $\Phi_1$ , but only to the second doublet  $\Phi_2$ , analogously to the SM minimal Higgs model. In model 2HDM-II,  $\Phi_1$  couples only to the down-type quarks and charged leptons and  $\Phi_2$  couples only to the up-type quarks and neutrinos.

Measurements of  $\mathcal{B}(B \rightarrow X_s \gamma)$  provide the main constraints on  $M_{H^\pm}$ . Results from Belle [96] and BABAR [97], compiled by HFAG [98]<sup>15</sup> lead to the lower limit  $M_{H^\pm} > 295$  GeV at 95 % C.L. [100].

The computation of the  $\mathcal{C}_{10}$ ,  $\mathcal{C}_S$ , and  $\mathcal{C}_P$  Wilson coefficients in the framework of the 2HDM-II was done in Refs [81, 101].  $\mathcal{C}_{10}$  is found unchanged with respect to its SM value. However, in the large  $\tan \beta$  limit,  $\mathcal{C}_P$  and  $\mathcal{C}_S$  receive sizable contributions from box and penguins diagrams involving  $H^\pm$  and  $W^\pm$  and from self-energy diagrams with neutral exchange, as shown in Fig. 1.6. The 2HDM-II specific Wilson coefficients read

$$\mathcal{C}_S = \mathcal{C}_P = \frac{m_\mu}{2M_W^2} \tan^2 \beta \frac{\ln r}{r - 1}, \quad \text{with} \quad r = \frac{M_{H^\pm}^2}{m_t^2}. \quad (1.34)$$

<sup>15</sup>The most recent HFAG publication [99] gives a very similar value for  $\mathcal{B}(B \rightarrow X_s \gamma)$ , leaving the constraints on  $M_{H^\pm}$  unchanged.

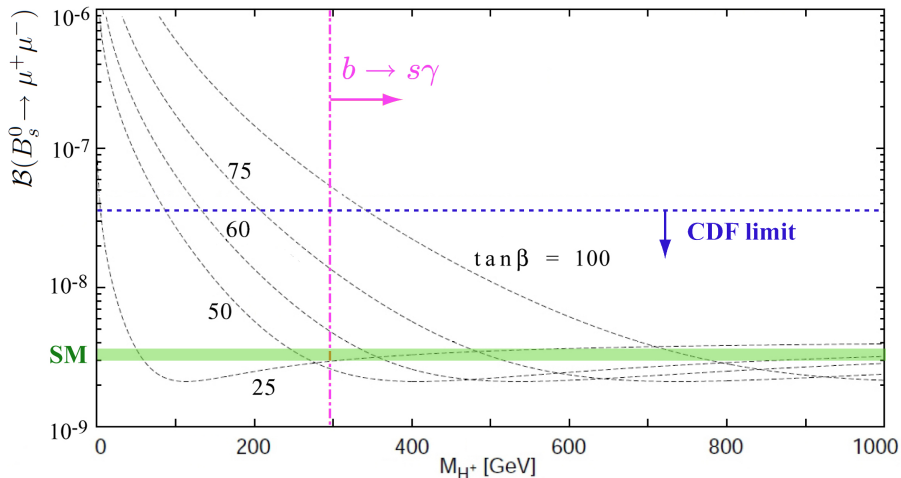


Figure 1.7:  $\mathcal{B}(B_s^0 \rightarrow \mu^+ \mu^-)$  in the 2HDM as a function of  $M_{H^\pm}$  for different values of  $\tan\beta$ . Modified from Ref. [101]. The current experimental upper limit [91] and the SM prediction for  $\mathcal{B}(B_s^0 \rightarrow \mu^+ \mu^-)$  [88] are shown as a dashed horizontal line and as a coloured area respectively. The lower bound on  $M_{H^\pm}$  coming from  $b \rightarrow s\gamma$  [100] is shown with a dot-dashed vertical line.

These coefficients depend only on two of the 2HDM parameters,  $\tan\beta$  and  $M_{H^\pm}$ , and thus the impact on  $\mathcal{B}(B_s^0 \rightarrow \mu^+ \mu^-)$  is easy to understand. The branching fraction gets proportional to  $\tan^4\beta \ln^2 r / (r-1)^2$ . Figure 1.7 shows the value of  $\mathcal{B}(B_s^0 \rightarrow \mu^+ \mu^-)$  in the 2HDM-II as a function of  $M_{H^\pm}$  for different values of  $\tan\beta$ . The constraint on  $M_{H^\pm}$  coming from  $b \rightarrow s\gamma$  is also shown. An enhancement with respect to the SM prediction exists only for very large  $\tan\beta$  value, and relatively light  $H^\pm$ . The constraint of  $M_{H^\pm}$  leads to a lower limit  $\tan\beta > 55$ , for a 2HDM-II contribution to be visible. With increasing  $M_{H^\pm}$  or decreasing  $\tan\beta$ , the branching fraction drops below the SM prediction.

### 1.4.3 Minimal Flavour Violation

It is popular these days to see the SM as an effective field theory valid up to a scale  $\Lambda$ , larger than the EW scale. From a naturalness argument (discussed in Section 1.2.1), this scale  $\Lambda$  is expected not to exceed a few TeV. If such a cut-off scale existed at the TeV level, deviations from the SM should have been seen in loop-induced flavour-violating processes. The Minimal Flavour Violation (MFV) [102] hypothesis explains the lack of observation. This hypothesis takes the Yukawa couplings as the only relevant breaking source for the  $SU(3)^5$  flavour symmetry also beyond the SM<sup>16</sup>. Thus, flavour mixing is still governed by the CKM matrix. Under

<sup>16</sup>The  $SU(3)^5$  is the largest group of unitary fields transformations that commute with the gauge group. It can be decomposed as

$$SU(3)_q^3 \otimes SU(3)_\ell^2 \otimes U(1)_B \otimes U(1)_L \otimes U(1)_Y \otimes U(1)_{\text{PQ}} \otimes U(1)_{E_R},$$

where

$$\begin{aligned} SU(3)_q^3 &= SU(3)_{Q_L} \otimes SU(3)_{U_R} \otimes SU(3)_{D_R} \\ SU(3)_\ell^2 &= SU(3)_{L_L} \otimes SU(3)_{E_R}. \end{aligned}$$

Three of the  $U(1)$  charges can be identified with baryon ( $B$ ) and lepton ( $L$ ) numbers and hypercharge ( $Y$ ). The  $U(1)_{\text{PQ}}$  and  $U(1)_{E_R}$  groups are related to  $D_R$  and  $E_R$  and to  $E_R$ , respectively.

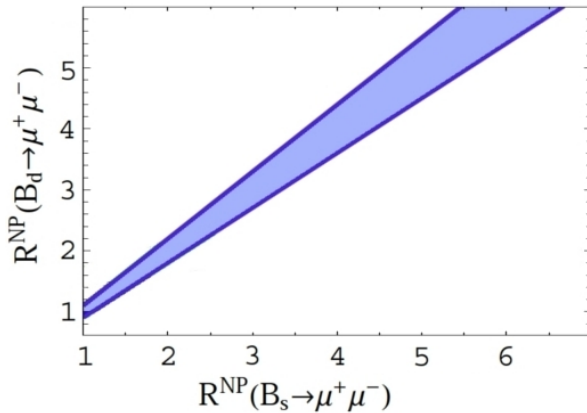


Figure 1.8: Correlation between  $\mathcal{B}(B_s^0 \rightarrow \mu^+\mu^-)$  and  $\mathcal{B}(B^0 \rightarrow \mu^+\mu^-)$  in the MFV hypothesis. The shaded area shows the range of  $\mathcal{B}(B^0 \rightarrow \mu^+\mu^-)$  as a function of  $\mathcal{B}(B_s^0 \rightarrow \mu^+\mu^-)$ , both normalised to their SM prediction. Modified from Ref. [104].

this assumption, non-standard contributions are suppressed to a level compatible with current observations also for  $\Lambda \simeq \mathcal{O}(1 \text{ TeV})$ . The constrained version of the MFV (CMFV) [103] further assumes no new flavour-changing operators besides the SM ones.

The main interest of the MFV model is that it allows a natural development of an effective theory for NP. While, by construction, NP predictions are much less dramatically different from SM ones than within other frameworks, the MFV hypothesis allows to establish an unambiguous relation between rare decays. The most constraining is the ratio [104]

$$\frac{\mathcal{B}(B_s^0 \rightarrow \ell^+\ell^-)}{\mathcal{B}(B^0 \rightarrow \ell^+\ell^-)} = \frac{f_{B_s^0} m_{B_s^0}}{f_{B^0} m_{B^0}} \left| \frac{V_{ts}}{V_{td}} \right|^2 + \mathcal{O}\left(\frac{m_s}{m_b}\right), \quad (1.35)$$

where  $f_{B_{(s)}^0}$  is the  $B_{(s)}^0$  decay constant,  $m_{B_{(s)}^0}$  the  $B_{(s)}^0$  mass and  $V_{tx}$  are CKM matrix elements. Figure 1.8 shows the relation between the  $B_s^0 \rightarrow \mu^+\mu^-$  and  $B^0 \rightarrow \mu^+\mu^-$  branching fractions with MFV.

As a conclusion, an enhancement of both  $\mathcal{B}(B_s^0 \rightarrow \ell^+\ell^-)$  and  $\mathcal{B}(B^0 \rightarrow \ell^+\ell^-)$  respecting the ratio of in Eq. (1.35) would be an unambiguous signature of MFV at large  $\tan\beta$  [86].

#### 1.4.4 MSSM with Anomaly Mediated Symmetry Breaking

AMSB employs the conformal anomalies that always arise when one tries to eliminate auxiliary background field from a softly broken Lagrangian, by making a Weyl rescaling [45]. The main point is that such anomalies are always present in a broken supersymmetric theory, whatever the nature of the breaking. The AMSB uses those anomalies to explain the masses of the gauginos, the soft supersymmetry breaking scalars and the trilinear coupling. It yields a very distinctive mass spectrum, in which the LSP is the neutral Wino and is therefore a Dark Matter candidate. The minimal AMSB approach has three parameters and a sign [105]:

$$\tan\beta, \quad m_{3/2}, \quad m_0, \quad \text{and} \quad \text{sign}(\mu),$$

with  $m_{3/2}$  the vacuum expectation of the auxiliary field,  $m_0$  a parameter used to avoid negative sleptons squared masses.  $\mu$ , which has the dimension of a mass, corresponds to a mass term for the two Higgs superfields in the superpotential.

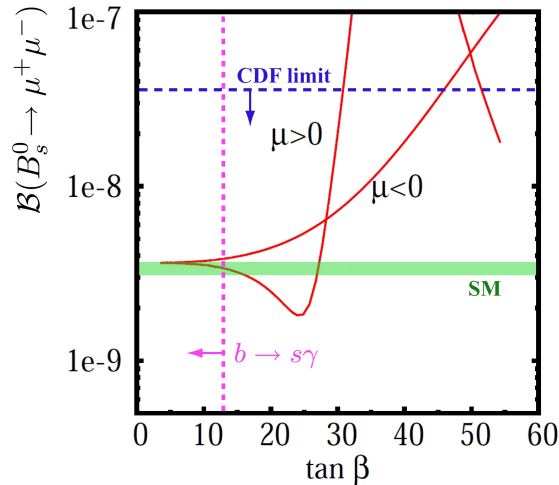


Figure 1.9:  $\mathcal{B}(B_s^0 \rightarrow \mu^+ \mu^-)$  as a function of  $\tan \beta$  in AMSB for  $m_{3/2} = 40$  TeV and either signs of  $\mu$ . The horizontal (dashed) line is the current experimental upper limit for  $\mathcal{B}(B_s^0 \rightarrow \mu^+ \mu^-)$ , the coloured area its SM prediction [88], and the vertical (dotted) line is the constraint coming from the  $b \rightarrow s\gamma$  measurements in the AMSB model [106]. Modified from Ref. [106].

In the frame of the AMSB, the measurement of the muon anomalous magnetic moment [22] is only compatible with a  $\mu > 0$  scenario. Furthermore, the  $b \rightarrow s\gamma$  measurements [99] bring a stringent constraint to the model. Under those conditions, the prediction for the  $\mathcal{B}(B_s^0 \rightarrow \mu^+ \mu^-)$  was computed in Ref. [106] for the AMSB realisation. In Fig. 1.9, the  $B_s^0 \rightarrow \mu^+ \mu^-$  branching fraction is depicted as a function of  $\tan \beta$  for both  $\mu$  signs and for  $m_{3/2} = 40$  TeV. Figure 1.10 shows  $\mathcal{B}(B_s^0 \rightarrow \mu^+ \mu^-)$  as a function of  $m_{3/2}$  and  $\tan \beta$ , for  $\mu < 0$  (left) and  $\mu > 0$  (right). One can see that the constraint coming from  $b \rightarrow s\gamma$  is the most stringent when  $\mu > 0$ , which is the only scenario compatible with the  $(g-2)_\mu$  result. Under those two constraints, AMSB leads to no significant enhancement of the branching fraction with respect to the SM prediction.

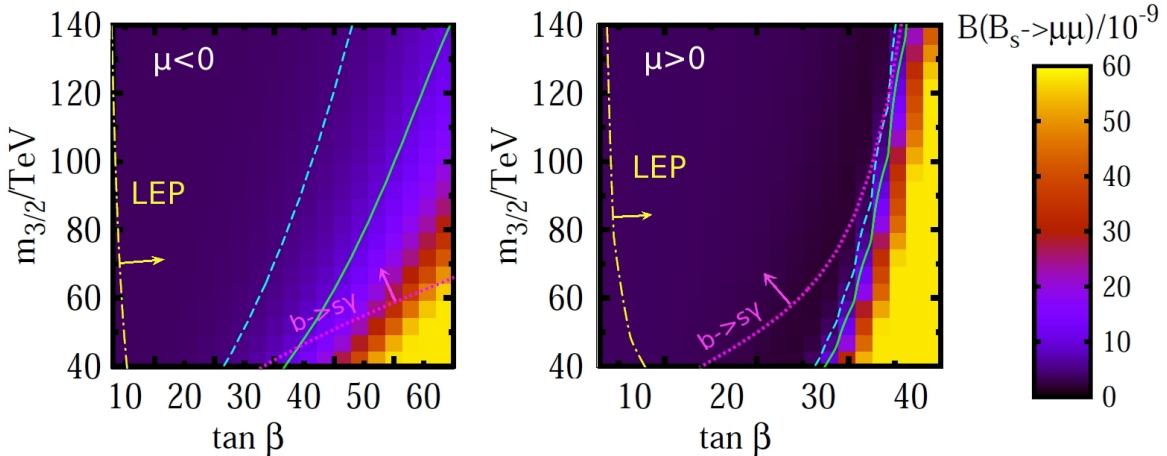


Figure 1.10:  $\mathcal{B}(B_s^0 \rightarrow \mu^+ \mu^-)$  in AMSB in the  $\tan \beta - m_{3/2}$  plane, for  $\mu < 0$  (left) and  $\mu > 0$  (right). The dot-dashed line represents the constraint coming from the LEP direct Higgs searches, the dotted line shows the constraint from the  $b \rightarrow s\gamma$  results. The solid and dashed curves define  $\mathcal{B}(B_s^0 \rightarrow \mu^+ \mu^-) = 10^{-8}$  and  $5 \times 10^{-9}$  contours, respectively. Modified from Ref. [106].

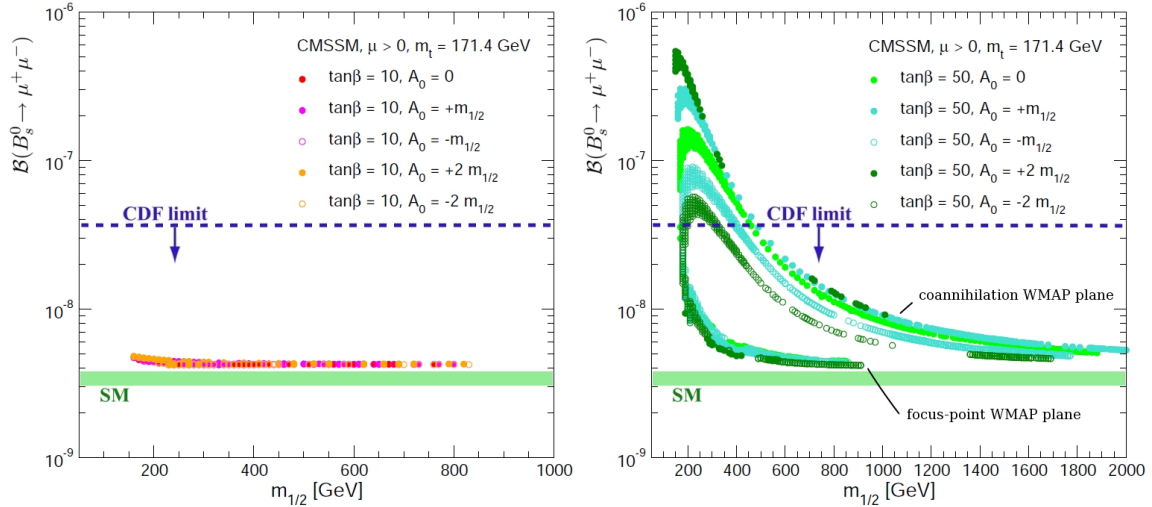


Figure 1.11: The CMSSM predictions for  $\mathcal{B}(B_s^0 \rightarrow \mu^+ \mu^-)$  as a function of  $m_{1/2}$  along the WMAP-compliant hyperplanes for  $\tan\beta = 10$  (left) and  $\tan\beta = 50$  (right) and different values of  $A_0$ . The horizontal dashed line indicates the current experimental exclusion bound, and the coloured area represents the SM prediction. Modified from Ref. [107].

#### 1.4.5 Constrained MSSM

A way to reduce the number of MSSM parameters is to assume that soft SUSY-breaking parameters are universal at GUT scale, before renormalisation. In the Constrained MSSM (CMSSM) all the soft SUSY-breaking scalar masses are assumed universal ( $= m_0$ ) at GUT scale, as are the SUSY-breaking gauginos ( $= m_{1/2}$ ) and the trilinear couplings ( $= A_0$ ) [107, 108]. Some of those assumptions are properly motivated. Universality of squarks and sleptons with the same gauge quantum numbers can explain the FCNC suppression. Some GUT scenarios require the universality of all the squarks and sleptons. Note that the CMSSM does not specify the nature of the soft SUSY-breaking mechanism. The free parameters are  $m_0$ ,  $m_{1/2}$ ,  $A_0$ ,  $\tan\beta$  and the sign of  $\mu$  [109].

In Ref. [107], the authors use precise electroweak observables,  $B$  physics observables and cosmology to further constrain the CMSSM<sup>17</sup>. The cosmological constraints lead to relations between the CMSSM parameters, defining two hyperplanes for the parameters, called coannihilation and focus-point planes. A best fit is performed on those two hyperplanes, using the electroweak and  $B$  physics measurements on input. This leads to best values of  $m_{1/2} \sim 300$  GeV and  $A_0 > 0$  at  $\tan\beta = 10$ , whereas, for  $\tan\beta = 50$ ,  $m_{1/2} \sim 500$  GeV and  $A_0 \leq 0$  are preferred. For both values of  $\tan\beta$ , the focus-point plane is disfavoured with respect to the coannihilation region.

The CMSSM predictions for the  $B_s^0 \rightarrow \mu^+ \mu^-$  branching fraction are depicted in Fig. 1.11. For  $\tan\beta = 10$  (left plot) the CMSSM prediction is not significantly above the SM prediction for all  $A_0$  values and either WMAP-compliant planes. The CMSSM coannihilation region for  $\tan\beta = 50$  (right plot) presents a strong enhancement with respect to the SM prediction, whereas the CMSSM prediction in the focus-point region is not significantly enhanced. The best-fit values  $m_{1/2} \sim 500$  GeV and  $A_0 \leq 0$  at  $\tan\beta = 50$  lead to a considerable enhancement of  $\mathcal{B}(B_s^0 \rightarrow \mu^+ \mu^-)$ .

<sup>17</sup>The electroweak inputs are the  $W$  mass, the  $Z$  width, the limit on the lightest MSSM Higgs mass, the weak mixing angle  $\sin\theta_W$ , and the anomalous magnetic moment of the muon. The  $B$  physics inputs are the branching fractions of  $b \rightarrow s\gamma$  and  $B^- \rightarrow \tau^- \bar{\nu}_\tau$ , the limit on  $\mathcal{B}(B_s^0 \rightarrow \mu^+ \mu^-)$  and the  $B_s^0$  mass mixing parameter  $\Delta m_s$ . The cosmology intervenes with the constraints on LSP from the cold dark matter density as observed by the WMAP surveys [34].

### 1.4.6 MSSM with Non-Universal Higgs Masses

The Non-Universal Higgs Masses (NUHM) model arises from the MSSM with the addition of universality assumptions, similarly to the CMSSM. However, if the universality of the scalar masses,  $m_0$ , is well motivated for squark and slepton families by the need to suppress FCNC, the universality of the Higgs masses is less motivated [110, 111]. The NUHM keeps the universality hypotheses concerning gauginos  $m_{1/2}$ , scalars  $m_0$  (but the Higgs) and trilinear couplings  $A_0$ , but does not assume universality for the Higgs masses. Consequently, the Higgs mixing parameter  $\mu$  and the mass of the  $\mathcal{CP}$ -odd neutral Higgs  $M_A$  can be treated as free parameters for any specified values of  $m_0, m_{1/2}, A_0$  and  $\tan\beta$ . This provides a good framework for the study of the phenomenology of the MSSM Higgs sector. Furthermore, electroweak observations are better accommodated with  $B$  physics observations within the NUHM than within CMSSM [107].

In Refs [107, 112], authors use electroweak,  $B$  physics and cosmology observables to further constrain the NUHM, performing a fit, and they extract a prediction for the  $B_s^0 \rightarrow \mu^+ \mu^-$  branching fraction. The constraints used are the same as those detailed in Section 1.4.5. Figure 1.13 shows such a prediction on the  $M_A$ – $\tan\beta$  plane for various combination of the other parameters. The  $B_s^0 \rightarrow \mu^+ \mu^-$  branching fraction most compatible with the best fit is at the  $2 \times 10^{-8}$  level, which represents a large enhancement with respect to the SM prediction and is very close to the current experimental upper limit.

In a recent paper [113], the use of the same input information results in a value for the preferred  $\mathcal{B}(B_s^0 \rightarrow \mu^+ \mu^-)$  at the level of the SM one, as shown in Fig. 1.12. However, it is also shown that values up to the current best limit are possible with a very gently deteriorated probability.

The NUHM potential to accommodate such large values of  $\mathcal{B}(B_s^0 \rightarrow \mu^+ \mu^-)$  is related to the fact that the heavy Higgses ( $A^0$ ,  $H^0$  and  $H^\pm$ ) can be much lighter in the NUHM than in other models.

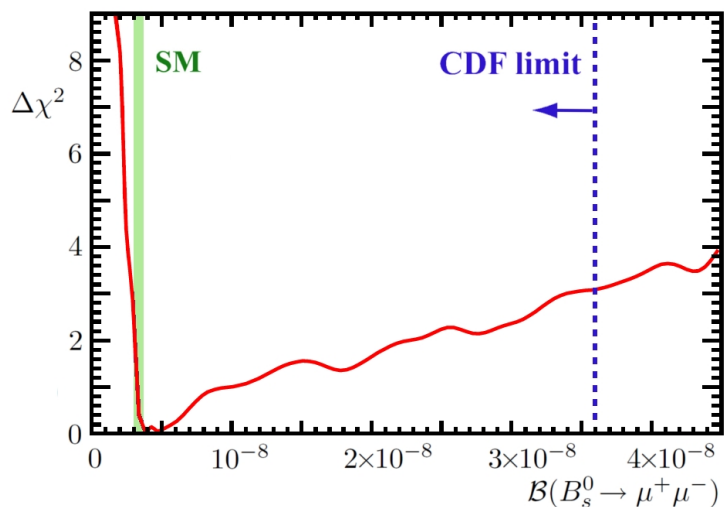


Figure 1.12: Likelihood function for the  $\mathcal{B}(B_s^0 \rightarrow \mu^+ \mu^-)$  in the NUHM, as obtained by a global fit. Modified from Ref. [113].

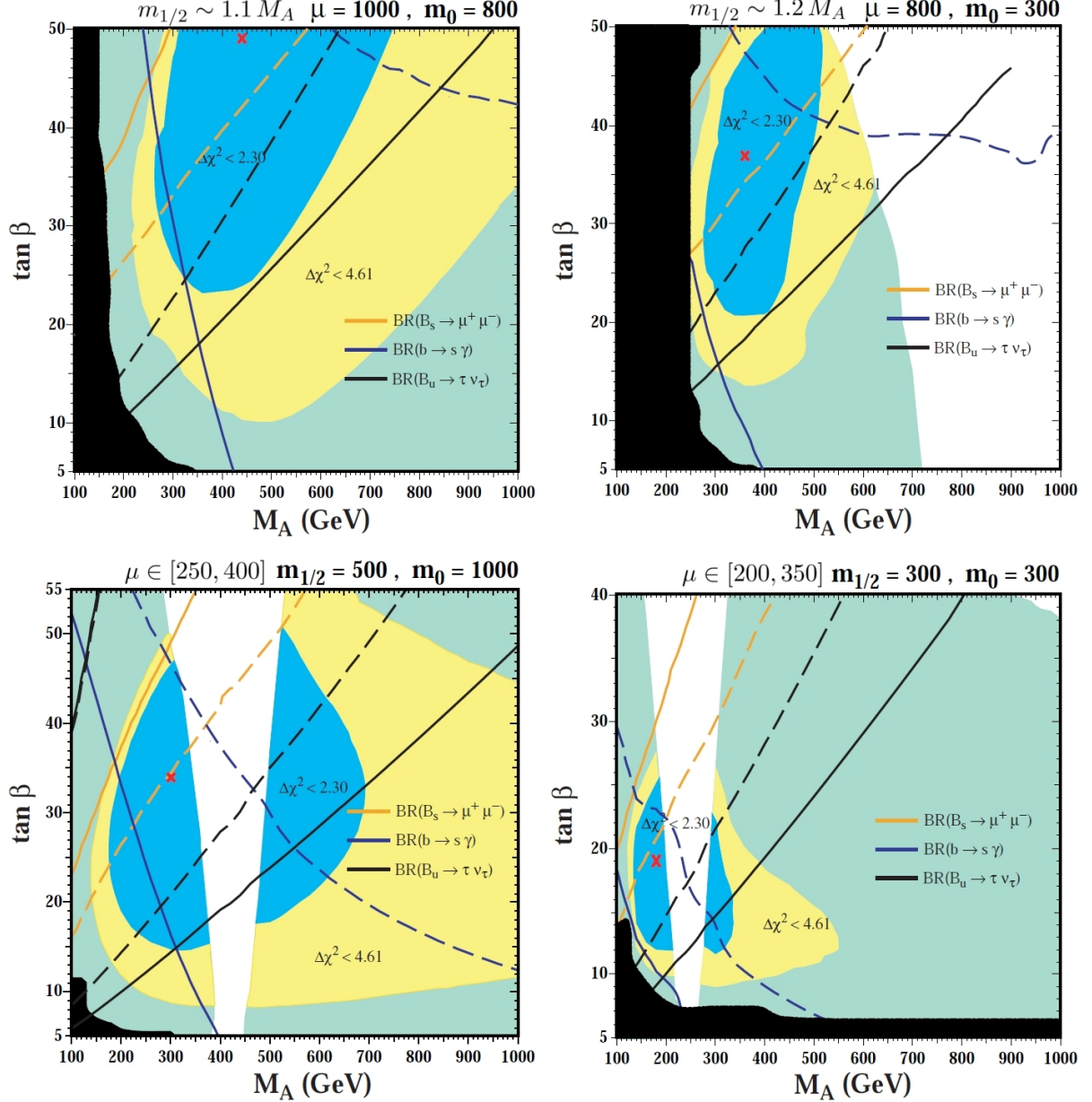


Figure 1.13:  $M_A$ - $\tan \beta$  planes for the NUHM benchmark surfaces, for  $A_0 = 0$ , and the various combination of fixed and varying parameters specified on each plot. The result of the best fit taking into account electroweak and  $B$  physics observables is pictured with the cross, and as  $\Delta\chi^2$  contours. The various lines indicate:  $\mathcal{B}(B_s^0 \rightarrow \mu^+ \mu^-) = 10^{-7} (2 \times 10^{-8})$  as solid (dashed),  $\mathcal{B}(b \rightarrow s \gamma) = 4 (3) \times 10^{-4}$  as solid (dashed),  $\frac{\mathcal{B}(B^- \rightarrow \tau \nu_\tau)_{\text{NUHM}}}{\mathcal{B}(B^- \rightarrow \tau \nu_\tau)_{\text{SM}}} = 0.9 (0.7)$  as solid (dashed). Note that the current experimental upper limit  $\mathcal{B}(B_s^0 \rightarrow \mu^+ \mu^-) < 3.6 \times 10^{-8}$  is lower than the solid orange curve. The dark-shaded (black) region corresponds to the parameter region that is excluded by the LEP Higgs searches, and the white regions corresponds to region excluded by cosmological constraints. Modified from Ref. [112].

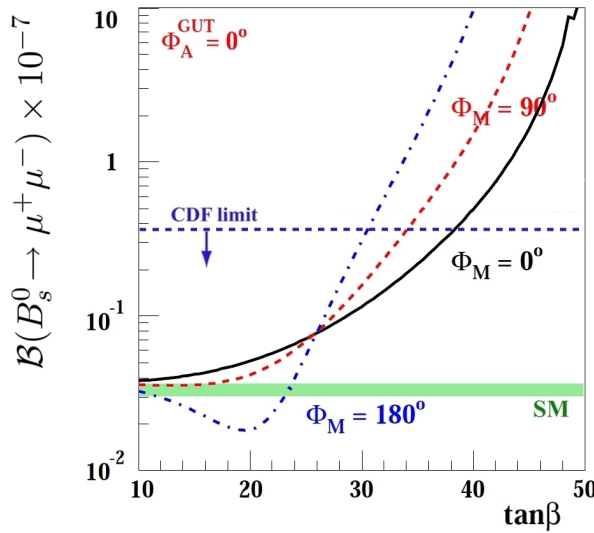


Figure 1.14: The branching fraction  $\mathcal{B}(B_s^0 \rightarrow \mu^+ \mu^-)$  in MCPMFV, as function of  $\tan \beta$ , for three values of the common phase:  $\Phi_M = 0^\circ$  (solid line),  $90^\circ$  (dashed line), and  $180^\circ$  (dot-dashed line) and for  $\Phi_A^{\text{GUT}} = 0^\circ$ . Modified from Ref. [114].

#### 1.4.7 Maximally $\mathcal{CP}$ -Violating MSSM with Minimal Flavour Violation

The Maximally  $\mathcal{CP}$ -Violating MSSM with Minimal Flavour Violation (MCPMFV) [114] extension of the MSSM aims at maximising  $\mathcal{CP}$  violation while staying in the MFV framework described in Section 1.4.3. Contrarily to the constrained MFV, which assumes no further  $\mathcal{CP}$  violating source than the one already present in the SM, the MCPMFV adds six additional  $\mathcal{CP}$ -violating phases to the SM CKM phases, by letting the three gauginos mass parameters and the three trilinear couplings to be complex. It results in 19 free parameters, six of them being the  $\mathcal{CP}$ -violating phases, in addition to the SM parameters. Such a model leads to potentially large values for the Wilson coefficients  $C_S$  and  $C_P$  and consequently an enhancement of  $\mathcal{B}(B_s^0 \rightarrow \mu^+ \mu^-)$  with respect to the SM prediction is possible.

A minimal MCPMFV realisation, imposing a unique phase for the gauginos mass parameters  $\Phi_M \equiv \Phi_1 = \Phi_2 = \Phi_3$  and for the trilinear couplings phase  $\Phi_A^{\text{GUT}} \equiv \Phi_{A_u} = \Phi_{A_d} = \Phi_{A_e}$  and reasonable CMSSM values for the 13 real parameters ( $m_0 = 250$  GeV,  $m_{1/2} = 100$  GeV, and  $A_0 = 100$  GeV), is studied in Ref. [114]. With these minimal assumptions, the authors compute predictions for rare  $B$  decays. Figure 1.14 shows how the  $B_s^0 \rightarrow \mu^+ \mu^-$  branching fraction can be largely enhanced at large  $\tan \beta$ , up to the level of the current limit. A value of  $\Phi_M \sim 60^\circ$  is favoured by the  $b \rightarrow s\gamma$  branching fraction observations.

#### 1.4.8 $\mathcal{R}$ -Parity Violating MSSM

The  $\mathcal{R}$ -Parity Violating (RPV) interaction, because of its non-trivial flavour structure, opens up the possibility of observable flavour-changing effects at the tree level. When one accounts for RPV effects, more terms contribute to the potential

$$W_R = \lambda_{ijk} L_i L_j E_k^c + \lambda'_{ijk} L_i Q_j D_k^c + \lambda''_{ijk} \bar{U}_i D_j^c \bar{D}_k + \epsilon_i L_i H_u, \quad (1.36)$$

in which  $L$  and  $Q$  are the left-handed lepton and quark superfields respectively,  $E, U, D$  are the right-handed lepton,  $u$ -type and  $d$ -type quark superfields respectively and  $i, j, k$  indices denote

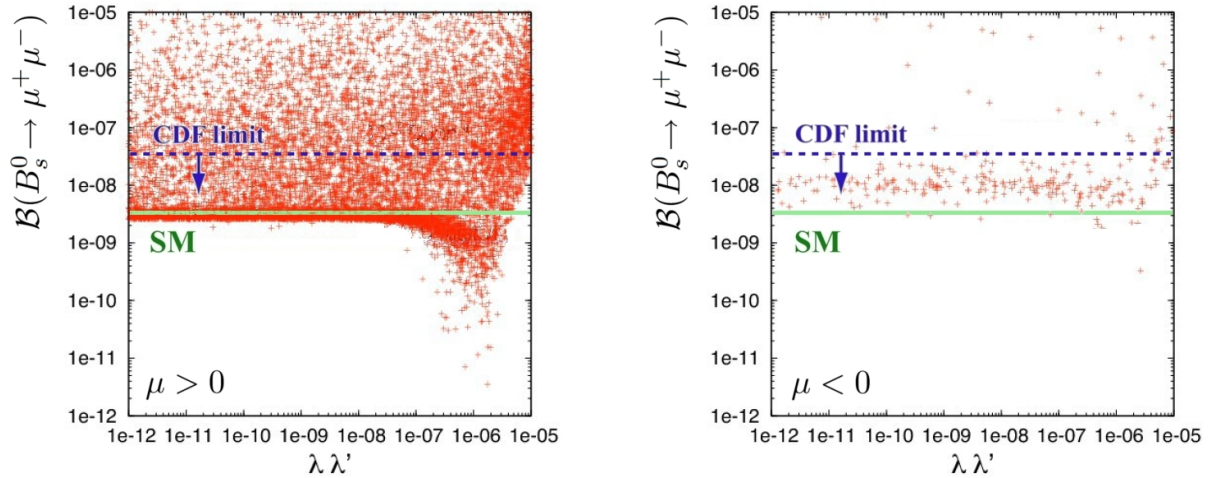


Figure 1.15: The branching fraction  $\mathcal{B}(B_s^0 \rightarrow \mu^+ \mu^-)$  in mSUGRA with  $\mathcal{R}$ -parity violation, as function of the RPV coupling product  $\lambda \lambda'$ , for either signs of  $\mu$ . The horizontal dashed line indicates the current experimental exclusion bound, and the coloured area represents the SM prediction. Modified from Ref. [115].

families. The terms proportional to the couplings  $\lambda_{ijk}, \lambda'_{ijk}$  and  $\epsilon_i$  violate the lepton number and the terms proportional to  $\lambda''_{ijk}$  violate the baryon number<sup>18</sup>.

The Wilson coefficients relevant to the  $B_s^0 \rightarrow \mu^+ \mu^-$  branching fraction arising from RPV were computed as [116, 117]

$$\begin{aligned} \mathcal{C}_P^{\mathcal{R}} &= \frac{\sqrt{2}\pi}{G_F \alpha V_{tb} V_{ts}^*} \sum_{i=1}^3 \frac{\lambda_{i\mu\mu}^* \lambda'_{i23} + \lambda_{i\mu\mu} \lambda''_{i32}^*}{m_{\tilde{\nu}_i}^2}, \\ \mathcal{C}_S^{\mathcal{R}} &= \frac{\sqrt{2}\pi}{G_F \alpha V_{tb} V_{ts}^*} \sum_{i=1}^3 \frac{\lambda_{i\mu\mu}^* \lambda'_{i23} - \lambda_{i\mu\mu} \lambda''_{i32}^*}{m_{\tilde{\nu}_i}^2}, \\ \mathcal{C}_{10}^{\mathcal{R}} &= \frac{\sqrt{2}\pi}{4G_F \alpha V_{tb} V_{ts}^*} \sum_{m,n,i=1}^3 \frac{V_{ni}^* V_{im} \lambda'_{\mu n3} \lambda''_{\mu m2}^*}{m_{\tilde{u}_i}^2}, \end{aligned} \quad (1.37)$$

where a  $\mu$  index represents a muon final state. One notes that there exists no contribution from  $\epsilon$  nor  $\lambda''$  couplings to the Wilson coefficients.

In Ref. [115], a prediction for  $\mathcal{B}(B_s^0 \rightarrow \mu^+ \mu^-)$  is given for the mSUGRA breaking scenario, including RPV contributions. It is further assumed that  $\lambda_{ijk} = \lambda$  and  $\lambda'_{ijk} = \lambda'$  at the electroweak scale. Constraints from electroweak observables — the bound on the supersymmetric contribution to the  $\rho$  parameter and the muon anomalous magnetic moment —, from  $B$  physics — the bounds on  $b \rightarrow s\gamma$  branching fraction —, from the LEP bound on the lightest neutral Higgs mass, and from the limit  $\lambda \lambda' < 10^{-5}$  from the constraints on the  $\mathcal{R}$ -parity are considered. Figure 1.15 shows the possible values of  $\mathcal{B}(B_s^0 \rightarrow \mu^+ \mu^-)$  in RPV mSUGRA as a function of  $\lambda \lambda'$ . One observes that a considerable enhancement is possible, although the most probable value is very close to the SM for  $\lambda \lambda' < 10^{-8}$ . Interestingly, for large  $\lambda \lambda'$  the branching fraction could be so suppressed that this decay would not be observed at LHC.

<sup>18</sup>The couplings  $\lambda_{ijk}$  and  $\lambda''_{ijk}$  are antisymmetric in the first and last two indices, respectively. This yields 45 independent coupling constants: 9 from  $\lambda_{ijk} + 27$  from  $\lambda'_{ijk} + 9$  from  $\lambda''_{ijk}$ .

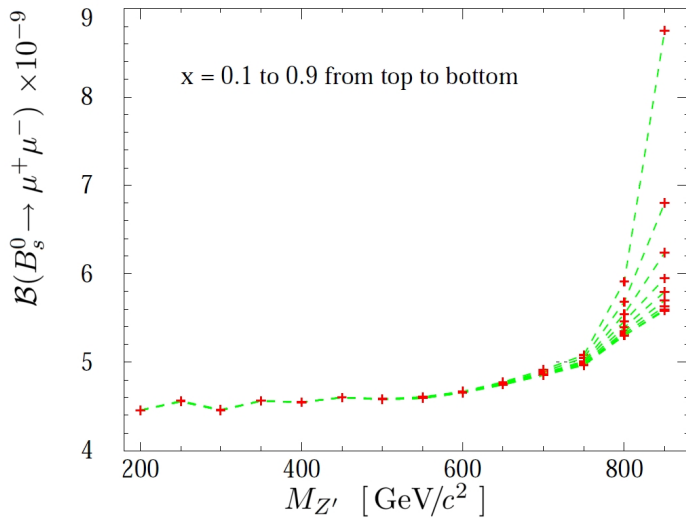


Figure 1.16: Dependence of the 95 % C.L. upper limit of  $\mathcal{B}(B_s^0 \rightarrow \mu^+ \mu^-)$  on  $M_{Z'}$ , for  $x$  ranging from 0.1 to 0.9.  $x$  denotes the ratio between the  $Z'$  coupling to the third family of left-handed quarks and to the first two families [120].

#### 1.4.9 $Z'$ Models

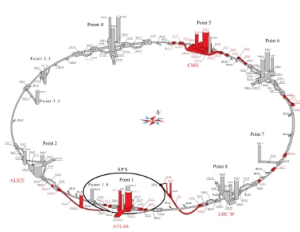
The existence of a bosonic neutral resonance, with a mass larger than the one of  $Z^0$  is predicted in a large number of models, such as Grand Unified Theories, superstring theories, and theories with extra dimensions [118]. Its nature differs among those models, particularly its spin, nevertheless it is generically called  $Z'$ . In some cases, this  $Z'$  is a new neutral gauge boson arising from an extension of the SM gauge group [119].

In Ref. [120], the effect of a string-inspired  $Z'$  on the  $B_s^0 \rightarrow \mu^+ \mu^-$  branching fraction is assessed. Using the 95 % C.L. upper limit on  $\sigma(Z') \times \mathcal{B}(Z' \rightarrow e^- e^+)$  from CDF, the resulting upper limit on  $\mathcal{B}(B_s^0 \rightarrow \mu^+ \mu^-)$  is plotted in Fig. 1.16. The maximal enhancement, found at large  $Z'$  mass, is about  $9 \times 10^{-9}$  for some part of the parameter space.



## Chapter 2

# CERN, the LHC Machine and its Experiments



CERN, the European Organisation for Nuclear Research, is an international laboratory which houses accelerators and experiments, and aims at probing the nature of matter. The CERN Laboratory sits astride the Franco-Swiss border near Geneva. The latest of CERN's accelerator is the Large Hadron Collider; it will accelerate and force protons to collide at the heart of four large detectors spread on the LHC ring.

CERN, together with its previous scientific achievements is presented in Section 2.1. Section 2.2 presents the most recent of CERN accelerators, the Large Hadron Collider, and the six experiments that will study the outcome of protons collisions it will produce.

### 2.1 The European Organisation for Nuclear Research CERN

One of the major positive outcomes of World War II is the change of spirit concerning international organisation. The war itself proved that alliance between countries are necessary. At the European Cultural Conference held in 1949 in Lausanne, the Nobel Prize recipient Louis de Broglie advocated for the creation of a European laboratory to revive European research. This led to the establishment of the European Council for Nuclear Research (CERN) in 1954, when the 12 founding member states ratified the Convention, and Geneva was chosen for its location. The laboratory and its installations actually sit astride the border between France and Switzerland, north-west from Geneva.

The history of CERN is filled with successes. Its ever-larger facilities allowed scientists to explore higher energies and to more deeply probe the structure of matter. Some of its noteworthy successes are:

- The uncovering of the Weak Neutral Current at the Gargamelle bubble chamber in 1973 [121];
- The construction of the Super Proton Synchrotron (SPS) in 1976. The invention of stochastic cooling [122] in 1979 enabled the SPS to operate as a proton-antiproton collider;

- The effective validation of the electroweak theory through the discovery of the  $W$  and  $Z$  bosons at the SPS in 1983 [123–125]. The Nobel Prize was awarded for this discovery one year later<sup>1</sup>.
- The famous Large Electron Position (LEP) collider, commissioned in July 1989 [126, 127]. Data from the LEP experiments allowed the determination of the existence of exactly three light neutrino species [3]. In addition, numerous other measurements provided unexpectedly successful tests of the Standard Model.

The LEP accelerator and its experiments were decommissioned and dismantled in late 2000. At that time, the decision to definitively shut-down LEP was controversial. Indeed, the Higgs boson, representing the last unobserved particle of the Standard Model, was thought to be within reach as there were (statistically not very significant) indications for it. The motivation for the dismantling was to allow for the civil engineering work to adapt the tunnel and the detector caverns for the next accelerator and its experiments.

## 2.2 The Large Hadron Collider

The Large Hadron Collider (LHC) [128] is the latest CERN achievement. It is the new world-leading particle accelerator, and has replaced the LEP accelerator in its original tunnel. It was primarily built to test the Standard Model (SM) through the search for the hypothesised Higgs boson and to uncover New Physics (NP) which is not described in the SM.

Collider performance is mainly characterised by two parameters: the energy of the accelerated particles and the luminosity [129, 130]. The beam energy governs the energy available in the particle collisions. Luminosity is a measure proportional to the collision rate. Particle physicists are interested in colliders that provide both high energy and high luminosity. This allows the possibility of creating and detecting yet-unseen particles within a reasonable period of time.

### 2.2.1 Luminosity

The machine luminosity can be written as:

$$\mathcal{L} = \frac{\mathcal{N}_b^2 n_b \nu}{\mathcal{F}}, \quad (2.1)$$

where  $\mathcal{N}_b$  is the number of particles per bunch,  $n_b$  the number of bunches per beam,  $\nu$  the frequency of revolution and  $\mathcal{F}$  is a factor grouping terms describing the beam geometry. From Eq. (2.1) it is clear that the luminosity can be increased through increasing the bunch density, the number of particles per bunch and the bunch crossing frequency.

The LHC design luminosity is  $10^{34} \text{ cm}^{-2} \text{ s}^{-1}$ . Achieving this luminosity using  $p\bar{p}$  collisions would require a production of anti-protons which far exceeds the capabilities of the LHC machine. The LHC was thus designed as a  $pp$  collider. Separate vacuum chambers, each bathed in a magnetic field with a direction opposed to the other one, are thus required for the arc sections of the ring, as shown in Fig. 2.1. The luminosity target is reached through a large number of bunches, 2808 per beam, and by the large revolution frequency of 11245 Hz. These characteristics

<sup>1</sup>Carlo Rubbia and Simon van der Meer were honoured with the 1984 Nobel Prize in Physics “for their decisive contributions to the large project, which led to the discovery of the field particles  $W$  and  $Z$ , communicators of weak interaction”.

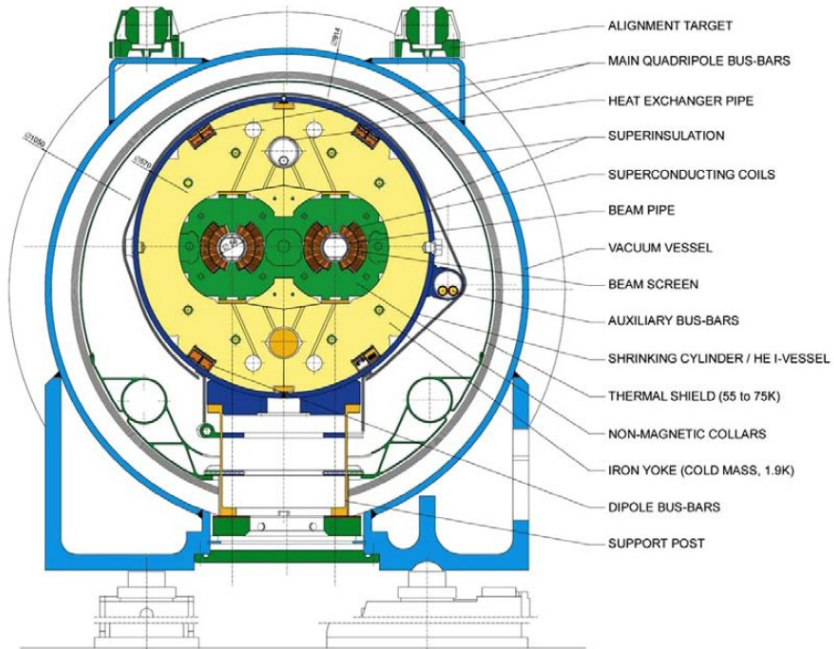


Figure 2.1: Cross section of a LHC superconducting dipole [128].

lead to a 25 ns period between two consecutive bunch crossings (of non-empty bunches). The bunches are squeezed into the desired shape and directed on a colliding course by magnets just before the interaction points. To a certain extent, the focus of those magnets can be adjusted to adapt the luminosity to the specific needs of each experiment. Symmetrical magnets restore the bunch shape after the interaction points.

### 2.2.2 Centre-of-Mass Energy

In order to significantly improve LEP [126, 127] and Tevatron [131, 132] results and to explore a yet-uncovered energy range, the LHC was conceived to provide centre-of-mass collision energies up to  $\sqrt{s} = 14$  TeV. The energy available at LHC represents a considerable step compared to Tevatron's  $\sqrt{s} \sim 2$  TeV. The excavation of a new ring, with a larger radius, was out of question for financial consideration, making the reuse of the LEP tunnel mandatory<sup>2</sup>. Thus, the intensity of the bending magnetic field had to increase considerably to 8.3 T, an intensity only reachable with superconducting electromagnets. Furthermore, since the energy loss by Bremsstrahlung would have been too high to use electrons as probes, protons are used. The Tevatron project was based on the same reasoning many years ago, using protons colliding with antiprotons. However, as mentioned earlier, the LHC will collide protons with protons.

Besides, the LHC will also collide heavy ions. Accelerated fully stripped lead ions,  $^{208}\text{Pb}^{+82}$ , with the nominal magnetic field of 8.3 T constraint, will have an energy of 2.76 TeV/nucleon, yielding a total centre-of-mass energy of 1.15 PeV and a nominal luminosity of  $10^{27} \text{ cm}^{-2} \text{ s}^{-1}$ .

The amount of energy stored in the proton beams adds up to 362 MJ. In addition, the electromagnetic energy stored as electrical current in the magnets is 600 MJ. Dedicated systems

<sup>2</sup>The building of such infrastructures is not trivial. The excavation of the LEP tunnel was one of Europe's largest civil-engineering projects before the realisation of the Channel Tunnel. Three tunnel-boring machines started excavating the tunnel in February 1985 and the ring was completed three years later [133].

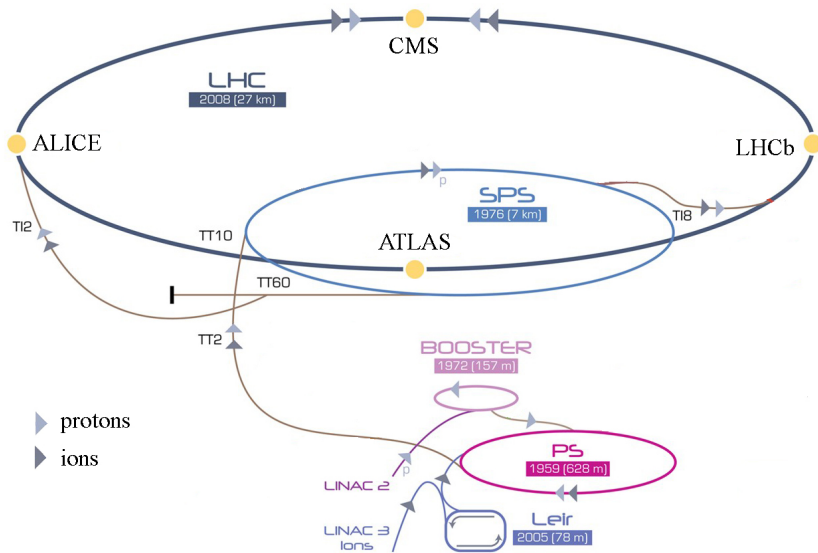


Figure 2.2: The LHC and its feeding accelerator chain. Note that this sketch is not to scale — the SPS ring diameter is 2.2 km while the LHC diameter is 8.5 km. Modified from Ref. [135].

can safely absorb the total of about 1 GJ in case of malfunction, emergency, or simply at the end of each run.

The superconducting magnets are cooled down to 1.9 K. In itself, the thermal energy density in the magnet cold mass is amazingly low. However, this is far from being a safe state. The difference of energy density between the magnet cold mass and the ambient environment in the tunnel is tremendous, and any thermal insulation weakness can have dramatic consequences. Particularly the incident of 19 September 2008 [134] illustrates such consequences. A bad electrical connection between two dipole magnets became more and more resistive in a thermal runaway process and an electric arc developed, releasing up to 4 MW. The bad connection was vaporised and the helium enclosure punctured by the electric arc. Helium was thus released from the cold mass into the insulation vacuum. The pressure was such that longitudinal forces developed, resulting in the displacement of cold masses and even entire magnets. Interconnections between magnets were crashed, some magnet supports were ruptured. The magnets were repaired and cleaned, and measures to reduce the impact of a possible future accident were implemented. The delay caused by this bad connection was about 14 months. It directly affected the content of this document, preventing the LHC to deliver collisions and consequently preventing LHCb to take data.

### 2.2.3 LHC Accelerator Chain and Experiments

The LHC uses previous accelerators to form the accelerating chain depicted in Fig. 2.2. The proton chain consists in accelerators with increasing energies, the Linac2, the Proton Synchrotron Booster, the Proton Synchrotron, the Super Proton Synchrotron, and finally the LHC. Already existing accelerators were upgraded to meet the stringent needs in terms of bunch intensity and emmittances.

There are four interaction points around the LHC ring, which host six experiments in total. The four largest are identified in Fig. 2.2 and the six LHC experiments are:

**ATLAS** [136] and **CMS** [137] are the two general-purpose experiments. They share the same wide interest physics goals, which are the searches for the Higgs boson and physics beyond the Standard Model. These detectors have similar huge barrel-shaped designs. ATLAS measures 45 m in length and 25 m in diameter, as illustrated in Fig. 2.3, and weighs about 7000 tons. CMS, shown in Fig. 2.4, is slightly smaller in size, but is heavier. Although they were designed for  $pp$  collisions, these experiments will also operate during heavy ions runs.

The **TOTEM** [138] experiment aims at the simultaneous measurements of the total  $pp$  cross section and the luminosity. It covers the very forward region in the pseudo-rapidity range  $3.1 \geq |\eta| \geq 6.5$ . TOTEM consists of Roman pots located several hundreds of meters on either side of the CMS interaction point, as well as detectors integrated in the CMS apparatus at about ten meters from the interaction point.

**LHCf** [139] is another very forward experiment. It is located at 140 meters on either side of the ATLAS interaction point. Its goal is to verify hadronic models at very high energy to be used in the understanding of ultra-high energy cosmic rays.

**ALICE** [140] is dedicated to the study of strongly interacting matter and quark-gluon plasma at extreme energy density and temperature, using heavy ions collisions. Figure 2.5 shows ALICE experimental layout. The main experimental challenge is to operate in the extreme multiplicity environment anticipated in Pb-Pb collisions.

**LHCb** [141] is the LHC experiment dedicated to the physics of the beauty quark, and will study  $\mathcal{CP}$ -violating processes and rare decays. It was designed as a single-arm forward spectrometer and is detailed in Chapter 3.

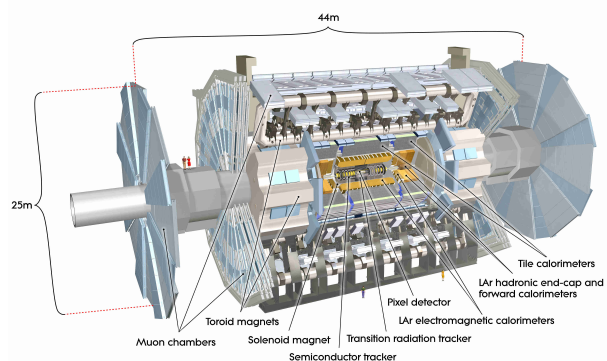


Figure 2.3: The ATLAS apparatus [142].

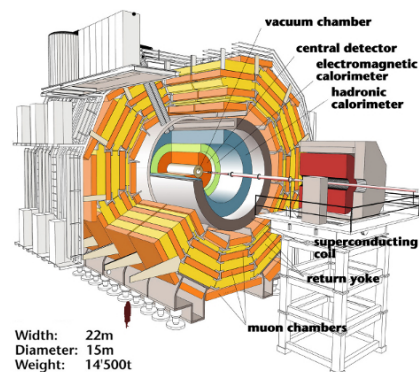


Figure 2.4: The CMS apparatus [143].

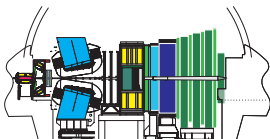


Figure 2.5: The ALICE apparatus [144].



# Chapter 3

## The LHC beauty Experiment



The LHC beauty experiment is one of the four large experiments at the LHC. Among LHC experiments, it singles itself out by being mainly dedicated to the study of  $\mathcal{CP}$ -violation and rare decays in the  $b$  realm.

---

The Large Hadron Collider beauty (LHCb) experiment is dedicated to the precise measurement of  $\mathcal{CP}$ -violating processes and rare decays [145], mainly in the realm of  $B$  mesons.

The  $b\bar{b}$  quark pairs are expected to be predominantly produced at small angles with respect to the beam axis with both quarks close in direction, as shown in Fig. 3.1. Taking advantage of this angular distribution, LHCb was designed as a forward spectrometer with an opening from 10 mrad to 300 mrad in the horizontal plane and to 250 mrad in the vertical plane. In terms of pseudorapidity, the LHCb acceptance covers the range  $1.6 < \eta < 4.9$ .

Within this document, one uses the right-handed coordinate system defined with the  $z$  axis along the beam, pointing from the Vertex Locator to the bulk of the experiment as shown in Fig. 3.3, and the  $y$  axis along the vertical direction, pointing upwards.

In the next pages, the LHCb subdetectors and main systems are presented. These were detailed in documents called Technical Design Reports (TDR) before their actual construction [146–158]. Some of the information contained in those documents is obsolete. More up-to-date information can be found in Ref. [141]. The description of the detector is organised in two main parts. The first part, in Section 3.1, deals with the tracking and the detectors associated with the tracking, as well as the track reconstruction. The second part describes the particle identification (PID) and the contributing detectors in Section 3.2. The trigger system and the software are presented in Sections 3.3 and 3.4, respectively.

### 3.1 The Tracking System

The measurement of passage points of charged particles is of fundamental importance. The non-trivial operation consisting in connecting the hits, taking into account the magnetic field effect, is called the track reconstruction. The reconstruction of a track allows the measurement of the

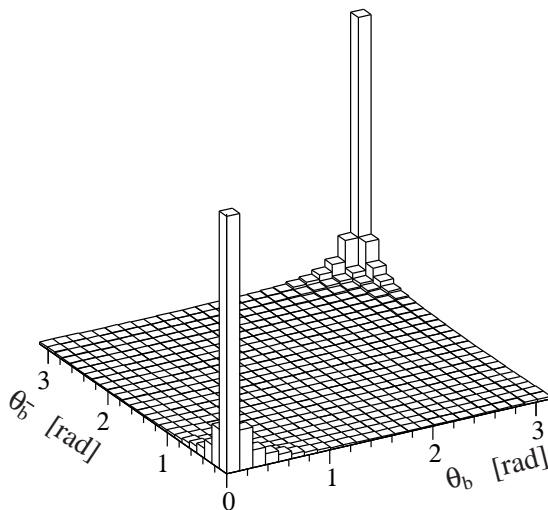


Figure 3.1: Simulated angular distribution of  $b\bar{b}$  pairs produced in  $pp$  collisions at LHC<sup>1</sup>. The peaked distribution at small angles is the reason for the design of LHCb as a forward spectrometer. LHCb will see only one of the peaks.

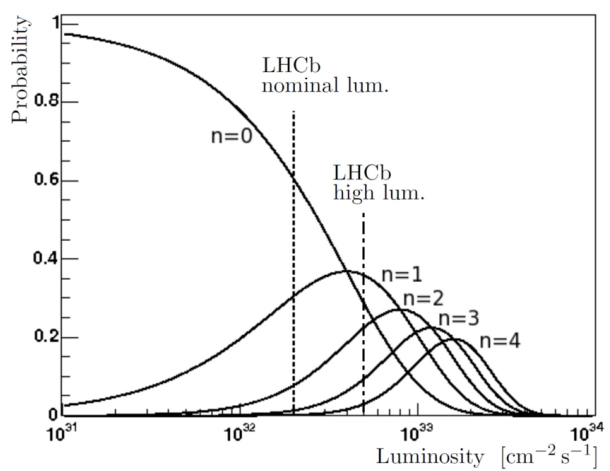


Figure 3.2: Probability to have  $n = 0, 1, 2, 3, 4$   $pp$  interactions per bunch crossing, as a function of the instantaneous luminosity. In order to get a clean signal, LHCb will collide  $pp$  at a luminosity less than the LHC nominal luminosity. The Monte Carlo samples used in this thesis were generated for luminosities of  $2 \times 10^{32}$  and  $5 \times 10^{32} \text{ cm}^{-2} \text{ s}^{-1}$ .

bending of the charged particle in the magnetic field and thus the measurement of its momentum and electric charge. Secondly, a reconstructed track can be interpolated and extrapolated in the other detectors and thus link the information gathered in those to the corresponding charged particle. Track reconstruction is also important to define vertices, getting their precise location and their charged track multiplicity.

The LHCb physics calls for excellent vertex and momentum resolution, which lead to excellent proper time and mass resolution. For example, a very good proper time resolution is needed to resolve the rapidly oscillating  $B_s^0 - \bar{B}_s^0$  meson system.

The tracking system, illustrated in Fig. 3.3, consists of several subdetectors. Surrounding the interaction point, one finds the Vertex Locator (VeLo) [152]. The next tracking subdetector is the Tracker Turicensis [157], just before the magnet [146]. The charged particles bent by the magnet then reach the tracking stations, which present themselves as three vertical stations. The inner part of these stations, surrounding the beam pipe, is referred to as the Inner Tracker [156]. The outer part, which covers the remaining acceptance, is called the Outer Tracker [153]. The Outer Tracker is a straw tube drift chamber detector, whereas the other trackers are silicon microstrip detectors. In the following sections, each of the tracking subsystems will be reviewed in more details.

### 3.1.1 The Vertex Locator

The main role of the Vertex Locator (VeLo) is to measure the coordinates of tracks close to the interaction point. It is located just around the region where the  $pp$  collisions will occur. The

<sup>1</sup>This figure was taken from Ref. [141]. Unless otherwise specified, all the figures of this chapter come from this reference, most of them with slight modifications.

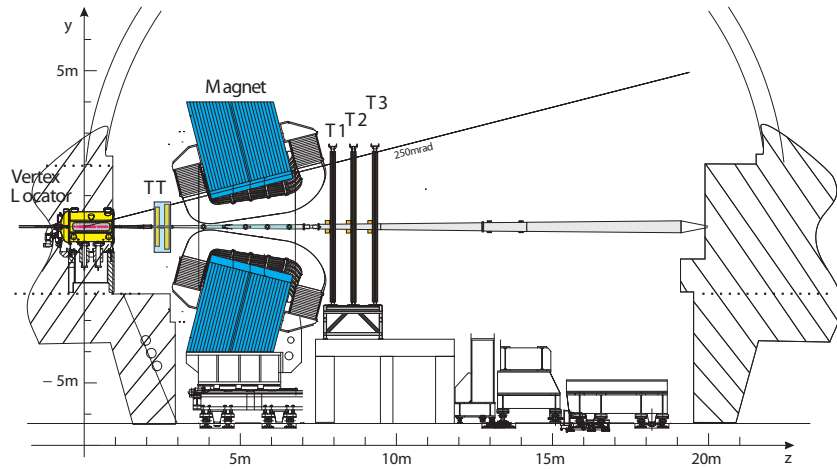


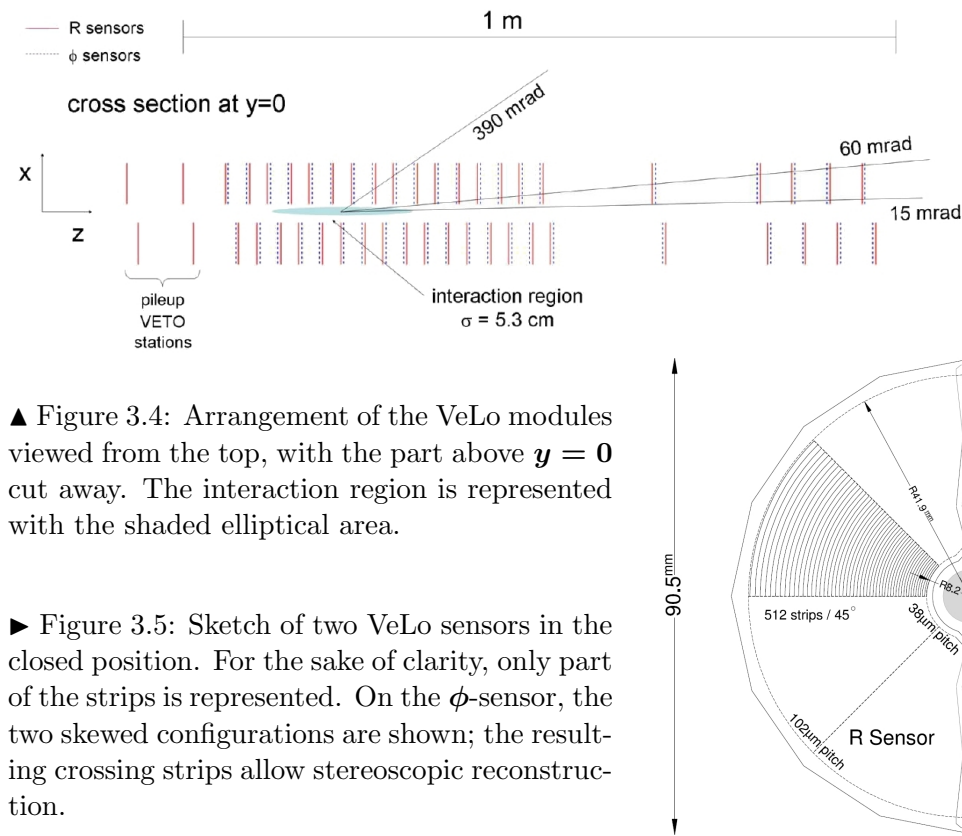
Figure 3.3: LHCb tracking system. In this figure, only the subdetectors involved in the tracking are represented. From the interaction point on the left, one finds the VeLo, the TT, the magnet, and the three tracking stations, T1, T2 and T3.

VeLo is used to:

- **locate the produced vertices** at each bunch crossing. By registering the passage of charged particles within its silicon sensors, and after reconstruction of forward and backward-going tracks, the VeLo allows the measurement of the coordinates of the vertices. The spatial resolution of this detector is crucial. Indeed, the distance between the point where a  $B$  meson is produced, the primary vertex (PV), and the point where it decays, the secondary vertex (SV), is a key observable for  $B$  physics.
- In the VeLo, the magnetic field is low enough not to bend significantly the trajectory of charged particles. Hits in the silicon are used to reconstruct straight track segments within the subdetector. Those tracks segments are used as **seeds for the LHCb track reconstruction software** [159].
- The VeLo is also used in the first-level L0 trigger, as **Pile-Up detector** [158, 160, 161]. The pile-up system consists in two planes of silicon strip detectors which are used to determine the number of primary interactions and the track multiplicity within one bunch crossing. The goal is to identify events that contain more than one interaction. Single interaction events are indeed easier to treat, both in the higher levels of trigger and the offline analysis. The VeLo is also used in the software High Level Trigger (HLT), together with the other LHCb subdetectors.

The Vertex Locator was designed as a set of  $2 \times 21$  sensor modules, spread along and perpendicularly to the beam axis, as shown in Fig. 3.4. Each half module consists of a sensor sensitive to the radial coordinate and a sensor sensitive to the azimuthal angle of a track, positioned back-to-back. The sensors use single-sided n-implants in n-bulk technology and are  $220\text{ }\mu\text{m}$  thick. They look like half compact-disks of 84 mm in diameter, see Fig. 3.5.

The choice of the  $(r, \phi, z)$  cylindrical coordinates was motivated by cylindrical geometry, but also to permit fast track reconstruction. Indeed, the reading of the  $r$ -sensors only is sufficient to estimate the impact parameter (IP) of a track with respect to the primary vertex. This allows



▲ Figure 3.4: Arrangement of the VeLo modules viewed from the top, with the part above  $y = 0$  cut away. The interaction region is represented with the shaded elliptical area.

► Figure 3.5: Sketch of two VeLo sensors in the closed position. For the sake of clarity, only part of the strips is represented. On the  $\phi$ -sensor, the two skewed configurations are shown; the resulting crossing strips allow stereoscopic reconstruction.

the separation of interesting tracks, not coming from the primary vertex, from prompt products of the collision. In the  $r - z$  projection, forward-going tracks with a high IP with respect to the primary vertex are easily identified.

The  $r$ -sensors are designed with concentric semi-circular microstrips, centred on the nominal LHC beam axis. In order to lower the occupancy and strip capacitance, the strips are subdivided in four  $45^\circ$  regions. The innermost strip lies at 8.2 mm from the nominal beam axis. At that position the pitch between two  $r$ -strips is 38  $\mu\text{m}$ , increasing linearly to 101.6  $\mu\text{m}$  at the outer radius of 41.9 mm. This varying pitch allows measurements along a track to contribute with an equal weight to the impact parameter measurement, and help to average the occupancy.

For resolution and occupancy reasons, the  $\phi$ -sensor is divided in two regions. The strips of the inner region are characterised by an angle with respect to the radial direction of  $\pm 20^\circ$  and a pitch between 35.5  $\mu\text{m}$  and 78.3  $\mu\text{m}$ . The inner region covers radii from 8 mm to 17.25 mm.

The outer region covers radii from 17.25 mm to 41.9 mm radius with a pitch between 39.3  $\mu\text{m}$  and 97  $\mu\text{m}$ . The strips of the outer region make a  $\pm 10^\circ$  angle with the radial direction, its sign being opposite to the one of the inner region. The modules are arranged so that two consecutive  $\phi$ -sensors have opposite skew orientation. This skewed strip design is motivated by pattern recognition efficiency.

The location of the primary vertex needs interpolation of the tracks. To minimise the interpolation distance and thus increase the resolution on the primary vertex, the innermost strip of the sensors should have a radius as small as possible. Various constraints lead to the design described above, where strips start at 8 mm of the beam axis. During the injection phase,

the beam aperture is much larger than its value when the beam is stable and could threaten the VeLo detector. The VeLo modules can therefore be retracted horizontally by 3 cm for safety reasons.

The VeLo modules are separated from the LHC vacuum by a thin aluminium foil, which preserves the LHC vacuum and shields the VeLo electronics against RF pickup from the bunches. The minimisation of the amount of matter crossed by a particle before reaching a sensor resulted in the complex design of this RF foil. The whole VeLo tank is bathed with the machine vacuum. Forward going tracks exit the VeLo, crossing a 2 mm thick aluminium window.

### 3.1.2 The Trackers

The aim of the Tracker Turicensis, and the detectors forming the tracking stations, the Inner Tracker and the Outer Tracker, is the detection of charged particles tracks. The track trajectory, bent by the magnetic field, is used to get the particle momentum. The momentum resolution of the flying particles directly affects the invariant mass resolution of the  $B$  meson that decays. The physics goals require a detector that can provide excellent momentum resolution of about  $\delta p/p \simeq 0.4\%$ . Furthermore, the reconstruction of high multiplicity  $B$  decays needs high tracking efficiency and low wrongly reconstructed track ratio. Since, the momentum resolution is strongly affected by multiple scattering, the tracking detectors design aims at the minimisation of the material in the LHCb acceptance.

#### 3.1.2.1 The Tracker Turicensis

Just in front of the magnet one finds a silicon microstrip detector, the Tracker Turicensis<sup>2</sup> (TT) [157]. The TT consists in four rectangular detection layers, which cover the full LHCb angular acceptance. The sensitive planes are about 150 cm wide and 130 cm high, as shown in Fig. 3.6. The total silicon surface adds up to  $8.4\text{ m}^2$  with more than 143 k readout channels. It uses  $9.64 \times 9.44\text{ mm}$  and  $500\text{ }\mu\text{m}$  thick silicon sensors, engraved by 512 strips with a  $183\text{ }\mu\text{m}$  pitch.

The layers are arranged in a stereo layout, the external layers having vertical strips, whereas the internal layers have strips oriented with a  $\pm 5^\circ$  angle with respect to the vertical. A layer is composed of modules, placed as illustrated in Fig. 3.6 to form a sensitive plane without gap. A TT module, shown in Fig. 3.7, consists of seven sensors arranged in two or three readout sectors. The division in readout sectors of different lengths is motivated by the spatial distribution of the particle flux and the minimisation of the number of readout channels.

#### 3.1.2.2 The Inner Tracker

The Inner Tracker covers a cross-shaped region around the beam pipe of the three tracking stations. It is a silicon micro-strip detector, like the VeLo and the TT. While it covers only about 1.3 % of a tracking station, approximately 20 % of the charged tracks produced close to the interaction point and going through the tracking stations cross it. Its surface has been optimised to be as small as possible while keeping the average Outer Tracker occupancy to a

<sup>2</sup> The TT was originally named Trigger Tracker. Indeed, the first motivation for its existence was to use the residual magnetic field between the VeLo and the TT to get a first rough estimate of the particle momentum and use this information in the trigger. The progress in term of computing performance allows nowadays to use information coming from all the tracking system in the trigger, giving only little sense to the original name of the detector.

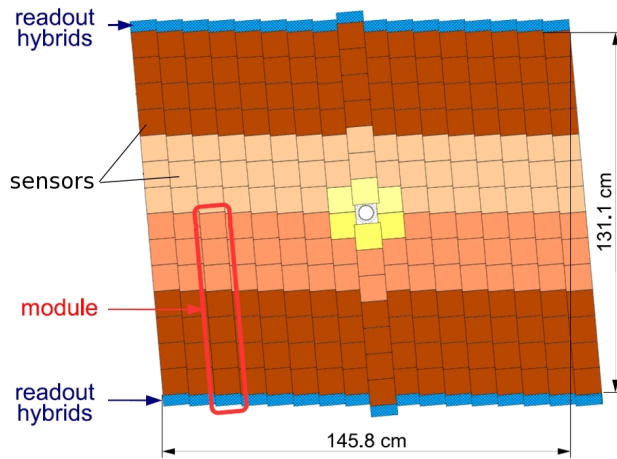


Figure 3.6: Layout of a TT detection layer. The different readout sectors are indicated by the sensor colour.

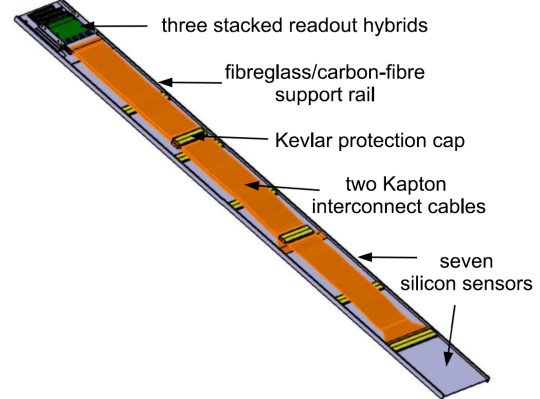
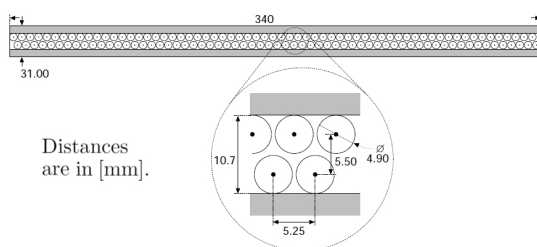
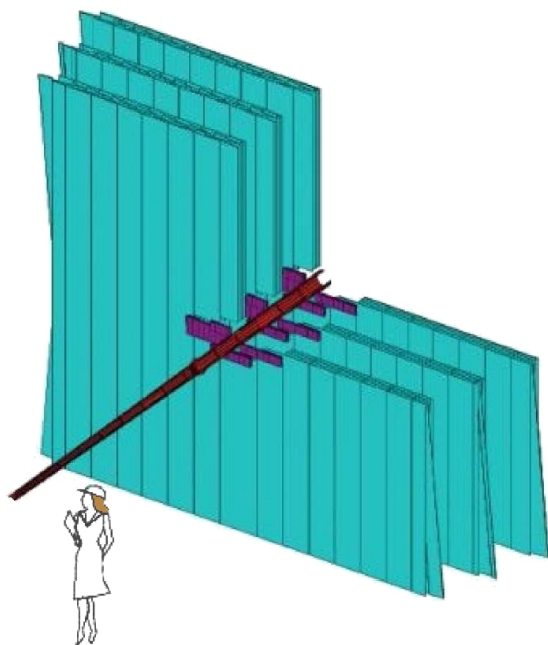


Figure 3.7: A TT module. This particular type of module, made of three readout sectors of one, two and four sensors, is used in the centre of the TT station.



▲ Figure 3.8: Cross-section of an OT module, showing straw-tubes.

► Figure 3.9: Arrangement of the Outer Tracker straw-tube modules, forming the outer part of the three tracking stations, a quadrant being cut away. The Inner Tracker, which covers the innermost part of the acceptance, and the conical beam pipe are also visible.



reasonable level. The detector localisation at the centre of the acceptance implies that parts of the front-end electronics, cooling, and cables have to be located inside the acceptance of the experiment. This poses stringent conditions on the design to minimise the material inside the acceptance. This subdetector and its construction are extensively described in Chapter 4.

### 3.1.2.3 The Outer Tracker

The Outer Tracker occupies the outer part of the tracking stations; the inner part being covered by the Inner Tracker. The requirements for that detector are similar to the ones of the other trackers, with the exception of a lower spatial resolution of about  $200\text{ }\mu\text{m}$  and the much larger area to cover,  $29\text{ m}^2$  per station.

Under those constraints, the OT was designed as a drift-time detector. Gas-tight straw-tubes form the anode and gold-plated tungsten wires the cathode. The counting gas is chosen to be a mixture of Argon (70 %) and CO<sub>2</sub> (30 %), to ensure fast drift time while keeping good drift position resolution. The straw-tubes are arranged in two layers, see Fig. 3.8, in module boxes providing gas tightness, shielding and rigidity. These modules are then positioned to form the outer part of a tracking station. The module layout is the classical stereoscopic arrangement, consisting of 2 layers with vertical strips enclosing 2 layers with strips oriented with a  $\pm 5^\circ$  angle with respect to the vertical. Figure 3.9 shows the three tracking stations.

### 3.1.3 The Magnet

The momentum of a charged particle is obtained by measuring how much its path is bent by a known magnetic field. For this, one needs tracking capabilities, and one obviously needs a well-known magnetic field.

The LHCb dipole magnet produces a magnetic field, mainly vertical, such that particle paths are bent in the horizontal  $x - z$  plane. The desired momentum resolution requires a 4 Tm integrated magnetic field over the tracking dedicated part of the detector. The boundary condition of the cavern itself, and the cost limitation were other constraints that drove the design. Particularly, a superconducting magnet as foreseen in the LHCb Technical Proposal [145] was unaffordable with regard to the investment costs and would have made its operation and the polarity reversals more complicated.

These requirements and constraints lead to the design of a warm dipole magnet. It consists of two coils, arranged symmetrically above and below the acceptance volume, inside the yoke. The coils are made of pure aluminium hollow conductor. The conductors forming the coils were extruded in a 320 m single length before being wound in a saddle shape. The total resistance of the two coils and supply bus bars add up to only  $130\text{ m}\Omega$  at  $20^\circ\text{ C}$ . The coils are water-cooled, with a flow in the conductors of  $150\text{ m}^3\text{ h}^{-1}$ . The yoke is made of steel plates, it is by far the main contribution to the magnet total weight of 1600 tons. The electric consumption of the magnet is 4.2 MW.

After the magnet assembly, a mapping of the magnetic field was performed. The three components of the magnetic field were measured by Hall probes on a  $8 \times 8 \times 10\text{ cm}^3$  grid in the tracking volume from the VeLo to the last of the tracking stations, and at the location of the RICH photodetectors. To control systematic errors, it is foreseen to periodically revert the field orientation, thus the field measurements were performed for both polarisations. The results for  $B_y$ , the main component is shown in Fig. 3.10.

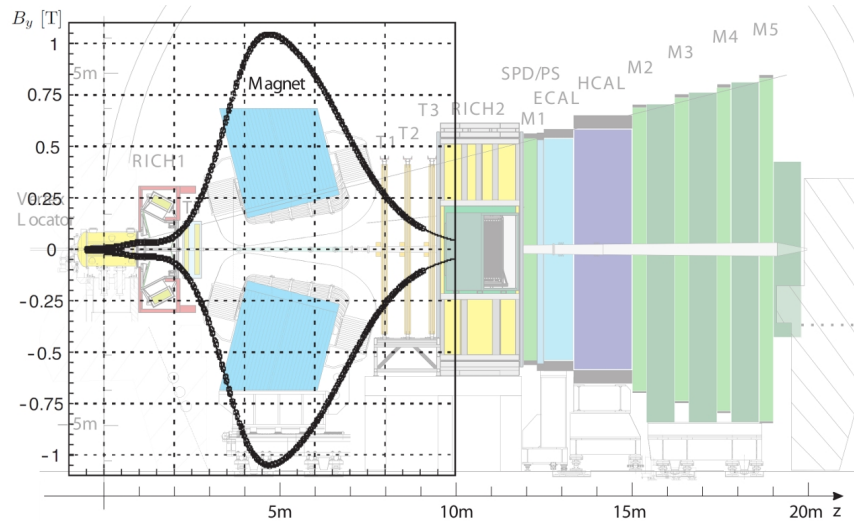


Figure 3.10: Main component of the LHCb magnetic field,  $B_y$ , as measured during its mapping, as a function of the distance  $z$  for  $x = y = 0$  and for both polarities. The detector layout is shown behind on the same horizontal scale.

### 3.1.4 The Track Reconstruction

The track reconstruction software combines hits in the VeLo, the TT, the IT, and the OT to form particle trajectories and compute their momentum. One classifies tracks depending on their trajectories in the detector, as shown in Fig. 3.11:

- **long tracks** traverse the entire tracking system, from the VeLo to the last tracking stations. Their momentum resolution is the most precise and thus they are the most important tracks for physics.
- **upstream tracks** traverse only the VeLo and the TT. In general those tracks are left by particles that were bent outside the acceptance by the magnetic field. The momentum resolution of the upstream tracks is rather poor. However, since they cross RICH1, they are important to interpret the ring patterns therein. Despite the poor momentum resolution, upstream tracks can be used for physics, in flavour tagging for example.
- **downstream tracks** traverse only the TT and the tracking stations. The most relevant downstream tracks are those produced by decay products of long-lived particles, such as  $\Lambda$  or  $K_S^0$  decaying outside the VeLo.
- **T tracks** are only measured in the tracking stations. Those tracks are generally produced by secondary interactions. Similarly to the upstream tracks for RICH1, T tracks are important for RICH2 pattern recognition.

The track reconstruction starts by identifying track seeds. The magnetic field is very weak in the VeLo (see Fig. 3.10), thus one looks for aligned clusters of hits in this detector. Such segments of tracks are called **VeLo track seeds**. Similarly, an iterative algorithm looks for segments of tracks in the T stations, using both OT and IT clusters of hits. Those track segments are called **T track seeds**.

The next step consists in trying to associate seeds to hits in the other tracking subsystems to form tracks. The procedure to find **long tracks**, defined above, is twofold. First, taking a

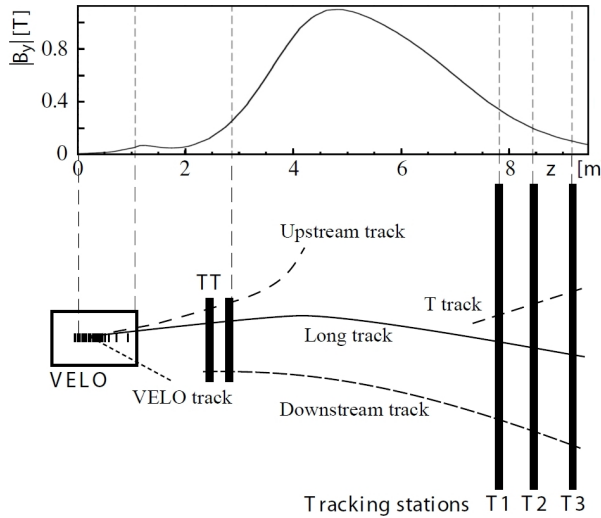


Figure 3.11: Categorisation of the tracks according to their topology in the LHCb detector. The main component of the magnetic field is also plotted.

VeLo seed and a hit in a T station, one looks for hits in the other T stations in a search window opened around the track candidate trajectory. If hits are found to confirm the track candidate and if its quality is sufficient, it becomes a long track. Hits in the TT corresponding to the track are added to it. Finally, the hits associated with the tracks are removed from the list of hits on which the algorithm has to run. This algorithm, called **the forward tracking**, reconstructs about 90 % of the long tracks.

Secondly, about another 4 % of the long tracks are reconstructed by the **track matching** algorithm. It tries to match pairs of VeLo and T seeds. Each of those seeds is extrapolated into the magnet region and their compatibility to form a track is assessed using their position and slopes, as well as the number of compatible clusters in the TT. The TT hits are added to successful candidates. The track reconstruction software fails to reconstruct the remaining 6 % of reconstructible long tracks.

There exist other algorithms to reconstruct the other types of track listed above. After tracks have been found, their trajectory is refitted with a Kalman filter which uses full magnetic mapping and accounts for multiple scattering and energy loss caused by crossed materials. In the track reconstruction process, it is possible for a physical track to be reconstructed by more than one algorithm, resulting in two clone tracks. In that case, only the best out of the two tracks is kept.

## Performance

The track reconstruction performance is assessed in terms of track reconstruction efficiency and ghost rate with Monte Carlo simulations. The reconstruction efficiency is the fraction of reconstructible tracks that are successfully reconstructed<sup>3</sup>. The ghost rate is the fraction of reconstructed tracks that are not matched to any Monte Carlo particle, *i.e.* those are bad interpretations of the hits measured in the tracking system. On Monte Carlo  $B^0 \rightarrow J/\psi K_S^0$  events, the track reconstruction efficiency was evaluated to be 94 % on average for particle

<sup>3</sup>A track is successfully reconstructed if at least 70 % of its associated hits originate from a single particle. A track is considered reconstructible if it has a minimum number of hits in the relevant tracking subdetectors.

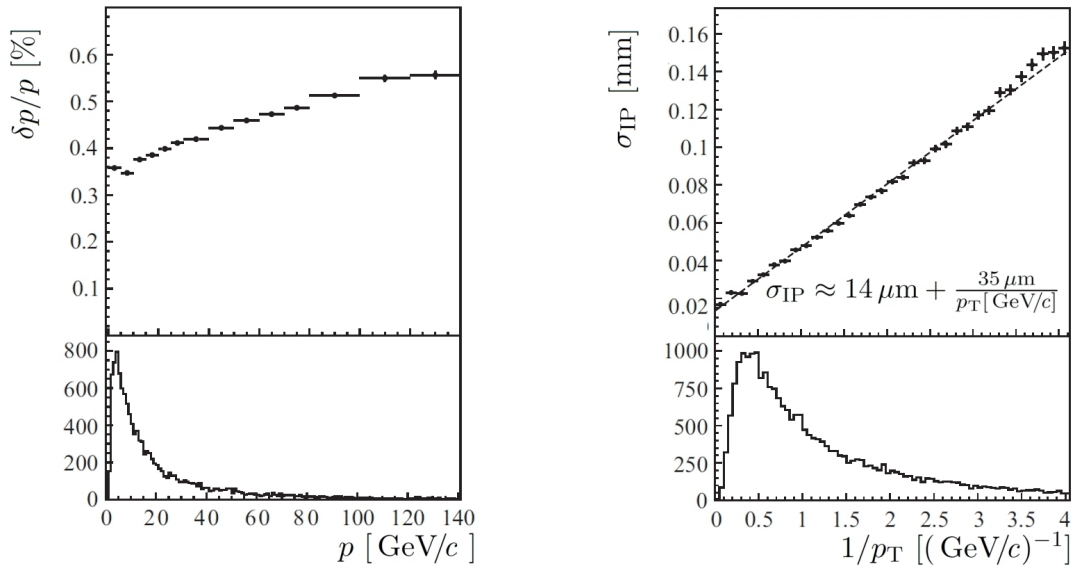


Figure 3.12: Momentum resolution as a function of the track momentum (left) and impact parameter (IP) resolution as a function of  $1/p_T$  (right) for Monte Carlo  $B^0 \rightarrow J/\psi K_S^0$  events. The IP resolution was computed as the quadratic sum of the errors in the three projections. The  $p$  and  $p_T$  spectra of the  $B^0$  daughter particles are shown in the lower part of the plots.

with momentum larger than  $10\text{ GeV}/c$ , and the ghost rate about 9 %. The momentum and IP resolutions of those tracks are  $\delta p/p \approx 0.4\%$  and  $\sigma_{IP} \approx 14\text{ }\mu\text{m} + \frac{35\text{ }\mu\text{m}}{p_T\text{ [GeV}/c]}$  with  $p_T$  in  $\text{GeV}/c$ . The distributions of those parameters are shown in Fig. 3.12.

### 3.2 The Particle Identification Devices

Altogether, the particle identification devices are required to distinguish electrons, muons, protons, kaons, charged pions, as well as photons and neutral pions from each other.

This is essential since it is only through these long-lived particles that we can access information about the mother particles. Thus, the identification of daughter particles is important to determine the flavor of the mother  $B$  meson, as well as to distinguish between kinetically and topologically similar decays. The LHCb particle identification devices, shown in Fig. 3.13, are:

- Two Ring Imaging Čerenkov (RICH) detectors. The first (RICH1) is located after the VeLo, and the second (RICH2) after the tracking stations. These two detectors are complementary in terms of angular and momentum coverage.
- The calorimeter system consisting of three subdetectors: the preshower (SPD/PS) detector, the electromagnetic calorimeter (ECAL) and the hadronic calorimeter (HCAL). These detectors are situated in the order given above, after RICH2.
- The muon system, made of five stations labelled M1 to M5. M1 is located between RICH2 and the preshower, whereas M2 to M5 are located after HCAL.

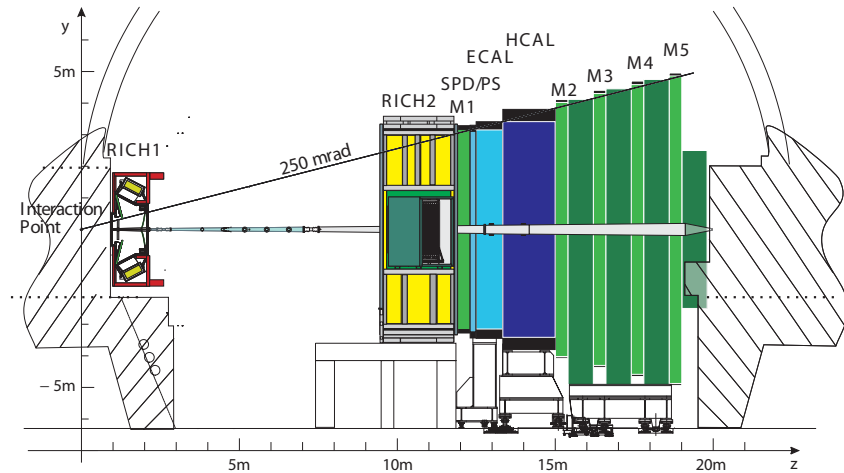


Figure 3.13: LHCb particle identification devices. On this figure, only the subdetectors involved in the particle identification are represented. From the interaction point on the left, one finds the Čerenkov detectors (RICH1 and RICH2), the calorimeters (SPD/PS, ECAL and HCAL) and the muon system (stations M1 to M5).

### 3.2.1 The Čerenkov Detectors

When charged particles traverse a dielectric medium, they polarise it locally. When the medium returns to equilibrium, photons are emitted. If the particle speed is smaller than the speed of light in that medium, the polarisation is spherically symmetric and the emitted photons destructively interfere with each other. However, if the particle speed is larger than the speed of light in that medium, the polarisation is not spherical, so that the photons coherently interfere and form a wavefront at a fixed angle,  $\theta_c$ , with respect to the particle direction [162]. This light emission is called the Čerenkov effect<sup>4</sup>.

The dependence of the angle  $\theta_c$  on the velocity of the particle is given by:

$$\cos \theta_c = \frac{1}{n\beta} \quad \text{with} \quad \beta = \frac{v}{c}, \quad (3.1)$$

where  $n$  is the refraction index of the medium.

The usefulness of the Čerenkov effect lies on the fact that the measurement of the angle  $\theta_c$  provides a direct measurement of the particle velocity  $\beta$ . The latest kind of Čerenkov detectors are the Ring Imaging Čerenkov (RICH) detectors, developed in the 1980s for the DELPHI [163] experiment at CERN. In a RICH detector, the Čerenkov light produced by a charge particle travelling fast enough in the radiator is reflected by a spherical mirror on a position sensitive planar detector. The Čerenkov photons hits allow the reconstruction of a ring on that plane, independently of the emission point along the particle track. The radius of the reconstructed ring is a measurement of the Čerenkov angle,  $\theta_c$ , and thus of the particle velocity.

To cover the whole momentum spectrum of the flying particles, the LHCb Čerenkov system is made of two complementary detectors. RICH1 is optimised for low momentum particles, ranging from 1 to 60 GeV/c. It is located 1 meter from the interaction point, and covers the whole LHCb geometrical acceptance. It uses two different radiators: the silicon aerogel yields

<sup>4</sup>Čerenkov, Frank, and Tamm shared the 1958 Nobel Prize in Physics “for the discovery and the interpretation of the Cherenkov effect”.

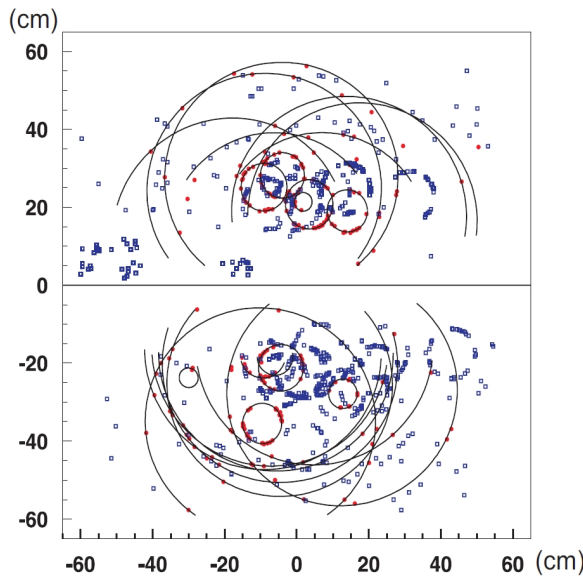


Figure 3.14: Display of a typical simulated event in RICH1.

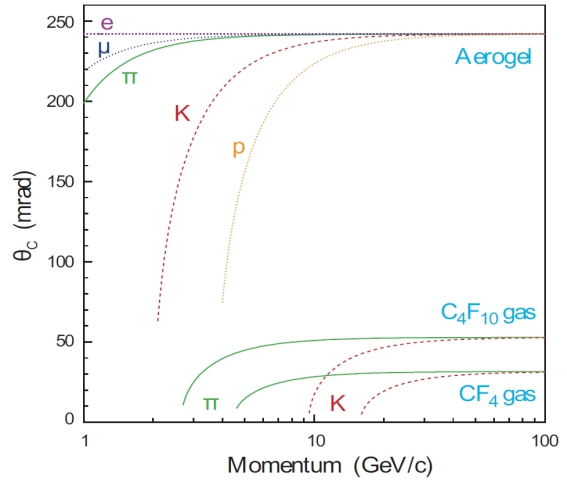


Figure 3.15: Čerenkov angle as a function of the particle momentum for the three RICH radiators and for different types of particle.

sensitivity to momenta up to  $10 \text{ GeV}/c$  and the  $\text{C}_4\text{F}_{10}$  to the  $10\text{--}60 \text{ GeV}/c$  momentum range. Its location upstream of the tracking stations stringently calls for material budget minimisation in the acceptance. For that purpose, all optical material is located outside the acceptance, but for the spherical mirrors. A new type of lightweight mirror was developed by LHCb [164].

RICH2 is dedicated to particles with momenta ranging from  $15$  to  $100 \text{ GeV}/c$ . Thus, it covers a limited area corresponding to the high momentum particles,  $\pm 120 \text{ mrad}$  and  $\pm 100 \text{ mrad}$  in the horizontal and vertical planes. The RICH2 uses a gaseous  $\text{CF}_4$  radiator.

The photodetectors are pixel Hybrid Photon Detectors (HPD), which were developed by LHCb [165]. They are characterised by a 1024-pixels silicon detector, corresponding to  $2.5 \times 2.5 \text{ mm}^2$  granularity, and high time resolution 25 ns. External magnetic field can degrade the performance of the HPDs. Thus, in order to reduce the residual magnetic field generated by the dipole magnet in the HPDs, they were shielded by thick 500 mm to 100 mm iron plates. The design of the shield was optimised to reduce the magnetic field in the HPDs while not degrading it in the LHCb acceptance. A particular care was taken for the RICH1 shield, in order to keep the magnetic field in the VeLo and TT, located either side of RICH1 as high as possible [166]. Dedicated systems are in place to understand the effect of the magnetic field in situ and to correct for it during the reconstruction stage.

## Performance

The Čerenkov rings are reconstructed based on the knowledge of the track direction and position, and using the Čerenkov hits on the sensitive HPD plane. A typical simulated event is shown in Fig. 3.14. The expected  $\theta_c$  resolution is 2.6 mrad for the aerogel, dominated by chromatic dispersion, and 1.5 mrad to 0.7 mrad for  $\text{C}_4\text{F}_{10}$  and  $\text{CF}_4$  respectively. For a given momentum, the measured Čerenkov angle depends on the particle mass. Figure 3.15 illustrates the separation power for the three radiators used in LHCb Čerenkov detectors.

### 3.2.2 The Calorimeters

The calorimeter system provides identification for the electrons, photons and hadrons while measuring their energies and positions. Particularly, the reconstruction of neutral particles,  $\pi^0$  and photons, is essential for LHCb the physics program. The calorimeters also provide critical information about transverse energy of hadron, electron and photon candidates to the first-level trigger.

First, in order to distinguish between charged particles and neutrals such as the photons and  $\pi^0$ , a layer of scintillators is placed just after the M1 station. This detector is the Scintillator Pad Detector (SPD). It achieves a good separation between the  $e^\pm$  and the photons which will have identical behaviour downstream in the ECAL. After a thin layer of lead, one finds a layer of scintillators almost identical to the SPD, the preshower (PS). Its goal is to distinguish between electrons and charged pions. Due to the difference in interaction lengths of electrons and pions in the lead, electrons produce showers that initiate in the lead converter, whereas pions do not. Those two detectors provide identification in a very fast way, to be used by the first-level trigger.

The purpose of ECAL is to measure the energy deposit of the electromagnetic showers. It is made of alternating layers of scintillators and lead. The  $E_T$  measurement of high energy electrons and conversion photons is of crucial importance for the L0 trigger. The optimal  $E_T$  resolution calls for the electromagnetic showers to develop completely within the ECAL volume, which corresponds to a depth of  $25 X_0$  [167]. On the other hand, the requirement on the energy resolution for the hadrons is not as stringent, thus the depth of the HCAL is only  $5.6 X_0$ .

All the calorimeters are designed along the same concept. A wavelength-shifting (WLS) fibre is coiled in a brick of scintillator to collect scintillation photons. The WLS fibre transmits the photons to a photomultiplier tube (PMT). The size of the scintillation cells is optimised in order to average the occupancy, leading to a segmentation in three different regions for the ECAL, also adopted projectively for the PS and SPD. Given the dimensions of the hadronic showers, the HCAL is segmented in two regions, with much larger cells than the other calorimeters.

### 3.2.3 The Muon Detectors

Muon triggering and offline reconstruction are of fundamental importance for LHCb. Muons are indeed present in the final states of many of the channels under study at LHCb, in particular the  $B_s^0 \rightarrow \mu^+ \mu^-$  decay, and thus high- $p_T$  muons are important heavy-flavour signature to trigger on. Furthermore, in  $\mathcal{CP}$  violation studies, muons are often used in the flavour tagging, such as in the analysis of the very promising  $B_s^0 \rightarrow J/\psi \phi$  decay.

The muon system [149–151] provides information about high transverse momentum muons to the first-level trigger, see Section 3.3.1, and muon identification to both the high-level trigger and offline analysis. For both purposes, the muon system exploits the large matter penetration power of muons w.r.t. hadrons, electrons and photons, which are attenuated by the shields interspersed between the stations.

Five rectangular stations, called M1–M5, placed along the beam axis, after the calorimeter — except for station M1 — form the muon system, as pictured in Fig. 3.16. Their dimensions follow approximately the LHCb angular acceptance, which contains about 20 % of the muons produced in  $B$  semileptonic decays. Each muon station is divided in four concentric regions arranged in a projective layout, such that the expected particle flux is roughly the same for each of them. Since the multiple scattering increases with the angle from the beam pipe, the detector granularity varies accordingly from one region to another, so that the outer regions have a worse spatial resolution than the inner ones. Iron absorbers of 80 cm thickness are interleaved between

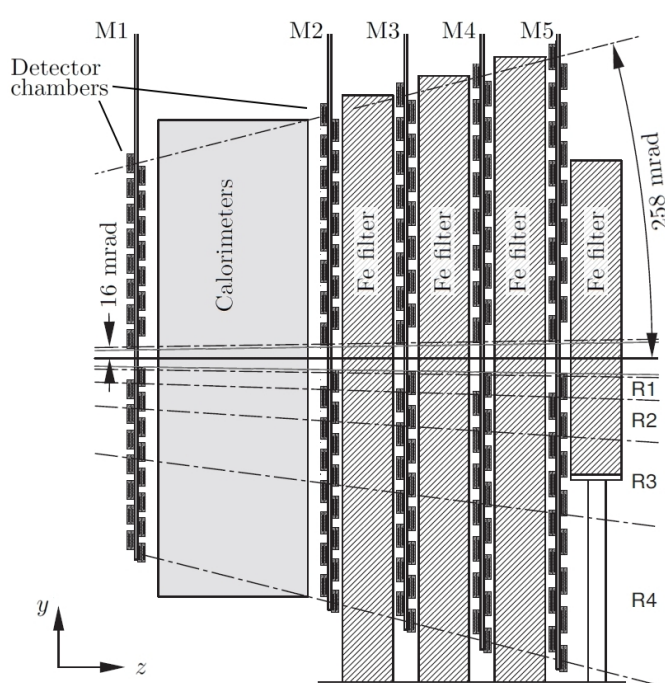
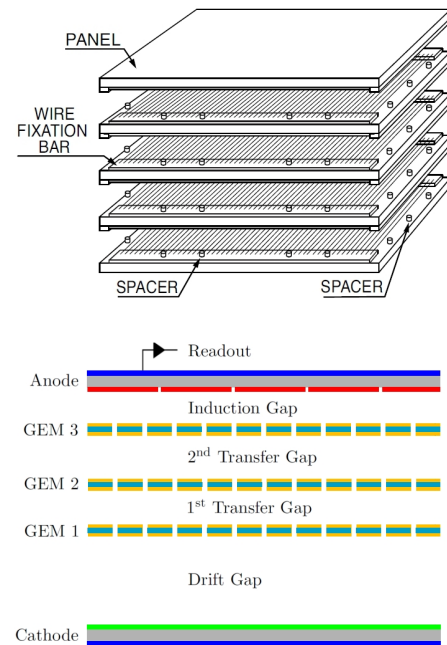


Figure 3.16: View of the five stations composing the muon system and the interleaved iron shields. Note the increasing dimensions of the chambers from M1 to M5 and the definition of the four regions, according to the projective layout.



▲ Figure 3.17: Detail of the composition of a Multiwire Proportional Chamber, which populates the bulk of the muon stations.

▲ Figure 3.18: Cross-section of a Gas Electron Multiplier chamber used in the innermost part of station M1.

the stations, from M2 to M5, to select penetrating muons. The whole detector, including the filters represent about  $20 X_0$ . Another iron wall after M5 shields LHCb from potential pollution coming from downstream. The projective layout of the stations and the absence of magnetic field make track reconstruction and  $p_T$  measurement fast and effective enough to be used in the trigger.

Station M1 to M3 are used to calculate the  $p_T$  of the muon candidate track with a 20 % resolution. To that end, those stations have a high spatial resolution along the  $x$  coordinate and the station M1 is located in front of the calorimeter. Stations M4 and M5 have a more coarse spatial resolution, their purpose being limited the identification of penetrating particles.

Two detector technologies are used: MultiWire Proportional Chambers (MWPC), shown in Fig. 3.17, cover most of the detector surface, while the innermost region of station M1 uses Gas Electron Multiplier (GEM) foils, as shown in Fig. 3.18. The GEM are needed because the fluence, at that location, is too high for MWPC to achieve the required efficiency.

A MWPC<sup>5</sup> is a gaseous detector composed of metallic wires tightened to form a plane between two conductive planes. A large voltage difference is applied between the wires and the two others planes and this system is bathed in a gas mixture. When a charged particle, crossing

<sup>5</sup>Georges Charpak was awarded the Nobel Prize in Physics, in 1992, “for his invention and development of particle detectors, in particular the multiwire proportional chamber”.

the detector, ionises the gas, teared-off electrons are amplified in the strong electric field in the gaseous medium by a cascade reaction and a signal is collected on adjacent wires.

The LHCb MWPC use 30  $\mu\text{m}$  gold-plated tungsten wires with a 2 mm pitch. The gas is a mixture of Ar, CO<sub>2</sub> and CF<sub>4</sub> at 40 %, 55 % and 5 % concentration, respectively. The operation voltage is 2.5 to 2.8 kV. The very high detection efficiency required is achieved by the redundant use of four sensitive gaseous layers in each chamber, logically connected so that a signal in one layer is sufficient.

A GEM foil consists in a thin Kapton foil sandwiched between copper films. This sandwich is pierced with bi-conical holes — 70  $\mu\text{m}$  outer diameters, 50  $\mu\text{m}$  inner diameter — with a 140  $\mu\text{m}$  pitch. When a voltage difference is applied between the copper films, a very strong electric field is created in the holes — 100 kV/cm is obtained for voltage of the order of 500 V — which leads to an electron multiplication factor of a few thousands.

The LHCb triple-GEM detector, whose cross section is detailed in Fig. 3.18, consist of four gaseous layers, delimited by three porous GEM foils. An electric field is applied in the whole system, so that ionisation electrons produced in the drift gap are forced to pass through the three GEM foils, in each of which they are multiplied. Finally, the induced current signal is collected on the anode pads.

### 3.2.4 Particle Identification

The information of the two RICHes, the calorimeters and the muon system is combined to identify charged particles ( $e$ ,  $\mu$ ,  $\pi$ ,  $K$ ,  $p$ ), whereas photons and neutral pions are identified using the electromagnetic calorimeter only.

#### Hadron Identification

The particle identification in the RICH system uses a log-likelihood optimisation to find which of the  $\pi$ ,  $e$ ,  $\mu$ ,  $K$  or  $p$  mass-hypotheses best fits each observed Čerenkov ring. The process is twofold [168]. First, the effective Čerenkov angle is calculated for each track–hit-pixel pair. This stage allows the assignment of each ring to a track.

Secondly, considering all tracks, and the rings coming from all radiators in one event, the log-likelihood is computed starting with the pion mass-hypothesis for all particles. An iterative optimisation of the log-likelihood is performed, which leads to a best PID hypothesis for each track. This information, together with the decrease in log-likelihood when changing the obtained PID for other hypotheses are made available for the analysis.

#### Muon Identification

For each track with  $p > 3 \text{ GeV}/c$ , hits in the muon stations are searched for in a window around the track extrapolation. A track is considered as a muon if the number of hits found is larger than a threshold value which depends on the track momentum.

#### Electron and Photon Identification

Electron are mainly identified trough the ratio of the energy released in the ECAL and their momentum. Further improvements also use the deposition of energy in the preshower and in the HCAL. Photons are identified by cluster in the ECAL which cannot be associated with any tracks.

For each charged particle, the contribution from the different particle identification devices can be combined into a log-likelihood difference (DLL) between a given PID hypothesis and the pion hypothesis. The DLL for a particle type  $a$  is then

$$\text{DLL}_a = \Delta \ln \mathcal{L}_{a\pi} = \ln \mathcal{L}_a - \ln \mathcal{L}_\pi = \ln \left[ \frac{\mathcal{L}_a}{\mathcal{L}_\pi} \right], \quad (3.2)$$

where  $\mathcal{L}_a$  is the likelihood of the  $a$  hypothesis, combined from the various identification devices. The DLL between two particle hypotheses  $a$  and  $b$  is then obtained:

$$\Delta \ln \mathcal{L}_{ab} = \Delta \ln \mathcal{L}_{a\pi} - \Delta \ln \mathcal{L}_{b\pi}. \quad (3.3)$$

### 3.3 The Trigger System

At LHCb nominal luminosity of  $2 \times 10^{32} \text{ cm}^{-2} \text{ s}^{-1}$ , inelastic  $pp$  collisions are expected at a rate of 16 MHz, of which 10 MHz are visible by the LHCb spectrometer, of which in turn 15 kHz are expected to contain at least one  $b$  hadron whose all the decay products are fully contained in the detector acceptance<sup>6</sup>. Since data storage space and computing power are limited, this rate has to be reduced. The role of the trigger is to identify and select interesting events, effectively reducing the rate of events permanently recorded on tape from 10 MHz to 2 kHz while enriching the proportion of interesting events in the recorded data. Therefore, the trigger is of crucial importance; it exploits the long life and relatively high mass of the  $b$  hadrons to select them amongst all collisions [141, 158, 170]. It is designed with a two-level architecture. The first-level trigger (L0) is implemented through custom electronics, and operates synchronously with the 40 MHz bunch crossing frequency, whereas the High Level Trigger (HLT) is software implemented and executed asynchronously on a processor farm. The trigger logical flow, together with the approximate output rate after each level, is illustrated in Fig. 3.19.

#### 3.3.1 First Level Trigger L0

The main goal of the L0 trigger is the reduction of the event rate from 10 MHz to 1.1 MHz for which the entire detector can be read out. To be able to operate at the 40 MHz bunch crossing frequency, the L0 uses only partial information from the detector. The main selection criteria derive from the large mass of the  $b$  hadrons, whose decay products often possess large transverse momentum ( $p_T$ ) and large transverse energy ( $E_T$ ). Crossings with multiple  $pp$  interactions lead to trigger decision more likely based on combinatorics than on a genuine  $b$  decay, and use a disproportional share of bandwidth and processing during the event building. For these reasons, the number of interaction within a crossing is taken into account. Exploiting those criteria, the L0 bases its decision on:

- the reconstruction of the hadrons, electrons, neutral pions and photons with the highest  $E_T$  in the calorimeters,
- the reconstruction of the muons with the highest  $p_T$  in the muon chambers,
- the track multiplicities and the number of interactions, reconstructed in the Pile-Up System.

---

<sup>6</sup>This computation assumes the following cross sections at 14 TeV:  $\sigma_{pp}^{\text{ine}} = 80 \text{ mb}$  for the inelastic  $pp$  interaction,  $\sigma_{pp}^{\text{vis}} = 50 \text{ mb}$  for the  $pp$  interactions visible by LHCb and  $\sigma_{b\bar{b}} = 0.5 \text{ mb}$  for the  $b\bar{b}$  production. An interaction is said to be visible if it produces at least two charged particles leaving enough hits in the VeLo and Tracking stations to be reconstructed. There exists a large uncertainty on those figures, for example PYTHIA 6.4 gives  $\sigma_{b\bar{b}} = 1.04 \pm 0.01 \text{ mb}$  [169].

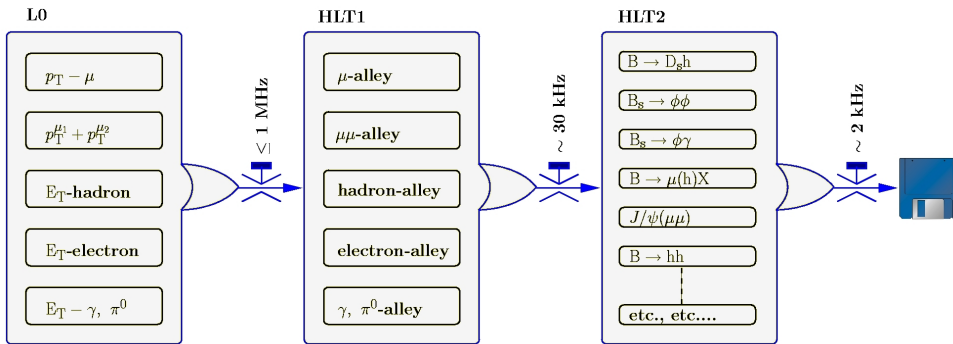


Figure 3.19: Schematic view of LHCb trigger flow.

**The L0 calorimeter trigger** looks for high  $E_T$  candidates among photons, electrons, neutral pions and single hadrons. It forms clusters of  $2 \times 2$  sensitive cells and selects the clusters with the highest energy. Exploiting the relative narrowness of the showers, the  $2 \times 2$  surface is large enough to contain most of the energy while being narrow enough to prevent for showers overlap. Difference of behaviour in the SPD, PS, ECAL and HCAL are used to identify the particles. Furthermore the total  $E_T$  is also computed to reject crossings without visible interaction and also to veto triggers from muons of the beam halo.

**The L0 muon trigger** is based on the track reconstruction using only information from the muon chambers. The track finding algorithm looks for hits on a straight line in the five muon stations. Hits in the first two stations combined with the hypothesis that the muon originates from the interaction point are used to determine the  $p_T$  with a resolution of 20 %. The two highest  $p_T$  candidates per quadrant are selected, resulting in up to eight candidates per event.

**The Pile-Up system** is composed of two  $r$ -sensitive silicon planes, perpendicular to the beam axis, and situated upstream of the VeLo, as described in Section 3.1.1. It is used to count the number and position along the beam axis of the primary vertices of a given bunch crossing, as well as the total multiplicity of backward charged tracks.

All this information is passed to the L0 Decision Unit (L0DU), a board which combines it and provides a logical decision per bunch crossing. The buffer implemented in the front-end readout chips of the entire detector fixes the L0 latency to exactly 160 bunch crossings, thus to  $4\ \mu s$ . The time-of-flight of the particles, the readout and cable delays already account for  $2\ \mu s$ , leaving the remaining  $2\ \mu s$  for processing the information and reaching a decision.

### 3.3.2 The High Level Trigger HLT

The HLT aims to reduce the event rate from 1.1 MHz to 2 kHz. It consists of a software application running on a processor farm. The HLT has access to all data of an event and thus could execute the offline selection algorithms. However, for efficiency sake, the bulk of the uninteresting events is rejected with partial reconstruction in a first stage called HLT1. For the remaining events, a full reconstruction is performed in the stage called HLT2.

#### HLT1

The HLT1 is organised in several parallel sequences of algorithms, called trigger alleys, each of which addresses one of the L0 trigger types, as shown in Fig. 3.19. About 15 % of the L0

triggered events are selected by multiple triggers, these events consequently go through more than one HLT1 alley. The HLT1 strategy is to confirm the L0 decision for each candidate that triggered the L0; such a particle is called an L0-object.

At each step of this algorithm sequence, additional information from the tracking is used, refining the procedure, notably by computing the transverse momentum  $p_T$  and the impact parameter IP with respect to the primary vertex.

After each step, the L0-object is required to be reconfirmed. The sequence stops as soon as a L0-object is not reconfirmed. For some of the alleys, additional particles are searched for to improve the discrimination. The dimuon alley is such an example, and is important for the  $B_s^0 \rightarrow \mu^+ \mu^-$  analysis. In that alley, if a L0 muon candidate is confirmed by the trackers, another muon is searched for in the muon stations. This extra muon is then tested against the trackers and required to make a good vertex with the first muon.

Although the HLT1 runs independently on the possible multiple alleys of a single event, the tracks and vertices are reconstructed only once and this information is available for all alleys.

When the L0-object is successfully confirmed by the sequence of tests, the HLT1 decision is reached. It is based on cuts on  $p_T$  and the IP of the confirmed L0-object, and if an extra track was reconstructed cuts on its  $p_T$  and IP, and on the distance of closest approach (DOCA)<sup>7</sup> of the two tracks are also considered. A large part of the dimuon events is triggered without IP cut, to allow for proper time unbiased analyses.

The output rate of the HLT1 is foreseen to be a few dozen of kHz. The relative bandwidth of the different alleys is not fixed and will certainly be adapted to the evolution of the LHCb physics goals. This illustrates the flexibility conferred by the software nature of the HLT trigger.

## HLT2

The second and last stage of the High Level Trigger, called HLT2, is also software implemented. It is more specifically driven by the physics analyses than the previous triggers. It is organised in two parallel processes, the inclusive and the exclusive selections, a final positive trigger decision being reached when either of the two selection gives a positive outcome.

The HLT1 output rate is low enough to allow for a full event reconstruction. HLT2 tracks differ from offline reconstructed tracks (see Section 3.1.4) only by not having been fitted with a Kalman filter and thus lack a full covariance matrix. From these reconstructed tracks, a subset is loosely selected on their momentum and IP. Then one tries to combine those selected tracks to make very common composite particles, such as  $K^* \rightarrow K^+ \pi^-$ ,  $\phi \rightarrow K^+ K^-$ ,  $D^0 \rightarrow hh$ ,  $D_s \rightarrow K^+ K^- \pi^-$  or  $J/\psi \rightarrow \mu^- \mu^+$ . This pool of composite particles is used in the computation to follow, thus avoiding multiple reconstructions.

The exclusive trigger selects events with decays in specific channels. It covers the needs of all LHCb physics analyses, running a selection for each signal channel and each control channel. The HLT track resolution being worse than the offline resolution, wide selections cuts are used.

The inclusive trigger aims at the selection of events containing resonances, which are likely to come from  $B$  decays, such as  $D^*$ ,  $J/\psi$  or  $\phi$ , and events containing muons. This is implemented in three lines, the  $D^*$  line, the inclusive dimuon line, and the inclusive single muon line.

---

<sup>7</sup>The DOCA reflects the quality of the vertex formed by these two tracks and also the quality of the di-particle mass.

## 3.4 The LHCb Software

The need for a stable software organisation, that can withstand evolutions in both software and technology over the life of the experiment, led to the development of the GAUDI [171] framework. GAUDI is an C++ object-oriented architecture, that provides a well-defined framework for software components and their interactions with each others. The LHCb software chain, from Monte Carlo simulated data generation to their physics analysis is described below [172].

GAUSS [173] is the Monte Carlo simulation application. It steers both the event generator and the simulation of the behaviour of the generated particles in the LHCb apparatus. The event generation phase uses PYTHIA [169] to simulate  $pp$  collisions, generate produced particles, defined by their energy-momentum four-vectors and to decay those particles. The decay of  $b$  hadrons is performed by the dedicated EVTGEN [174] package. Both PYTHIA and EVTGEN are anterior to LHCb<sup>8</sup> and available to the HEP community; they were tuned according to LHCb needs. Multiple  $pp$  interactions are generated according to the luminosity of the simulation. The detector simulation phase uses the particles produced at the previous step, with the description of the detector to simulate the physical processes that those particles undergo when travelling through the experimental setup. This simulation is done by the GEANT4 [175] application. The description of the detector includes the mapping of the magnetic field, and the size, position, and atomic composition of the detector elements, so that the effect of magnetic field on charged particles, the energy loss through radiation and interaction with material, as well as the multiple scattering effect are taken into account. Particularly, the interaction of the particles in the sensitive materials is crucial for the next step.

BOOLE [176] is the digitisation application; it finalises the LHCb detector simulation. BOOLE takes as input the Monte Carlo hits previously generated in sensitive detectors by the GAUSS simulation application. The digitisation simulates the subdetectors and the response of the readout chain electronics to those hits, taking into account electronics efficiency and known biases. The effect of spillover, the possible pollution to the electronic signal coming from the two preceding and the one following bunch crossings is introduced. The L0 trigger response is also simulated. After the BOOLE application, the Monte Carlo simulated data has the same format as the real raw data.

BRUNEL [177] is the reconstruction application. It proceeds from hits to reconstruct tracks, computes their momenta, and extracts the particle identities (PIDs) using the data from the RICHes, calorimeters and Muon System. BRUNEL outputs are stored as a DST<sup>9</sup> to be used for the physics analyses.

DAVINCI [178] and BENDER [179] are the physics analysis frameworks. DAVINCI is used by end-users to perform physics analysis of the data. It provides effective C++ functions for the reconstruction of vertices, and the computation of physical values to be used as selection criteria. Eventually, the running of selection algorithms provides a set of events with the desired characteristics. BENDER is based on PYTHON [180]. It takes advantage of the flexibility of the PYTHON scripting language and since it delegates time consuming tasks to C++ functions, almost no computing time penalty arise from using this non-compiled language.

There are others programs, among them PANORAMIX [181], which provides graphical display for the detector geometry and event data.

---

<sup>8</sup>PYTHIA was developed and is maintained by the Lund University, in Sweden. EVTGEN was developed by the BABAR collaboration.

<sup>9</sup>Data Summary Tape



## Chapter 4

# Production and Assembly of the Inner Tracker



THE AUTHOR IN DEEP REFLEXION

The Inner Tracker is part of the LHCb tracking system; it provides information about the point of passage of the charged particles flying close to the beam pipe. It is a silicon microstrip detector whose sensitive surface adds up to approximately  $4.2\text{ m}^2$  with more than 129 k readout channels.

At the location of the Tracking Stations, see Fig. 3.3, the LHCb acceptance, *i.e.* the area for the tracking devices to cover is  $\approx 27\text{ m}^2$ . The large variation in terms of particle flux that exists between the central region, where the flux is maximal, and the peripheral region of a tracking station, where it is negligible, calls for the use of two different detector technologies. As a consequence, while most of the surface is covered with straw-tube drift chambers forming the Outer Tracker (OT), the innermost region is covered with silicon microstrips forming the Inner Tracker.

The specifications of the silicon sensors — and the associated front-end electronics — used in the Inner Tracker are obtained by considering the following competing requirements:

**Minimisation of the material** At LHCb, multiple scattering dominates the momentum resolution up to  $80\text{ GeV}/c$ . As the Inner Tracker front-end electronics, mechanical support and cooling are located inside the LHCb acceptance, minimisation of the material budget is an important consideration. The design of the support mechanics has been done with the goal of minimising the material while keeping sufficient rigidity and precision. The silicon of the sensors represents an important contribution to the amount of material. Consequently, the sensor thickness has to be minimum. However, reducing the silicon thickness worsens the signal-to-noise ratio, which needs to be larger than 12 for a good hit efficiency. As a compromise, a silicon sensor thickness of  $320\text{ }\mu\text{m}$  for the one-sensor modules, and of  $410\text{ }\mu\text{m}$  for the two-sensors modules, is chosen [157].

**Spatial resolution** The LHCb physics goals translate into a required momentum resolution of  $\delta p/p \approx 0.4\%$ , which in turn translates to a rather moderate spatial resolution of  $70\text{ }\mu\text{m}$  for the Inner Tracker. Considering one-strip clusters this requirement calls for a strip pitch  $p$

of  $240\text{ }\mu\text{m}$  ( $\sigma_{\text{hit}} = \frac{p}{\sqrt{12}}$ ). With such a pitch, a ballistic deficit effect was seen for particles crossing the silicon between two strips. This loss of charge translates into an unacceptable decrease in single-hit efficiency of 3 %. It was shown that for a  $198\text{ }\mu\text{m}$  pitch the efficiency drop was only about 1 %, which led to this pitch choice [182, 183]. The same charge loss effect drove the choice of the strip implantation width,  $w$ . While a small  $\frac{w}{p}$  ratio reduces the strip capacitance and consequently the preamplifier noise, the charge collection was found to be deteriorating at small  $\frac{w}{p}$  values. Test-beam measurements allowed to find the optimal configuration as  $\frac{w}{p} \approx 0.25$  [183].

**Hit occupancy** For a typical event, a charged particle density of  $1.5 \times 10^{-2}\text{ cm}^{-2}$  is expected close to the beam pipe and  $2 \times 10^{-3}\text{ cm}^{-2}$  in the outer regions [156]. The maximal strip occupancy should not be in excess of a few percent. This requirement translates into a condition on the product of the pitch and the length of the strips.

**Signal shaping time** At the LHC bunch crossing frequency, collisions potentially occur every 25 ns. The front-end electronics amplifier has to be able to shape the signal in that period, to avoid significant superposition of consecutive events (spill-over). Simulation showed that the track reconstruction is possible if the remaining fraction of the signal amplitude at the sampling time of the next bunch crossing does not exceed 30 % [183].

**Single-hit efficiency** A detection efficiency for a Minimum Ionising Particle (MIP)<sup>1</sup> close to 100 %, for each single layer is sought. However, the noise hit rate should be low; test beam showed that a noise rate of  $10^{-4}$  was achieved. Test beam have also shown that the single-hit requirement is only fulfilled, over the ten years lifetime of the experiment, for an initial signal-to-noise ratio<sup>2</sup> larger than 12 [182, 183].

**Resistance to radiation damage** A 1 MeV neutron equivalent fluence of  $9 \times 10^{12}\text{ cm}^{-2}$  is expected in the innermost region of the Inner Tracker for ten years of operation. The radiation damage to the silicon induces leakage currents. The leakage current also increases with temperature, and above some temperature threshold a thermal runaway process occurs, leading to the destruction of the sensor. Consequently, due to the front-end electronics power dissipation, active cooling of the Inner Tracker is required, to keep the sensor below 5 °C. This cooling is done by liquid C<sub>6</sub>F<sub>14</sub> at -25 °C [184]. As a consequence, the humidity in the detector enclosure has to be controlled to avoid dew or even ice; this is achieved by a constant flow of N<sub>2</sub> and good air tightness of the box envelope.

**Dimensions** The maximal sensor dimensions are driven by the production process. The silicon crystal, which composes the bulk of the sensor, was grown using the floating zone method in the form of a cylinder. This cylinder is then cut in disks, called wafers, on which the required doping and metalisation layers are applied. The floating zone produces a very pure monocrystal, but limits its diameter<sup>3</sup> to 150 mm, which in turn limits the dimensions of the sensor that can be cut from such a disk. In the last decade, it was shown that crystals obtained with the Czochralski method, which is the most popular in the silicon industry, are more radiation tolerant than the floating zone processed crystals [185].

Taking into account these considerations, the Inner Tracker sensors have the characteristics given in Table 4.1.

<sup>1</sup>For a given material and a given particle, the MIP is the energy or momentum, for which the energy loss per unit of length in the material is minimal. It corresponds to the minimum of the Bethe-Bloch formula. Typically, for common material, it is around 0.3 GeV/c for  $\mu$  and 0.5 GeV/c for  $\pi$  particles.

<sup>2</sup>The signal-to-noise ratio,  $S/N$ , is defined as the most probable MIP signal amplitude divided by the RMS of the strip noise distribution.

<sup>3</sup>The 150 mm ( $\approx 5.9$  inches) wafers are often called 6-inch wafers.

Table 4.1: Specifications of the Inner Tracker silicon sensors.

Overall length	$110 \text{ mm} \pm 5 \mu\text{m}$
Overall width	$78 \text{ mm} \pm 5 \mu\text{m}$
Thickness	$320 \mu\text{m} \pm 5 \mu\text{m}$
	$410 \mu\text{m} \pm 5 \mu\text{m}$
Bulk crystal orientation	$\langle 100 \rangle$
Bulk resistivity	$(2.5 - 7) \text{ k}\Omega \text{ cm}$
Strip minimum active length	108 mm
Strip pitch	$(198 \pm 1) \mu\text{m}$
Strip implant width	$(50 \pm 1) \mu\text{m}$
Strip metalisation width	$(58 \pm 1) \mu\text{m}$
Number of strips per sensor	384
Number of bad strips per sensor <sup>4</sup>	< 4

The Inner Tracker external dimensions and shape are driven by the following considerations:

- The average occupancy of the OT module where the particle flux is the highest should not exceed 10 % at the nominal luminosity;
- The overall IT area should be minimal, as silicon sensors are expensive;
- An overlap of 1 cm between the IT and OT areas is needed to prevent gaps in the acceptance;
- The modularity of both detectors, defined by the dimensions of their modules, must be respected.

The solution found for the Inner Tracker consists in an arrangement of four independent boxes covering a cross-shaped area around the beam pipe. The detector boxes are placed above, below, and on either side of the beam pipe, as shown in Fig. 4.1. The boxes above and below the beam pipe are called respectively Top and Bottom central boxes, whereas the boxes on each side of the beam pipe are called Access and Cryo side boxes, following the LHCb naming convention. Each detector box contains four layers of seven detector modules, the external layers with vertical strips, the inner layers with strips oriented at  $\pm 5^\circ$  with respect to the vertical. The central boxes are composed of one-sensor modules, with 11 cm long strips, while the side boxes are composed of two-sensors modules, resulting in 22 cm long strips.

This chapter describes the detector modules production and the assembly and mounting of the Inner Tracker detector boxes. First, the origin of the components used in the production process of the modules or in the detector box assembly and whose fabrication was not within EPFL’s responsibility is detailed. Section 4.2 presents the detector module production by the gluing of the silicon sensors and of the front-end electronics on a support. This operation was performed at EPFL. The assembly of the detector boxes was done in the hall of the PH Department Silicon Facility in building 186, at CERN, in a custom-built controlled environment, the *clean tent*. In Section 4.3, the various components needed to build an Inner Tracker detector box are briefly presented and Section 4.4 details the assembly process. The box assembly procedure was published in Ref. [186].

<sup>4</sup>Bad strips are strips with one or more of the following defects: pinhole, open strip or shorted strips.

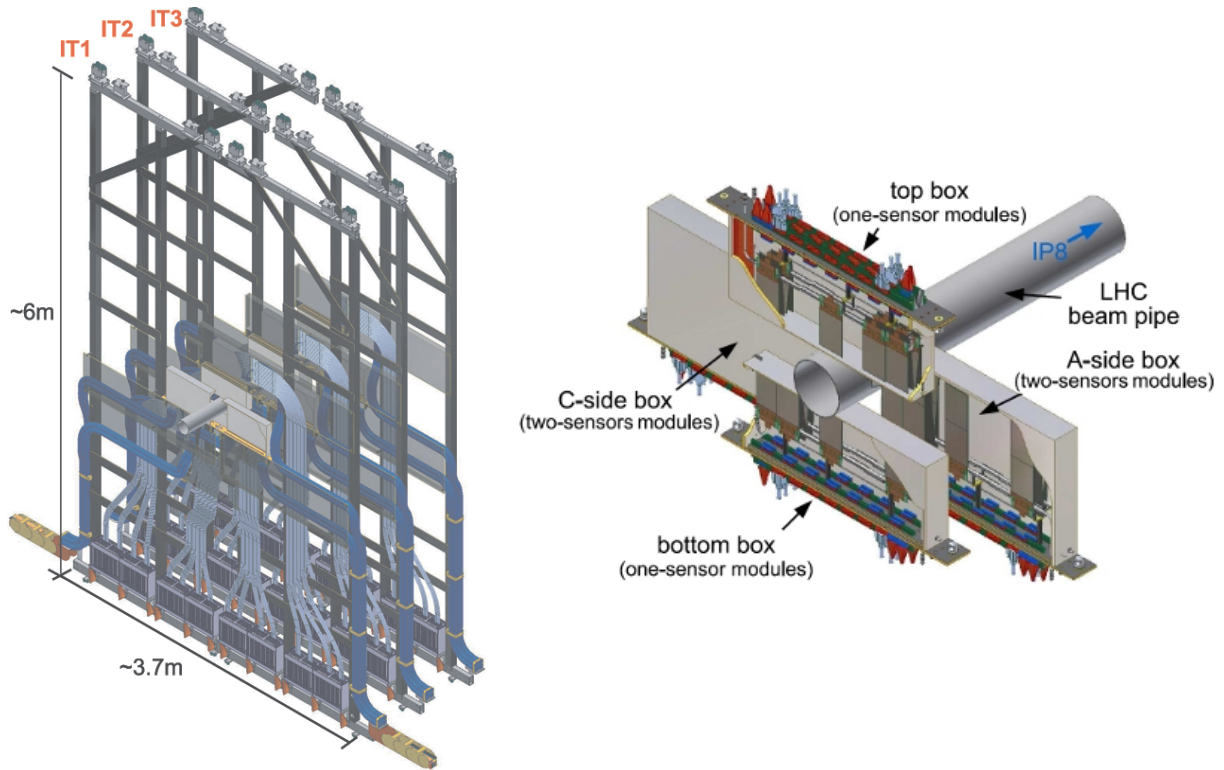


Figure 4.1: The Inner Tracker detector consists of three stations IT1, IT2 and IT3 (left), each broken down into four independent detector boxes located around the beam pipe (right). The boxes above and below the beam pipe are called Top and Bottom central boxes and contain one-sensor modules, whereas the boxes on the side of the beam pipe, called Access and Cryo side boxes, contain two-sensors modules.

#### 4.1 Origin of the Elements Composing the Inner Tracker

The silicon sensors with the specifications optimised for the Inner Tracker needs have been produced by Hamamatsu Photonics K.K. (HPK) [187], in Japan. This company also produced the silicon sensors for the Tracker Turicensis (TT). Upon delivery, the TT and IT sensors have been tested at the University of Zürich to check the fulfilment of the contractual requirements in terms of faulty strips, IV behaviour, and dimension tolerance were met [188]. Furthermore, those tests allow the assignment of a quality figure to each sensor. This quality score is used to match the sensors composing the two-sensor modules in pairs of sensors of similar quality. Similarly, once the modules are produced and tested, an updated quality score is used to decide the positioning of each sensor in the detector box, the best sensors being used where the particle flux is the highest.

A radiation hard readout chip, called *Beetle*, was designed for the LHCb experiment [189] at the University of Heidelberg and the Max-Planck-Institute in Heidelberg, together with the NIKHEF/Free University Amsterdam and Oxford University. Three Beetle chips, together with passive electronic components, and a ceramic pitch adaptor mounted on a flexible polyimide printed circuit board (PCB) form the front-end hybrid [190]. The ceramic pitch adaptor is needed to match the silicon sensor pitch to the pitch of the Beetle input pads. The pitch

adaptor production and the assembly of the hybrids was done by RHe Microsystems [191], in Germany.

The detector box containers, whose use in the box assembly process is detailed in Section 4.3.2, have been designed and prototyped at EPFL. At that occasion, the composition of the wall and their thickness was optimised to minimise the material and allow the sensors to be as close as possible of the beam pipe, while keeping a sufficient thermal insulation. The containers were produced by the Universidade de Santiago de Compostela workshop, in Galicia.

The readout electronics chain comprises, after the Beetle chip, the signal digitisation and optical multiplexing in electronic service boxes, situated just outside of the acceptance at the foot of the T stations, and then the final data acquisition is performed in a counting house, shielded from radiation by a concrete wall. The digitisation of the Beetle signal is done by an electronic card called Digitiser Board [192]. Each Digitiser Board treats signals coming from one detector module, and its output is multiplexed and sent via optical fibre to the counting house. The Digitiser Boards were designed and produced under the responsibility of the University of Zürich. In each service box, a Control Board provides Time, Trigger and Control (TTC) signals, as well as slow control interface (ECS) for the Digitiser Boards and Beetle chips; it also has the task to monitor the temperature and the humidity in the services boxes and detector boxes [193]. The Control Boards were designed and produced under the responsibility of the Universidade de Santiago de Compostela.

The position of the Inner Tracker at the centre of the detector acceptance calls for the extensive use of light but rigid materials. Those competing requirements are best met by the use of composite materials. The structure of the Inner Tracker stations consists in pillars made of carbon fibre and glass fibre sandwich and in lightweight plates made of honeycomb-carbon fibre sandwich. The module support, on which the silicon sensors and a hybrid are glued, also uses a carbon fibre sandwich structure. All those elements have been produced by a small company, Composite Design [194], specialised in the manufacturing of high precision composite parts.

## 4.2 Production of the Detector Modules

Figure 4.2 shows the composition of a detector module. It consists of one or two silicon sensors bonded via a pitch adaptor to a front-end hybrid. The support structure is made of a layer of Airex foam sandwiched between two sheets of high thermal conductivity carbon fibre; a Kapton sheet is glued on top of this structure for electrical insulation. The balcony, a small aluminium insert, is embedded into the module support at the location of the readout hybrid. It provides a direct heat path between the front-end chips and the aluminium cooling rod onto which the modules will be mounted. It is also in the balcony that are drilled the alignment holes that allow for a precise positioning of the module on the cooling rods.

### Gluing of the front-end hybrid

The three Beetle chips of each hybrid are read out on a dedicated test stand to check their basic functionality. A visual inspection of the pitch adaptor is performed under binocular, to look for shorted strips or pollution on the bond pads that could prevent bonding. The support is positioned on a dedicated *hybrid gluing jig*, shown on the right in Fig. 4.2, using the alignment hole of the balcony. The function of this jig is to constrain the position of the hybrid with respect to the alignment holes, more specifically, the important point is that the edge of the

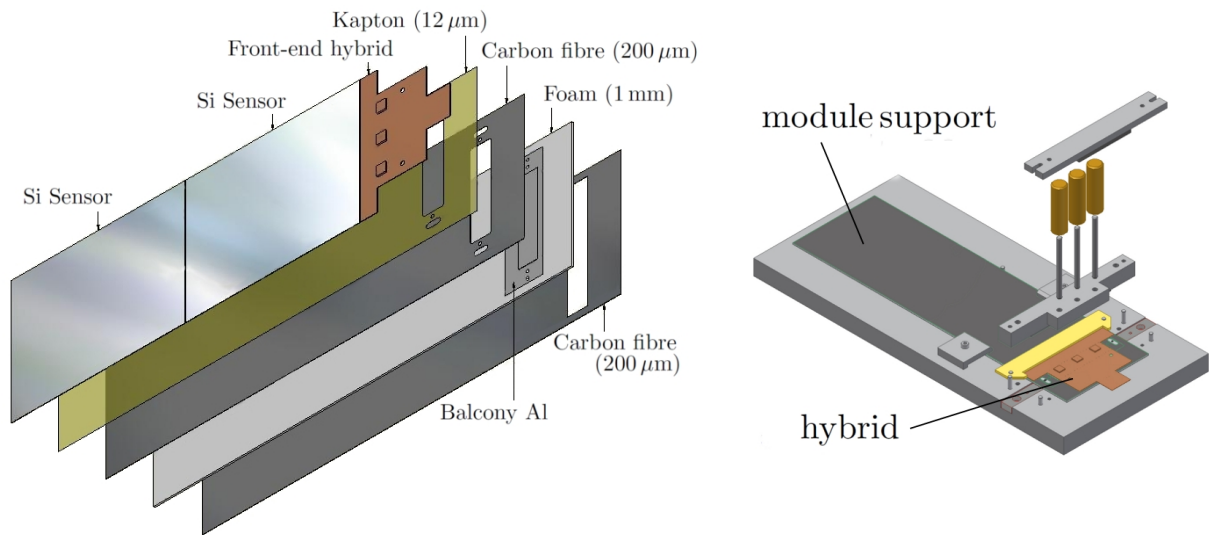


Figure 4.2: Left: Detector module composition. Right: Sketch of the jig used for the gluing of the hybrid on the module support.

pitch adaptor is correctly positioned to allow for the sensor-pitch adaptor bonding. Lines of glue are laid on the module support by a glue-dispenser robot. The glue is a mixture of conventional slow-cure Araldite to which 1% in weight of hollow glass microspheres are added in order to increase the viscosity and make the use of the glue dispenser possible. To ensure electrical and thermal conduction between the front-end Beetle chips and the aluminium balcony, a small quantity of silver epoxy glue is laid on the back of each Beetle chip. The hybrid is then put in place on top of the support, its position being constrained by the jig, and dedicated pieces maintain a small pressure on the hybrid and on top of each of the Beetle chips while the glue is curing. After a night of curing the hybrid is read out again to check that it was not damaged during the procedure.

### Gluing of the silicon sensors

A second type of jig, called *sensor gluing jig*, is used for the gluing of the sensors. A sketch of such a jig is visible on the right in Fig. 4.3. The role of this jig is to ensure the precise positioning of the sensors with respect to the alignment holes of the module. Provided the gluing of both the hybrid and the sensor are well done, this also ensure that the edges of the sensor and the pitch adaptor are parallel. The support, on which the hybrid is already glued, is placed on a sensor gluing jig. The glue dispenser is used for the application of two (or four) lines of silicone-based glue on the support. The dispenser is programmed so that the glue lines are positioned just below the sensor bond pads, so that the strain sustained by the sensor during the bonding process is minimal.

After a visual inspection and a cleaning with ionised Nitrogen, one or two sensors, depending on the type of module, are laid on a third type of jig, the *sensor positioning jig*, shown on the left in Fig. 4.3, whose role is to constrain the position of the sensor and the relative position between the two sensors, if applicable. This jig offers two Teflon pads, whose dimensions are slightly smaller than the ones of a sensor and in which grooves are engraved; those grooves can be connected to a network with a light vacuum. The sensor positioning jig presents two alignment

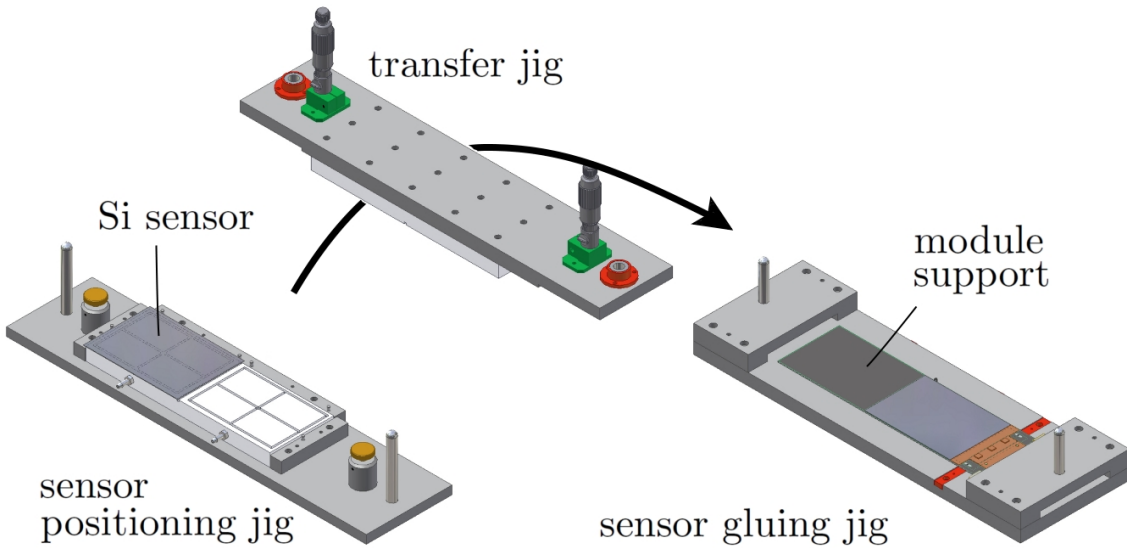


Figure 4.3: Sketch of the jigs used in the sensor gluing process. The sensors are positioned on the positioning jig, and then vacuum-transferred *via* the transfer jig to their final position on the sensor gluing jig<sup>6</sup>.

pins on the length of each pad and one pin on the width of each pad that is not adjacent to the other pad. The sensor, laying on the pad, is gently pushed until two of its edges rest against the pins, and the sensor is maintained by the application of the vacuum under it, which sucks it in place. The contact is checked under binocular and so is the parallelism of the inter-sensor gap, if present. If needed, the suction is stopped, corrections are applied, and the suction is reapplied.

The sensors are then vacuum-transferred from the sensor positioning jig to the sensor gluing jig, using a fourth type of jig, the *transfer jig*, and delicately laid on the previously drawn silicone glue lines, as illustrates Fig. 4.3. Figure 4.4 shows a daily production of two-sensor detector modules after curing of the glue. The modules still lie in the gluing jigs, and transfer jigs can be seen in the background.

The detector modules are then shipped to CERN for the last step of the production, which is the wire bonding. First, only the bias voltage and ground connections are bonded and a HV test is performed. Upon success of the HV test, the readout strips are bonded, from the Beetles to the pitch adaptor, from the pitch adaptor to the first sensor and in-between sensors, if applicable.

The bonded modules undergo a series of test motivated by quality assurance and ranking of the modules. A metrological survey, and a 48-hour burn-in test is performed on each module. The delay between the module production and the final tests was kept small in order to limit the affected batch of modules in case of a systematic defect uncovered by the tests. No important defects were revealed, but observations from the bonding technician allowed to fine tune the position of the glue lines below the sensor. The burn-in and testing procedures are documented in Ref. [196].

<sup>6</sup>Note the interesting semantic field arising from the tree-step procedure using tree jigs and the three-step jig dance. Merriam-Webster [195] indeed states:

- jig** ◦ any of several lively springy dances in triple rhythm; music to which a jig may be danced;
- a device used to maintain mechanically the correct positional relationship between a piece of work and the tool or between parts of work during assembly.

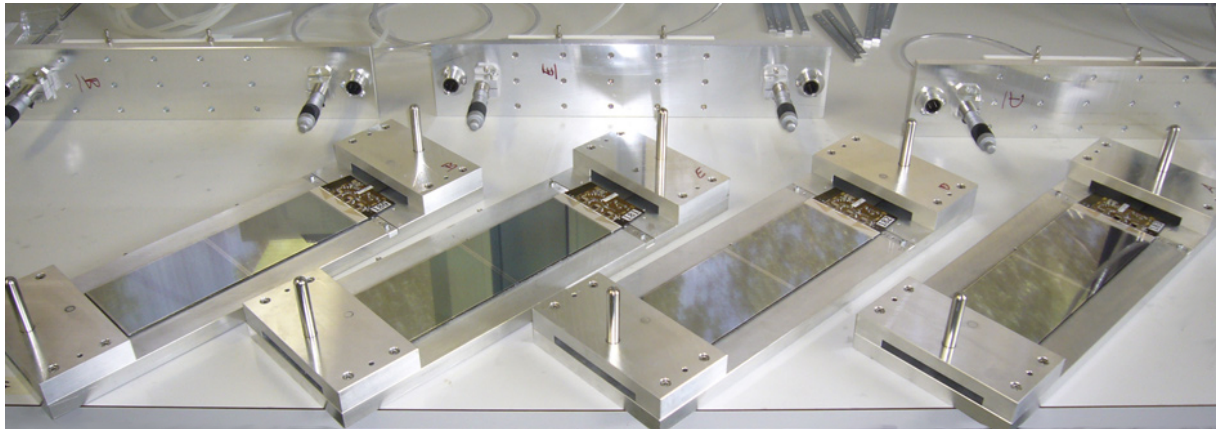


Figure 4.4: Daily production of Inner Tracker detector modules.

### 4.3 Detector Box Components

In this section, we describe the components entering in the assembly of an Inner Tracker box. We indicate how each item was prepared for use in the assembly procedure detailed in Section 4.4.

#### 4.3.1 The Cover

The cover fulfils several roles. It provides a mechanical interface between the Inner Tracker support frame (Fig. 4.1, left) and the detector modules inside the box (Fig. 4.1, right), as well as an electronics and power interface between the cables and the front-end hybrids (see Section 4.3.4 and Fig. 4.2). Being part of the whole box envelope, the cover provides a thermal insulation, as well as electric and light shielding.

The cover is made of foam<sup>7</sup> sandwiched between carbon fibre sheets (Fig. 4.5). This sandwich is covered on both sides with 81 µm thick aluminium foil<sup>8</sup>. Four printed circuit boards (interface PCBs) are glued into slits in the cover, one for each layer of detector modules. They:

- act as the interface of the electrical connections from the outside to the inside of the box;
- contain lines for the high- and low-voltage supply, I2C and data lines of the readout hybrids, four temperature probes of the box container and one humidity sensor located on one of the PCBs;
- contain lines for the grounding of the container inner shield and for the grounding of the detector modules.

A line of epoxy resin, mixed with hollow glass microspheres to increase its viscosity, is used on both sides of the PCB to ensure air tightness. This glue mixture is applied using a syringe with a flexible plastic needle made out of a plastic tube with 0.8 mm inner diameter.

The cover provides mechanical fixation for the sensor support structure, which is attached to it via three M3×20 screws. The cover is fixed to the box container using twelve nylon M2.5×20 screws. In the LHCb cavern, the detector box is fixed to its final position using three M4 nylon screws on both sides of the cover. The cover either rests on (Top boxes) or hangs under

<sup>7</sup>Airex R82

<sup>8</sup>3M 1170 Tape

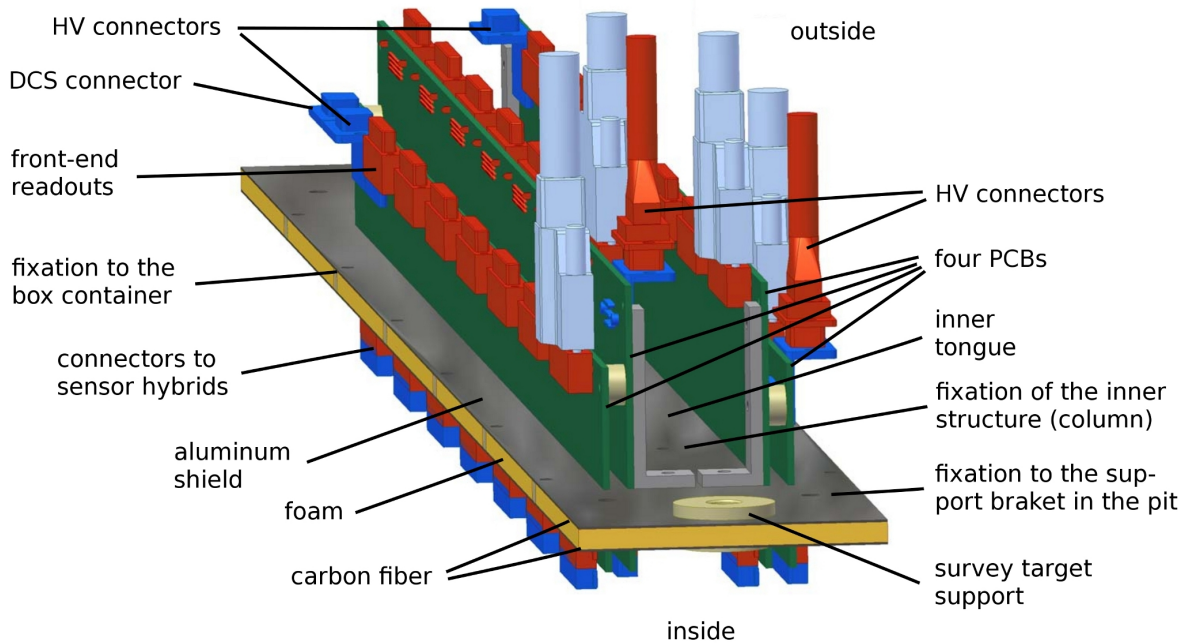


Figure 4.5: Schematic view of a cover.

(Bottom, Access and Cryo boxes) two carbon fibre brackets of the Inner Tracker support frames. On both sides of the cover, a stesalite insert was designed to house a survey target for theodolite measurements [197].

An aluminium cooling pipe runs along both cooling rods (Section 4.3.3) and both ends are passed through the cover through two custom made round polyamid pieces with an internal O-ring providing an air tight fitting.

### Features of the Cover Construction

Electrical shorts have been found between HV lines of the PCBs and carbon fibres of the cover as well as between LV lines and the carbon fibre in the first mounted box. To prevent this from happening, the interface PCBs have been covered with an additional layer of Kapton tape prior to insertion into the slits of the cover.

After the PCBs are inserted into the cover, they are fixed with screws and glued to the cover along their edges. The PCBs act as a stiff skeleton for the part of the cover that is between the inner PCBs, called the tongue (Fig. 4.5), which is quite flexible. It is important to control the position of this tongue before gluing, else the position of the modules was found to be unreliable. This is done using a dedicated jig, which controls the position of the tongue while gluing it.

After several connectivity problems with the first cover, leading to dead readout ports being discovered during the full electronic test (see Section 4.4.10), all the 64 lines of each of the 28 connectors in a cover plate have been tested as a standard procedure of cover testing. The test consists in the checking of the continuity of each line using a multimeter.

Thermoswitches<sup>9</sup>, which are required inside the detector boxes by the Detector Safety System (DSS) [198], have been tested for operation in high magnetic field [199]. As their presence was

<sup>9</sup>Thermik CO 60 model

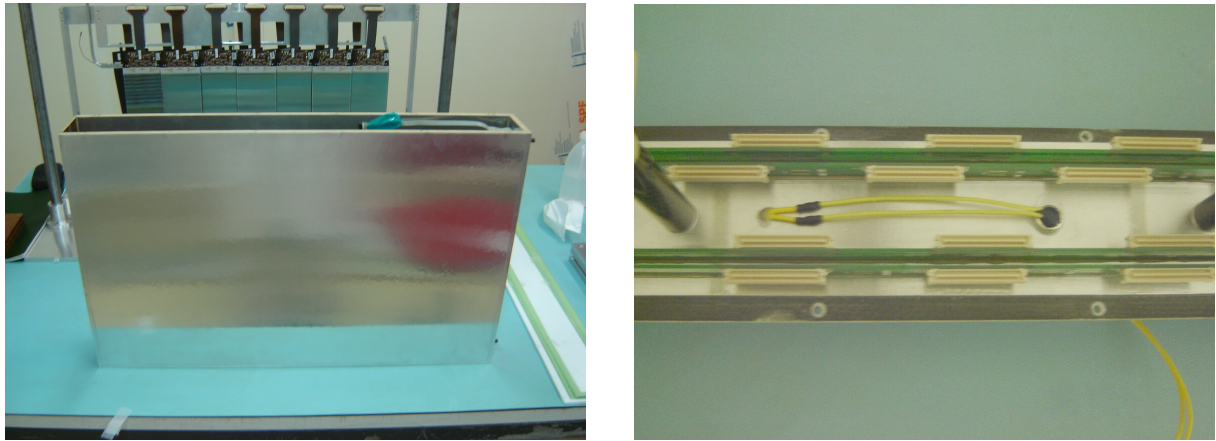


Figure 4.6: An empty box container (left). The wires visible, scotched on the inner wall, are the temperature probes readout and the inner shield ground wires. This bunch of wires will be connected to a PBC on the inside of the cover, when the modules are slid down in the box container (Section 4.4.12). The thermoswitch is glued under the cover to prevent it from touching the sensors (right), its wires traversing the cover structure through a hole ultimately filled with Araldite.

not foreseen in the initial design, no line was available in the interface PCBs. A small hole is therefore drilled in the sandwich structure of the cover to allow for the thermoswitch circuit wires to cross it. One thermoswitch is glued to the bottom side of each cover with Araldite (Fig. 4.6). The hole in the cover is then filled with Araldite from both sides.

A small PCB has been designed as a mini patch-panel for the DSS thermoswitch and the BEAMS circuit (see Section 4.3.2 for a description of the BEAMS system). It consists of a  $4 \times 3$  cm PCB glued on the 2 inner PCBs as shown on Fig. 4.7.

### Cover Preparation

The cover is first mounted on its support, taking care that the latter is adapted to the kind of boxes, side or central boxes, as they do not have the same dimensions. Figures 4.8, 4.22 (left) and 4.23 (right) show the whole set-up with a mounted cover. A screw at each end keeps a small pressure on the cover to prevent it from moving. A piece of plastic is placed between the cover and the screw to prevent it from damaging the cover (Fig. 4.17). The support allows the cover to be moved up and down, a vertical screw controlling this motion.

The cover is then carefully cleaned with compressed air and alcohol to remove the residual dust. As shown in Fig. 4.8, the columns (a) are fixed to the cover, using M3×20 screws and hard-paper collars, in order not to damage the thin aluminium film that makes the cover a Faraday cage.

A stesalite transverse piece (b), called a fork, is screwed to each column using a M3×8 screw. The fork connects the columns to two colonnettes (Fig. 4.9), the whole having the shape of a fork. The dimension of this piece is larger than the distance between the two cooling rods. The extremities of the forks are 0.5 mm away from the container wall. This is done to prevent any damage to the detector modules in case of shock to the box, the extremities of the forks stopping the movement before the sensors could touch the container wall. Furthermore, to prevent grounding loops, it is made of stesalite.

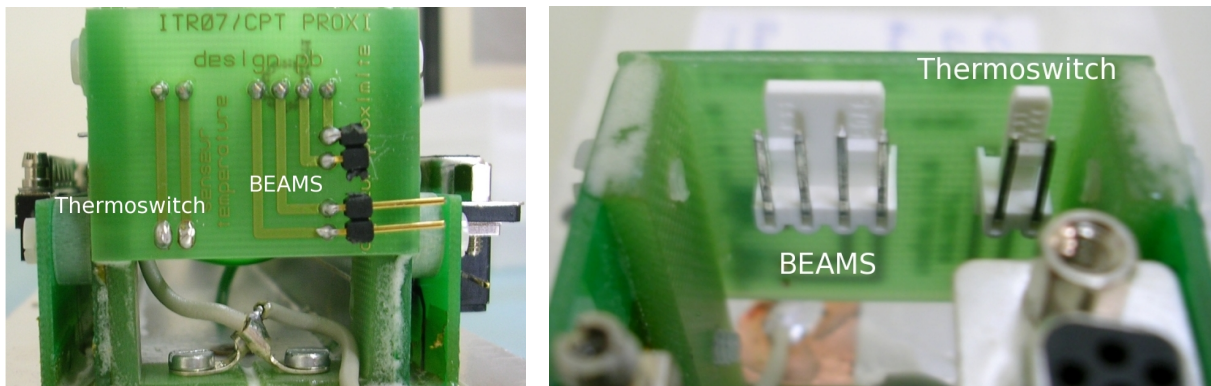


Figure 4.7: The same mini patch-panel for BEAMS and thermoswitch connections, viewed from either direction. In the left picture, the connectors to which the BEAMS device wires will be connected once the box is assembled can be seen. In this particular cover belonging to a side box, thus equipped with only one BEAMS device, the upper connectors were cut away leaving only the needed connectors, as can be seen in the left picture. The right picture depicts the same mini patch-panel from the opposite point of view.

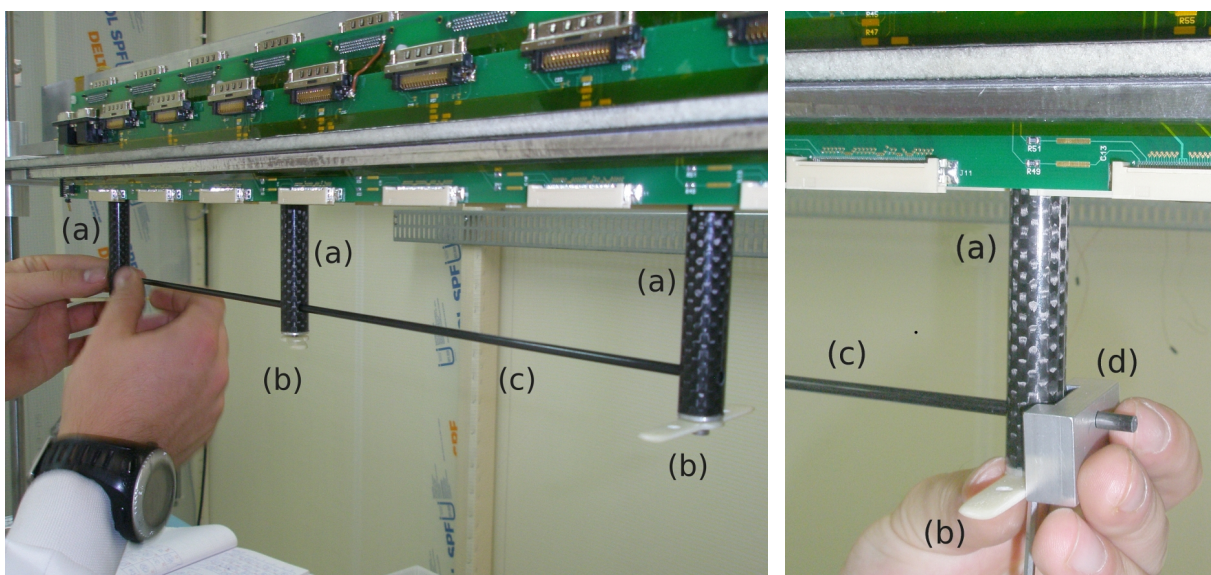
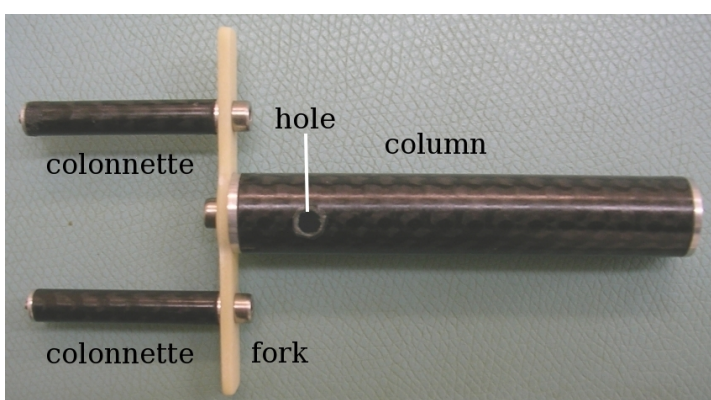


Figure 4.8: A cover mounted on its support. (a) columns, (b) fork, (c) bar, (d) special piece to control the position of the fork while it is being screwed tight.



◀ Figure 4.9: Detail of the assembly of a column, a fork, and two colonnettes. The hole in the column tube through which the carbon fibre bar is inserted when the fork is aligned can be seen. On this picture the alignment was not done, thus the hole is not centred with respect to the fork.

Each extremity of a fork has a bevelled edge to be placed downwards to avoid potential damage to the inner walls of the box when the cover is moved downwards into the box. There are holes at the bottom of each column to allow a thin carbon fibre bar (c) to be inserted through the three columns (a). This bar is used only to align the three forks while they are screwed in place. For this a special piece (d) is used to get the forks perpendicular to the carbon fibre bar. The thin bar (c) is then removed.

#### 4.3.2 The Box Container

The box container is made of a sandwich of glass fibre and PIR-foam covered with aluminium shielding on the inside and outside. The foam walls are 8 mm thick, except for the walls close to the beam pipe, which are 3 mm thick to allow the sensitive parts of the detector to lie closer to the beam pipe.

The box enclosure will be continuously flushed with N<sub>2</sub> to prevent condensation inside the box. The humidity has to be such that the dew point remains above the temperature of the coldest element in the box (which is at the coolant temperature). The incoming N<sub>2</sub> flow is spread within the box volume using a perforated channel made out of glass fibre.

Before using the box container in the assembly, several tasks are performed:

**Depth measurement** The depth of the container are measured with a gauge, from the lip of the container to its inside bottom, at six places along the container length. The measurement locations are defined by the position of the screw holes on the container lip. Conservatively, the minimal depth is considered when assessing whether the detector modules will fit the container. For central boxes, the modules are very close ( $\sim 0.5$  mm) to the bottom of the box container. For side boxes, this distance is not as small, but the container depth is measured anyway.

**Temperature probes** Four PT1000 temperature probes are placed inside the box container in addition to the probe installed on each readout hybrid. These measure the temperature of the box environment. Three of them are located at the bottom of the box and one on the side wall facing the beam pipe (side boxes) or opposite of the N<sub>2</sub> inlet (central boxes).

**Inner shield grounding** The inner and outer shieldings of the container are connected to the ground by a wire glued onto the aluminium shielding. Before gluing the wire on the shielding using conductive glue, the insulation of the wire is removed on approximately 2 cm. After two days of drying, a protective layer of Araldite is applied on top. The grounding of the inner shielding is soldered to the ground of the temperature probes, which is connected to the ground of the cover during the assembly process. The grounding of the outer shield (Fig. 4.10, right) connects to the ground line on one of the PCBs via a small connector.

**Verticality control** As the containers are standing on the base plate during the sensor modules insertion procedure, their verticality is important. Therefore, it is carefully checked and, if needed, corrections are brought by applying 100  $\mu$ m-thick layers of Kapton tape on the appropriate side of the container bottom.

**RMS support** The Radiation Monitoring System (RMS) detector [200] is supported by three out of the four IT container boxes of station T2 (Top, Access, Cryo). Therefore, stesalite pieces to fix the RMS detector are glued onto the wall of the appropriate containers. To maximise the adherence of the glue, the aluminium shielding is locally removed, the glass fibre surface is scratched and three small holes are cut into the glass fibre surface. A

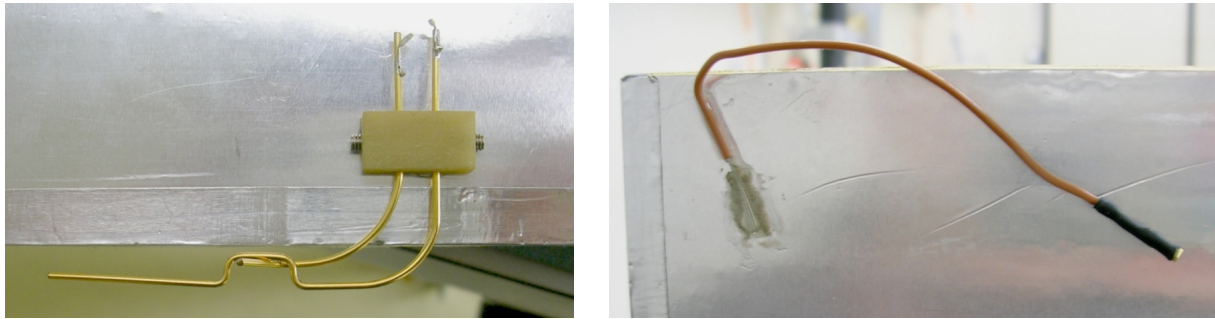


Figure 4.10: A BEAMS device (left) and the ground wire of the box external shield (right). This particular BEAMS device is located on the long edge of a central box, in such a position that it will lie just above or below the beam pipe, once the IT station is closed. This picture allows to understand how the BEAMS electric circuit opens if something pushes the lower finger up.

dedicated jig is used to constrain the relative position of the RMS support pieces with one another during the glue drying process.

**Beam pipe Approach Monitoring System (BEAMS)** The BEAMS is a safety device that raises an alarm in case a detector box is too close to the beam pipe in order to avoid possible damage. The nominal distance of the detector boxes to the beam pipe is 7 mm, and anything closer to 5 mm is supposed to trigger the alarm.

It consists of two gold plated metallic fingers which are in contact with each other in their nominal position (Fig. 4.10, left). The touching fingers are part of an electric circuit which is closed in nominal position. If the outermost finger touches the beam pipe, the fingers would separate from each other and consequently open the circuit.

There are six BEAMS devices per station, distributed as follows: two of them on each central detector box, and one on each side box. On the central boxes, one BEAMS device is located in front of the edge of the container which passes close to the beam pipe during the closure procedure of each half-station, like a bumper. This device is only useful during the closure of the half station, preventing a collision of the top or bottom boxes with the beam pipe. The other BEAMS device is located on the wall that is close to the beam pipe, so that it faces the beam pipe when the station is completely closed (the device in Fig. 4.10 is of that type). On the side boxes, there is just one BEAMS sensor such that the sensitive finger is at the level of the beam pipe 5 mm away from it.

The BEAMS system is fixed on the box containers. The stesalite pieces that support the fingers (Fig. 4.10, left) are glued to the container wall using a similar procedure as the RMS support. Their location is given by a dedicated jig.

### 4.3.3 The Cooling Rod

The cooling rods provide mechanical support, cooling, and grounding to the sensor modules. They consist of an aluminium part, with a complex crenellated design, glued to a pure aluminium tube (external diameter 6 mm, wall thickness 0.3 mm) in which the coolant liquid flows (Figs 4.11 and 4.12). Pure aluminium is highly ductile. Aluminium was chosen as it has a relatively low radiation length ( $X_0 = 24.3 \text{ gcm}^{-2}$ ) and can easily be bent into the desired shape without

inducing cracks in the thin walls of the tube. Due to their extreme fragility, the cooling rods have to be manipulated with great care.

To measure the path of a particle in 3 dimensions the Inner Tracker is made of four sensitive layers in a typical stereo layout. The two external layers, called X1 and X2, are made of sensors with microstrips aligned vertically, whereas the two internal layers, called U and V, have strips which form a  $\pm 5^\circ$  angle with the vertical axis. A cooling rod supports two layers of 7 modules. There are therefore two different types of cooling rod: the type A supporting V-X2 layers and the type B supporting X1-U layers.

Looking at a cooling rod, a crenellated structure can be seen (Fig. 4.11). This induces a slight staggering between a module and its neighbours and consequently ensures an overlap of the sensitive area. Thus, there is no dead space between two sensors, preventing the existence of gap in the sensitive surface. The length of the gap between two crenels is also the best way to distinguish between cooling rods of A or B type. This length is indeed about 0.5 mm larger for the U or V layers than for the X1 or X2 layers, as shown in Fig. 4.11. Thus, orientating the cooling rod so that the long tube (the part exiting the cover) is on the left-hand side in front of us, a B type (X1-U) cooling rod will have the longer interval on the side close to us.

Within the support structure of the sensor modules, there is an aluminium piece called the *balcony*. This piece provides stiffness and acts as a thermal bridge. The precision holes that govern the positioning of the module are machined in the balcony. The back of the front-end chips are glued on the balcony with conductive glue and the balcony is in direct contact with the cooling rod. The precise positioning of the sensor modules is achieved by the use of pins fixed to the cooling rod, which are inserted in the holes of the balcony. While mounting the first modules, it has been noticed that the distribution of the angle of the modules with respect to the vertical direction was very broad. Consequently, most of the modules were neither vertical, nor parallel with each other. The cause was traced back to the alignment pins of the cooling rod. Although they were machine-inserted into the cooling rod, their orientation was found to be inaccurate. Therefore, each pin has been straightened using a small lever.

The cooling rods are individually tested for leaks. The procedure consists in blocking one end of the cooling tube and connecting the other end to a manometer. The cooling rod is filled with Argon up to about 4.8 bars and the circuit closed (Fig. 4.12). After two days, the pressure is checked again. If any significant variation of pressure (more than a few tenths of bars) is noted and the test redone. A cooling rod would be rejected if the second test failed, too; this did not happen.

Finally, a ground wire is screwed on each cooling rod (Fig. 4.13, right). The three colonnettes (35 mm carbon fibre) are also screwed and secured with Loctite 932 to the cooling rod (Fig. 4.13, left).

#### 4.3.4 The Detector Modules

Inside an IT detector box, the sensor modules are partitioned in groups of four modules. The modules within a group are supplied with sensor bias voltage from a single HV channel. The main criterion used for the positioning of individual modules in a box is therefore based on the depletion voltage. Groups of four modules with close depletion voltage are formed.

An other criterion is the overall quality of the sensor in terms of shorted, open or pinholed channels. The sensor specifications, which we adopted also for the modules, demanded  $\leq 1\%$  of faulty channels. Most of the modules installed are 100 % working, but 111 strips are faulty out of 129 k. The modules with faults (while still meeting the specifications) are placed where the particle density is expected to be the smallest.

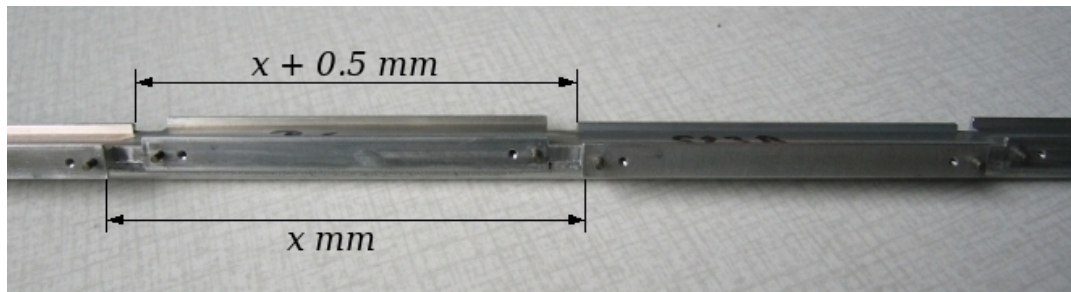


Figure 4.11: The length of the interval between two crenels is about 0.5 mm longer on the U and V layers than on the X1 and X2 layers.

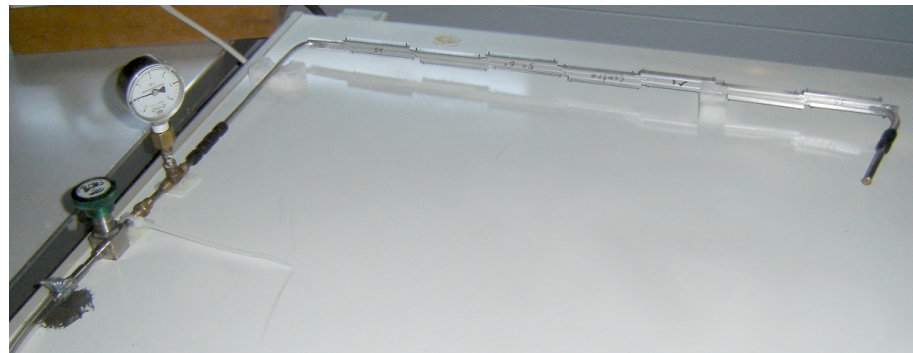


Figure 4.12: A cooling rod under pressure test.



Figure 4.13: View of a cooling rod mounted on its support (left) with the help of the three colonnettes of 35 mm screwed on it (right). The thread for the grounding is also visible (right).

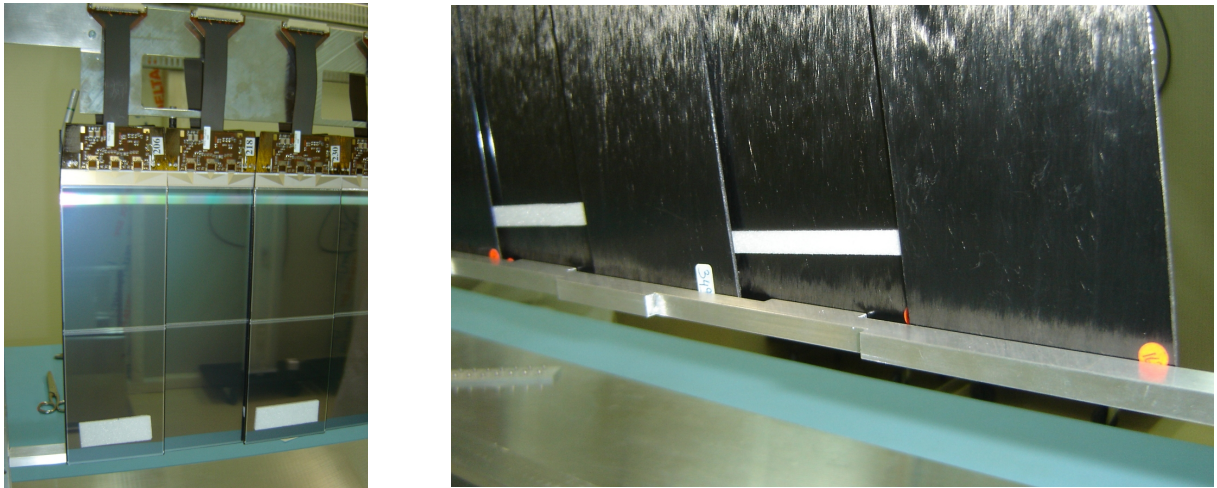


Figure 4.14: View of the foam protections glued on forward sensors of the external layers to prevent them from touching the inner walls of the IT detector boxes (left) and at the rear of all the forward modules to protect the backward sensors from being touched by those (right).

The modules are cleaned with air to remove residual dust on the sensors. The bonds around the beetles, between the pitch adaptor and between two sensors are checked visually with a magnifying glass to ensure that there is no dust nor carbon fibre element between them.

For the external layers (X1 and X2), there is a risk that the sensors, or the bonds, would touch the inner container wall. To prevent this, a foam buffer (Rohacell) of about 55 mm × 27 mm is centrally glued with double-faced adhesive tape (3M type 467MP) on top of the forward sensors, at about 15 mm from the bottom of the modules (Fig. 4.14, left).

To have complete spatial coverage, the modules within a layer are staggered in the  $z$  direction by four millimetres. Thus, to prevent the back of one module from touching the sensor behind, foam buffers of about 80 mm × 10 mm are glued at the rear of the forward modules at about 20 mm from the bottom of the modules (Fig. 4.14, right). Each module is identified with a module number given at the production. In addition, a bar-code sticker is glued on the back of each module (Fig. 4.15) to identify it within a central database [201–203].

### 4.3.5 The Assembly Set-ups

Two set-ups were used in the assembly process. A sketch of the first set-up, called the *cooling rod station*, is shown in Fig. 4.16 (left) and a picture in Fig. 4.13 (left). Its function is to hold a cooling rod during the mounting of the modules. The second set-up, called *sliding set-up*, allows to hold the cover while the cooling rods are mounted on the cover and to control the sliding of the modules into the box container. It is shown in Fig. 4.16 (right) and it is pictured in Fig. 4.23 (right).

The cooling rod station consists of an aluminium frame on which a cooling rod can be fixed with three screws the same way it would be with an actual cover. The whole frame can be rotated along a vertical axis, so that the operator can access both sides of the cooling rod without moving the set-up base plate. An aluminium bar with specially designed crenellated shapes on both sides can be inserted in the frame. The bar acts as a stop, preventing the back of outer modules from touching the sensors or the bonds of the inner modules during the mounting



Figure 4.15: View of the sticker glued at the rear of the detector modules allowing their identification. The operator is applying thermal grease on the module balcony in preparation of the mounting of the module, as explained in Section 4.4.3.

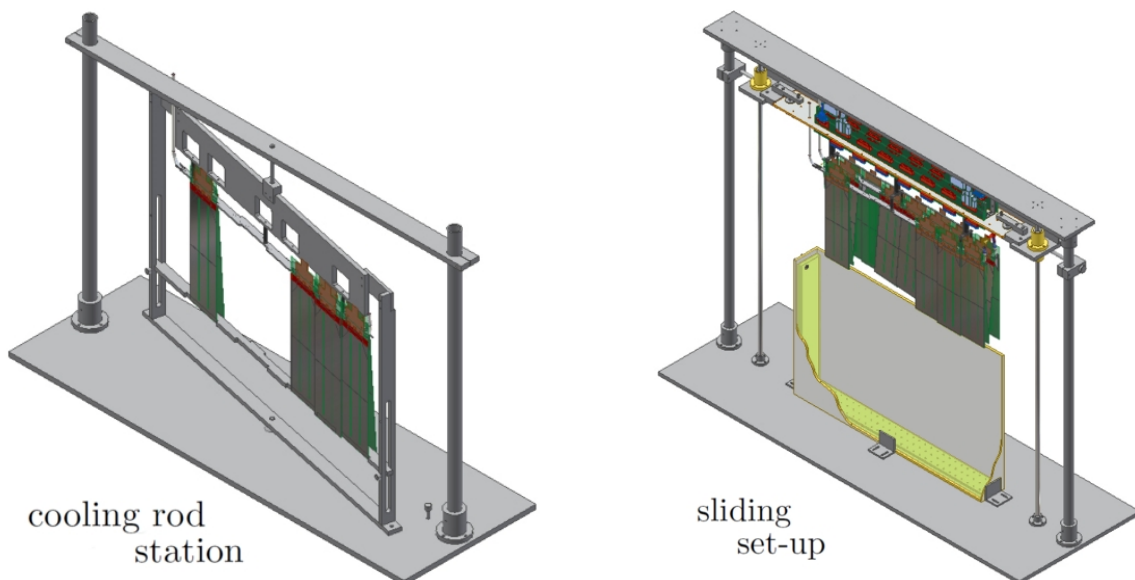


Figure 4.16: Sketches of the set-ups used in the assembly procedure. The set-up on the left is the cooling rod station; it is used to maintain a cooling while the modules are mounted on it. On the right, the sliding setup is pictured. It is used to slide the cover in a box container. Note that the vertical screw that control the descent is not shown on this sketch.

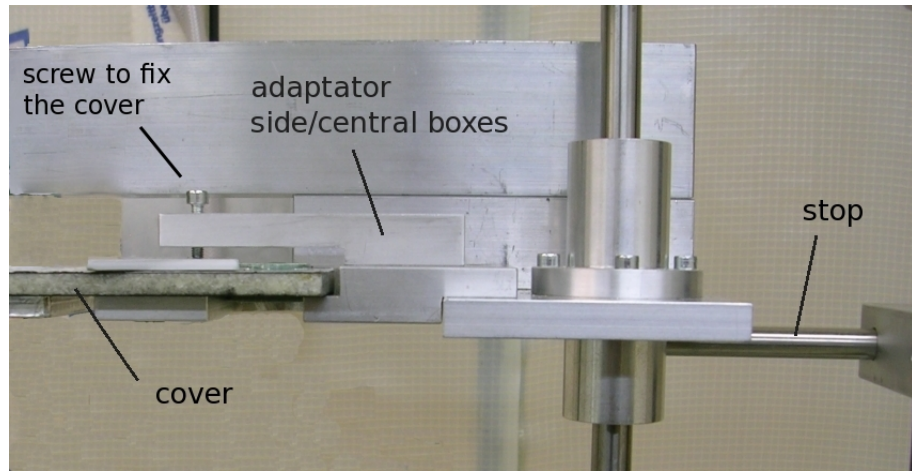


Figure 4.17: The cover is just laid on the set-up, while a screw keeps a small pressure on the cover. A piece of plastic is inserted between the cover and the screw to prevent it from damaging the cover. On the right, a stop is visible.

of the modules (Fig. 4.14, right). Two different bars are used, one for the X1-U cooling rods, and one for the V-X2 cooling rods.

The sliding set-up consists of two vertical round bars held at the bottom by a heavy stable base-plate and at the top by a bar. Two trolleys, one on each vertical bar on which they can slide, are linked together by an horizontal bar, whose vertical position can be controlled by a long vertical screw. The sliding trolleys have to be adapted to either central or side boxes, since the overall length of the cover is different according to the type of the box, as shown in Fig. 4.17. Thus, the correct adaptor piece has to be screwed in place. The horizontal bar linking the trolleys is bulky and limits the working space. Thus, the set-up is oriented so that the main operator of the assembly works with this bar away from him.

There is another set-up that is used for the survey measurements [197]. This set-up was particularly designed to cope with the little space available in the clean tent. It allows to survey both external sensitive layers alternatively without losing information about their relative distance.

Before each use, the surfaces of the set-ups are cleaned with an alcohol soaked tissue. The cleaning of the upper bar of the sliding set-up is important, because dust could fall from there directly on the modules. Particularly, attention is paid to the brass piece holding the vertical screw. At this location, tiny metal chips from the screw are produced when the screw is used. A careful cleaning is needed there to prevent any of those metal chips to fall on sensor bonds or into open connectors.

## 4.4 Assembly Procedure of an Inner Tracker Detector Box

After the preparation of the various components and definition of the assembly plan considering the different sensor modules characteristics, the assembly procedure can be broken down into the following sequence:

1. Mounting of the cover on the sliding set-up;
2. Adjustment of the detector box container position;
3. Mounting of two layers of modules on each side of the first cooling rod;
4. Mounting of the cooling rod on the support below the cover;
5. Mounting of two layers of modules on each side of the second cooling rod, and mounting of this cooling rod on the support;
6. HV test of the modules;
7. Closing of the cooling circuit by connecting the two cooling rods;
8. Cooling circuit leak test;
9. Survey of the visible layers X1 and X2;
10. Full electrical tests;
11. Test of the height of the modules;
12. Final insertion of the detector into container.

Those assembly steps are detailed below.

### 4.4.1 Mounting of the Cover on the Sliding Set-up

We took the convention to orientate the cover on the sliding set-up so that the cooling pipe exit holes lie on the left-hand side when one faces the set-up, as illustrated in Fig. 4.22, left. The cover is maintained by a small pressure from a screw on each side. A piece of plastic is placed between the screw and the cover to protect the aluminium shield integrity, as can be seen in Fig. 4.17. With this convention, the type B (V-X2) cooling rod is behind the type A (X1-U) and thus has to be mounted first.

### 4.4.2 Adjustment of the Detector Box Position

On the base plate of the sliding set-up, stops can be adjusted in order to maintain the box container at a precise location when the modules are slid down into the box container. The precise location of those stops has to be set before the assembly process of the detector box. The empty box container is placed on the base plate so that the cover would fit into it when slid down. When the box container is at the correct location, the stops are adjusted and screwed in place. The stop on the back of the box container and the stops on each side of the container are used. The stops on the front side of the box container would be in the way when manipulating the container, consequently they are removed and never used. For the side boxes, the position of the right-hand stop is set in order to have about 1 cm between the stop and the box wall. This precaution is needed because the distance between the edge of the module and the box inner wall is only 0.5 mm on this side. Thus, during the module insertion, one increases this distance for safety reasons. Once the stops are adjusted, the cover is moved up and the box removed.

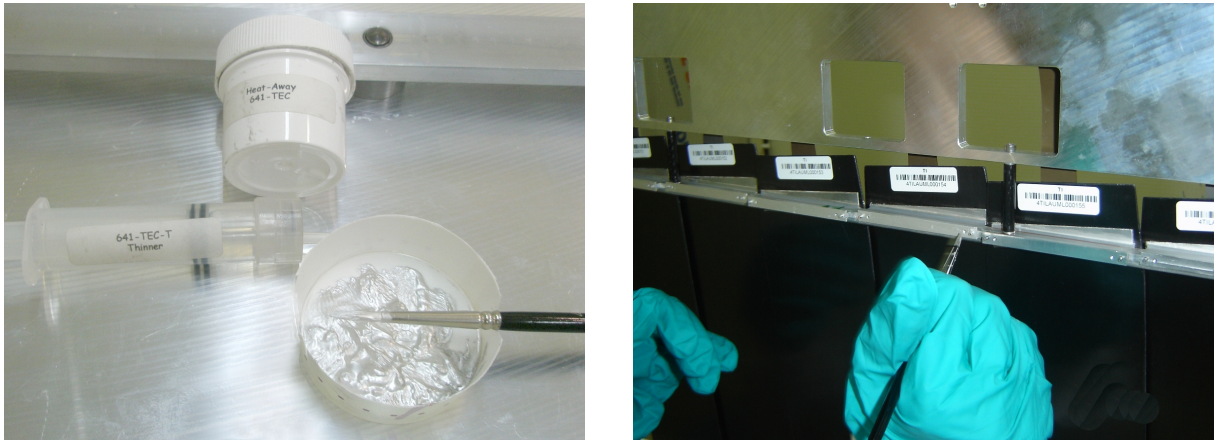


Figure 4.18: The thermal and electric conductive grease (left) is spread on the cooling rod (right) where the modules are intended to be fixed.

#### 4.4.3 Mounting the First Cooling Rod (Type B or V-X2)

The first cooling rod to be populated is a cooling rod of type B (supporting the V-X2 detection layers), because of the convention explained in Section 4.4.1. The cooling rod is prepared as detailed in Section 4.3.3. A final cleaning with alcohol is performed, specially for the surface that will be in contact with the modules. The cooling rod is fixed to the cooling rod station set-up (Fig. 4.13, left).

To maximise the thermal transfer between the cooling rod and the back of the detector modules, a layer of thermally conductive grease is spread on the contact surfaces. The thermal grease used is Aremco Heat-Away 641-TEC, together with the Aremco Heat-Away 641-TEC-T thinner (Fig. 4.18, left). This grease is electrically conductive, which is important in this case. The thinner allows the control of the grease viscosity, which has to be such that the grease could be spread effortless with a paintbrush. It is important not to use any force to spread it, due to the fragility of the modules. The grease is spread on the contact surfaces on each side of the cooling rod (Fig. 4.18, right), as well as at the rear of each module on a line linking the two alignment holes (Fig. 4.15).

The modules are placed starting with the ones located behind and finishing with the ones located in front (Fig. 4.19). They are fixed with one M1.6×3 screw<sup>10</sup> at each side of the alignment pins (Fig. 4.19, right). This has to be done with great care, in order not to damage the aluminium screw threads.

The bonds of each module are inspected with the help of a magnifying glass before and after the mounting procedure. Several damaged HV bonds were observed<sup>11</sup>. Usually, these could be pulled and replaced by new ones, as the HV bonds pads are quite large.

<sup>10</sup>Since the screws are important in the grounding scheme they have to be electrically conductive rather than passivated.

<sup>11</sup>the HV bonds are the outermost bonds and as such are more likely to be damaged during module manipulations.

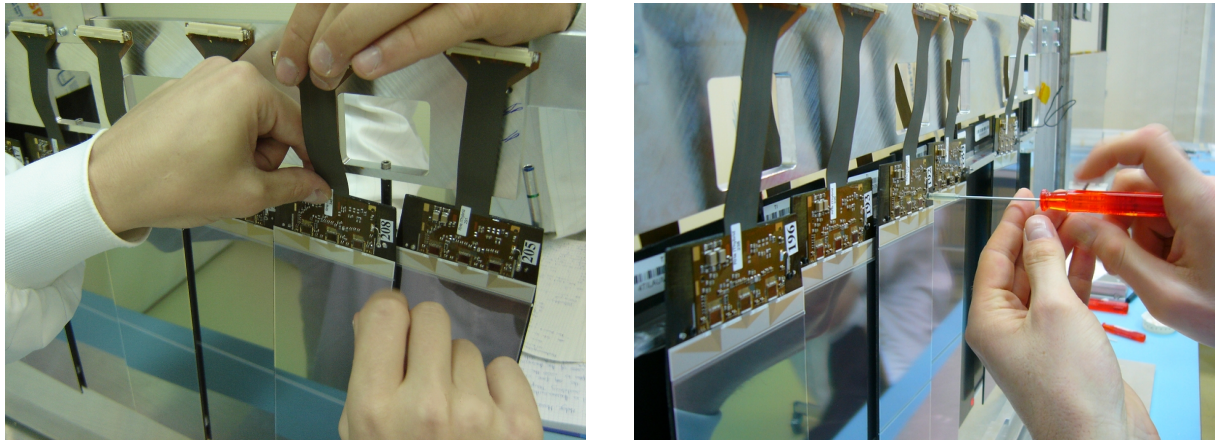


Figure 4.19: View of the fixing of the modules on the cooling rod, starting with the backward modules and finishing with the forward modules.

#### 4.4.4 Fixation of the First Cooling Rod under the Cover

The cooling rod, populated with modules, is handled carefully by a first person, who hold it at both ends. This person has to control the pressure he applies on the aluminium tube, since he could crush it quite easily. The long pipe extremity is inserted into a hole in the cover. A second operator helps sliding the pipe through the cover without bending it, while the first operator moves up the cooling rod, taking care that it remains horizontal. While the first person holds the cooling rod, the second person screws it in place. This operation is delicate, since a falling screw could severely damage bonds or sensors.

#### 4.4.5 Mounting of the Second Cooling Rod

The procedure described in Sections 4.4.3 and 4.4.4 is repeated for the type A cooling rod. At the end of the step, the two cooling rods are fixed on their support.

Once the two cooling rods are screwed in place, the detector modules can be connected to the inside connectors on the cover. One has to check that the male connectors are fully inserted. The ground thread of each cooling rod is also connected to the cover, and the thread is secured to the vertical cooling pipe with a little band of Kapton tape. Bubble wrap is used to prevent the Kapton tails from touching one another, which is potentially a source of noise.

At this stage, we do not complete the cooling circuit. Closing/disconnecting the cooling circuit are delicate, accident-prone operations. Thus, to minimise the number of those operations, one performs an HV test, as described below, to detect and replace the possible faulty modules before closing the cooling circuit.

#### 4.4.6 HV Test of the Modules

After the assembly of the cooling rods and their mounting on the cover plate (just before connecting the cooling rods together), a HV test of the modules is performed. HV problems were the most frequent disturbances during the module production and the HV bonds are the ones closest to the edges of the modules and hence most prone to accidental damages. Therefore, we check for HV problems before the cooling rods are connected to each other, in case a module has to be exchanged. For the HV test, no cooling is necessary.

The test is done by inserting the assembly into a large aluminium test box, which provides light shielding for the modules. This box allows for easy placement of the assembly without the insertion set-up needed for the real detector boxes where the box walls are much closer to the modules. Furthermore, this box has windows that can be opened to access the readout hybrids, which is helpful in tracing possible problems. The CAEN power supplies are then connected to the HV connectors on the outside PCBs, as described in the full module test (Section 4.4.10). The modules bias voltage is slowly ( $\simeq 3$  min) ramped to 500 V and the test is passed if none of the modules shows signs of a breakdown. Typical leakage currents of the sensors are 200 nA and 400 nA for short and long modules, respectively. The leakage currents rarely exceeds 1.5  $\mu$ A.

#### 4.4.7 Closing of the Cooling Circuit by Connecting the Two Cooling Rods

Once the modules are HV tested and the faulty modules exchanged, the cooling circuit can be completed. The missing piece of the circuit is a steel tube bent in a U-shape. The use of steel is motivated by the observation that it is not possible to bend an aluminium tube to such a small radius without crushing it. For the same reason it was not possible to use plastic tube either.

It is difficult to insert the U-shaped tube into the Legris connectors, mainly because the ends of the cooling rods are usually not parallel to each other. A considerable strength is required but the cooling rods are fragile. To ease the process, the best way is to measure the distance between the connectors and to adjust the bend of the U-shaped tube accordingly. Using two screwdrivers, inserted into each end of the tube, and grabbing them as pliers, one can adjust the shape of the tube.

It is not straightforward to assess whether the U-shaped tube is fully inserted in the Legris connectors or not. Thus, before installing the tube, one inserts a Legris connector in each end of the tube and draw a line on the steel tube with a permanent marker.

Even with the U-shaped tube adjusted, the closing of the cooling circuit is still the most delicate step of the box assembly. Two people have to slowly insert both ends of the tube simultaneously, and to push it until it reached the marker line on the tube. During the operation, both cooling rod ends have to be held tightly to minimise the strain applied on them. Figure 4.20 shows the steel U-shaped piece in its final position.

Once the cooling circuit closed, the distance between the cooling rods is measured. If the measured distance is found smaller than the nominal one, one inserts a spacer cut at the right length in a carbon fibre rod. This spacer is secured in place with Kapton tape.

#### 4.4.8 Cooling Circuit Leak Test

An electronic device was designed to read out a pressure probe<sup>12</sup> and to display the measured pressure. The test set-up consists of a bottle of argon (Ar), the pressure probe, a valve on one side, and a brass plug on the other side. The tests consists in putting the cooling circuit under pressure for some time and to record any pressure drop.

The Ar bottle, pressure probe and valve are connected to one end of the cooling circuit with a Legris connector and the air it contained was flushed away with some Ar. Then, the other end of the circuit is blocked with the brass plug via a Legris connector. This is secured with Kapton tape, preventing it from flying around in case the Legris connector is faulty. The circuit is pressurised up to about 5 bars, the valve is closed, isolating the cooling circuit, and the Ar bottle is disconnected.

<sup>12</sup>the pressure probe model is Sensorscience CTE9010AQ4, available at CERN store (SCEM 22.64.12.026.8)

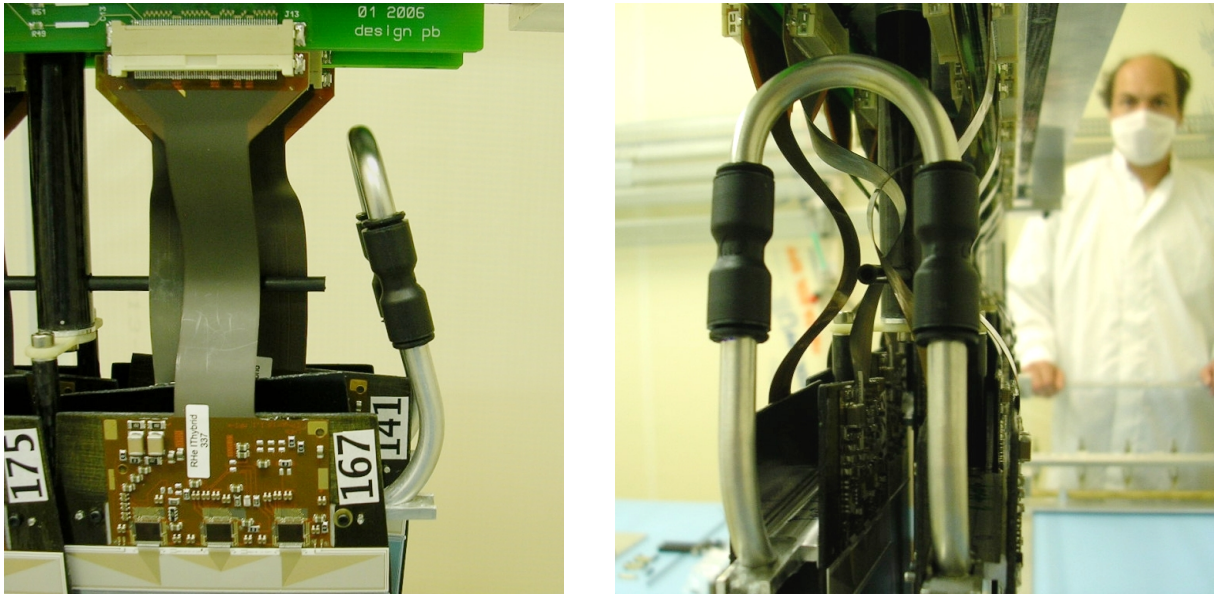


Figure 4.20: The cooling circuit is closed when one connects both cooling rods via the steel U-shaped tube.

To compute a leak rate, one records the initial pressure in the circuit, the temperature and pressure of the room, and the time. After about two days, the same physical quantities are measured again. These data allows to compute the leak rate of  $C_6F_{14}$  in cubic centimetres per year. This computation and the conversion from Ar leak rate to  $C_6F_{14}$  leak rate is based on the method used for the ATLAS TRT and documented in Ref. [204].

If the leak rate is found to be higher than tolerated, which happened a few times, two actions are taken: the connectors of the pressure set-up are tightened, the set-up itself is retested and the four Legris connectors composing the cooling circuit are changed for new ones. Eventually, all the twelve detectors boxes were found to be OK. Once the cooling circuit is validated as leak free, it is possible to circulate coolant. It is then safe to power up the beetles and to perform a full electric test.

#### 4.4.9 Survey of the Visible Layers X1 and X2

The goal of the survey is to provide first estimates of the position of the sensors. No hardware correction can be performed to correct imperfect positioning, the alignment will be done by software using tracks. However, the more accurately the position of the modules is known the better the result of the software alignment. Cross-shape fiducial marks engraved on each silicon sensor are surveyed by theodolite. Their coordinates are calculated with respect to targets located on the cover of the detector box, which are still visible once the box is close and installed in the LHCb cavern. The details of the survey procedure can be found in another LHCb note [197].

#### 4.4.10 Full Electrical Tests

A full readout test of a cooling rod assembly with 28 modules is carried out before the assembly is placed in the final detector box container. This is done in the large aluminium box used for the HV test (Section 4.4.6) which provides an easy access to the hybrids. The readout system used for this test acted as a development bench of the PVSS control system for the ST<sup>13</sup> subdetectors. It uses all the final parts of the detector readout [205]. It consists of:

- Two IT Service Boxes, each containing a Control Board (CB) [193] and 16 (or 12)<sup>14</sup> Digitiser Boards (DB) [192]. These are the final Service Boxes as used in the experiment including the water cooling of the backplanes.
- Three A1511B High-Voltage CAEN Power supplies modules [206], in a CAEN SY1527 crate [207], to provide the 500 V bias voltage to the sensors;
- One Wiener Maraton Low-Voltage Power supply [208] to power the Service Boxes that distribute the power to the Control Boards, the Digitiser Boards and to the front-end chips on the detector modules;
- Four TELL1 boards [209] for the data collection and one ODIN board [210] for clock and Timing and Fast Control (TFC) signals distribution;
- One optical splitter to dispatch the TFC signals from the ODIN to the TELL1 boards;
- An Ethernet switch to interconnect the TELL1 boards and the readout PC;
- A PC running a Gaudi job to read and analyse the data;
- N<sub>2</sub> supply to lower the humidity in the detector boxes and two water cooling circuits. The first circuit uses a reservoir of distilled water as cold source to absorb the heat released by the hybrids front-end electronics. This is connected to the box cooling circuit. The second, connected to a PC water cooling circuit, is used to cool the Service Boxes.
- A set of 28 data readout cables, the same cables as in the experiment with 3.3 m and 3.9 m length, connecting the readout hybrids to the Digitiser Boards.

The box is connected to the cooling circuit, the N<sub>2</sub> supply, the HV and the readout. The LV power to the Service Boxes, from which the readout hybrids on the modules receive their power is switched on and the power consumption is verified. Before switching on the power to the modules, one has under normal circumstances  $\simeq 0.3$  A on channel 1 (5.5 V) and  $\simeq 1.3$  A on channel 2 (7.5 V). The low-voltage power supply has to be switched on before the high-voltage is applied to the sensors, as the grounding potential in the detector is given via the LV power supply. (This could not be done for the HV test of Section 4.4.6, as in that case, the cooling circuit is not closed and hence the hybrids can not be cooled.)

Next, the sensors are slowly ramped up to 500 V, testing for leakage current and possible early break down. Afterwards the readout hybrids are powered and configured. The configuration is done via an I2C integrated circuit which allows reading the data back and checking them against what has been programmed. The power consumption of the Service Boxes with powered hybrids is then also verified to be  $\simeq 11$  A (9 A) on channel 1 and  $\simeq 8.5$  A (7 A) on channel 2 for the service box with 16 (12) Digitiser Boards, respectively. Any significant deviation is an

---

<sup>13</sup>The Silicon Tracker project regroups the Inner Tracker and the Turicensis Tracker subdetectors. In particular most of the readout electronics is common.

<sup>14</sup>One detector box is read out by 2 service boxes, one containing 16 Digitiser Boards and a second one, only partially filled with 12 Digitiser Boards, giving a total of 28 Digitiser Boards, one for each module.

indication of a problem. We never had significant over currents, but smaller currents typically hints to missing configuration of parts of the detector.

After configuration of the TELL1 readout boards and the ODIN readout supervisor, raw data is recorded for all modules. Data is taken both with and without (pedestal) test-pulse injection into the Beetle readout chips.

A typical problem observed is that channels belonging to a common individual Beetle readout port<sup>15</sup> show very low noise and no test-pulse signal. This was attributed to the hybrid-PCB connections in the box, as it usually disappears after re-plugging. The most likely origin is bad soldering or cracks on the female connectors (on the PCBs, inside the box) as those connectors are delicate to solder, but actual cracks were never really found. During the box test, all the observed *open ports* (typically 0 or 1 per box) vanished after re-plugging the cable.

However, this obviously does not repair any micro cracks, but only provides temporary connection. In the installed detector we observe 7 faulty ports, most likely due to this crack/soldering problem, among them some appear to be working "sometimes", just as expected.

During these tests, some problems have been identified and dealt with. Two modules presented high common mode noise although the previous individual test were all right for each of them. Those modules have been replaced. In one case, a badly soldered ground wire on the hybrid was causing the noise, it was later fixed. In addition, one faulty interface PCB in the detector box cover was discovered as somehow causing a *delay* in the signal line, as the channels of the readout of one module was shifted compared to all other modules. Although it was not understood how this could be introduced, exchanging the cover solved the problem (while exchanging the module did not).

The four temperature probes (PT1000) inside the detector box (in addition to the probes on each hybrid) are read out and the temperature reading is checked. The same is done for the HMX2000 humidity sensors. The operating temperature of the boxes is about 25° C, which was far outside the temperature range for which the humidity sensors are calibrated<sup>16</sup>. Therefore, the actual humidity output can not be reliably checked against other measurements, but we check that the measurements reacted to humidity changes and that the measured value is in a reasonable range (40–60 % R.H.).

#### 4.4.11 Test of the Height of the Modules

With this operation, we check whether the sensor modules fit in the box container, such that they do not touch the bottom of the container. For this, we measure the distance between the lower edge of the modules and the lip of the cover and compare this value with the depth measurement of the container to be used, as explained in Section 4.3.2. For the central boxes, the nominal space between the bottom edge of the modules and the bottom of the box container is 0.5 mm. The motivation for such a tiny distance is to have the sensitive area as close to the beam pipe as possible. For side boxes, the space underneath the tip of the modules is not critical in term of acceptance and hence the space is much larger ( $\approx$  5 mm). The minimal distance is found between the lateral edge of some modules and the container side wall facing the beam pipe which is only 0.5 mm, for the same acceptance reason.

<sup>15</sup>A readout port is a block of 32 consecutive channels. There are 4 ports per Beetle, and three Beetles per detector module. A detector box represents thus  $28 \times 3 \times 4 = 336$  readout ports.

<sup>16</sup>Each humidity sensor is provided with an individual calibration data sheet by the manufacturer Hygrometrix, Alpine CA, USA. For the readout we use per sensor a linear interpolation + offset to the calibration data giving the measured sensor output voltage as a function of the temperature and the humidity.

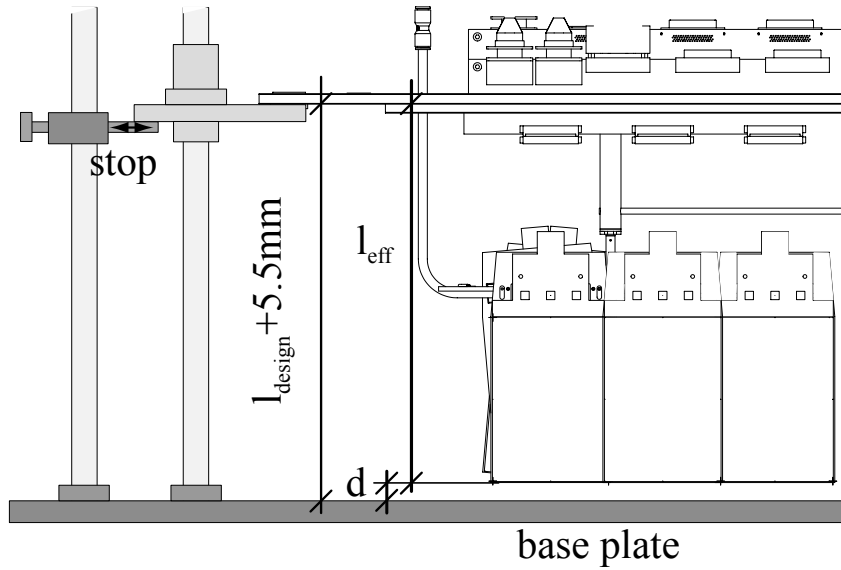


Figure 4.21: Scheme of the different distances involved in the measurement of the distance between the cover and the tip of the sensor modules.

It is not straightforward to measure the distance from the bottom of the lip of the cover to the bottom tip of the module support,  $l_{\text{eff}}$ , as defined in Fig. 4.21. The solution consists in the permanent installation, on the sliding set-up, of two pairs of stops, one pair for the central boxes and one for the side boxes. Those stops can be engaged or disengaged. When a pair of stops is engaged, the sliding bar of the set-up can rest on it, as shown in Fig. 4.17, and the cover-module ensemble is maintained. The stops are positioned so that, when the sliding bar rests on the stops, the distance between the tip of the module supports and the base plate is 5.5 mm, nominally. This means that the bottom lip of the cover lies at  $l_{\text{design}} + 5.5$  mm from the base plate. The positioning of the four stops was performed using an electrical height gauge<sup>17</sup> to control the distance to the base plate. Thus, by measuring this distance, we measure the deviation of the actual assembly from the nominal design. This distance,  $d$ , is measured using calibrated wedges and precision blades (Fig. 4.22, right). The simple arithmetic of Eq. (4.1) allows to get the effective distance  $l_{\text{eff}}$ .

$$l_{\text{eff}} = l_{\text{design}} + 5.5 \text{ mm} - d \quad (4.1)$$

Conservatively, we consider the minimal depth measurement of the box container from which one subtracts the maximal  $l_{\text{eff}}$  value to assess whether the modules fit into the box container.

If it is not the case, an appropriate number of 0.2 mm thick glass fibre frames are added between the cover and the top of the box container. To raise its upper lid is equivalent to increase the depth of the container. The eventual glass fibre frames are fixed using Kapton tape. A strip is centred on the frame and secured on the inside and outside wall of the container on each four sides of the container lid. The result of this operation is a flat lid, without any ripple, enhancing the air-tightness of the detector box. The Kapton covering the screw holes is removed with a lancet blade.

<sup>17</sup>TESA Micro-Hite 600 Electric Height Gauge

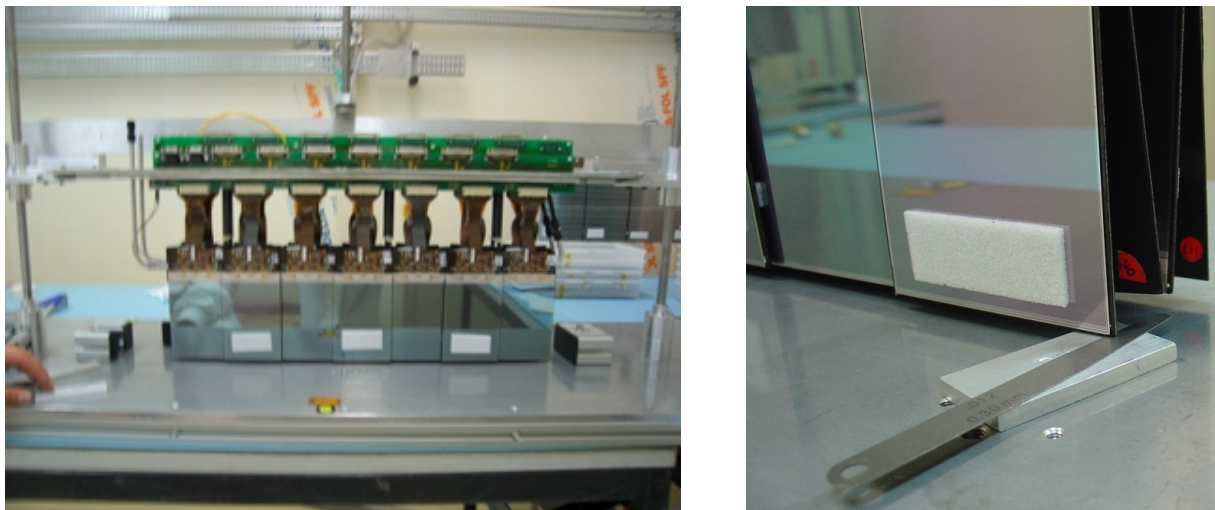


Figure 4.22: Resting on the dedicated stops, an assembly is ready for the test of the height of the sensor modules (left). On the right, one measures the distance,  $d$ , between the base plate and the bottom of the module supports, as shown on the drawing of Fig. 4.21, using a calibrated wedge and precision blades.



Figure 4.23: A glass frame used to adapt the depth of the container (left). The sliding set-up and a box being closed (right).

#### 4.4.12 Final Insertion of the Detector into the Container

The verticality of the box container and the height of the module have been checked before. The box container is placed under the cover according to the stops set on the base plate as mentioned in Section 4.4.2. The detector box is then ready to be closed (Fig. 4.23, right). The ensemble composed of the cover and the detector modules is slowly moved down into the container, operating the vertical screw on top of the set-up. One person operates the vertical screw while another person supervises the process. Critical moments are when the bottom of the modules, then the inter-sensor bonds (for the side boxes), and then the sensor-hybrid bonds enter the container. The descent is not perfectly smooth and the modules can slightly shake. This is mainly due to the screw and is negligible at low descent speed. At each of these moments, the second person check that the container is properly placed and that there is no danger of collision.

For the side boxes, one of the lateral wall of the container is only at 0.5 mm from the edge of the modules. Thus, for the delicate insertion operation, one shifts the container laterally so that this distance is increased to a safe value of 1–2 cm.

A few centimetres before the completion of the insertion process, the temperature probes and the inner shield ground thread (Fig. 4.6, left) have to be connected to one PCB. The bundle of wire is secured to one of the cooling pipe to prevent any constraint on the connector, which can lead to a disconnection.

A part of the cover has to enter in the container. So, just before the inside of the cover reached the lip of the container, one can readjust its position to allow a smooth entry of the cover in the container. With certain covers, this is not straightforward and one has to help by slightly opening further the container mouth. Particularly, for the side boxes, it is also time to shift the container back at its nominal position. This operation should be performed very carefully, because of the tiny distance from the wall to the modules.

Once the box is closed, and before the screws are inserted in their holes, a large band of Kapton tape is glued on the cover so that it covers the screw holes and so that a larger part is in the air, not glued to anything. Then, the screw holes are pierced in the Kapton and the cover is screwed to the container with 12 M2.5×20 plastic screws. When the screws are tightly screwed, the free part of the Kapton tape is glued to the container wall. In the process, the Kapton band also covers the foam section (Fig. 4.5) of the cover. The motivation for the Kapton seal is to maximise the air tightness of the detector boxes. The air tightness is crucial to minimise the transfer of humidity to the inside of the box.

### 4.5 Commissioning and Performance of the Inner Tracker

The installation of the twelve assembled detector boxes in the LHCb pit was complete in early Summer 2008, before the start of the commissioning phase [211]. I was not involved in the commissioning phase. However, for the people involved in the detector construction, the commissioning represents a first global quality test of their work, the ultimate test being that the detector yields data of good physics quality. Therefore, we want to conclude the chapter on the Inner Tracker construction by summarising on the current state of the detector.

The commissioning of the detector requires particles crossing it. Secondary particle showers from cosmic rays represent a natural source of particles. However, the LHCb detector is not favourably oriented to use cosmics. Indeed, the general trajectory of the cosmic secondary par-

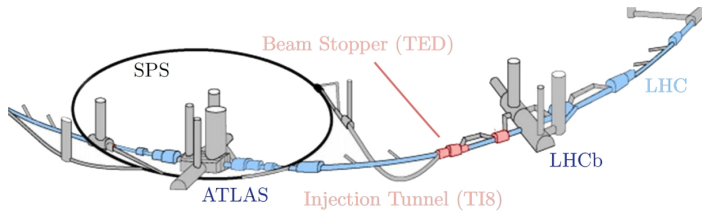


Figure 4.24: Schematic view of the CERN underground area involved in the injection tests. Protons bunches are transferred from the SPS ring towards the LHC ring, and dumped on a beam stopper called TED just on reaching the LHC tunnel. Some of the secondary particles produced there cross the LHCb detector, which lies 350 m downstream.

ticles available at 100 m underground is orthogonal to those of the particles LHCb was designed to measure. Fortunately, a source of particles with a suitable direction (if not sense) became available. In September 2008 and June 2009, in the frame of the commissioning of the LHC machine, injection tests were performed. During these tests, bunches of  $2\text{--}5 \times 10^9$  protons at 450 GeV were transferred from the SPS towards the LHC ring and dumped onto a beam stopper (TED) just before reaching the LHC tunnel, as shown in Fig. 4.24. Secondary particles<sup>18</sup> produced at that occasion reach LHCb, located at 350 m downstream.

For each shot on the TED, a copious amount of particles cross LHCb; they have been used to align the detector in time and space, and to extensively test the full readout chain [212]. Several faults were found and fixed in the readout chain downstream of the detector boxes. Currently, 99.26 % of the channels are operational, as illustrated in Fig. 4.25. Two modules are disabled; for each, the malfunction is thought to lie in the connectors between the module and the cover PCB<sup>19</sup>. Two other modules show large common mode noise, which is thought to be caused by a degradation of their grounding. The exact causes are not likely to become known until the affected boxes are open for investigation, certainly not before the next extended shut-down period.

The TED splashes deliver a particles flux ten times higher than the flux expected in a typical  $b\bar{b}$  event. This leads to a very high occupancy up to 8 %. Furthermore, particles originating from a point 350 m away from LHCb have parallel trajectories in the detector. This situation is far from ideal for software alignment. The high track multiplicity increases the number of ghost tracks and makes the tracking more difficult. In addition, the parallel nature of the trajectories limits the number of IT elements that it is possible to couple and reduces the possibility to link hits in-between subdetectors, particularly to vertices in the VeLo, as it would be for tracks originating from collisions. Nevertheless, the software alignment of the Inner Tracker was possible, in standalone mode, using the data collected during the 2008 and 2009 TED runs [213–215].

The alignment was validated on an independent TED data sample by studying unbiased residuals<sup>20</sup>. For each detector module, the unbiased residuals of all the hits in that module are computed. This distribution is fitted with a Gaussian. Finally, the histogram of the means

<sup>18</sup>Monte Carlo simulations indicate that the particles reaching the detector are mainly muons of 10 GeV.

<sup>19</sup>The problem of one module is related to HV. The status of the second disabled module, which is simply not configuring, varies with the time. It works for some time (it was operational during the November 2009 data taking) and then is not responding anymore; this behaviour is compatible with a connector malfunction.

<sup>20</sup>A residual is the distance between the measured hit and the point of intersection of the track on the sensitive plane. The unbiased residual of a hit is the residual between it and the track refitted without the information of this particular hit.

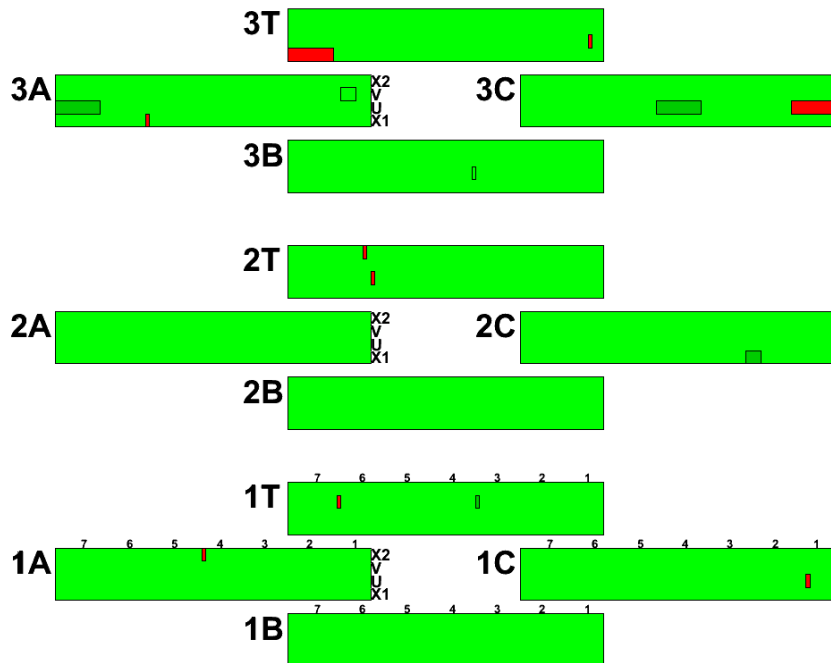


Figure 4.25: Map of the status of the Beetle ports for the twelve Inner Tracker detector boxes. Each of the 4032 Beetle readout ports (32 consecutive silicon strips) are displayed. Most of the Inner Tracker behaves nominally (light green), ports showing unusually large noise while still functional are painted in dark green, whereas dead ports are painted in red. Frames around functional ports indicates that they are affected by a minor malfunction in their readout chain.

of these 336 — the number of IT modules — Gaussians is constructed. The width of these distributions is a measure of our knowledge about the actual positioning of the detector elements. This process is done, first using only information from survey measurements [216, 217], and secondly, under the conditions yielded by the software alignment.

Figure 4.26 shows distributions of the mean of unbiased residuals. The precision of the position of the modules is given by the RMS of those distributions. After software alignment, the precision is  $19\text{ }\mu\text{m}$  ( $17\text{ }\mu\text{m}$ ) for modules in X layers of the Top/Bottom boxes (Access/Cryo side boxes) and  $22\text{ }\mu\text{m}$  ( $18\text{ }\mu\text{m}$ ) for modules in the stereo U/V layers of the Top/Bottom (Access/Cryo) boxes. The overall precision of the module position is hence on average  $19\text{ }\mu\text{m}$  along the  $x$  direction after alignment, compared to a single-hit resolution of  $57\text{ }\mu\text{m}$ . For the reasons given above, the on-going alignment using tracks originated from collisions will strongly improve this figure.

The constructing of LHCb Inner Tracker was presented in this chapter, from the production of the detector modules to the assembly of the twelve detector boxes. This detector is in good shape, fully operational and can be software aligned. It has seen tracks from collisions in the LHC in December 2009, as illustrated in Fig. 4.27.

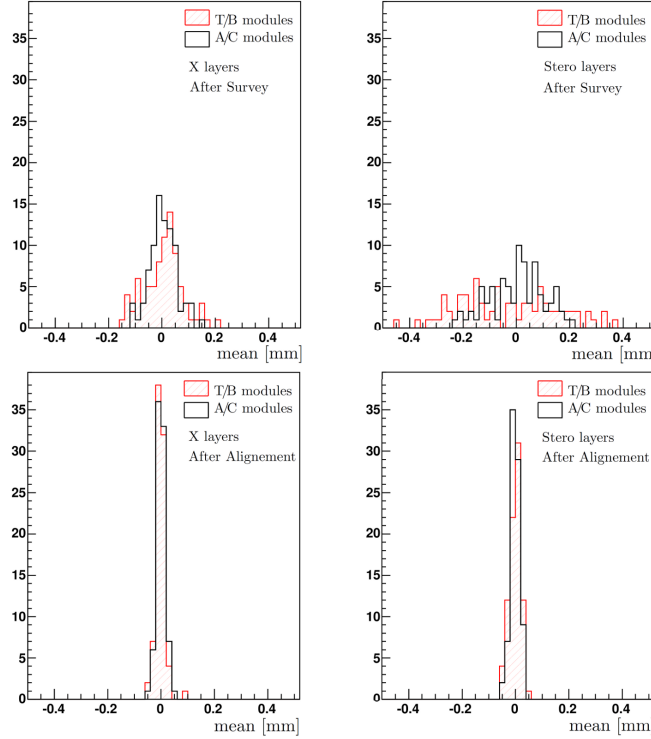


Figure 4.26: Distributions of the mean of the unbiased residual distributions for hits grouped by detector modules. The top row corresponds to the situation before software alignment, in which only the information obtained from the survey measurements is used. Since stereo layers are expected to give a worse resolution than the X layers for geometrical reasons, they are shown in the right-hand side and the latter in the left-hand side. The bottom row is the situation after software alignment; the width of the mean of the unbiased residual distributions is reduced to an average of 19  $\mu\text{m}$ . Modified from Ref. [215].

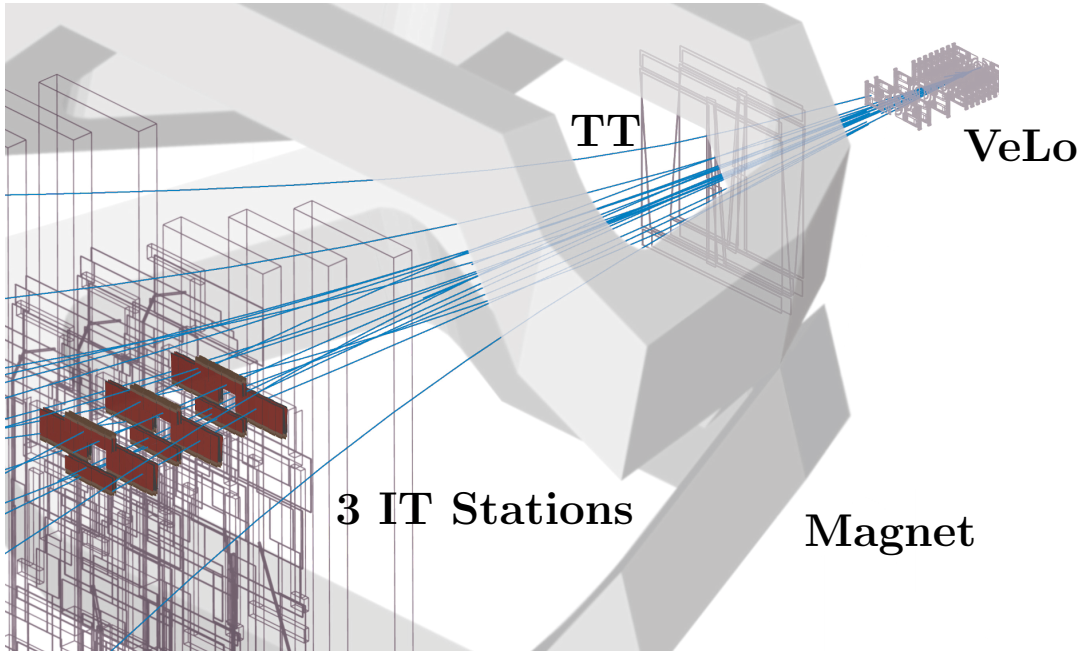
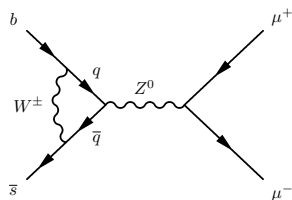


Figure 4.27: Tracks of a collision event recorded on 2009 December 15<sup>th</sup>, during the 2.36 TeV LHC run (runNumber 63949, evtNumber 103). From Vincent Fave.



## Chapter 5

# Analysis for the $B_s^0 \rightarrow \mu^+ \mu^-$ Decay Search



The branching fraction measurement of the yet unobserved  $B_s^0 \rightarrow \mu^+ \mu^-$  decay is of great interest in the indirect search for Physics beyond the Standard Model. LHCb potential to either measure or exclude this branching fraction is assessed with the use of two different sets of variables.

LHCb has been preparing an analysis for the  $B_s^0 \rightarrow \mu^+ \mu^-$  branching fraction measurement for years. It is the collaborative work of a dozen of people, this number growing with time. This analysis, which we refer to as the **standard analysis** in this document was extensively described in Refs [72, 218, 219]. With the standard analysis reaching a mature state, the interest for a concurrent analysis grew.

The motivations for an **alternate analysis** are several:

- As presented in Section 5.7, there is a non negligible potential to get a very early result. We have to prepare to exploit data taken with a not yet completely understood detector. To that end, the use of variables less sensitive to a not fully calibrated detector is preferred. There does not exist a set of variable immune to the bias induced by a young detector. We assume that the ability to correctly estimate errors on tracking parameters will be limited at the beginning and we think that an analysis avoiding the use of error estimates, without becoming totally immune to a badly understood instrument, will be less affected by it, and consequently more robust. This reasoning is disputed among the collaboration, mostly by the people responsible for the tracking. Eventually, the relevance of this approach will be judged by the data collected with the LHCb detector. In any case, this exercise can at least be seen as an assessment of the additional sensitivity brought to the analysis by the use of error estimates, in case of an ideal detector.
- Secondly, an alternate analysis will provide a second result in the search for the  $B_s^0 \rightarrow \mu^+ \mu^-$  decay. Two concurrent analyses yielding compatible results will grant more confidence in a possible measurement, particularly in the early phase of the experiment. Such cross-checking is more comfortable for the people involved in the analyses and provides a further argument to defend the result.

- Finally, since both analyses share a substantial fraction of the software tools and analysis techniques, the development of an alternate analysis was an opportunity to question and review the standard analysis.

For all these reasons, an alternate and possibly more robust analysis was desirable. The mandate was to identify a different set of variables, and to assess the impact of this new set of variables on the overall analysis sensitivity.

In this chapter, an analysis, based on a set of variables different from the standard one, is presented. The alternate selections of the signal channel, and of the relevant calibration and control channels are presented. A powerful variable called the geometry likelihood, on which the analysis relies for the background discrimination, is adapted to the alternate analysis. The impact on the expected sensitivity is also shown. This change of variable is transparent for some of the methods developed in the frame of the standard analysis, which can consequently be used without modifications. To improve the readability and completeness of this document, these methods, which concern calibration, as well as trigger and reconstruction efficiencies, are also presented.

## 5.1 Strategy for the $B_s^0 \rightarrow \mu^+\mu^-$ Decay Search

The current LHCb strategy for the  $B_s^0 \rightarrow \mu^+\mu^-$  decay search can be summarised as follows:

- A loose selection will be applied with the goal of removing obvious background while avoiding a significant loss of signal events. Our selection is detailed in Section 5.3.
- The analysis relies on three independent variables, related to the dimuon invariant mass, to the particle identification of the two muon daughters, and to geometrical information from the decay topology. Since the three variables are uncorrelated, they will be calibrated independently. The calibration methods are designed to rely solely on real data, through control channels. The calibration of the geometrical variable will use  $B_{(s)}^0 \rightarrow h^+h^-$  decays and  $B_s^0 \rightarrow \mu^+\mu^-$  sideband candidates, as described in Section 5.4.3. The mass calibration, presented in Section 5.5 will be achieved using  $B_s^0 \rightarrow K^+K^-$  and  $B_{(s)}^0 \rightarrow h^+h^-$  decays, and  $B_s^0 \rightarrow \mu^+\mu^-$  sideband candidates, while the muon identification calibration, mentioned in Section 5.6 will use the  $\Lambda \rightarrow p\pi^-$  and  $J/\psi \rightarrow \mu^+\mu^-$  decay modes.
- For each event, the value of each of the three variables will be calculated. A tridimensional histogram will be populated with the observed events.
- The compatibility of the observed histogram will be tested against different  $B_s^0 \rightarrow \mu^+\mu^-$  branching fraction hypotheses, using the Modified Frequentist analysis [220–222] with the calibrated distributions for signal and background. The final result will be either a measurement or an upper limit of the  $B_s^0 \rightarrow \mu^+\mu^-$  signal yield. Since no — or not enough — data is available yet, the expected sensitivity was computed using Monte Carlo full simulation and is presented in Section 5.7.
- Since the number of  $B_s^0$  produced is not precisely known, the use of a normalisation channel with a well known branching fraction is required in order to obtain an absolute measurement or upper limit of the  $B_s^0 \rightarrow \mu^+\mu^-$  branching fraction. The normalisation channels considered are  $B^+ \rightarrow J/\psi(\mu\mu)K^+$ ,  $B^0 \rightarrow K^+\pi^-$  and possibly  $B_s^0 \rightarrow D_s^-\pi^+$  in the future. The normalisation, described in Appendix A.1, calls for the use of control channels to get efficiency ratios from data. The  $B^0 \rightarrow J/\psi(\mu\mu)K^{*0}(K^+\pi^-)$ ,  $B^0 \rightarrow K^+\pi^-$

and  $B_{(s)}^0 \rightarrow h^+h^-$  decay modes are used by the methods presented in Section 5.3 and Appendices A.2 and A.3.

## 5.2 Fully Simulated Monte Carlo Samples

The study presented in this chapter was performed on Monte Carlo simulated events produced in the frame of LHCb Data [*sic*] Challenge DC06<sup>1</sup>.

The process of Monte Carlo generation consists in the following sequence. Pile-up events are simulated for two different instantaneous luminosities of  $2 \times 10^{32} \text{ cm}^{-2} \text{ s}^{-1}$  and  $5 \times 10^{32} \text{ cm}^{-2} \text{ s}^{-1}$ , assuming a  $4\pi$  inelastic  $pp$  cross section of 80 mb at  $\sqrt{s} = 14 \text{ TeV}$  and a non-empty bunch crossing rate of 30 MHz. PYTHIA is used to simulate the  $pp$  interactions from QCD knowledge. The  $b\bar{b}$  production cross section given by PYTHIA is  $698 \pm 1 \mu\text{b}$ , however we conservatively assume  $\sigma_{b\bar{b}} = 500 \mu\text{b}$  when computing yields, since a large theoretical uncertainty exists on this value.

Inclusive  $b\bar{b}$  events are obtained by filtering minimum bias events and requiring at least one  $b$  hadron with a true momentum vector within 400 mrad of the  $z$  axis, which represents a  $(43.7 \pm 0.1)\%$  efficiency. If this condition is not reached, it is tested again with the whole event reversed  $z \rightarrow -z$ , which saves processing time by recovering events that would have been discarded. All the particles are then decayed using EVTGEN.

The Monte Carlo production for specific exclusive decays is similar for all of them; we describe here the case of  $B_s^0 \rightarrow \mu^+\mu^-$ . Inclusive  $b\bar{b}$  events are used and the hadronisation step in PYTHIA is repeated on the  $b$  hadron within 400 mrad of the  $z$  axis until it becomes a  $B_s^0$ . This  $B_s^0$  is then forced to decay into two muons with EVTGEN, while all the other particles in the event are randomly decayed. Finally, the momentum vector of each of the  $B_s^0$  daughters — the two muons — is required to make an angle with the  $z$  axis comprised between 10 and 400 mrad. The interaction of the particles with the detector, the digitisation, and the reconstruction are then performed. Requiring the  $B$  and the decay products in the detector acceptance induces some inefficiency, which depends on the decay channel. The generator-level cut efficiencies for the channels considered in this study are collected in Table 5.1.

Knowledge about the background is fundamental because of the very low  $B_s^0 \rightarrow \mu^+\mu^-$  branching fraction. The background was consequently carefully studied at the beginning of the preparation of this analysis within LHCb [218].

First, inclusive  $b\bar{b}$  events were analysed. After selection and trigger, the composition of the survivor sample whose impact on the analysis final sensitivity is important<sup>2</sup> was scrutinised. This study showed that the most annoying background consists of fake combinations of two real muons unrelated to each other, that are mistaken for signal events.

Secondly, specific background sources, with properties that could mimic the signal, were identified. The largest contribution comes from the  $B_c^+ \rightarrow J/\psi(\mu\mu)\mu^+\nu_\mu$  decay with three muons produced at the same displaced vertex. However, it was shown that due to the presence of the neutrino, the reconstructed invariant mass of most of the  $B_s^0 \rightarrow \mu^+\mu^-$  candidates is below the  $B_s^0$  mass. This reason renders the  $B_c^+ \rightarrow J/\psi(\mu\mu)\mu^+\nu_\mu$  background negligible compared to the dimuon background.

The  $B_{(s)}^0 \rightarrow h^+h^-$  background was also shown to be under control. Its contribution comes either from a combination of a muon originating from a primary vertex and a misidentified

<sup>1</sup>The samples were generated with **Gauss** v25, steering **Pythia** v6.3 for the event generation and **EvtGen** v8 for the  $B$  decays, digitised with **Boole** v12 and reconstructed using **Brunel** v30 and v31.

<sup>2</sup>The criterion was  $GL > 0.3$ ; the GL will be introduced in Section 5.4. It takes values between 0 and 1, events with large GL values are signal-like.

Table 5.1: Monte Carlo samples used in this analysis. The instantaneous luminosity the generator-level cut efficiency  $\epsilon^\theta$  with its statistical uncertainty are reported [223].

	$\mathcal{L}$ [cm $^{-2}$ s $^{-1}$ ]	$\epsilon^\theta$ [%]
$B_s^0 \rightarrow \mu^+\mu^-$	$2 \times 10^{32}$	$20.05 \pm 0.09$
	$5 \times 10^{32}$	$20.06 \pm 0.06$
$B^+ \rightarrow J/\psi(\mu\mu)K^+$	$2 \times 10^{32}$	$17.89 \pm 0.03$
$B_d^0 \rightarrow \pi^+\pi^-$	$2 \times 10^{32}$	$20.15 \pm 0.12$
inclusive dimuon	$2 \times 10^{32}$	$0.966 \pm 0.003$
	$5 \times 10^{32}$	$0.996 \pm 0.003$

hadron from the  $B$  decay or from a combination of two misidentified hadrons (mostly due to decays in flight), with an equal share. Such events can be easily distinguished from signal using geometrical information and have a large invariant mass spread. As such, the  $B_{(s)}^0 \rightarrow h^+h^-$  background was shown to be negligible.

In conclusion, the relevant background for this study was thus identified as the combinations of real muons, and consequently an inclusive dimuon Monte Carlo sample was used. It contains events with at least one  $b$  hadron within 400 mrad around the  $z$  axis and at least two muons of opposite signs, with an invariant mass smaller than  $100 \text{ GeV}/c^2$  and each with a momentum forming an angle with the  $z$  axis between 10 mrad and 400 mrad. The requirements on the muons have an efficiency depending on the event multiplicity and thus on the instantaneous luminosity. This explains the two different generator-level cut efficiencies in Table 5.1. Note that the final state muons are not required to be related to a  $b$  hadron in the event.

### 5.3 Event Selection

The selection for this particular analysis uses unusually loose cuts. The goal is to reduce the size of the data sample to analyse, keeping most of the signal and rejecting obvious background events. Another requirement is to have selections as common as possible for signal, normalisation and control channels. The use of similar selections for all the decay channels is motivated by the desire to have close selection efficiencies between the signal and the normalisation channels and to have similar phase space of the selected  $B$ . This results in a drop of signal selection efficiency, which is acceptable since the events lost in the process were shown not to yield a significant sensitivity. This selection yields a very poor signal over noise figure, however it is not a problem, since most of the discriminating power comes later in the analysis process, mainly through the Geometrical Likelihood detailed in Section 5.4.

Our alternate selection was derived from the standard selection. Its variables were chosen with the idea of finding an alternative for each of the standard variables with similar physical meaning, but that does not involve an error estimate. Two slightly different selections are used, one for the two-body decay channels ( $B_s^0 \rightarrow \mu^+\mu^-$  and  $B_{(s)}^0 \rightarrow h^+h^-$ ) and another for the three- and four-body decay channels ( $B^+ \rightarrow J/\psi(\mu\mu)K^+$  and  $B^0 \rightarrow J/\psi(\mu\mu)K^{*0}(K^+\pi^-)$ ).

The alternate variables are:

**Invariant Mass of the  $B_s^0$**  Two mass windows are defined centred on the nominal  $B_s^0$  mass value. A large mass window cut of  $\pm 600 \text{ MeV}/c^2$  is always applied. On the signal channel,

a tight mass cut of  $\pm 60 \text{ MeV}/c^2$  is applied eventually. This variable is common to both the standard and the alternate analyses.

**Distance Of Closest Approach of the two muons (DOCA)** It is the distance between the two straight lines defined by the muon candidate momentum vectors, in the VeLo region. Since the muons should arise from the same vertex, their DOCA should be zero. It can only take positive values. The related standard variable is the  $\chi^2$  of the secondary vertex (SV). The secondary vertex is obtained by vertexing the two muon candidate tracks; cutting on the vertex quality is highly related to a cut on the distance between the two muon tracks.

**Impact Parameter of the  $B_s^0$  candidate w.r.t. the primary vertex (IP)** It is the distance between the straight line defined by the  $B_s^0$  candidate momentum vector and the vertex identified as the primary vertex (PV). In case there are several PVs in one event, the vertex for which the  $B_s^0$  IP is minimum is considered. The IP is ideally zero and can only take positive values. The related standard variable is the  $B_s^0$  IP significance (IPS),  $\frac{\text{IP}}{\sigma_{\text{IP}}}$ .

**Flight Distance of the  $B_s^0$  (FD)** This is the distance between the primary vertex and the secondary vertex, where the  $B_s^0$  candidate decays. The related standard variable is the  $B_s^0$  FD significance (FDS),  $\frac{\text{FD}}{\sigma_{\text{FD}}}$ .

**Transverse momentum of the  $B_s^0$  ( $p_T$ )** This variable is common to both the standard and the alternate analyses.

**Smallest Impact Parameter of the muons w.r.t. all PVs** The reason behind the use of this variable is to avoid prompt muons, coming from other PVs of the event. Thus, muon candidates are not allowed to fly closer to a PV than a given distance. The standard analysis uses the minimal IPS of the muons w.r.t. all PVs.

### 5.3.1 $B_s^0 \rightarrow \mu^+ \mu^-$ Selection

Table 5.2 shows the standard and alternate selection variables for the two-body channels. The cut values on the alternate variables are set so that the selection efficiencies on true Monte Carlo signal are close to those of the related standard variables. The obtained cut values and efficiencies, after reconstruction but before trigger (according to the definition of  $\epsilon^{\text{sel}|\text{rec}}$  in Section A.1) are shown in Table 5.2.

Note that, to a large extent, the yield is common to the two selections. For  $B_s^0 \rightarrow \mu^+ \mu^-$  events, 95 % of the events selected by the alternate selection, and 94 % of those selected by the standard selection are identical.

Figures 5.1 and 5.2 show the distributions of the alternate variables for selected  $B_s^0 \rightarrow \mu^+ \mu^-$  events. The blue solid line corresponds to events selected by the alternate selection, while the light blue dashed line corresponds events selected by the standard selection. Plots in the left column show all the selected events. To get rid of the difference in total selection efficiency, and to allow a better reading, both histograms are arbitrary normalised to 1000 events. Note that since the aim of those plots is to compare the two selections, the events plotted are those remaining after all the cuts were applied. In order to highlight the differences between the two selections, histograms for the events exclusively selected by each of the selections are plotted in the right column. The exclusive histograms for the alternate selection are normalised so that the number of exclusively selected events is correct according to the normalisation chosen for

the left column histograms. This illustrates how common the yield of the two selections is. The histograms of the events selected exclusively with the standard selection are normalised to the corresponding histograms for the alternate selection. With this normalisation, the comparison is easier.

In Fig. 5.1, the first row shows the  $B_s^0$  events mass with very similar distributions for both selections. The second row shows the distance of closest approach (DOCA) between the two muons. These distributions are also very similar, however, on the exclusively selected histograms, two slight differences are noticeable. First, the alternate distribution is less peaked at small values than the standard one is, secondly, the effect of the cut at 0.1 mm is clearly seen. Those two differences are of the order of one per mill. The last row of Fig. 5.1 shows the  $B_s^0$  events impact parameter distributions, which are also very similar. The exclusive histograms show that the standard selection is slightly more peaked at the per mill level.

The first row of Fig. 5.2 depicts the  $B_s^0$  events transverse momentum. The two distributions are identical. The second row shows the  $B_s^0$  FD. The effect of the alternate selection cut,  $B_s^0$  FD  $> 1.7$  mm, is clear. About 4 % of the events selected by the standard selection are excluded by the alternate selection. This effect is discussed below. Apart from that, the distributions are similar. The last variable of Fig. 5.2 is the smallest IP of the muons. Again the effect of the cut on this variable can be seen.

In Fig. 5.3, distributions of the  $B_s^0$  momentum and  $B_s^0$  pseudorapidity are shown. While those distributions are similar, there exists a systematic difference between the two selections. The difference can be related to the difference in the FD distribution of the  $B_s^0$ . By cutting away  $B_s^0$  events with FD  $< 1.7$  mm, a bias on the  $B_s^0$  momentum arises. Indeed, small FD values tend to correspond to small  $B_s^0$  momenta, despite the  $B_s^0$  proper distribution. This also explains the

Table 5.2: Variables, cut values and selection efficiencies on  $B_s^0 \rightarrow \mu^+ \mu^-$  for both the standard selection and the alternate selections. Efficiencies are computed after the previous cuts are applied and for reconstructed events, before any trigger. The largest statistical error on the efficiencies is less than 0.2 %.

Standard Analysis			Alternate Analysis		
Variable	Cut	Efficiency [%]	Variable	Cut	
$B_s^0$ mass	$\pm$ 600 MeV	97.3	97.3	<i>idem</i>	
$\chi^2$ of SV	< 14	98.2	97.5	$\mu$ 's DOCA	< 0.1 mm
$B_s^0$ IPS	< 6	98.4	98.9	$B_s^0$ IP	< 0.1 mm
$B_s^0$ $p_T$	> 700 MeV	98.0	98.0	<i>idem</i>	
$B_s^0$ FDS	> 12	76.6	77.2	$B_s^0$ FD	> 1.7 mm
$\min(\mu \text{ IPS}_{\text{all PVs}})$	> 3.5	92.9	91.4	$\min(\mu \text{ IP}_{\text{all PVs}})$	> 0.06 mm
All cuts above		65.5	64.8	All cuts above	
$B_s^0$ mass	$\pm$ 60 MeV	90.7	90.4	<i>idem</i>	
All cuts above		58.5	57.7	All cuts above	

difference visible on the  $B_s^0$  pseudorapidity distribution, since the pseudorapidity is

$$\eta = \frac{1}{2} \ln \left( \frac{1 + \sqrt{1 - \frac{p_T^2}{p^2}}}{1 - \sqrt{1 - \frac{p_T^2}{p^2}}} \right). \quad (5.1)$$

Hence, as the top histogram in Fig. 5.2 allows to fix the value of  $p_T$ , when the momentum  $p$  increases, the pseudorapidity  $\eta$  increases as well.

The distribution of the  $B_s^0 \rightarrow \mu^+ \mu^-$  events selected by the alternate and the standard selections for interesting variables are very close and the few differences are understood. However, what is more important is the agreement in terms of the selected  $B$  phase space between the signal channel and the control channels. This will be shown in Section 5.3.4.

The distributions of the standard variables can be found in Appendix B. Their interpretation is very similar to the one provided above.

The alternate analysis is found to be less efficient in rejecting background than the standard selection. The remaining dimuon background is in excess of 14 % for the alternate selection with respect to the standard selection at nominal luminosity. This figure increases to 34 % in excess at higher luminosity of  $5 \times 10^{32} \text{ cm}^{-2} \text{ s}^{-1}$ . However, this is not important since the selection is not where the discrimination power lies.

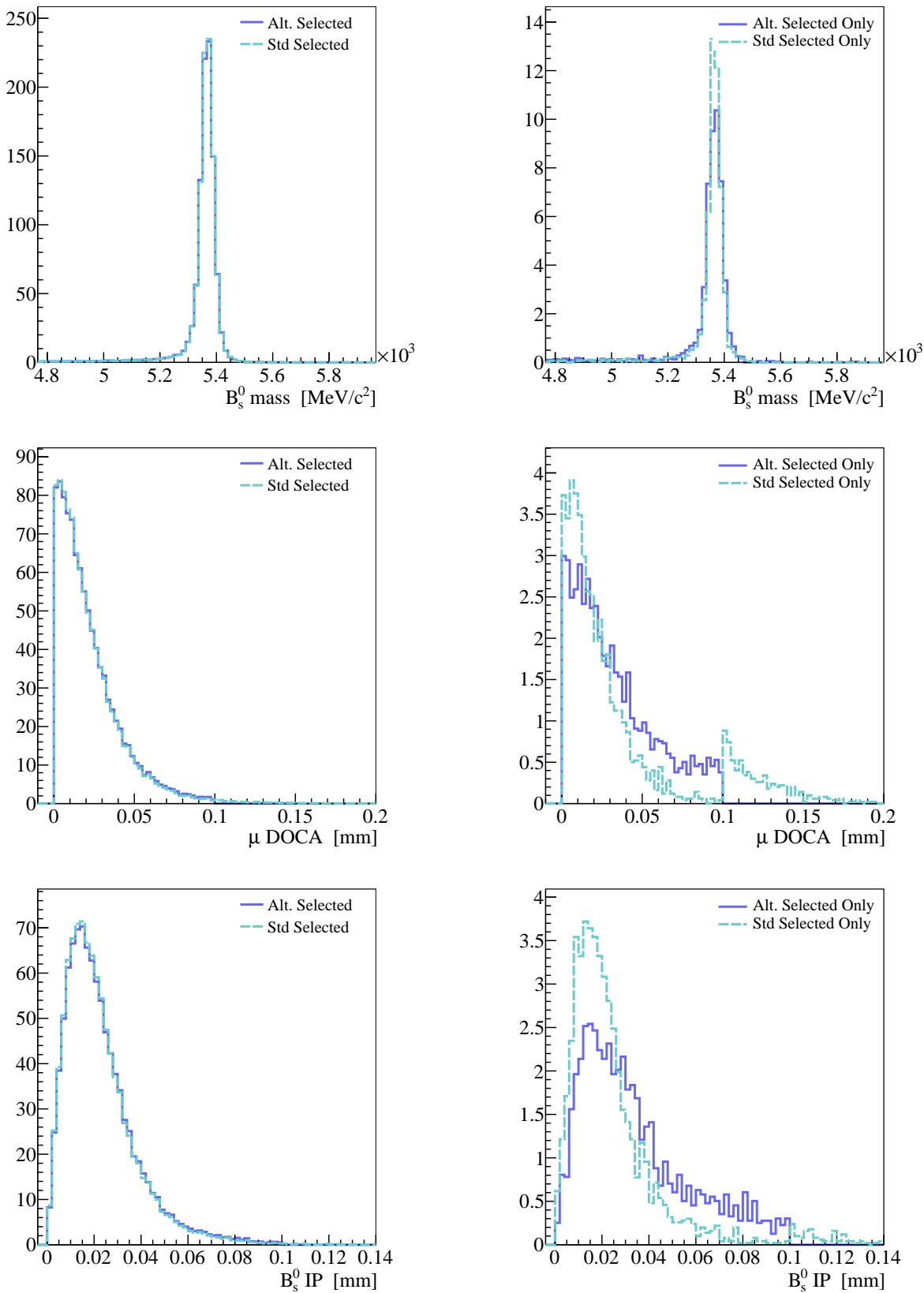


Figure 5.1: Left: Distributions of the  $B_s^0$  mass (top), the  $\mu$  DOCA (middle) and the  $B_s^0$  IP (bottom) for  $B_s^0 \rightarrow \mu^+\mu^-$  events passing the alternate (solid blue) and the standard (dashed light blue) selections. Right: Same distributions for events passing only one of the selections.

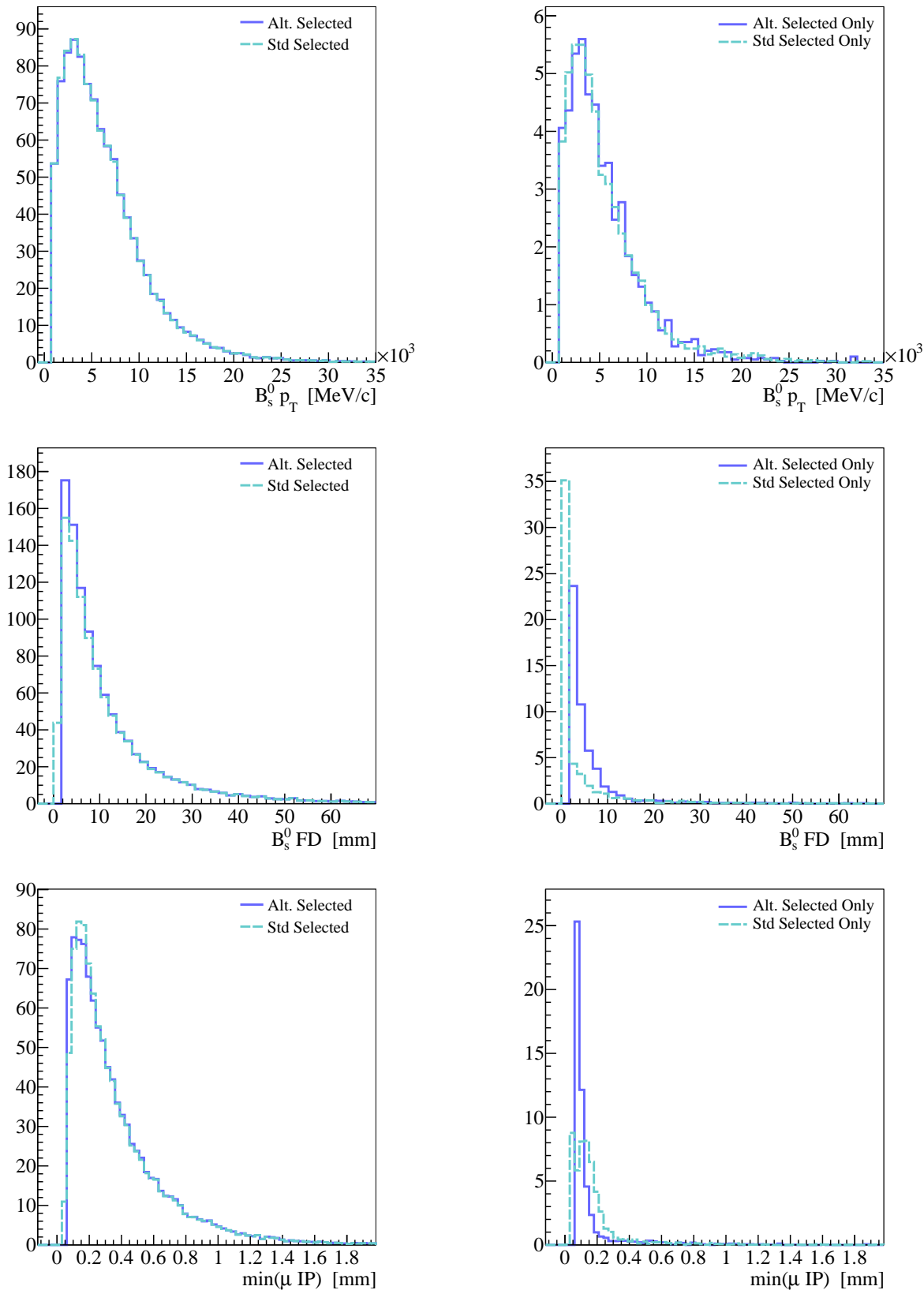


Figure 5.2: Left: Distributions of the  $B_s^0$   $p_T$  (top), the  $B_s^0$  FD (middle) and the smallest  $\mu$  IP (bottom) for  $B_s^0 \rightarrow \mu^+ \mu^-$  events passing the alternate (solid blue) and the standard (dashed light blue) selections. Right: Same distributions for events passing only one of the selections.

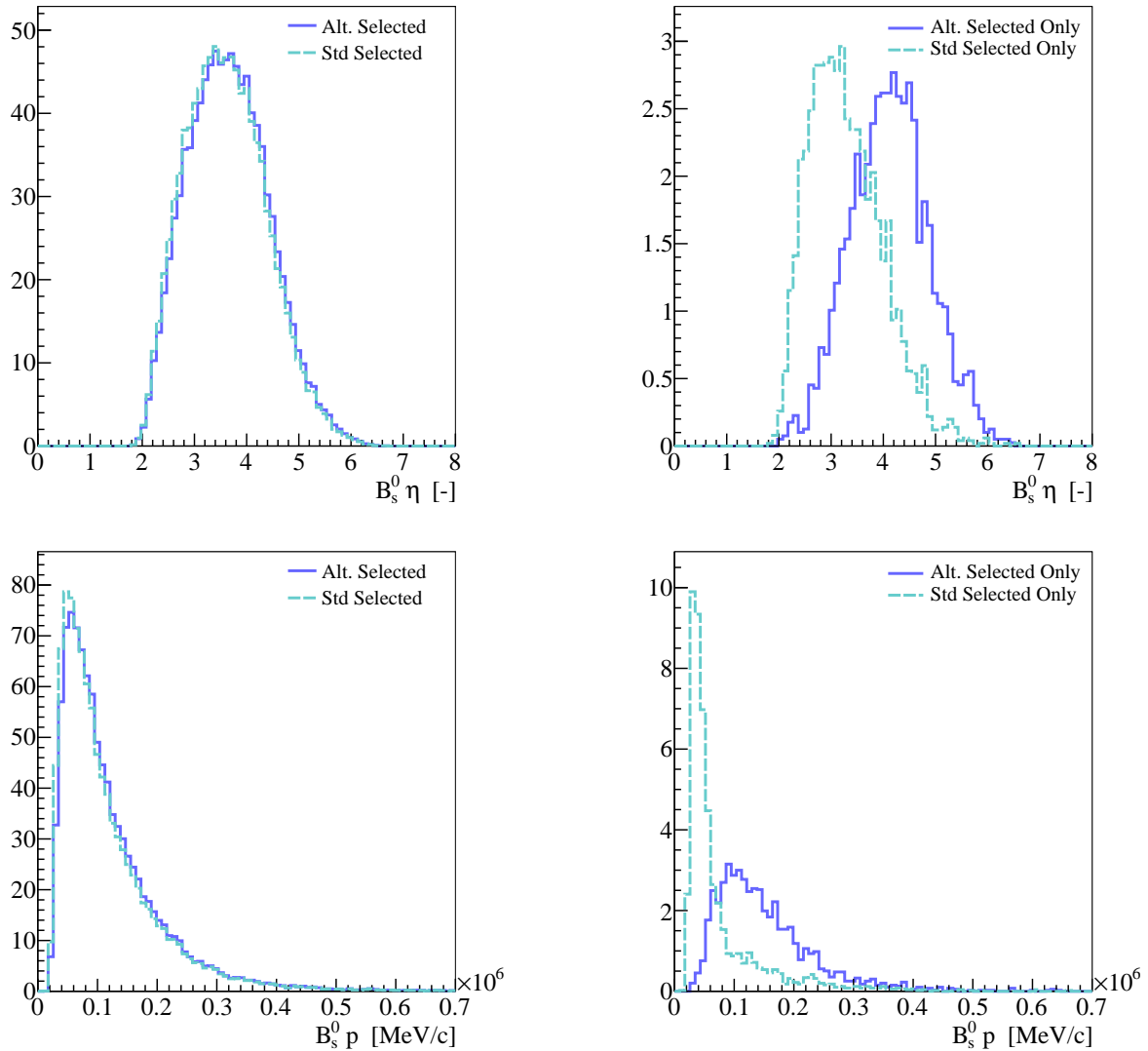


Figure 5.3: Left: Distributions of the  $B_s^0$  pseudorapidity (top), the  $B_s^0$  momentum (bottom) for  $B_s^0 \rightarrow \mu^+ \mu^-$  events passing the alternate (solid blue) and the standard (dashed light blue) selections. Right: Same distributions for events passing only one of the selections.

### 5.3.2 $B_{(s)}^0 \rightarrow h^+h^-$ Selection

The alternate selection defined on the  $B_s^0 \rightarrow \mu^+\mu^-$  signal is used for the  $B_{(s)}^0 \rightarrow h^+h^-$  decay channel selection, with the only exception of the large mass window, which is only  $\pm 500 \text{ MeV}/c^2$  around the  $B^0$  mass. The alternate and standard selection efficiencies for this decay channel are grouped together in Table 5.3.

For  $B_{(s)}^0 \rightarrow h^+h^-$  events also, most of the events selected by one selection are also selected by the other selection. 94 % of the events selected by the alternate selection, and 93 % of those selected by the standard selection are common.

The distributions of the alternate and standard variables after both selections are shown in Appendix B.

Table 5.3: Variables, cut values and selection efficiencies on  $B_{(s)}^0 \rightarrow h^+h^-$  for both the standard selection and the alternate selections. Efficiencies are computed after the previous cuts are applied and for reconstructed events, before any trigger. The largest statistical error on the efficiencies is less than 0.4 %.

Standard Analysis			Alternate Analysis		
Variable	Cut	Efficiency [%]	Variable	Cut	
$B_{(s)}^0$ mass	$\pm 500 \text{ MeV}$	92.3	92.3	<i>idem</i>	
$\chi^2$ of SV	< 14.	97.3	96.3	$h$ 's DOCA	< 0.1 mm
$B_{(s)}^0$ IPS	< 6.	97.3	98.0	$B_{(s)}^0$ IP	< 0.1 mm
$B_{(s)}^0$ $p_T$	> 700 MeV	97.9	97.9	<i>idem</i>	
$B_{(s)}^0$ FDS	> 12.	76.0	77.6	$B_{(s)}^0$ FD	> 1.7 mm
$\min(h \text{ IPS}_{\text{all PVs}})$	> 3.5	91.7	91.0	$\min(h \text{ IP}_{\text{all PVs}})$	> 0.06 mm
All cuts above		59.6	60.2	All cuts above	

### 5.3.3 $B^+ \rightarrow J/\psi(\mu\mu)K^+$ Selection

The selection for the  $B^+ \rightarrow J/\psi(\mu\mu)K^+$  three-body channel differs from that for the two-body channels on some of the variables:

**Flight Distance of the  $J/\psi$**  is used instead of the  $B_s^0$  FD. This is not the distance of flight of the  $J/\psi$  *per se*, but the distance from the PV to the  $J/\psi$  vertex. Its standard equivalent is the  $J/\psi$  FD significance, with the same language stretch.

**Impact Parameter of the kaon w.r.t. any PV** is used instead of the smallest IP of the muons. Prompt kaons are avoided by requiring a minimal distance between their track and any PV.

Since this is a different selection, the alternate cut values were set so that the efficiency is close to that of the standard selection for each variable, similarly to what has been done with the two-body selection. The obtained cut values, as well as the selection efficiencies for both the standard and the alternate selections are shown in Table 5.4.

Again a large part of the yield is common to the two selections: 92 % of the alternate selected events and 93 % of the standard selected events are common.

The distributions of the alternate and standard variables after both selections are shown in Appendix B.

### 5.3.4 Interchannel Comparison of the $B$ Phase Space

The simplification of the ratio of selection efficiencies, as introduced by Eq. (A.1) in Appendix A.1, is not the only reason for choosing close selections among channels. The similarity of the  $B$  phase space of the selected events among the different channels is even more important. This property is used in the calibration of the geometrical likelihood variable, as explained in Section 5.4.3 and in the computation of the trigger efficiencies ratio, described in Section A.3.

Figure 5.4 shows the pseudorapidity, the momentum and the transverse momentum distributions of the  $B$  for the three channels, using the alternate and the standard selections. The histograms are normalised to 1000 selected events. One can see that the  $B$  phase space for the three channels is similar, that no pathological difference is found, and that the alternate selection leads to an agreement between channels comparable to that of the standard analysis.

Table 5.5 groups together the alternate selection efficiencies for the  $B_s^0 \rightarrow \mu^+ \mu^-$ ,  $B_{(s)}^0 \rightarrow h^+ h^-$  and  $B^+ \rightarrow J/\psi(\mu\mu)K^+$  decay channels.

Table 5.4: Variables, cut values and selection efficiencies on the three-body  $B^+ \rightarrow J/\psi K^+$  channel for both the standard selection and the alternate selection. Efficiencies are computed after the previous cuts are applied. The largest statistical error on the efficiencies is less than 0.05 %.

Standard Analysis			Alternate Analysis		
Variable	Cut	Efficiency [%]	Variable	Cut	
$B^+$ mass	$\pm$ 500 MeV	98.8	98.8 <i>idem</i>		
$\chi^2$ of SV	< 14.	99.2	99.1	$\mu$ 's DOCA	< 0.17 mm
$B^+$ IPS	< 6.	98.3	98.8	$B^+$ IP	< 0.1 mm
$B^+$ $p_T$	> 700 MeV	98.3	98.3	<i>idem</i>	
$J/\psi$ FDS	> 12.	75.6	74.9	$J/\psi$ FD	> 2.4 mm
$K^+$ IPS	> 3.5	92.5	92.8	$K^+$ IP	> 0.08 mm
All cuts above		65.4	66.0	All cuts above	

Table 5.5: Selection efficiencies, expressed as percentages, for the alternate selection. The variables reported are those of the  $B_s^0 \rightarrow \mu^+ \mu^-$  channel selection, the associated cut values are detailed in Table 5.2. The variables and cut values for the corresponding variables for the  $B_{(s)}^0 \rightarrow h^+ h^-$  and  $B^+ \rightarrow J/\psi K^+$  channels are detailed in Tables 5.3 and 5.4. Efficiencies are computed after the previous cuts are applied.

	$B_s^0 \rightarrow \mu^+ \mu^-$	$B_{(s)}^0 \rightarrow h^+ h^-$	$B^+ \rightarrow J/\psi K^+$
$B_s^0$ mass ( $\pm 600$ MeV/ $c^2$ )	97.3	92.3	98.8
$\mu$ 's DOCA	97.5	96.3	99.1
$B_s^0$ IP	98.9	98.0	98.8
$B_s^0$ $p_T$	98.0	97.9	98.3
$B_s^0$ FD	77.2	77.6	74.9
$\min(\mu \text{ IP}_{\text{all PVs}})$	91.4	91.0	92.8
All Cuts above	$64.8 \pm 0.2$	$60.2 \pm 0.35$	$66.0 \pm 0.05$
$B_s^0$ mass ( $\pm 60$ MeV/ $c^2$ )	97.3	—	—
All Cuts above	$57.7 \pm 0.2$	—	—

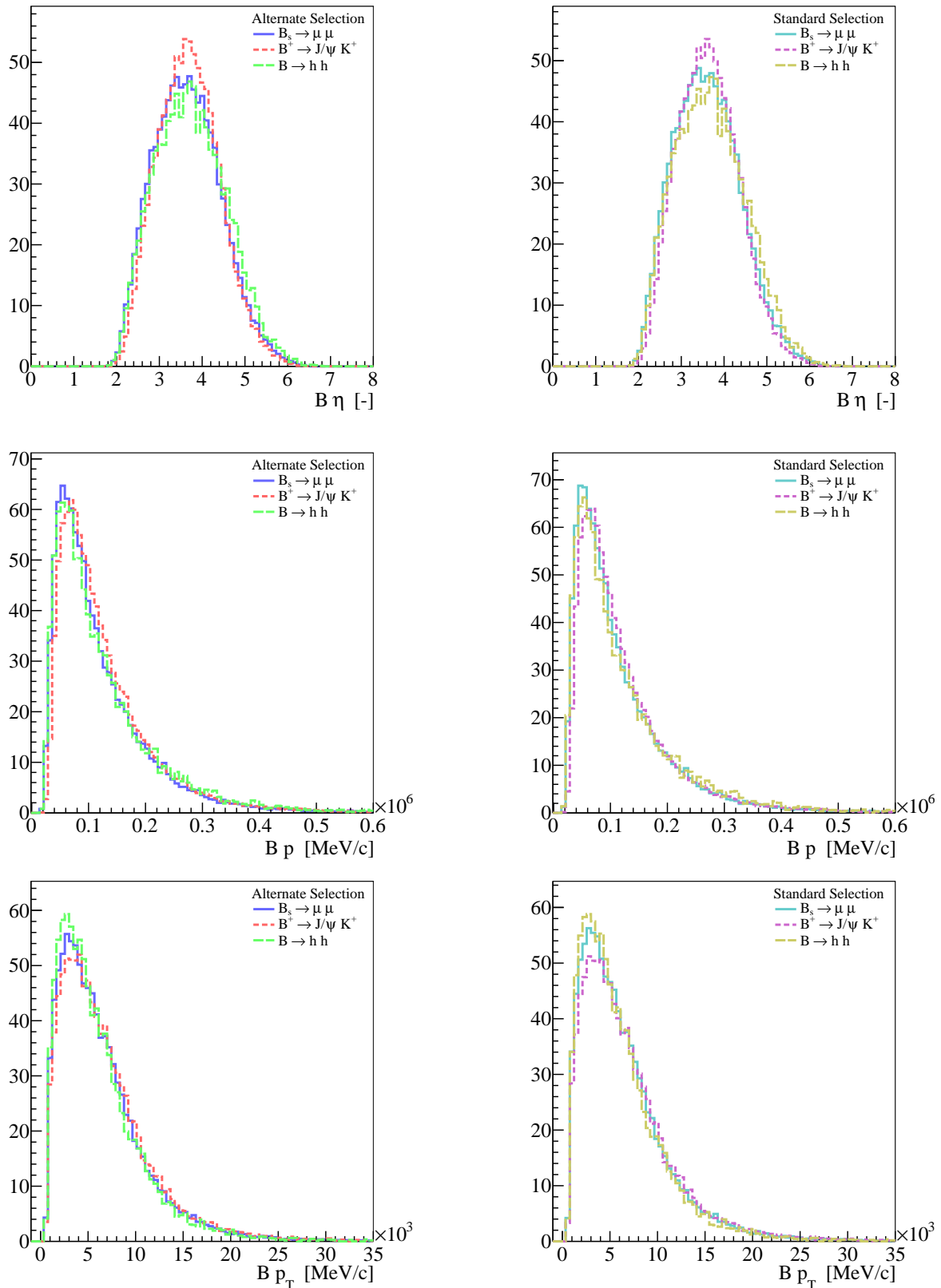


Figure 5.4: Distributions for the  $B$  pseudorapidity (top), the  $B$  transverse momentum (middle) and the  $B$  momentum (bottom) for  $B_s^0 \rightarrow \mu^+\mu^-$  (solid),  $B^+ \rightarrow J/\psi K^+$  (dashed) and  $B_{(s)}^0 \rightarrow h^+h^-$  (long dashed) events passing the alternate (left) and the standard (right) selections.

## 5.4 Geometrical Likelihood

The Geometrical Likelihood (GL)<sup>3</sup> groups together kinematic and topological information of the decay. Again, an alternate version of the tool developed for the standard analysis was defined, which differs only from the standard version of the GL by one variable. The six variables used in the alternate version are:

### Distance Of Closest Approach of the two muons

**$B_s^0$  proper time** This variable is the proper time of the  $B_s^0$  candidate, computed from the positions of the primary and secondary vertices, and from the  $B_s^0$  momentum and mass. Note that this variable is not used in the selection.

### Impact Parameter of the $B_s^0$ candidate w.r.t. the PV

**Isolation of each muon** For each of the muon candidates a variable called *isolation* is computed, based on the number of tracks forming a *good* vertex with the muon track. More precisely the isolation is defined as the number of long tracks<sup>4</sup>, different from the other muon track, that satisfy all the following requirements:

- the DOCA between the track and the muon should be  $< 200 \mu\text{m}$ ;
- the  $z$  coordinate of the vertex formed by the muon and the track,  $z_{\mu,t}$  should satisfy  $0 < z_{\mu,t} - z_{\text{PV}} < 30 \text{ mm}$ ;
- the angle  $\alpha$  between the sum of the muon and track momenta and the direction between the PV and the muon+track vertex must satisfy

$$\frac{|\mathbf{p}_\mu + \mathbf{p}_t| \alpha}{|\mathbf{p}_\mu + \mathbf{p}_t| \alpha + p_{T,\mu} + p_{T,t}} < 0.4,$$

where  $\mathbf{p}_\mu$  and  $\mathbf{p}_t$  ( $p_{T,\mu}$  and  $p_{T,t}$ ) are the (transverse) momenta of the muon and the track, respectively.

There are ongoing studies to refine the definition of the isolation, to render the isolation continuous and improve its discrimination power.

**Smallest Impact Parameter of the muons w.r.t. all PVs** Note that it is the only variable that is different from the standard definition of the GL, which uses the muon IP significance instead.

The construction of the GL requires separate datasets of signal and background events. We use Monte Carlo simulation for the  $B_s^0 \rightarrow \mu^+\mu^-$  signal and dimuon background, both generated at  $\mathcal{L} = 2 \times 10^{32} \text{ cm}^{-2} \text{ s}^{-1}$ , as defined in Section 5.2. Section 5.4.3 explains how data could be used instead.

The construction of the GL can be broken down in two steps. First, the distributions of the input variables for both signal and dimuon background are transformed into normal Gaussian distributions, uncorrelated with each other. This step is detailed in Section 5.4.1. Subsequently, the differences between the signal and background distributions are used to construct a powerful discriminant, as explained in Section 5.4.2.

<sup>3</sup>Note that while the GL, as a difference of  $\chi^2$  is a log-likelihood, it is its p.d.f. that is used in the final computation, as explained in Section 5.7.2.

<sup>4</sup>A long track is a track with hits in all the tracking dedicated region, *i.e.* in the VeLo, the TT, and the three tracking stations.

### 5.4.1 Gaussianisation and Decorrelation of the Input Distributions

The method described here shares some similarities with the statistical method described in Ref. [224].

The function that transforms a variable  $x$ , characterised by a probability density function (p.d.f.)  $p(x)$ , into a variable  $y(x)$  distributed along a normal Gaussian distribution (of mean 0 and variance 1) is

$$y(x) = \sqrt{2} \operatorname{erf}^{-1} [2 F(x) - 1] \quad (5.2)$$

where  $\operatorname{erf}^{-1}$  is the inverse function of

$$\operatorname{erf}(x) = \frac{2}{\sqrt{\pi}} \int_0^x e^{-z^2} dz, \quad \text{called the } \textit{error function}, \text{ and where}$$

$$F(x) = \int_{-\infty}^x p(z) dz \quad \text{is the cumulative distribution function of } p.$$

Let's first consider the signal distributions of the six variables  $x_i$ ,  $i = 1, \dots, 6$  entering in the GL definition. Each variable  $x_i$  is converted into a Gaussian distribution, using the transformation defined in Eq. (5.2).

The  $6 \times 6$  covariance matrix of the resulting variables is computed. This matrix allows to get rid of the correlations between the variables, by the mean of a rotation of the variable axes. This rotation yields a new set of variables, each being a linear combination of all the variables before decorrelation.

Finally, each of the decorrelated variables is gaussianised a last time using relation (5.2), and we get six final variables

$$y_{s,j} = T_{s,j}(x_1, \dots, x_6) \quad \text{with } j = 1, \dots, 6,$$

gaussianly distributed, uncorrelated with each other and each potentially depending on all the initial variables  $x_i$ . Note that the transformations  $T_{s,j}$  yield Gaussian distributions only if the input variables are distributed exactly as in the dataset used to defined them; applied to datasets with different distributions, *e.g.* background, the obtained distributions are not Gaussian and may be correlated. The same procedure is applied to background distributions, which yields another set of six variables  $y_{b,j} = T_{b,j}(x_1, \dots, x_6)$ .

The motivation for the first gaussianisation is the factorisation of the scaling and rotation effects. By gaussianising the variables before the decorrelation, one reduces the decorrelation down to a pure rotation, without any scaling of the axes. This factorisation of the transformations makes it easier to understand the content of the new variables in terms of the physical variables. The computation of the GL, as explained in Section 5.4.2, requires gaussianly distributed variables used as input. While each variable is gaussianly distributed to a good approximation before the rotation, the 6-dimensional distribution made from these variables is, in general, not a 6-dimensional Gaussian distribution. If it was the case, then the result of any rotation around the origin would still be a 6-dimensional Gaussian and by consequence so would be the projection on each axis. In the general case, the decorrelation does not necessarily yield gaussianly distributed variables, which calls for the second gaussianisation process.

Figures 5.5 and 5.6 illustrate the treatment of the distributions used as input for the definition of the GL, for  $B_s^0 \rightarrow \mu^+ \mu^-$  signal and dimuon background, respectively. Similar figures for the case of a GL defined without the muon isolations are shown in Appendix C.

### 5.4.2 Construction of the Geometrical Likelihood

The second step consists in the construction of the GL itself. For each event  $e$  in the signal sample, one computes two quantities, describing how well the event suits the signal and background hypotheses, respectively,

$$\begin{aligned}\chi_s^2(e) &= \sum_{j=1}^6 \frac{(T_{s,j}(e) - \mu_{s,j})^2}{\sigma_{s,j}^2} = \sum_{j=1}^6 (T_{s,j}(e))^2 \quad \text{and} \\ \chi_b^2(e) &= \sum_{j=1}^6 (T_{b,j}(e))^2,\end{aligned}$$

remembering that the  $T_{s,j}$  (and  $T_{b,j}$ ) are gaussianly distributed with mean  $\mu = 0$  and variance  $\sigma^2 = 1$  and decorrelated.

These  $\chi^2$  are combined to define

$$\Delta\chi_S^2(e) = \chi_s^2(e) - \chi_b^2(e).$$

A small value of  $\Delta\chi_S^2$  indicates compatibility with the signal, while a large value indicates compatibility with the background.

The same is performed on the background sample and yields a  $\Delta\chi_B^2$  distribution. Finally,  $\Delta\chi_S^2$  is transformed in order to have it uniformly distributed between 0 and 1. The same transformation is applied to  $\Delta\chi_B^2$ , which gives a distribution peaked at zero and decreasing fast when going towards 1. The numerical values in the [0,1] interval obtained from the input physical variables after all the transformations explained above represent the GL. Figure 5.7 shows the distributions of the GL for the signal and dimuon background events that were used to define it. The few dimuon background events characterised by large GL values consist of muons from  $b$  decays in 60 % of the cases, of muons from  $b$  decays with  $c$ -flavoured intermediate states in 30 % of the cases and of pions misidentified as muons.

Note that the discrimination power of the GL is maximal when the  $n$  distributions used to define it form a  $n$ -dimensional Gaussian distribution. Figures C.1 and C.2, in Appendix C, show scatter plot of the input variables plotted against each other in pairs, for the signal and the background, respectively. While most of the pairs of variables form good approximations of 2-dimensional Gaussian distributions, some clearly do not. Even though, it is not dramatic, it results in a loss of discrimination power, not all the information about either the signal or the background has been used. This arises because the variables, although uncorrelated with each other to a good approximation, are not independent. Reference [224] provides some ideas to improve this situation; an effort in that direction may worth trying.

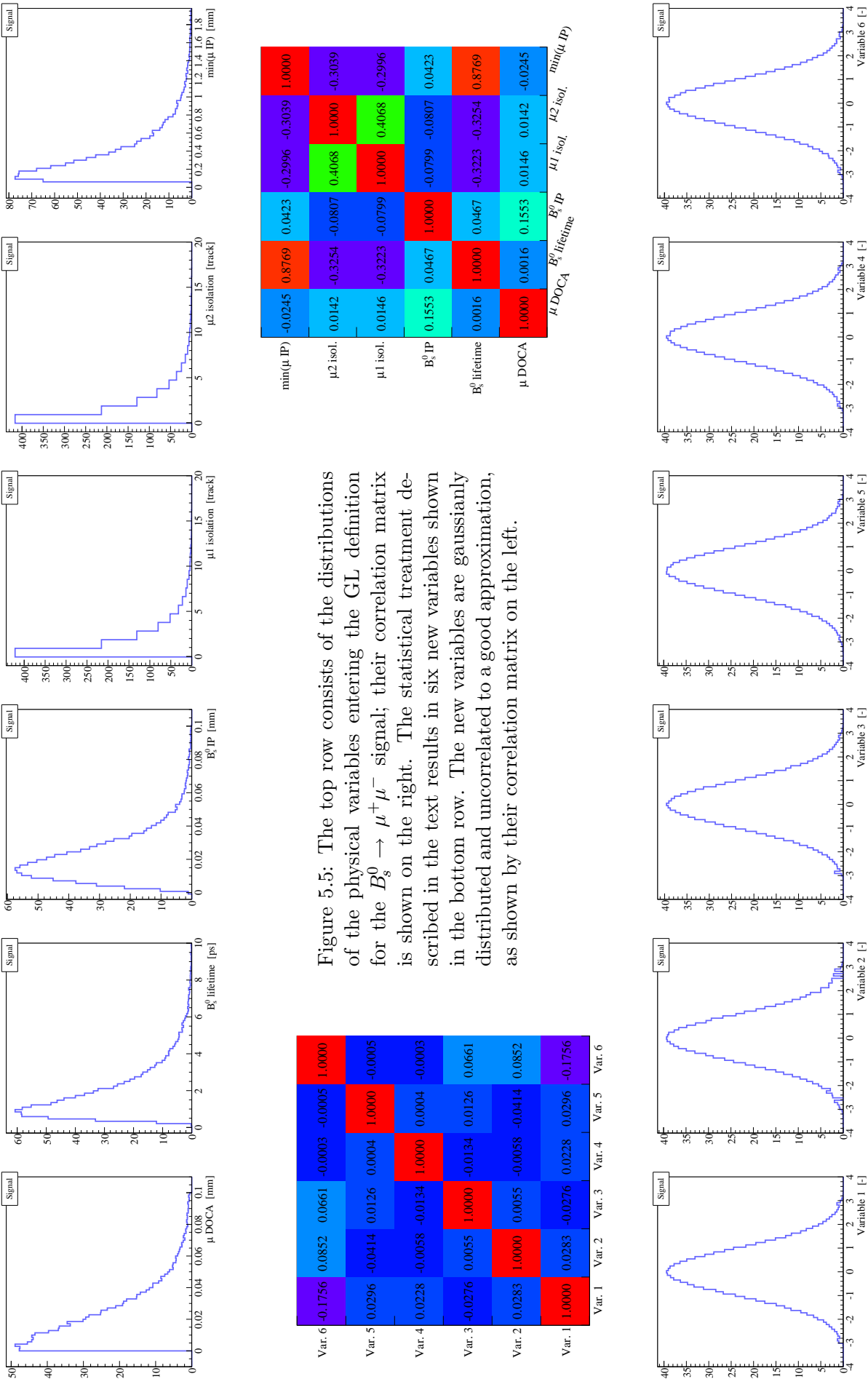
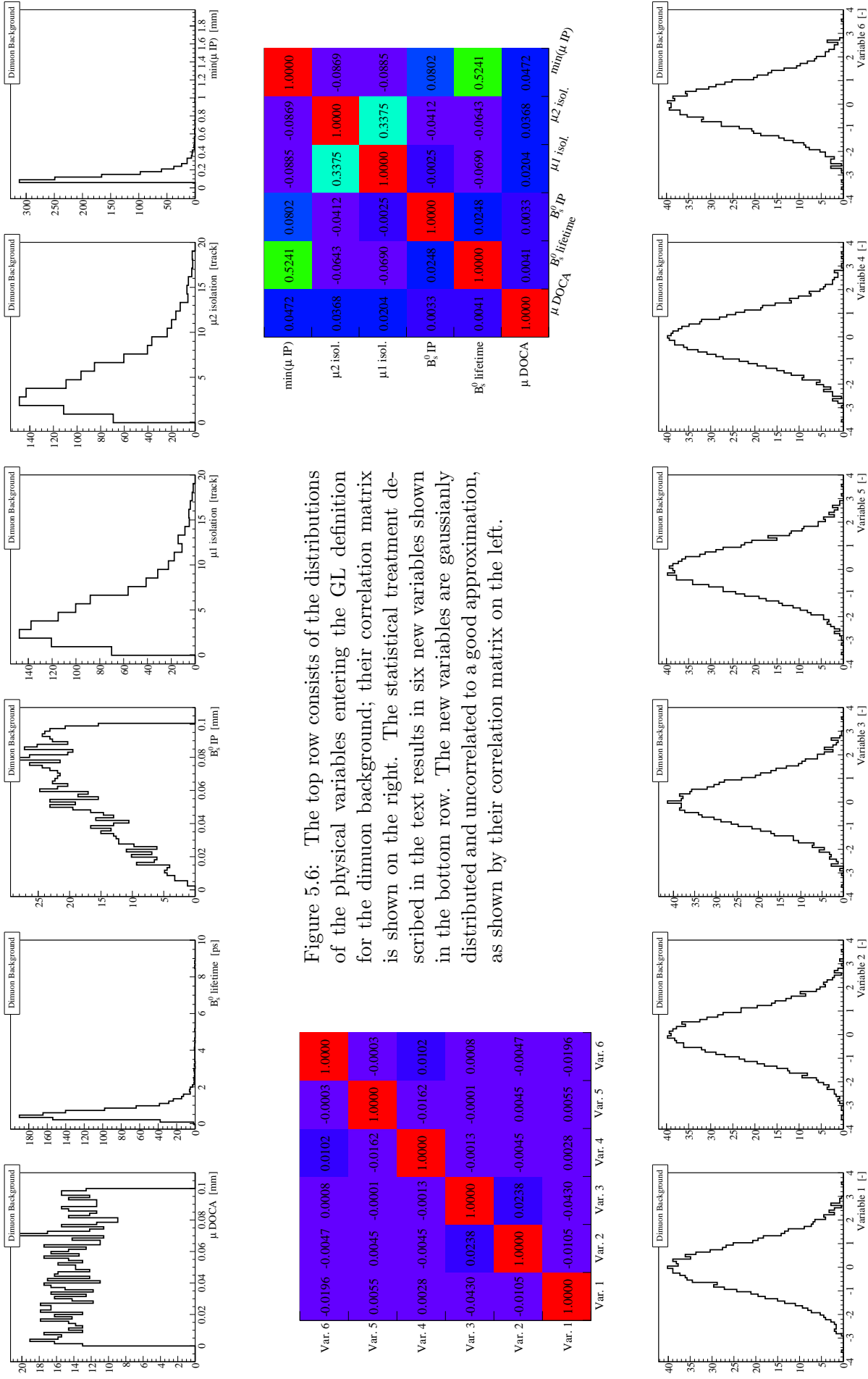


Figure 5.5: The top row consists of the distributions of the physical variables entering the GL definition for the  $B_s^0 \rightarrow \mu^+ \mu^-$  signal; their correlation matrix is shown on the right. The statistical treatment described in the text results in six new variables shown in the bottom row. The new variables are gaussianly distributed and uncorrelated to a good approximation, as shown by their correlation matrix on the left.



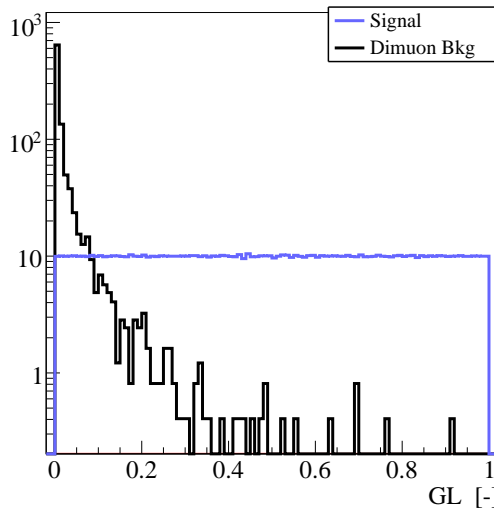


Figure 5.7: Distribution of the GL for  $B_s^0 \rightarrow \mu^+\mu^-$  signal (solid blue) and dimuon background (dashed black). The GL is uniformly distributed for signal events, whereas the background is concentrated at small values.

### 5.4.3 Calibration of the Geometrical Likelihood

We have to differentiate the definition of the GL, given above, from its calibration. The GL can be defined with real data using two separate samples of signal and background events. Even though such a data-driven definition is desirable, it is not absolutely necessary at first. However, the calibration of the GL with real data will be absolutely necessary, since it enters in the final measurement as a p.d.f.

Candidates in the sidebands of the invariant mass distribution will be used to calibrate the GL on background. For the signal,  $B_{(s)}^0 \rightarrow h^+h^-$  events, that have identical topological characteristics will be used. However, the trigger represents a major difference between the  $B_{(s)}^0 \rightarrow h^+h^-$  and  $B_s^0 \rightarrow \mu^+\mu^-$  channels, and biases the data sample. Methods using TIS<sup>5</sup> events have been studied to factorise out the trigger effect and allow the GL calibration [72].

## 5.5 Invariant Mass

The selection presented in Section 5.3 has a large mass window of  $\pm 600 \text{ MeV}/c^2$  around the  $B_s^0$  mass. This large mass window is ten times larger than the final mass window of  $\pm 60 \text{ MeV}/c^2$ . The events in those two sidebands are used to interpolate the combinatorial background in the tight mass window. The p.d.f. for the mass distribution of the background is then obtained from a simple parametrisation of those sidebands, as shown on the left of Fig. 5.8.

For the signal mass calibration, the strategy is to use  $B_s^0 \rightarrow K^+K^-$ . A strong PID cut is required to get a high purity sample. As a consequence of the PID cut, the momentum distribution is biased, which in turn affects the mass resolution. The effect of this PID cut on the mass resolution is evaluated considering the effect of the PID cut on the mass resolution of  $B_{(s)}^0 \rightarrow h^+h^-$  events. After correcting for the PID cut, the  $B_s^0 \rightarrow K^+K^-$  is fitted with a

<sup>5</sup>TIS events are defined in Appendix A.3.

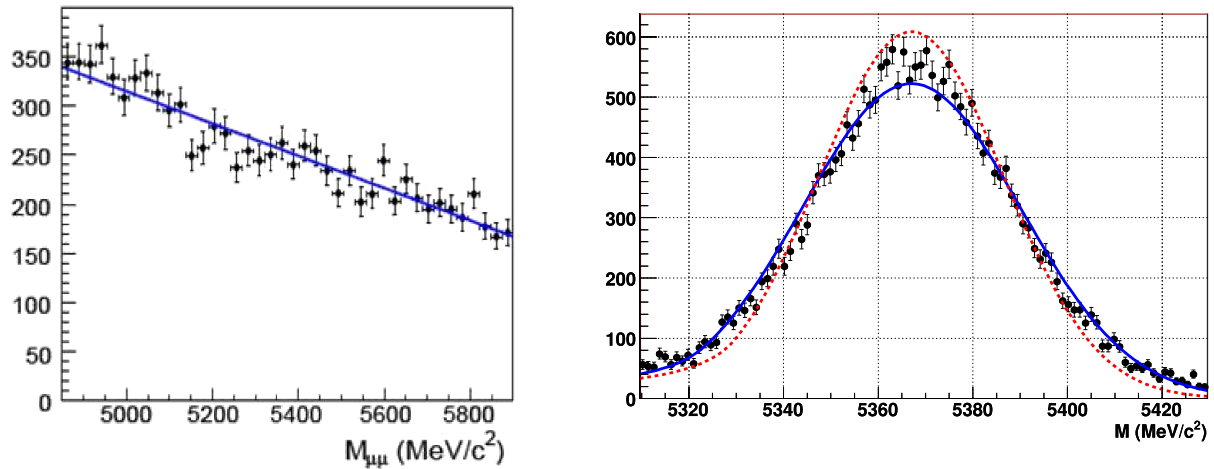


Figure 5.8: Left: Invariant mass distribution for combinatorial background. A linear fit (blue line) is used as parametrisation. Taken from Ref. [72]. Right: Invariant mass distribution for  $B_s^0 \rightarrow \mu^+\mu^-$  candidates (data points), together with the fit of the  $B_s^0 \rightarrow K^+K^-$  candidates distributions, before (red dashed curve) and after the PID correction (solid blue curve). Taken from Ref. [72].

Crystal-Ball parametrisation and used as mass p.d.f. for the signal, as illustrated on the right of Fig. 5.8. This method results in a mass resolution of  $\sigma = 21.5$  MeV/c<sup>2</sup>.

## 5.6 Muon Identification

The muon identification is a two-stage process.

First, for each track, hits in the muon system are search around its extrapolated trajectory in that detector. The track is required to have at least one hit in a set of muon stations that depends on the track momentum. If this criterion is reached then the track is flagged as IsMuon<sup>6</sup>. This Boolean flag is required for the two muon candidates. The muon identification is first used in the reconstruction, since the two muon candidate tracks are required to have a minimum number of hits in the muon stations.

The second step, more fine, aims at the evaluation of the compatibility of the final states with the muon hypothesis. To that end, one constructs a discriminating variable taking into account the distribution of the hits associated with the track in the muon system. This information, together with information from the other PID devices, is used to compute a difference of log-likelihood between the muon and the alternate non-muon hypotheses. The calibration of this variable requires separate samples of muon and non-muon particles. The developed method, using hadrons from the  $\Lambda \rightarrow p\pi^-$  decay as non-muon particles and  $J/\psi \rightarrow \mu^+\mu^-$  decays as source of muons, is illustrated in Fig. 5.9. The p.d.f.s extracted from those distributions for signal and background are used as input in the final measurement.

<sup>6</sup>Note that another criterion will be used on the first data, IsMuonLoose, with relaxed requirements less dependent on the muon chamber performance.

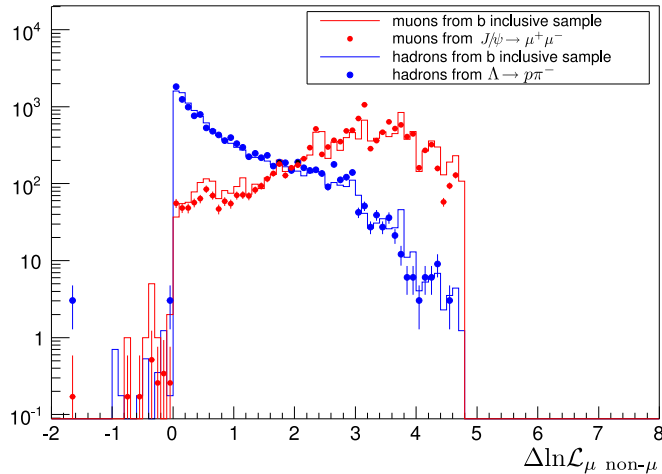


Figure 5.9: Difference of log-likelihood between the muon and non-muon hypotheses from an inclusive  $b\bar{b}$  sample. The blue histogram corresponds to the expected values for non-muons while the red histogram is those for muons. The blue and red data points correspond to the distributions obtained from the  $\Lambda \rightarrow p\pi^-$  and  $J/\psi \rightarrow \mu^+\mu^-$  calibrations samples, respectively. Taken from Ref. [72].

## 5.7 Sensitivity to the $B_s^0 \rightarrow \mu^+\mu^-$ Branching Fraction

Since real data is available neither with sufficient statistics nor with sufficient quality for the search of  $B_s^0 \rightarrow \mu^+\mu^-$  yet, there is no result to quote. Instead, we assess the LHCb sensitivity to a range of  $\mathcal{B}(B_s^0 \rightarrow \mu^+\mu^-)$  values. To that end, we use the tools derived by the collaborative effort and detailed in the previous parts of this chapter to analyse the outcome of toy Monte Carlo experiments. By varying the branching fraction hypothesis for  $B_s^0 \rightarrow \mu^+\mu^-$ , we quantify the sensitivity for a given integrated luminosity.

The statistical framework used to quote an exclusion limit or a branching fraction measurement with a given confidence level is detailed in Section 5.7.1. In Section 5.7.2, we detail the input and justify the assumptions that are used in Section 5.7.3 to compute the sensitivity with toy Monte Carlo experiments. The results of this study are finally presented and discussed in Section 5.7.4.

### 5.7.1 The Modified Frequentist Approach: $CL_s$

The measure of the strength of a limit is given by its confidence level. The difficulty to find a satisfactory concept in case of a search, either within the purely frequentist approach or in the Bayesian one, is not new [225]. In this analysis, we plan to use the  $CL_s$  method, which is the outcome of the thoughts of the *LEP Working Group for Higgs Boson Searches*, when confronted to the similar situation of excluding a Higgs mass range [220–222]. The final combination of the LEP Higgs searches [36] uses this method.

The search for a signal can be formulated in terms of a hypothesis test. The null hypothesis is the absence of signal — and thus the observation of background only — and the alternate hypothesis is its existence — and thus the observation of signal and background. The analysis aims at quantifying to which extent those hypotheses are favoured or excluded by the outcome of an experiment. To that end, a test-statistic is built, which is a function of the physical

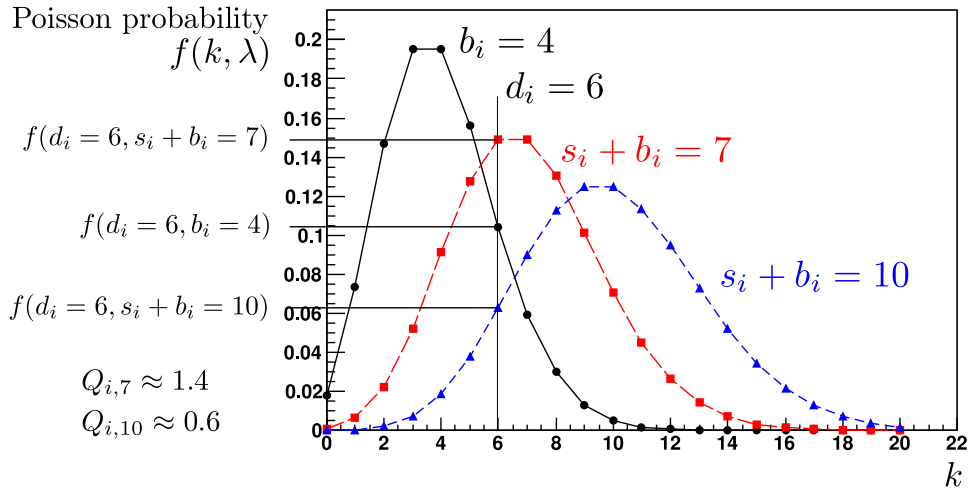


Figure 5.10: Illustration of the effect of different branching fraction hypotheses on the likelihood ratio  $Q_i$  in the  $i$ -th bin for a background expectation  $b_i = 4$  and two different numbers of expected signal events  $s_i = 3$  and  $s_i = 6$ . An experiment has measured  $d_i = 6$  events in this bin. In the case of the small signal hypothesis, the resulting likelihood ratio  $Q_{i,7}$  is 1.4, whereas in the large signal hypothesis  $Q_{i,10}$  is 0.6 and thus much less compatible with the s+b hypothesis.

observables allowing the discrimination between signal-like and background-like observations. One also needs to define rules for exclusion or discovery, which should express the significance of the result: those are the confidence levels C.L. In case of exclusion, a 90 % C.L. is quoted, whereas a  $3\sigma$  or  $5\sigma$  deviation from the background hypothesis is conventionally required in the HEP domain to claim the observation of a signal.

The computation of confidence levels using several variables can be reduced to the combination of counting-only searches in different channels through the binning of the measured variables. The combination of the result of each bin is brought by an appropriate test-statistic. A convenient test-statistic is the ratio of the probability density for the signal+background hypothesis to the background only hypothesis. Such a likelihood ratio increases monotonically for increasing signal-like observations. For  $s_i$  and  $b_i$  expected signal and background events, and  $d_i$  observed events in the  $i^{\text{th}}$  bin (out of  $n$ ), the likelihood ratio is defined as

$$Q = \prod_{i=1}^n Q_i, \quad (5.3)$$

where

$$Q_i = \frac{f(d_i, s_i + b_i)}{f(d_i, b_i)} = \frac{(s_i + b_i)^{d_i} e^{-(s_i + b_i)}}{d_i!} \frac{d_i!}{(b_i)^{d_i} e^{-b_i}} = e^{-s_i} \left(1 + \frac{s_i}{d_i}\right)^{d_i},$$

$f(k, \lambda)$  being the probability of observing  $k$  occurrences while expecting  $\lambda$  occurrences and assuming the observed phenomenon follows Poisson's law. Figure 5.10 illustrates what is happening in a bin  $i$ , and how the value of the likelihood ratio  $Q_i$  varies for two different hypotheses on the signal, which could be two different branching fraction hypotheses.

Note that Eq. (5.3) simplifies to

$$Q = e^{-s_{\text{tot}}} \prod_{i=1}^n \left(1 + \frac{s_i}{d_i}\right)^{d_i}.$$

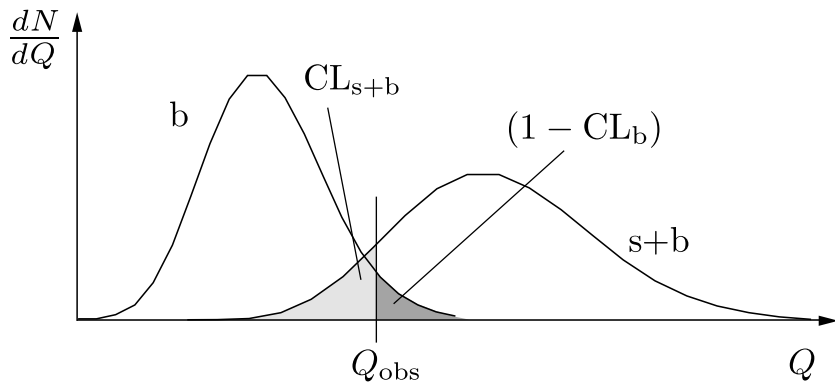


Figure 5.11: Illustration of the  $\text{CL}_{s+b}$  and  $\text{CL}_b$  quantities. The curves represent the distributions of the test-statistic  $Q$  for the background only ( $b$ ) and the signal+background ( $s+b$ ) hypotheses.

We then consider the probability that  $Q$  be smaller than the test-statistic  $Q^{\text{obs}}$  computed from the observations

$$\text{CL}_{s+b} = \text{Prob}(Q \leq Q^{\text{obs}})_{s+b} = \int_{-\infty}^{Q^{\text{obs}}} \frac{1}{N_{s+b}} \frac{dN_{s+b}}{dQ} dQ \quad (5.4)$$

where  $\frac{1}{N_{s+b}} \frac{dN_{s+b}}{dQ}$  is the probability distribution of  $Q$  for signal+background hypothesis, as illustrated in Fig. 5.11. In practice, this integral is computed using a Monte Carlo method

$$\text{CL}_{s+b} = \sum_{d'_i \mid Q(d'_i) \leq Q^{\text{obs}}} \prod_{i=1}^n f(d'_i, s_i + b_i),$$

where the sum runs over all the possible outcomes  $d'_i$  yielding a test-statistic  $Q(d'_i)$  smaller than  $Q^{\text{obs}}$ . Small values of  $\text{CL}_{s+b}$  indicate poor compatibility with the signal+background hypothesis and favour the background hypothesis, as illustrated in Fig. 5.11.

Similarly, one defines

$$\text{CL}_b = \text{Prob}(Q \leq Q^{\text{obs}})_b = \sum_{d'_i \mid Q(d'_i) \leq Q^{\text{obs}}} \prod_{i=1}^n f(d'_i, b_i) \quad (5.5)$$

for the background hypothesis. Values of  $\text{CL}_b$  very close to one indicate poor compatibility with the background and favour the signal+background hypothesis, as illustrated in Fig. 5.11.

$\text{CL}_b$  is used to quantify the confidence of a potential discovery, as it expresses the probability that background processes would lead to a value of  $Q$  smaller than the observed one. In the next section, when assessing LHCb discovery potential for the  $B_s^0 \rightarrow \mu^+ \mu^-$  decay, we will use  $\text{CL}_b$  as confidence level. A discovery with a significance of  $5\sigma$  ( $3\sigma$ ) will be claimed if

$$1 - \text{CL}_b < \alpha = 5.7 \cdot 10^{-7} \quad (\alpha = 2.7 \cdot 10^{-3} \text{ for } 3\sigma), \quad (5.6)$$

where  $\alpha$  is the area of the tail outside a  $\pm 5\sigma$  ( $\pm 3\sigma$ ) interval centred on the mean of a Gaussian distribution [10]. However, the use of  $(1 - \text{CL}_{s+b})$  to quote exclusion limits is not satisfactory, since it has the disturbing property that if too few occurrences are observed to account for the

expected background, then any signal as tiny as possible, can be excluded with a high confidence level. The Modified Frequentist confidence level

$$CL_s = \frac{CL_{s+b}}{CL_b} \quad (5.7)$$

is brought into play to improve the situation. It allows a sensible exclusion limit for the signal even if the observation is so low that the background hypothesis is called into question. Although  $CL_s$  is not a confidence level — but rather a ratio of confidence levels —, the signal hypothesis will be excluded at 90 % C.L. if

$$1 - CL_s \leq 90\%. \quad (5.8)$$

### 5.7.2 Input and Assumptions

**Geometrical Likelihood (GL)** On the data the GL will be calibrated using  $B_{(s)}^0 \rightarrow h^+h^-$  events as explained in Section 5.4.3. For this sensitivity study, we use the Monte Carlo probability density functions (p.d.f.) of the GL for both signal and background. We define four GL bins with boundaries at 0, 0.25, 0.5, 0.65 and 1. Note that while the GL was defined on Monte Carlo signal and background samples simulated for an instantaneous luminosity of  $2 \times 10^{32} \text{ cm}^{-2} \text{ s}^{-1}$ , we use another set of samples for this study. It is performed on Monte Carlo simulation generated at higher instantaneous luminosity of  $5 \times 10^{32} \text{ cm}^{-2} \text{ s}^{-1}$  for both the signal and the dimuon background. The increase in luminosity directly affects the event track multiplicity, affecting in turn the muon isolation variables and favouring the combinatorial background. The use a GL on samples different from those defining it constitutes a test of the GL robustness against the differences between Monte Carlo and real data, since it is foreseen to use initially a Monte Carlo defined GL, as explained in Section 5.4.3.

**Invariant Mass** The  $120 \text{ MeV}/c^2$  mass range of the tight mass window is divided in five bins, limited by the 5309.6, 5331.5, 5353.4, 5384.1, 5406.6 and  $5429.6 \text{ MeV}/c^2$  mass values<sup>7</sup>. With real data the signal p.d.f. for the invariant mass will be obtained from the  $B_s^0 \rightarrow K^+K^-$  channel, whereas the background one will come from the  $B_s^0 \rightarrow \mu^+\mu^-$  candidates in the mass sidebands. However, in the frame of this study, we use the distributions from the Monte Carlo samples.

Note that while the signal does not suffer from lack of statistics in Monte Carlo, the dimuon background does. To artificially increase the dimuon sample, one takes advantage of the absence of correlation between the reconstructed  $B_s^0$  mass and the other variables considered, and reassign a  $B_s^0$  mass value chosen in the tight mass windows to each event. This operation results in the multiplication of the equivalent statistics by a the ratio of the number of background event in the large mass window over those in the tight mass window, which is of the order of 10. Note that the background will certainly not be statistically limited once we collect data. The effective sizes of the Monte Carlo samples are  $1223 \text{ fb}^{-1}$  and  $0.04 \text{ fb}^{-1}$  for the signal and the background, respectively.

<sup>7</sup>This binning choice is related to the mass calibration procedure using  $B_s^0 \rightarrow K^+K^-$  decays as explained in Section 5.5. The central bin was chosen to be  $2\frac{\sigma_M}{\sqrt{2}}$  wide and centred on the mean of the  $B_s^0 \rightarrow K^+K^-$  mass distribution. The  $B_s^0 \rightarrow K^+K^-$  mass mean value obtained in the calibration process was slightly larger than the nominal  $B_s^0$  mass (by about  $2.5 \text{ MeV}/c^2$ ) and the resolution was found to be  $\sigma_M = 21.5 \text{ MeV}/c^2$ . The remaining intervals on either side of the central bin were each split in two bins meant to be of equal width in absence of a typo. This particular choice is not the most meaningful and will be made more aesthetic.

**Muon Identification** In the context of this Monte Carlo study, since the background considered is composed of events with real muons as final states, the muon identification would not help to discriminate the latter from signal. Consequently, the description below differs from what will be done with real data. However, it is foreseen to use the muon identification on data and including this information does not represent any difficulty and does not change the procedure. Actually, one of the advantages of the proposed procedure is the ease to add information — through the addition of bins as additional single search-channels — and therefore to combine data acquired under different conditions or even coming from different experiments. The understanding and the calibration of the muon identification is a non-trivial task, and was mentioned in Section 5.6.

The binning of the GL and the mass described above results in 20 bins — a total of 60 bins is foreseen when the muon identification variable will also be used.

**Annual yields** The signal and background yields for an integrated luminosity of  $2 \text{ fb}^{-1}$ , corresponding to one effective year ( $t = 10^7 \text{ s}$ ) of data-taking at the nominal luminosity of  $\mathcal{L} = 2 \times 10^{32} \text{ cm}^{-2} \text{ s}^{-1}$ , are used to normalise the samples.

The signal yield  $\mathcal{Y}_{\text{signal}}$  is a function of the  $b\bar{b}$  cross section  $\sigma_{b\bar{b}}$ , the probability for a  $b$  quark to hadronise into a  $B_s^0$  meson  $f_s$ , the  $B_s^0 \rightarrow \mu^+ \mu^-$  branching fraction, the selection efficiency (considering the tight  $\pm 60 \text{ MeV}/c^2$  mass window), and the trigger ( $\text{L0} \times \text{HLT1} \times \text{HLT2}$ ) and reconstruction efficiencies:

$$\begin{aligned}\mathcal{Y}_{\text{signal}} &= 2 \times \mathcal{L}_{\text{int}} \times \sigma_{b\bar{b}} \times f_s \times \epsilon^{\text{rec}} \times \epsilon^{\text{sel|rec}} \times \epsilon^{\text{trig|sel}} \times \mathcal{B}(B_s^0 \rightarrow \mu^+ \mu^-) \\ &= 2 \times 2 \times (5 \times 10^{11}) \times 0.1 \times 0.116 \times 0.577 \times 0.94 \times \mathcal{B}(B_s^0 \rightarrow \mu^+ \mu^-).\end{aligned}$$

For example, assuming the SM prediction  $\mathcal{B}(B_s^0 \rightarrow \mu^+ \mu^-) = 3.35 \times 10^{-9}$  one gets  $\mathcal{Y}_{\text{signal}} = 42.15$  events.

For the background, we compute the yield from the number of reconstructed, selected and L0 triggered events; it reads

$$\begin{aligned}\mathcal{Y}_{\text{dimuon}} &= \mathcal{L}_{\text{int}} \times \sigma_{b\bar{b}} \times \epsilon_{\text{dimuon}}^\theta \times (\epsilon^{\text{rec}} \times \epsilon^{\text{sel|rec}}) \times \epsilon^{\text{trig|sel}} \\ &= 2 \times (5 \times 10^{11}) \times 0.00996 \times (1.09 \times 10^{-5}) \times 0.9 \\ &= 97707 \text{ events.}\end{aligned}$$

**Normalisation** In the frame of this Monte Carlo study, we do not use the normalisation procedure required with data and detailed in Appendix A.1.

### 5.7.3 Toy Monte Carlo Method

To assess the analysis sensitivity, one uses toy Monte Carlo experiments. These need probability density functions (p.d.f.) as input, which are determined separately for signal and background using the full Monte Carlo samples.

Since we have a large number of Monte Carlo signal events, we use the normalised two-dimensional histogram — with the four GL and five mass bins defined above — to get the signal probability in each bin. For the dimuon background, we get the binned mass and GL p.d.f. from the Monte Carlo sample and we convolute them. However, even after the artificial multiplication of the equivalent statistics of the dimuon background sample mentioned above, this study still

suffers from limited statistics for the background, impeding its significance. Particularly, some bins may have no — or insignificant low — background expectation, in which case any signal in the bin may get an artificially high weight. To protect from an overestimation of the sensitivity due to poorly simulated background expectation, the background expectation in each bin is shifted to a larger value. First, the content of each bin is shifted to its 90 % upper limit assuming a Poisson law. Then all bins are scaled by a common factor such that there is a 90 % probability that the initial number of background events in the  $GL > 0.5$  region be smaller than the number of background events after the operation in the same region, assuming a Poisson distribution. This operation leaves no bins without background expectation, smoothing the dimuon Monte Carlo joint p.d.f.

For each integrated luminosity,  $\mathcal{L}_{\text{int}}$ , a range of branching fraction hypotheses is scanned, from a small to a large branching fraction, until the significance condition is met on either  $\text{CL}_b$  or  $\text{CL}_s$  defined in Eqs (5.6) and (5.8). In the following paragraphs, we describe the process, schematised in Fig. 5.12, for a given integrated luminosity.

The integrated luminosity is used to compute the total number of expected background events. This number is fluctuated by a Poisson random draw, to get  $b_{\text{tot}}^{\text{obs}}$ . The integrated luminosity and the branching fraction hypothesis are used to compute the total number of expected signal events. This number is also Poisson fluctuated, yielding  $s_{\text{tot}}^{\text{obs}}$ . Then, the binned p.d.f.s of the mass and GL, for the signal and background are used to perform two multinomial random draws yielding  $s_i^{\text{obs}}$  and  $b_i^{\text{obs}}$  in each bin  $i$ , respectively, and such that  $s_{\text{tot}}^{\text{obs}} = \sum s_i^{\text{obs}}$  and  $b_{\text{tot}}^{\text{obs}} = \sum b_i^{\text{obs}}$ . In each bin,  $s_i^{\text{obs}}$  and  $b_i^{\text{obs}}$  are added to get the number of observed events  $d_i^{\text{obs}}$ , which is the result of this toy experiment. When assessing the exclusion potential, we assume that only background is observed, and thus the toy experiment described above yields  $d_i^{\text{obs}} = b_i^{\text{obs}}$ .

These numbers  $d_i^{\text{obs}}$ , together with the expected numbers  $s_i$  and  $b_i$  of signal and background events depending on the luminosity and branching fraction (for the signal), are used to compute  $\text{CL}_b$ , as described in Section 5.7.1 and using the code of Ref. [222]. In case of exclusion, the  $\text{CL}_s$  is computed. The obtained  $\text{CL}_b$  is compared to the condition for a  $3\sigma$  significant evidence defined in Eq. (5.6). If the condition is not met, the branching fraction hypothesis is increased and a new toy experiment is run. Because an increase of signal translates into a better separation of the background and signal+background hypotheses, one gets closer to the condition on  $\text{CL}_b$  at each branching fraction increase. Upon reaching the condition, the branching fraction is recorded and the whole process is repeated for another integrated luminosity. In the case of 90 % C.L. exclusion, the condition is rather that defined in Eq. (5.8) but the rest of the process is identical.

The whole sequence is repeated forty times, and their results averaged, to get the figure quoted in the next section.

#### 5.7.4 Results

Unless the branching fraction of the  $B_s^0 \rightarrow \mu^+\mu^-$  decay is strongly enhanced, the first result will be an exclusion limit. Consequently, the LHCb exclusion potential for  $B_s^0 \rightarrow \mu^+\mu^-$  was computed not only for the nominal condition of  $\sqrt{s} = 14$  TeV but also for  $\sqrt{s} = 7$  TeV collisions, foreseen for the 18-months long run to start in Spring 2010<sup>8</sup>. This energy condition translates

---

<sup>8</sup>To quote Niels Bohr, prediction is very difficult, especially about the future. Prediction about the future of the LHC is even more difficult. This information is only estimate from the LHC Operation Group leader, dated January 2010 and collected in Ref. [226].

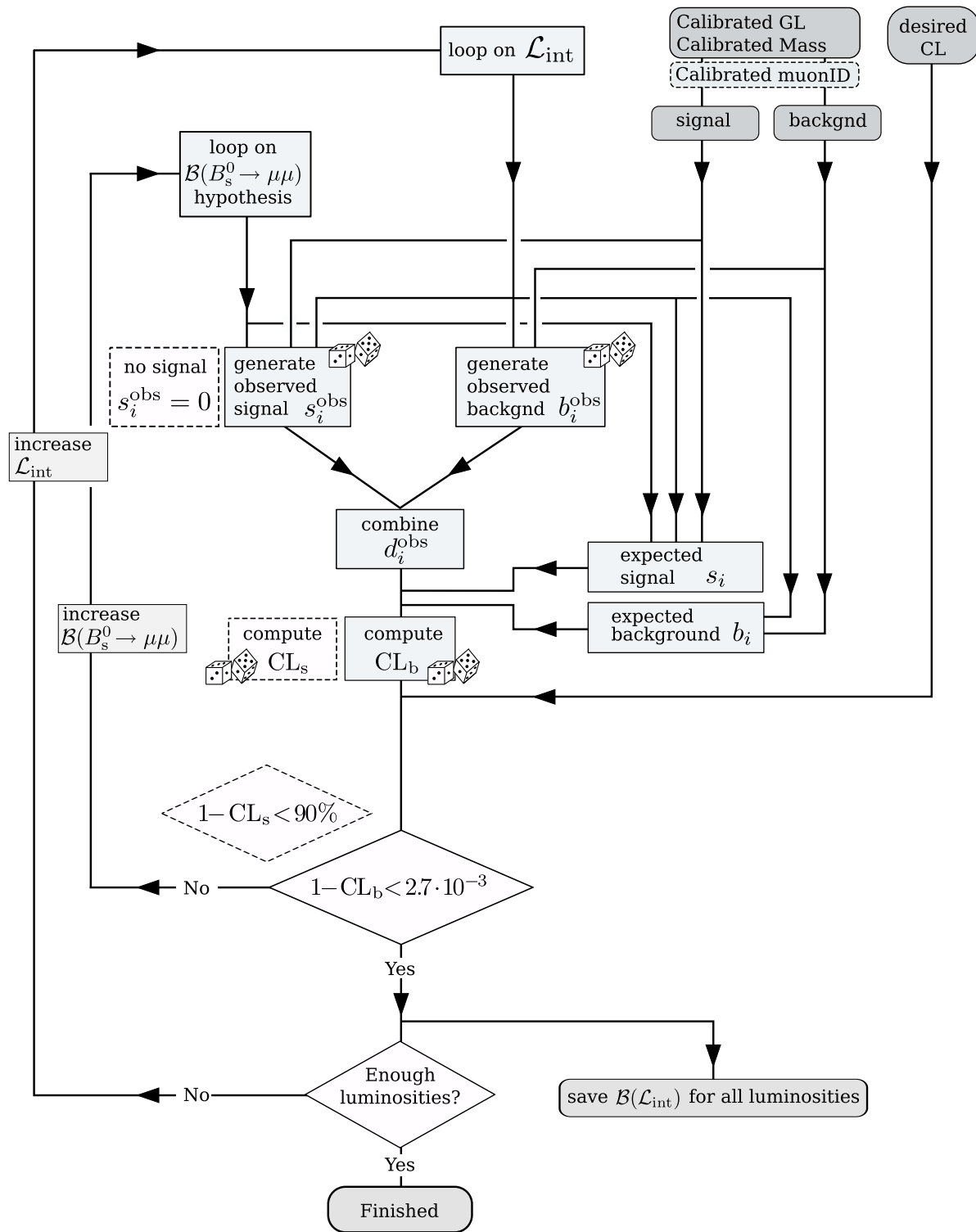


Figure 5.12: Flow-chart of the sensitivity study. For a given integrated luminosity and branching fraction hypothesis, one computes the expected numbers of signal and background events from the mass and GL p.d.f.s. In parallel, one performs a toy Monte Carlo experiment whose yield is compared to the expected numbers. The compatibility of the toy experiment outcome to the expected outcome is assessed in terms of  $\text{CL}_b$  or  $\text{CL}_s$  in the case of exclusion study. If the compatibility is not sufficient, new pseudo-experiments are conducted with growing branching fraction hypothesis, until the required compatibility level is reached.

into

$$\sigma_{b\bar{b}}^{7\text{ TeV}} = \sigma_{b\bar{b}}^{14\text{ TeV}} \times \frac{\sigma_{b\bar{b}}^{\text{PY}, 7\text{ TeV}}}{\sigma_{b\bar{b}}^{\text{PY}, 14\text{ TeV}}} = 218\text{ }\mu\text{b}$$

where we assume  $\sigma_{b\bar{b}}^{14\text{ TeV}} = 500\text{ }\mu\text{b}$  and where  $\sigma_{b\bar{b}}^{\text{PY}}$  are the values given by PYTHIA 6.418 and collected in Ref. [227]. Note that by doing so we neglect some aspects. The effect of the change in  $B$  phase space which in turn affects the number of decays fully contained within the detector acceptance is neglected. We also assume that the background production scales with the  $b\bar{b}$  production, which is not unjustified since the dominant background consists of muons from  $B$  decays. Since the instantaneous luminosity will be below LHCb nominal luminosity, and since the bunch crossing frequency will increase only step by step to the nominal figure of 25 ns, LHCb will relax its requirement in terms of the number of pile-up events accepted. The effects of the low instantaneous luminosity and of the increase of the number of triggered events with multiple interactions are assumed to compensate each other such that the combinatorics does not change.

Figure 5.13 shows the expected 90 % C.L. upper limit on the branching fraction in the absence of signal, as a function of the integrated luminosity for the conditions expected for the 2010–2011 physics run detailed above. The blue filled region corresponds to the exclusion potential using the alternate analysis, while the red shaded region corresponds to that of the standard analysis. Each band is centred on the mean of the branching fraction limits computed at a given integrated luminosity by the toy Monte Carlo experiments, as explained in Section 5.7.3, and its half-width is equal to their standard deviation. The exclusion potential with  $\sqrt{s} = 14\text{ TeV}$  for both analyses is shown in Fig. 5.14 for an integrated luminosity up to  $2\text{ fb}^{-1}$  corresponding to one year of data-taking at nominal conditions. Those figures show that the analyses yield compatible sensitivities, with the alternate analysis systematically slightly less sensitive.

In case a signal is measured, the branching fraction for which a  $5\sigma$  discovery (or a  $3\sigma$  evidence) is expected is shown in Fig. 5.15 as a function of the integrated luminosity and for  $pp$  collisions at  $\sqrt{s} = 14\text{ TeV}$ . The integrated luminosity axis extends up to  $10\text{ fb}^{-1}$  which corresponds to five years of data taking at LHCb nominal conditions. The expectation obtained by the alternate analysis is shown in blue and that obtained by the standard analysis is shown in a red shade. Although slightly degraded, the sensitivity of the alternate analysis is again compatible with that of the standard analysis.

We split the discussion into two parts, first we compare the sensitivity of the alternate analysis to that of the standard one and draw some conclusions from that comparison. Secondly, we discuss the LHCb exclusion and observation sensitivities to the  $B_s^0 \rightarrow \mu^+\mu^-$  branching fraction in absolute terms.

Assuming the error estimates given by the LHCb tracking are correct, the substitution of variables using significances by variables which avoid their use leads to a slight degradation of the sensitivity. This degradation is expected since less information is used to discriminate signal from background. However, if the LHCb detector proves to be difficult to understand and if its calibration extends over a long period, then the alternate analysis would be a valuable alternative to the standard analysis.

Reversing the point of view, the comparison of the two analyses is also an assessment of the degree to which the standard analysis relies on error estimates. Since the two analyses differ only by the use or not of significances, the compatibility between the two analyses, as observed in Figs 5.14 and 5.15, proves that the use of error estimates does not enhance much the sensitivity.

Preliminary studies of the first data taken in 2009 have triggered a considerable work on both the tuning of the Monte Carlo and the tracking and reconstruction algorithms. Currently, the

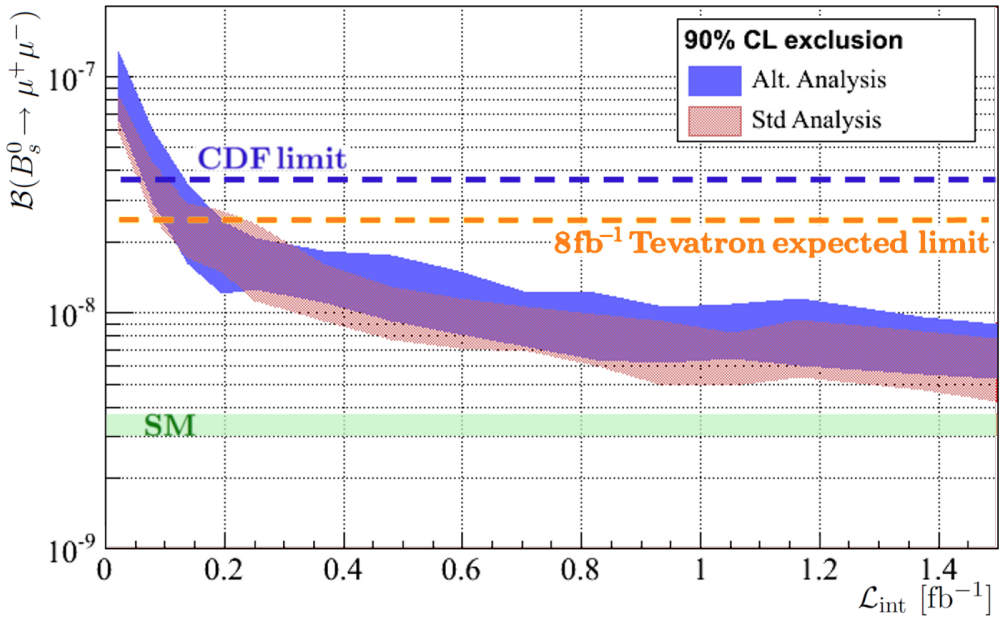


Figure 5.13: Expected 90% CL upper limit on  $\mathcal{B}(B_s^0 \rightarrow \mu^+\mu^-)$  in absence of signal as a function of the integrated luminosity for  $\sqrt{s} = 7$  TeV collisions, as expected for the 2010-2011 long run. The blue filled region is the result of the alternate analysis, and the red shaded region is the result of the standard analysis. The meaning of the bands is detailed in the text. The background estimate has conservatively been set to its 90% CL upper limit. The current limit [92], together with the expected Tevatron final limit are indicated in blue and orange, respectively. The SM prediction [88] is drawn in light green.

imperfect alignment of the tracking detectors is still impeding the resolution of tracking-related parameter, which show deviation with respect to the Monte Carlo. A large improvement is expected with the data to come. In this unclear situation, the existence of a alternate analysis is an asset.

In any case, the alternate analysis represents a welcome cross-check and consistency test for the standard analysis. Two compatible results, even if they are not completely independent, are more comfortable to defend and certainly bring a gain of confidence.

Figure 5.13 shows that in the conditions expected for the 2010-2011 long run, LHCb will compete with the Tevatron with approximately  $100 \text{ pb}^{-1}$  of data and overtake its expected limit at  $8 \text{ fb}^{-1}$  of data collected<sup>9</sup> with less than  $300 \text{ pb}^{-1}$ . In the LHCb nominal condition, and in absence of signal, the  $B_s^0 \rightarrow \mu^+\mu^-$  branching fraction can be excluded to the level of the SM with just more than  $2 \text{ fb}^{-1}$ . In such a situation, New Physics models with a large value of  $\tan\beta$  would be ruled out, or at the very least strongly constrained.

In the case of signal present at the level predicted by the SM, approximately  $3 \text{ fb}^{-1}$  are enough for a  $3\sigma$  observation, while a  $5\sigma$  discovery will need approximately  $10 \text{ fb}^{-1}$ . If any enhancement of the  $B_s^0 \rightarrow \mu^+\mu^-$  branching fraction driven by New Physics exists, it will be observed sooner and particularly, if its value is as high as  $2 \times 10^{-8}$ , as predicted within MSSM with non-universal Higgs masses [112] (see Section 1.4.6), a  $5\sigma$  discovery is possible with as little as  $400 \text{ pb}^{-1}$  of data in the 2010 conditions.

<sup>9</sup>The expected combined limit from the Tevatron is obtained by extrapolating the latest limit [92] based on  $3.7 \text{ fb}^{-1}$  to a total integrated luminosity of  $8 \text{ fb}^{-1}$  per experiment, giving  $\mathcal{B}(B_s^0 \rightarrow \mu^+\mu^-) < 24 \times 10^{-9}$  at 90 % C.L.

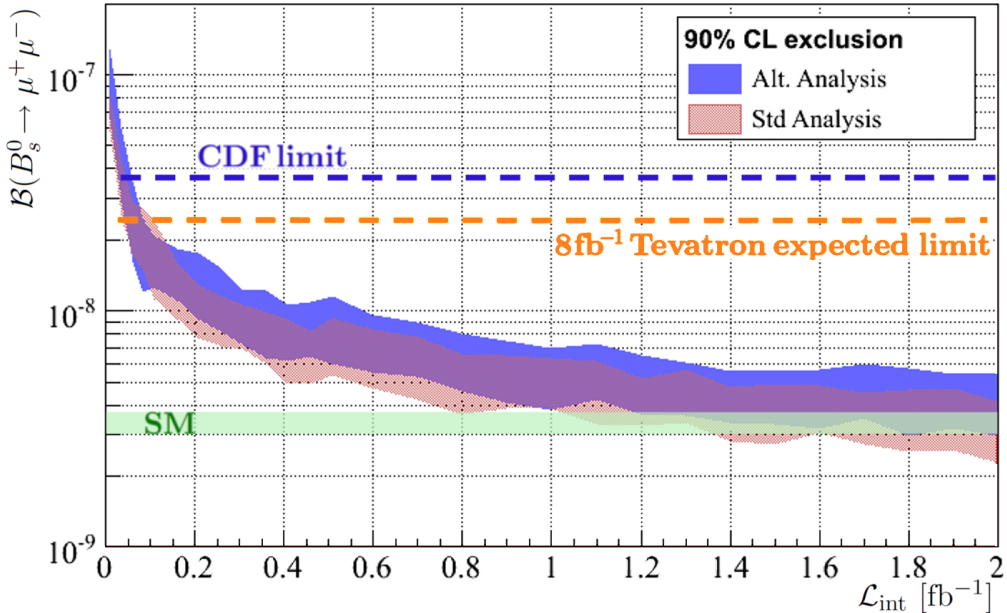


Figure 5.14: Expected 90% CL upper limit on  $\mathcal{B}(B_s^0 \rightarrow \mu^+ \mu^-)$  in absence of signal as a function of the integrated luminosity for the nominal condition of  $\sqrt{s} = 14$  TeV. The blue filled region is the result of the alternate analysis, and the red shaded region is the result of the standard analysis. The meaning of the bands is detailed in the text. The background estimate has conservatively been set to its 90% CL upper limit. The current limit [92], together with the expected Tevatron final limit are indicated in blue and orange, respectively. The SM prediction [88] is drawn in light green.

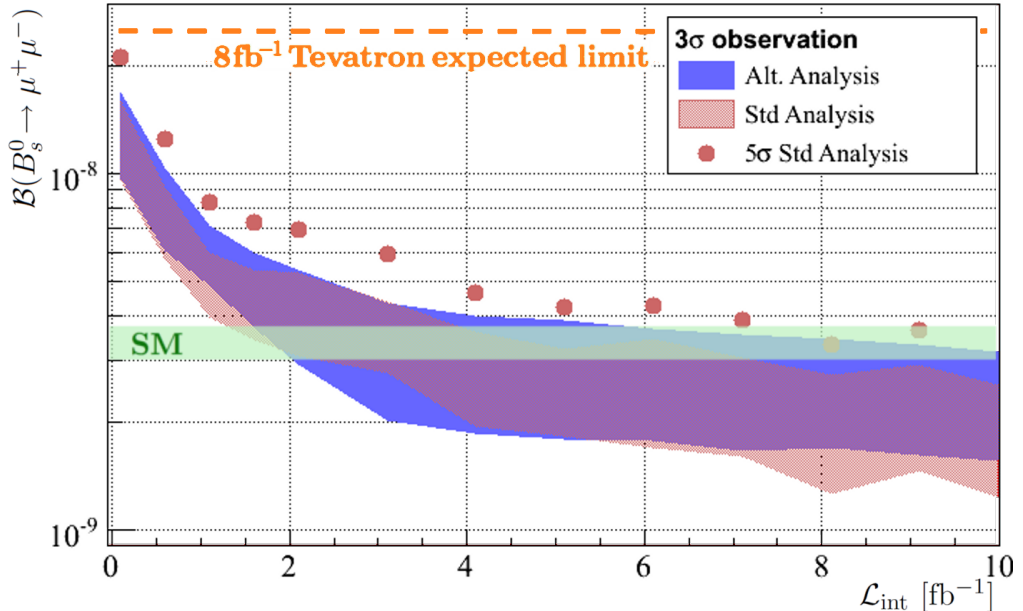


Figure 5.15: Branching fraction of the  $B_s^0 \rightarrow \mu^+ \mu^-$  decay at which a 5 $\sigma$  discovery (points) or a 3 $\sigma$  evidence is expected for 14 TeV collisions as a function of the integrated luminosity. The blue filled region is the result of the alternate analysis, and the red shaded region is the result of the standard analysis. The meaning of the bands is detailed in the text. The background estimate has conservatively been set to its 90% CL upper limit. The expected Tevatron final limit, extrapolating the current result [92], is indicated in orange. The SM prediction [88] is drawn in light green.



# Conclusion

This thesis covers different aspects of a scientific experiment, reflecting my contribution to the LHCb. An experiment of the size of LHCb possesses a time scale hardly compatible with that of a PhD thesis. LHCb has been formally proposed in 1995 [228], after which a period of extensive R&D preceded the construction of the subdetectors. LHCb has just started its data acquisition phase at the end of 2009. I was fortunate to join the collaboration at a very interesting time, which allowed me to participate in the construction of the experiment and to prepare for data analysis. But for an inter-magnet electrical connection *soldered* without soldering alloy [134], I could even have analysed data. The important aspects of this work are briefly reviewed hereafter.

I was heavily involved in the construction of the LHCb Inner Tracker, a silicon microstrip detector covering the innermost region of the detector acceptance. After taking responsibilities for the production of the detector modules, I assembled a detector box prototype where every single element — but the container — required either design adjustments or a complete redesign. I then led the assembly of the twelve Inner Tracker detector boxes that are now integrated in LHCb. The Inner Tracker has been software aligned, using data from LHC injection test down to a precision of  $19\,\mu\text{m}$ . The fine alignment using collision data is ongoing and will certainly lower this figure. Thanks to the careful assembly and to the quality checks along this procedure, the Inner Tracker is in very good shape and presents less than 1% of dead or very noisy strips. Proton-proton collisions have occurred in the LHC for the first time at the end of 2009. Upon declaration of stable beam the fragile silicon sensors of the Inner Tracker were powered and performed as expected.

In preparation for the analysis of the data to be recorded soon, I was particularly interested in the search of the  $B_s^0 \rightarrow \mu^+\mu^-$  decay. A measurement of the branching fraction of, or the strengthening of the constraints on this yet unobserved decay is awaited by the HEP community. Indeed it is of great interest in the indirect search for Physics beyond the Standard Model (SM). In models characterised by a large value of  $\tan\beta$  the branching fraction of the  $B_s^0 \rightarrow \mu^+\mu^-$  decay can be considerably enhanced with respect to its very precise prediction within the SM, making its measurement a double-edged result. Either the branching fraction is measured at a level incompatible with the SM prediction, and New Physics is discovered, or no enhancement is revealed and models with large  $\tan\beta$  are ruled out.

In that context, I prepared an alternate analysis for the  $B_s^0 \rightarrow \mu^+\mu^-$  decay search at LHCb. I studied the sensitivity of LHCb to the search of  $B_s^0 \rightarrow \mu^+\mu^-$  in the frame of the analysis previously developed within the LHCb collaboration, and in that of an alternate analysis, based on a different set of variables, meant to be less sensitive to an imperfectly understood detector. I showed that this alternate analysis, while slightly less sensitive than the standard analysis, constitutes a valuable choice and can provide a second result, bringing a gain of confidence. With this option, the LHCb collaboration is prepared for the unfortunate case where the LHCb detector would prove to be difficult to understand. The LHCb sensitivity to the exclusion of the  $B_s^0 \rightarrow \mu^+\mu^-$  branching fraction is expected to overtake the Tevatron limit already in 2010 and approximately  $3\,\text{fb}^{-1}$  of data are enough for a  $3\sigma$  evidence of an SM signal.



## Appendix A

# Normalisation, Trigger and Reconstruction Efficiencies

### A.1 Normalisation

The branching fraction of the  $B_s^0 \rightarrow \mu^+ \mu^-$  decay can be written as the ratio of the number of  $B_s^0$  mesons decaying into  $\mu^+ \mu^-$  final states over the total number of  $B_s^0$  produced:

$$\mathcal{B}(B_s^0 \rightarrow \mu^+ \mu^-) = \frac{\mathcal{N}(B_s^0 \rightarrow \mu^+ \mu^-)}{\mathcal{N}(B_s^0)} = \frac{\mathcal{N}^{\text{obs}}}{2 \times \sigma_{b\bar{b}} \times \mathcal{L}_{\text{int}} \times f_s \times \epsilon} \quad (\text{A.1})$$

Since no experimental setup is perfectly efficient, the observed quantity is in fact  $\mathcal{N}^{\text{obs}} = \epsilon \times \mathcal{N}(B_s^0 \rightarrow \mu^+ \mu^-)$  with  $\epsilon$  the total experimental efficiency. In the denominator, one explicits the number of  $B_s^0$  mesons produced as  $2 \times \sigma_{b\bar{b}} \times \mathcal{L}_{\text{int}} \times f_s$  where  $\sigma_{b\bar{b}}$  is the  $b\bar{b}$  pair production cross section in  $pp$  collisions,  $\mathcal{L}_{\text{int}}$  is the integrated luminosity,  $f_s$  is the probability for a  $b$  ( $\bar{b}$ ) quark to form a  $\bar{B}_s^0$  ( $B_s^0$ ) meson (after hadronisation and decay of strong resonances) and the factor 2 is present because this analysis is equivalent for  $B_s^0$  and  $\bar{B}_s^0$  mesons.

Since  $\sigma_{b\bar{b}}$  is not precisely known, the number of  $B_s^0$  mesons produced is not known either. Thus a normalisation channel is needed in order to access this information. Hence, by counting the number of events,  $\mathcal{N}_{\text{norm}}^{\text{obs}}$ , of a process with a known branching fraction  $\mathcal{B}_{\text{norm}}$ , one can deduce the number of produced  $b\bar{b}$  pairs:

$$2 \times \sigma_{b\bar{b}} \times \mathcal{L}_{\text{int}} = \frac{\mathcal{N}_{\text{norm}}^{\text{obs}}}{\mathcal{B}_{\text{norm}} \times f_{\text{norm}} \times \epsilon_{\text{norm}}} \quad (\text{A.2})$$

Together, Eqs (A.1) and (A.2) give:

$$\mathcal{B}(B_s^0 \rightarrow \mu^+ \mu^-) = \mathcal{B}_{\text{norm}} \times \frac{f_{\text{norm}}}{f_s} \times \frac{\epsilon_{\text{norm}}^{\text{rec}} \epsilon_{\text{norm}}^{\text{sel|rec}} \epsilon_{\text{norm}}^{\text{trig|sel}}}{\epsilon_{B_s^0 \rightarrow \mu^+ \mu^-}^{\text{rec}} \epsilon_{B_s^0 \rightarrow \mu^+ \mu^-}^{\text{sel|rec}} \epsilon_{B_s^0 \rightarrow \mu^+ \mu^-}^{\text{trig|sel}}} \times \frac{\mathcal{N}_{B_s^0 \rightarrow \mu^+ \mu^-}^{\text{obs}}}{\mathcal{N}_{\text{norm}}^{\text{obs}}} \quad (\text{A.3})$$

The quantities  $\mathcal{N}_{B_s^0 \rightarrow \mu^+ \mu^-}^{\text{obs}}$  and  $\mathcal{N}_{\text{norm}}^{\text{obs}}$  will be measured in LHCb, while  $\mathcal{B}_{\text{norm}}$  and  $\frac{f_{\text{norm}}}{f_s}$  were measured in previous experiments. The total efficiency  $\epsilon$  is factorised as  $\epsilon = \epsilon^{\text{rec}} \times \epsilon^{\text{sel|rec}} \times \epsilon^{\text{trig|sel}}$ , where

Table A.1: Possible normalisation channels, with their current branching fraction experimental values [10] and the product of the branching fraction and hadronisation ratio. To ease comparison, relative errors are also tabulated. In the case of  $B^+ \rightarrow J/\psi(\mu\mu)K^+$ , the sub-decay  $J/\psi \rightarrow \mu^+\mu^-$  is included.

Channel	$\mathcal{B}_{\text{norm}}$	$\mathcal{B}_{\text{norm}} \times \frac{f_{\text{norm}}}{f_s}$
$B^0 \rightarrow K^+\pi^-$	$(1.94 \pm 0.06) \times 10^{-5}$	$\pm 3.0\%$ $(7.18 \pm 0.92) \times 10^{-5}$ $\pm 12.8\%$
$B^+ \rightarrow J/\psi(\mu\mu)K^+$	$(6.06 \pm 0.21) \times 10^{-5}$	$\pm 3.6\%$ $(2.24 \pm 0.29) \times 10^{-4}$ $\pm 12.9\%$
$B^0 \rightarrow \pi^+\pi^-$	$(5.13 \pm 0.24) \times 10^{-6}$	$\pm 4.7\%$ $(1.90 \pm 0.25) \times 10^{-5}$ $\pm 13.3\%$
$B_s^0 \rightarrow D_s^-\pi^+$	$(3.67 \pm 0.73) \times 10^{-5}$	$\pm 20\%$ $(3.67 \pm 0.73) \times 10^{-5}$ $\pm 20\%$

$\epsilon^{\text{rec}}$  is the efficiency to reconstruct all the tracks relevant to the channel considered; this factor includes the effect of the limited detector acceptance and the effect of the IsMuon requirement for each of the two final states (see Section 5.6),

$\epsilon^{\text{sel|rec}}$  is the efficiency to select events after their reconstruction, and

$\epsilon^{\text{trig|sel}}$  is the efficiency of the trigger on reconstructed and selected events.

An ideal normalisation channel would have the following properties:

- It should have a rather high branching fraction with respect to the signal for one cannot afford to be statistically limited by the normalisation channel.
- Its branching fraction should be precisely known, since this value is used directly in Eq. (A.3). This requirement concurs with the previous one, since it is likely that the branching fraction of a relatively abundant decay channel would be measured rather accurately.
- The uncertainty attached to the  $\frac{f_{B^+}}{f_s} = \frac{f_{B^0}}{f_s}$  ratio is  $\approx 13\%$  [99], using LEP and Tevatron measurements. Note that the hadronisation probabilities may depend on the energy and that there is no measurement of  $f_s$  at 14 TeV, hence the quoted uncertainty is only an approximation. To cancel the  $\frac{f_{\text{norm}}}{f_s}$  ratio by the use of a  $B_s^0$  decay as normalisation channel is therefore very interesting. However the idea does not work in the (rather frequent) case where a ratio of hadronisation probabilities was used to get the absolute branching fraction of the considered  $B_s^0$  decay mode. Actually, the product whose uncertainty should be considered when assessing normalisation possibilities is  $\mathcal{B}_{\text{norm}} \times \frac{f_{\text{norm}}}{f_s}$ , as reported in Table A.1.
- Finally, the normalisation and signal channels should have similar properties in order to minimise the Monte Carlo dependence of the efficiency ratio in Eq. (A.3).

The channels being considered for the normalisation are listed in Table A.1, together with their branching fraction. Those are:

$B^+ \rightarrow J/\psi(\mu\mu)K^+$  has a rather large branching fraction. The two muons in the final state are very interesting trigger-wise. The difference in the reconstruction efficiency  $\epsilon^{\text{rec}}$  between  $B_s^0 \rightarrow \mu^+\mu^-$  and  $B^+ \rightarrow J/\psi(\mu\mu)K^+$  mainly lies in the extra  $K^+$  track to reconstruct and also to a lesser extent in the difference of phase space of the muon pairs.

$B^0 \rightarrow K^+\pi^-$  has also a fairly large branching fraction. The main difference with respect to the signal comes from the trigger and the particle identification.

$B^0 \rightarrow \pi^+ \pi^-$  was considered but not retained due to its smaller branching fraction.

$B_s^0 \rightarrow D_s^- \pi^+$  was recently measured at Belle [229] with a 20% uncertainties dominated by systematics, and specially by the uncertainty on  $f_s^{\Upsilon(5S)}$ , the  $B_s^0$  fraction at the  $\Upsilon(5S)$  resonance. However, there are prospects to refine the knowledge on  $f_s^{\Upsilon(5S)}$  [230], which could lead to an uncertainty on  $\mathcal{B}(B_s^0 \rightarrow D_s^- \pi^+)$  of the order of 10%, in which case this channel would become interesting for the  $B_s^0 \rightarrow \mu^+ \mu^-$  normalisation.

Two complementary normalisation channels were chosen for the  $B_s^0 \rightarrow \mu^+ \mu^-$  analysis,  $B^+ \rightarrow J/\psi K^+$  and  $B^0 \rightarrow K^+ \pi^-$ . While the former mainly differs from the signal by the reconstruction of the extra kaon track, the latter mainly differs because of the trigger and the particle identification. In Appendix A.2, the method developed to estimate the track reconstruction efficiency  $\epsilon^{\text{rec}}$  within the  $B_s^0 \rightarrow \mu^+ \mu^-$  working group is illustrated for the case of the  $B^+ \rightarrow J/\psi K^+$  decay. The ratio of trigger efficiencies  $\epsilon^{\text{trig|sel}}$  is addressed in Appendix A.3, while the ratio of  $\epsilon^{\text{sel|rec}}$  is discussed in Section 5.3.

## A.2 Reconstruction Efficiency

The estimation of the track reconstruction efficiency ratio between the normalisation and the  $B_s^0 \rightarrow \mu^+ \mu^-$  channels,  $\frac{\epsilon_{\text{norm}}^{\text{rec}}}{\epsilon_{\text{sig}}^{\text{rec}}}$ , as defined in Appendix A.1, is important for the normalisation. If the  $B^0 \rightarrow K^+ \pi^-$  decay channel is used as normalisation channel, the reconstruction efficiency ratio is expected to be close to one, except for the effect of material and of the muon acceptance. However, the situation is not obvious in case  $B^+ \rightarrow J/\psi K^+$  is used for the normalisation. The reconstruction of  $B^+ \rightarrow J/\psi K^+$  indeed differs from that of  $B_s^0 \rightarrow \mu^+ \mu^-$  because of the presence of an extra kaon track.

In the absence of real data, the track reconstruction efficiencies are hard to predict from Monte Carlo for several reasons. First, the track finding algorithms are sensitive to the occupancy of the tracking detectors, which depend on the multiplicity of the events. It is unlikely that an untuned Monte Carlo correctly estimates the track multiplicity.

Secondly, the probability to reconstruct a track depends on its momentum. The multiple scattering is indeed inversely proportional to the momentum, making the low momentum particle less efficiently reconstructed. Furthermore, particles with a very low momentum are subject to be driven out of the detector geometric acceptance by the magnetic field.

Thus, current Monte Carlo simulations, affected by our imperfect knowledge about the  $b$  hadron momentum spectrum and event multiplicity cannot reliably predict the track reconstruction efficiency. Therefore, the evaluation of the track reconstruction efficiency ratio should be obtained by the following methods:

- Monte Carlo simulation can be used after tuning using real data. In particular, the  $B$  momentum spectrum and the tracking detector occupancies should be tuned to reproduce the measurements with real data. This scenario, developed by the tracking experts, is not the first choice for the  $B_s^0 \rightarrow \mu^+ \mu^-$  analysis that ideally should not rely on MC simulation. Furthermore, the delay before the Monte Carlo is satisfactorily tuned may be too long for this method to be used for the first  $B_s^0 \rightarrow \mu^+ \mu^-$  result.
- The second method, avoiding the need to rely on Monte Carlo, consists in the assessment of the impact on the efficiency of the reconstruction of an extra track. The idea is that, with similar phase space, the reconstruction efficiency ratio between a two-body decay and

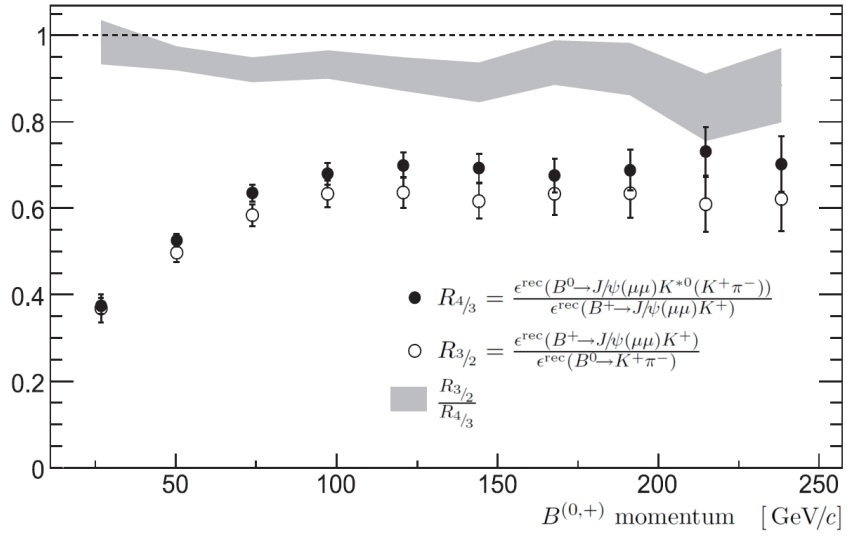


Figure A.1: Ratio of reconstruction efficiency between four- and three-body decays ( $R_{4/3}$ ), and between three- and two-body decays ( $R_{3/2}$ ), as a function of the  $B$  momentum. The double ratio,  $\frac{R_{3/2}}{R_{4/3}}$ , is shown as a greyed area. Modified from Ref. [72].

a three-body decay is close to the one between a three-body and four-body decay. This method is detailed hereafter.

The method is based on the assumption that the loss in reconstruction efficiency caused by the need to reconstruct three tracks instead of two is close to the loss caused by the reconstruction of four tracks instead of three. This assumption motivates the first equality of the following equation:

$$\frac{\epsilon_{\text{norm}}^{\text{rec}}}{\epsilon_{\text{sig}}^{\text{rec}}} \approx \frac{\epsilon_{\text{rec}}^{\text{rec}}|_{\text{4tracks}}}{\epsilon_{\text{rec}}^{\text{rec}}|_{\text{3tracks}}} \quad (\text{A.4})$$

$$\approx \frac{\epsilon_{\text{rec}}^{\text{rec}} \epsilon_{\text{sel}}^{\text{sel}} \epsilon_{\text{trig}}^{\text{trig}}|_{\text{4tracks}}}{\epsilon_{\text{rec}}^{\text{rec}} \epsilon_{\text{sel}}^{\text{sel}} \epsilon_{\text{trig}}^{\text{trig}}|_{\text{3tracks}}} \quad (\text{A.5})$$

$$\begin{aligned} &\approx \frac{2\sigma_{b\bar{b}} \mathcal{L}_{\text{int}} f_3 \mathcal{B}_3 \mathcal{N}_4^{\text{obs}}}{2\sigma_{b\bar{b}} \mathcal{L}_{\text{int}} f_4 \mathcal{B}_4 \mathcal{N}_3^{\text{obs}}} \\ &\approx \frac{\mathcal{B}_3 \mathcal{N}_4^{\text{obs}}}{\mathcal{B}_4 \mathcal{N}_3^{\text{obs}}} \end{aligned} \quad (\text{A.6})$$

where the 3 and 4 indices denote channels with three and four tracks respectively, and where  $f$ ,  $\mathcal{B}$  and  $\mathcal{N}^{\text{obs}}$  denote the hadronisation probability, the branching fraction and the number of observed event respectively. The second equality uses  $\epsilon_{\text{4tracks}}^{\text{sel}} = \epsilon_{\text{3tracks}}^{\text{sel}}$  and  $\epsilon_{\text{4tracks}}^{\text{trig}} = \epsilon_{\text{3tracks}}^{\text{trig}}$ , which is justified in Section 5.3 and Appendix A.3. Finally, the last equality uses  $f_3 = f_{B^+} = f_{B^0} = f_4$ .

The dependence of relation (A.4) on the  $B$  momentum was checked on Monte Carlo and is reported in Fig. A.1. It shows, as a function of the  $B$  momentum, the ratio of reconstruction efficiency between four- and three-body decays

$$R_{4/3} = \frac{\epsilon^{\text{rec}}(B^0 \rightarrow J/\psi(\mu\mu)K^{*0}(K^+\pi^-))}{\epsilon^{\text{rec}}(B^+ \rightarrow J/\psi(\mu\mu)K^+)}, \quad (\text{A.7})$$

the ratio of reconstruction efficiency between three- and two-body decays

$$R_{3/2} = \frac{\epsilon^{\text{rec}}(B^+ \rightarrow J/\psi(\mu\mu)K^+)}{\epsilon^{\text{rec}}(B^0 \rightarrow K^+\pi^-)}, \quad (\text{A.8})$$

as well as their ratio  $\frac{R_{3/2}}{R_{4/3}}$ . Both efficiency ratios are very similar for all the phase space. The double ratio is above 0.90 for a large part of the spectrum. This test will be performed on the first data, to assess the method.

A first check of the method on Monte Carlo was performed. Using  $B^+ \rightarrow J/\psi(\mu\mu)K^+$  and  $B^0 \rightarrow J/\psi(\mu\mu)K^{*0}(K^+\pi^-)$  as three- and four-body control channels respectively, one can compute the ratio of Eq. (A.6). With the equivalent of  $0.1 \text{ fb}^{-1}$  we get [72]

$$\frac{\epsilon_{\text{norm}}^{\text{rec}}}{\epsilon_{\text{sig}}^{\text{rec}}} \approx \frac{\mathcal{B}_3 \mathcal{N}_4^{\text{obs}}}{\mathcal{B}_4 \mathcal{N}_3^{\text{obs}}} = 0.627 \pm 0.006 \quad (\text{A.9})$$

If we compute directly the ratio, on Monte Carlo, for the  $B_s^0 \rightarrow \mu^+\mu^-$  and  $B^+ \rightarrow J/\psi(\mu\mu)K^+$  we get

$$\frac{\epsilon_{\text{norm}}^{\text{rec}}}{\epsilon_{\text{sig}}^{\text{rec}}} = \frac{\epsilon_{B^+ \rightarrow J/\psi(\mu\mu)K^+}^{\text{rec}}}{\epsilon_{B_s^0 \rightarrow \mu^+\mu^-}^{\text{rec}}} = 0.589 \pm 0.005 \quad (\text{A.10})$$

which is close to the ratio of Eq. (A.9).

Another pair of control channels for the assessment of the reconstruction efficiencies ratio may be  $B_{(s)}^0 \rightarrow h^+h^-$  and  $B^\pm \rightarrow h^+h^-h^\pm$ .

### A.3 Trigger Efficiency

The normalisation introduces a ratio of trigger efficiencies in Eq. (A.3). Furthermore, as shown in Appendix A.2 such a ratio also appears in Eq. (A.5). Thus, methods have been developed to estimate it; a first method which requires a non-negligible yield is used for the control and normalisation channels, and other methods are valid for the tiny yield expected for the signal channel.

The method for the control channels uses information about the reasons why a particular event is triggered. One can define three not mutually exclusive classifiers:

**TIS** (Triggered Independently of Signal) An event is labelled TIS if no information associated with the particular channel considered (called signal hereafter) is required for its trigger.

**TOS** (Triggered On Signal) An event is TOS if the information associated with the signal under study is enough for its trigger.

**TOB** (Triggered On Both) An event is TOB if both signal and non-signal information is **required** to trigger it. This term can be misleading and should not be confused with TIS&TOS defined hereafter.

An event can be both TIS and TOS, labelled TIS&TOS if it is triggered by both signal and non-signal information, while each of them would have been **sufficient** to trigger it.

This classification is very useful to study trigger efficiencies, using the following equation:

$$\epsilon^{\text{trig}} = \frac{\mathcal{N}^{\text{trig}}}{\mathcal{N}^{\text{sel}}} = \frac{\mathcal{N}^{\text{TIS}}}{\mathcal{N}^{\text{sel}}} \frac{\mathcal{N}^{\text{trig}}}{\mathcal{N}^{\text{TIS}}} = \epsilon^{\text{TIS}} \frac{\mathcal{N}^{\text{trig}}}{\mathcal{N}^{\text{TIS}}} \quad (\text{A.11})$$

in which  $\epsilon^{\text{TIS}}$  is the efficiency of triggering without information from the signal for a given channel, while  $\mathcal{N}^{\text{trig}}$  and  $\mathcal{N}^{\text{TIS}}$  are observables, available from LHCb trigger.  $\epsilon^{\text{TIS}}$  is rather independent of the channel considered and depends on selection cuts, mostly through the correlation between the  $B$  and the rest of the event (which was a source of trigger). Provided the selections pick reasonably similar  $B$  phase space,  $\epsilon^{\text{TIS}}$  is similar for all channels and thus cancels out in any trigger efficiency ratio.

Because of the low  $B_s^0 \rightarrow \mu^+ \mu^-$  yield the previous method cannot be used for the signal. Another procedure has been developed, which consist in the assessment of the extraction of the trigger effect on  $B_s^0 \rightarrow \mu^+ \mu^-$  events from data (trigger emulation). First, one needs to gain information about the properties of the  $B_s^0$  daughters before trigger. This can be done using TIS  $B_{(s)}^0 \rightarrow h^+ h^-$  events, since this decay is kinetically identical to  $B_s^0 \rightarrow \mu^+ \mu^-$ . Then, a sample of TIS muons pairs is collected; there are plenty of about source of muons pairs for example  $B^+ \rightarrow J/\psi(\mu\mu)K^+$ . In case the phase space of the dimuon sample is not compatible with the characteristics dimuon coming from  $B_s^0 \rightarrow \mu^+ \mu^-$ — and obtained from  $B_{(s)}^0 \rightarrow h^+ h^-$ — corrections are brought through binning and reweighting. The trigger is then applied offline on the dimuon sample, which allows the study of its effect.

## Appendix B

# More on Event Selection

Information that, for the sake of conciseness, could not be included in Section 5.3 is reported in this section, which is organised by channels. In particular, the distributions of the standard variables for events selected with the alternate selection and with the standard selection are presented for each channels. Furthermore, the information exposed here is similar to that described in the main text, and so is its interpretation.

### Selection of the $B_s^0 \rightarrow \mu^+\mu^-$ Channel

Figure B.1 shows the distributions of the standard variables for  $B_s^0 \rightarrow \mu^+\mu^-$  events selected with the alternate selection and with the standard selection. The distributions of the alternate variables are shown and discussed in Section 5.3.1, where the normalisation of the different histograms is explained. The considerations relative to the alternate variables are also valid for the standard variables.

Figure B.2 shows distributions for the  $B_s^0$  proper time and the isolation of both muons, which enter in the definition of the geometry likelihood. The two selections yield very similar distributions.

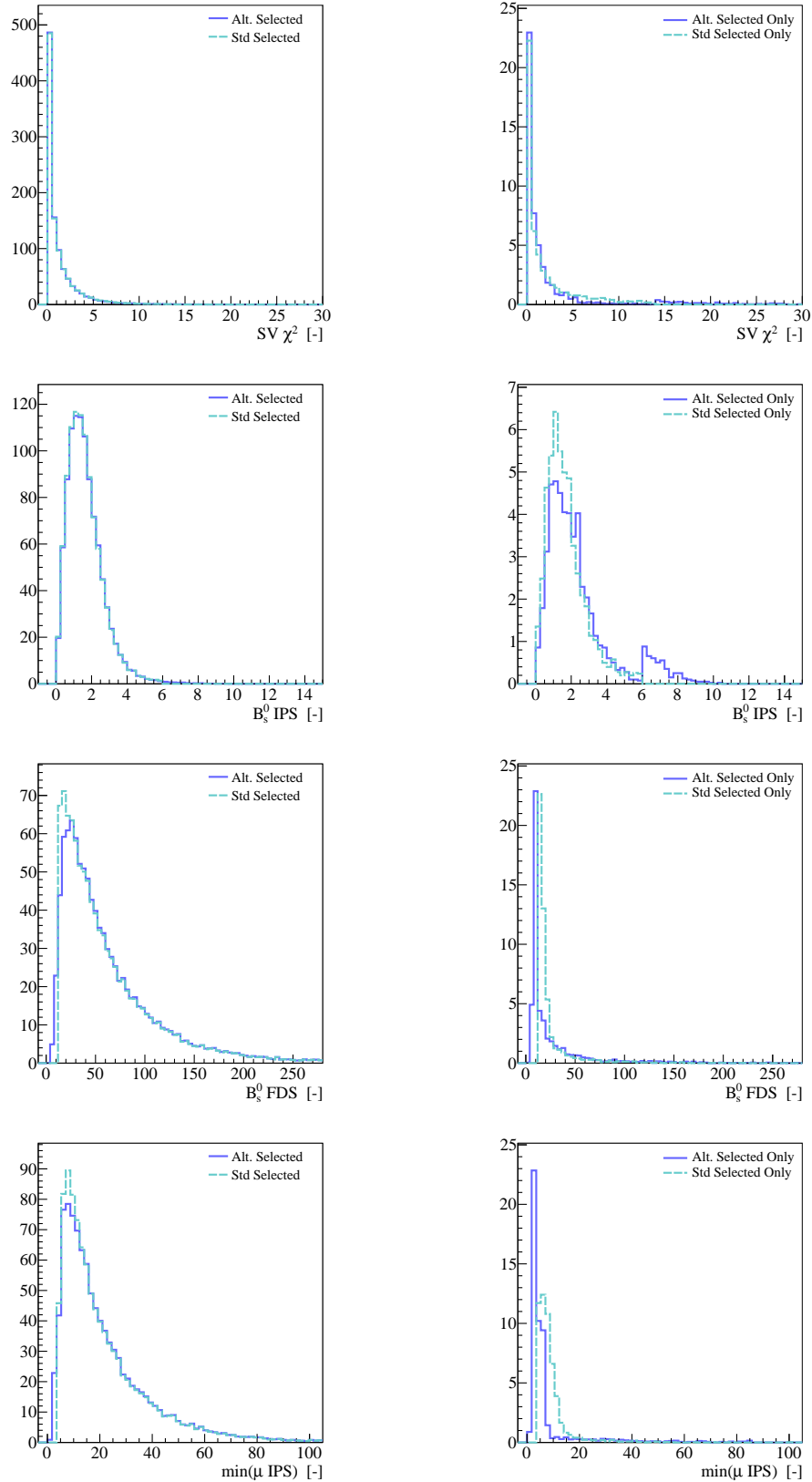


Figure B.1: Left: Distributions of the  $SV\chi^2$  (first row), the  $B_s^0$  IPS (second row), the  $B_s^0$  FDS (third row) and the smallest  $\mu$  IPS (fourth row) for  $B_s^0 \rightarrow \mu^+\mu^-$  events passing the alternate (solid blue) and the standard (dashed light blue) selections. Right: Same distributions for events passing only one of the selections.

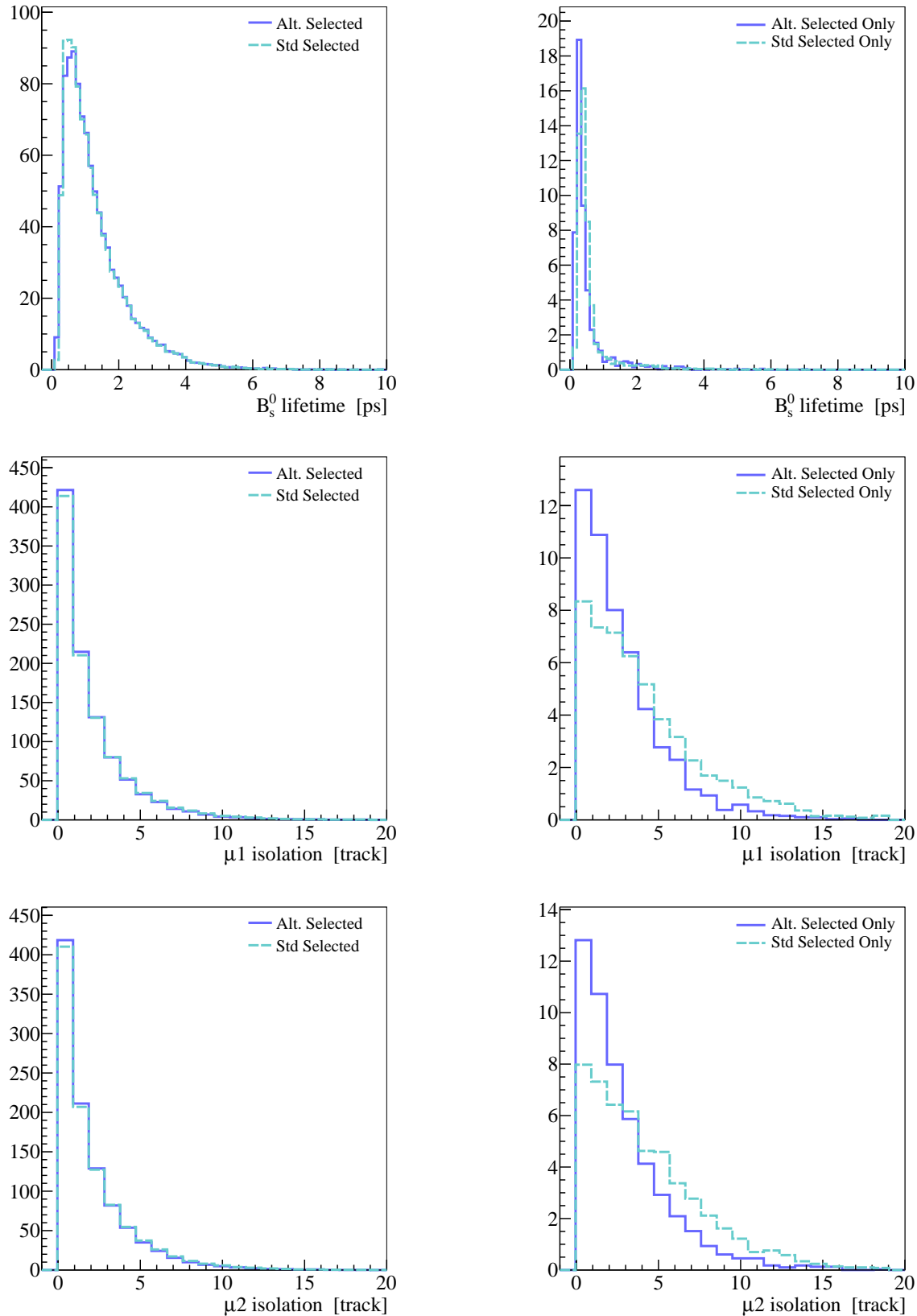


Figure B.2: Left: Distributions of the  $B_s^0$  proper time (top), the  $\mu^+$  (middle) and the  $\mu^-$  isolations (bottom) for  $B_s^0 \rightarrow \mu^+ \mu^-$  events passing the alternate (solid blue) and the standard (dashed light blue) selections. Right: Same distributions for events passing only one of the selections.

## Selection of the $B_{(s)}^0 \rightarrow h^+h^-$ Channel

Figures B.3 and B.4 show the distributions of the alternate variables for  $B_{(s)}^0 \rightarrow h^+h^-$  events selected with the alternate selection and with the standard selection. One finds in Fig. B.5 distributions of the standard variables and in Fig. B.6 distributions of the  $B_{(s)}^0$  pseudorapidity and  $B_{(s)}^0$  momentum. The normalisation of each histogram is defined in Section 5.3.1, where the distributions of the alternate variables are discussed for  $B_s^0 \rightarrow \mu^+\mu^-$  events. Since the distributions for  $B_{(s)}^0 \rightarrow h^+h^-$  are similar and show features related to those discussed for the  $B_s^0 \rightarrow \mu^+\mu^-$  case, the reader is invited to refer to Section 5.3.1. Figure B.7 shows histograms of the  $B_s^0$  proper time and the isolation of both muons.

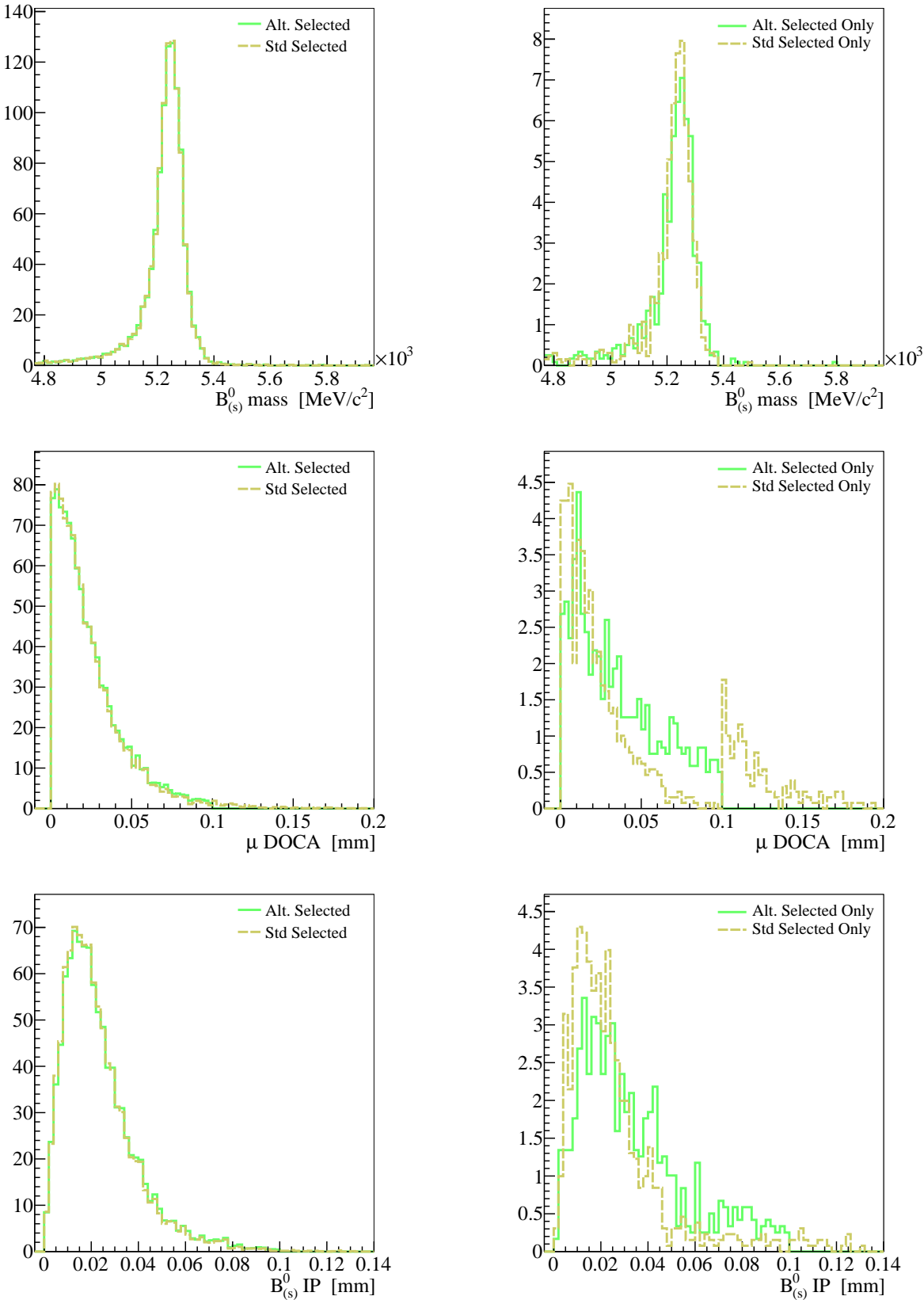


Figure B.3: Left: Distributions of the  $B_{(s)}^0$  mass (top), the  $\mu$  DOCA (middle) and the  $B_{(s)}^0$  IP (bottom) for  $B_{(s)}^0 \rightarrow h^+h^-$  events passing the alternate (solid green) and the standard (dashed khaki) selections. Right: Same distributions for events passing only one of the selections.

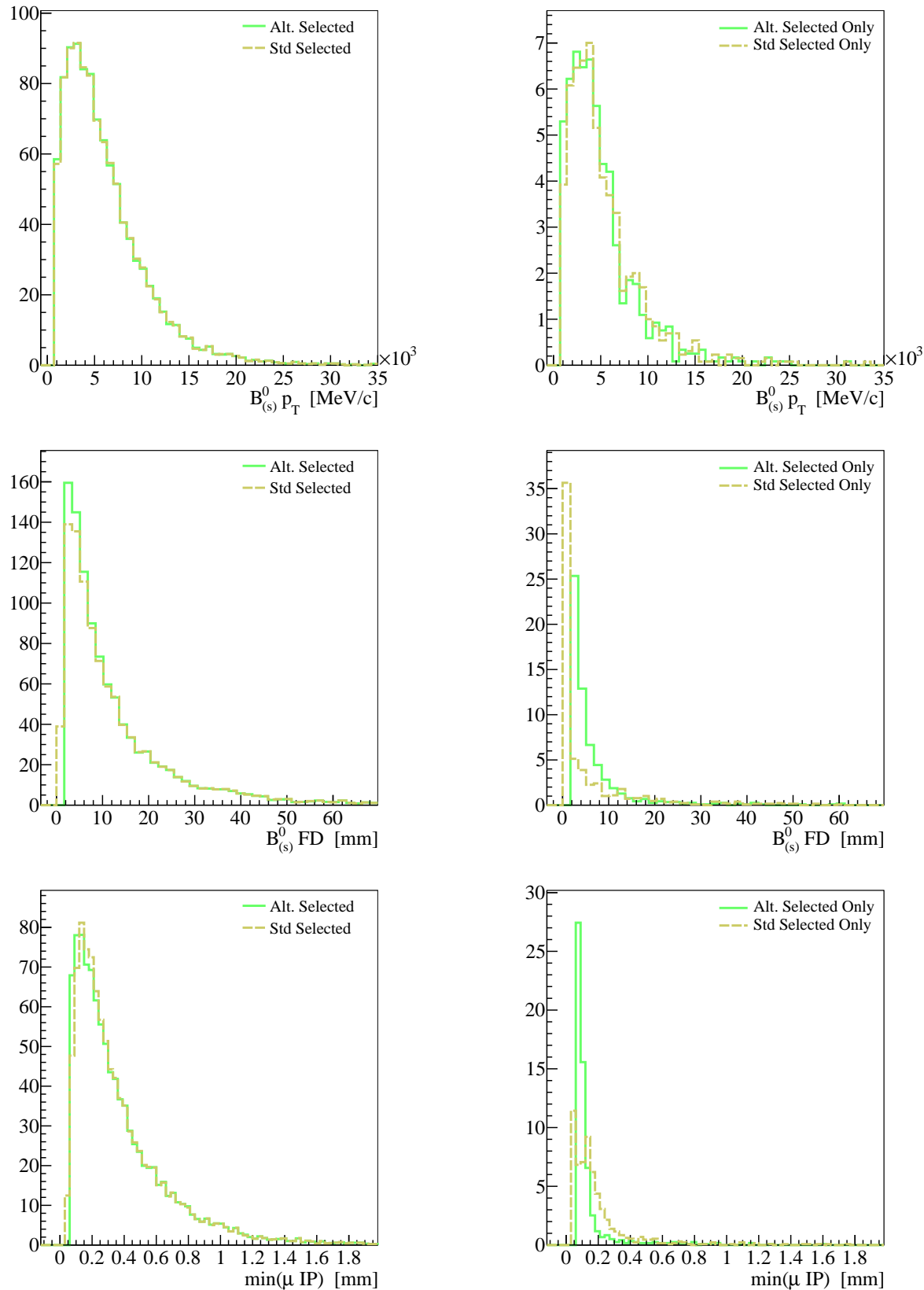


Figure B.4: Left: Distributions of the  $B_{(s)}^0$   $p_T$  (top), the  $B_{(s)}^0$  FD (middle) and the smallest  $h$  IP (bottom) for  $B_{(s)}^0 \rightarrow h^+h^-$  events passing the alternate (solid green) and the standard (dashed khaki) selections. Right: Same distributions for events passing only one of the selections.

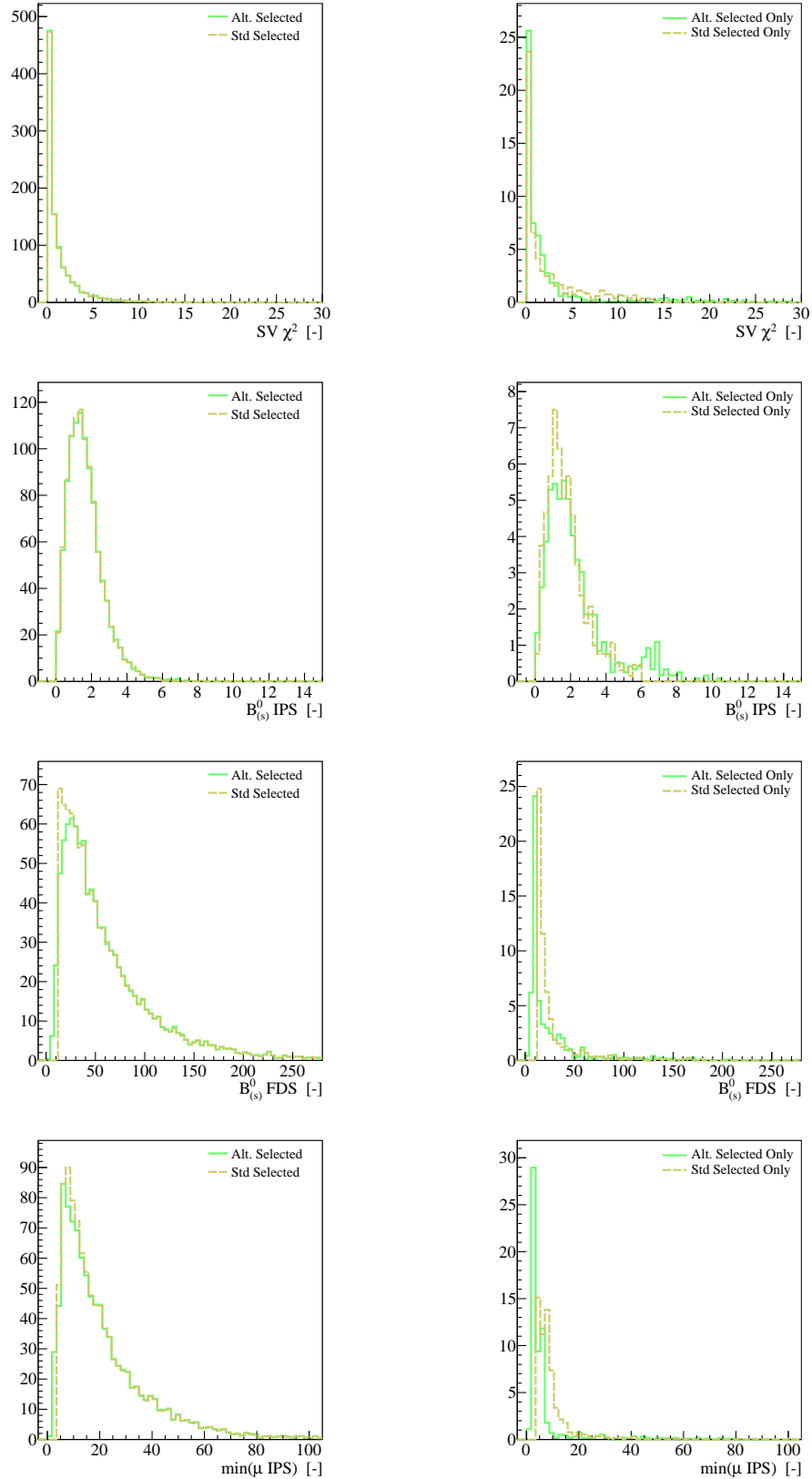


Figure B.5: Left: Distributions of the  $\text{SV } \chi^2$  (first row), the  $B_{(s)}^0 \text{ IPS}$  (second row), the  $B_{(s)}^0 \text{ FDS}$  (third row) and the smallest  $h$  IPS (fourth row) for  $B_{(s)}^0 \rightarrow h^+h^-$  events passing the alternate (solid green) and the standard (dashed khaki) selections. Right: Same distributions for events passing only one of the selections.

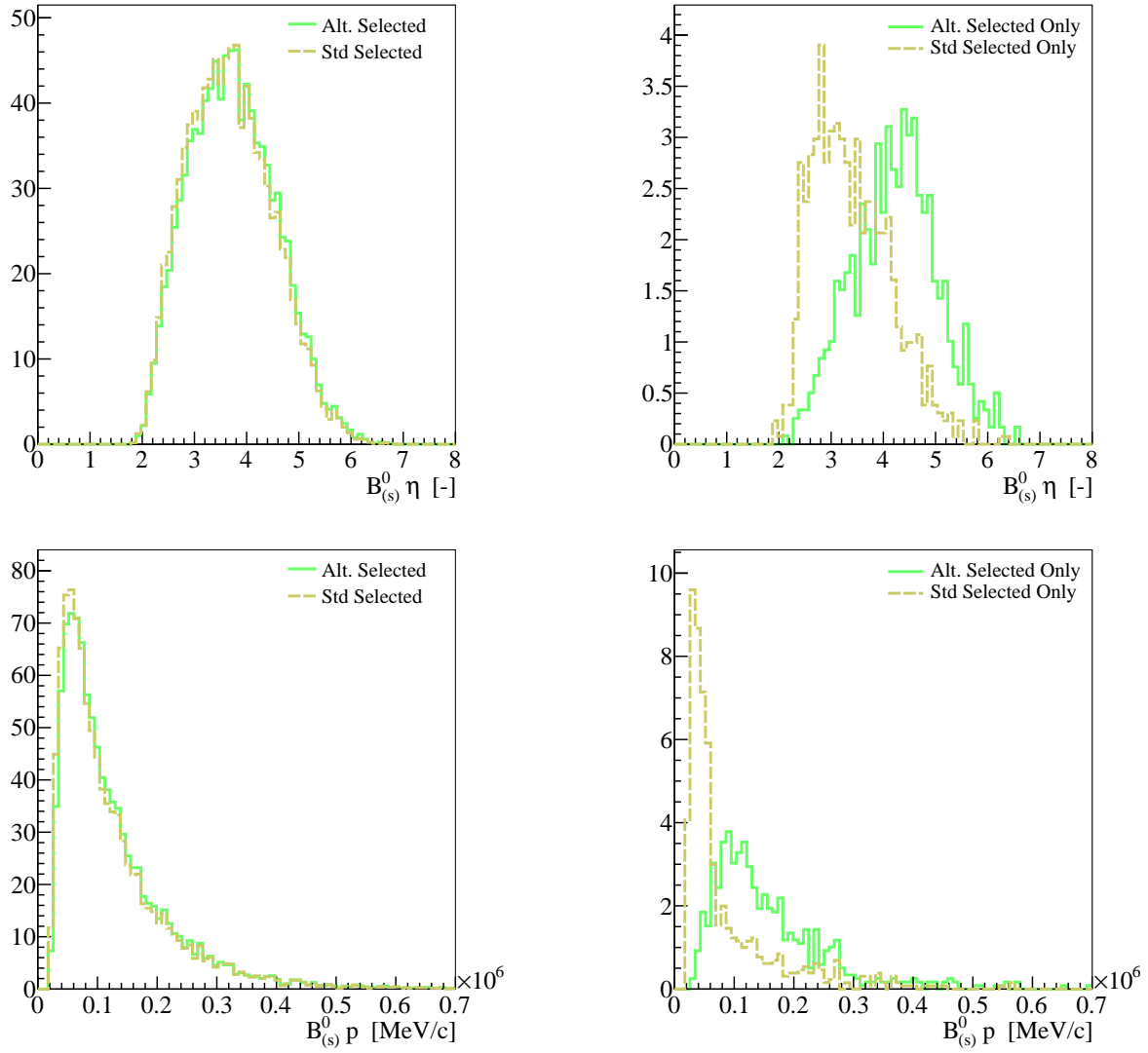


Figure B.6: Left: Distributions of the  $B_{(s)}^0$  pseudorapidity (top), the  $B_{(s)}^0$  momentum (bottom) for  $B_{(s)}^0 \rightarrow h^+h^-$  events passing the alternate (solid green) and the standard (dashed khaki) selections. Right: Same distributions for events passing only one of the selections.

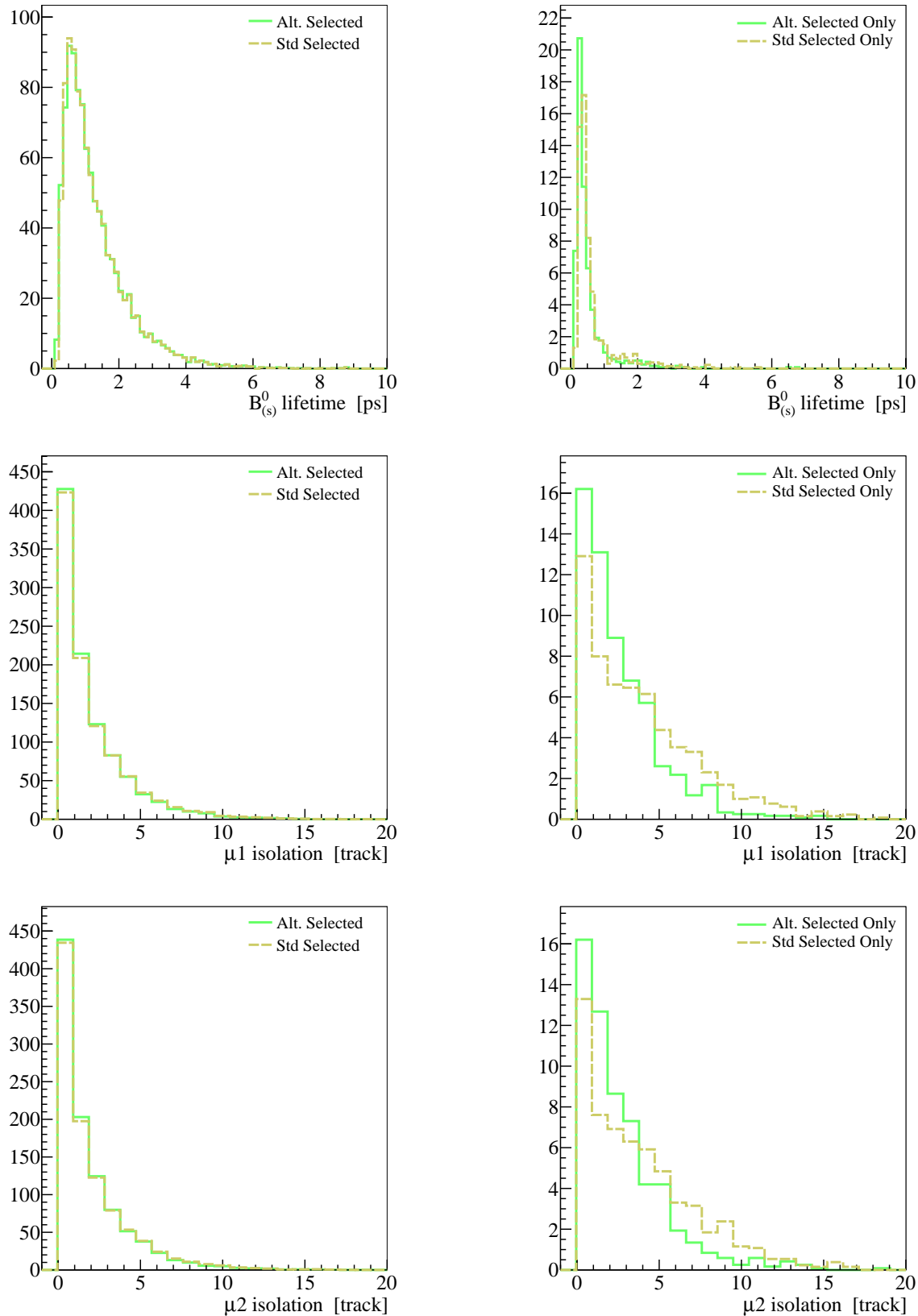


Figure B.7: Left: Distributions of the  $B_s^0$  proper time (top), the  $\mu^-$  (middle) and the  $\mu^+$  isolations (bottom) for  $B_{(s)}^0 \rightarrow h^+h^-$  events passing the alternate (solid green) and the standard (dashed khaki) selections. Right: Same distributions for events passing only one of the selections.

## Selection of the $B^+ \rightarrow J/\psi(\mu\mu)K^+$ Channel

Figures B.8 and B.9 show the distributions of the alternate variables for  $B^+ \rightarrow J/\psi(\mu\mu)K^+$  events selected with the alternate selection and with the standard selection. Figure B.10 shows histograms for the standard variables and Fig. B.11 distributions of the  $B^+$  pseudorapidity and  $B^+$  momentum. The normalisation of each histogram is defined in Section 5.3.1, where the distributions of the alternate variables are discussed for  $B_s^0 \rightarrow \mu^+\mu^-$  events. Since the distributions for  $B^+ \rightarrow J/\psi(\mu\mu)K^+$  are similar and show features related to those discussed for the  $B_s^0 \rightarrow \mu^+\mu^-$  case, the reader is invited to refer to Section 5.3.1.

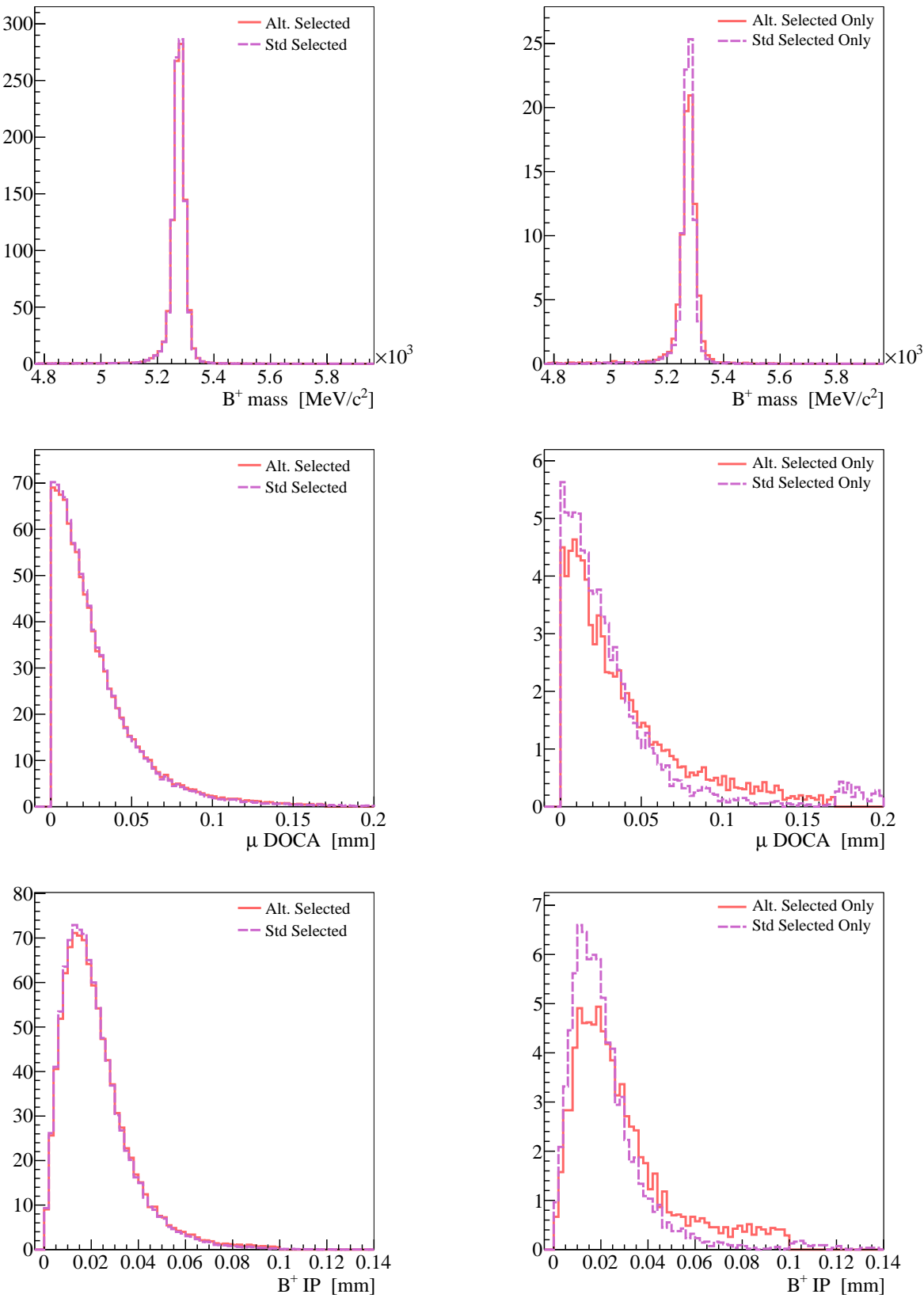


Figure B.8: Left: Distributions of the  $B^+$  mass (top), the  $\mu$  DOCA (middle) and the  $B^+$  IP (bottom) for  $B^+ \rightarrow J/\psi K^+$  events passing the alternate (solid red) and the standard (dashed purple) selections. Right: Same distributions for events passing only one of the selections.

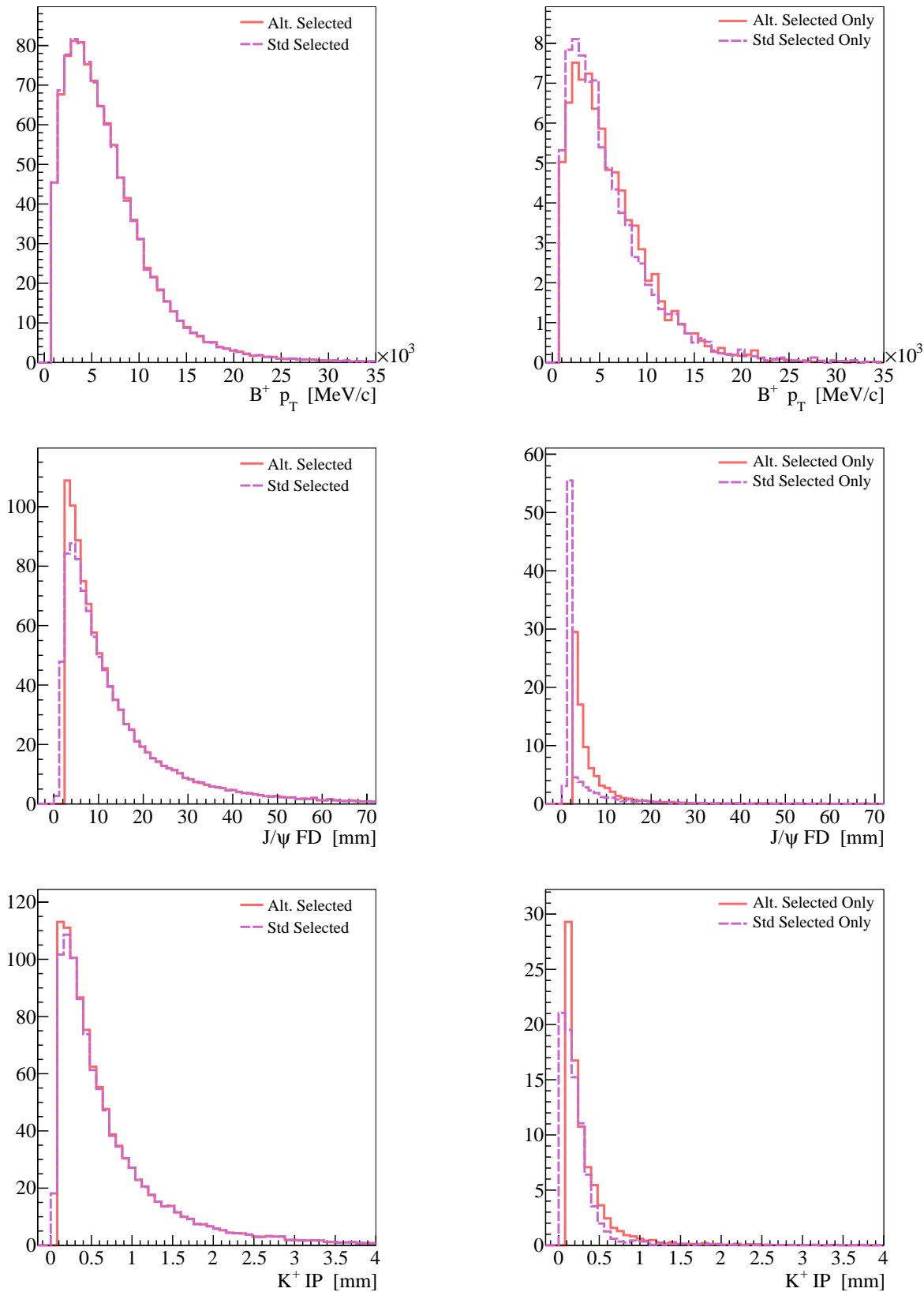


Figure B.9: Left: Distributions of the  $B^+$   $p_T$  (top), the  $J/\psi$  FD (middle) and the  $K^+$  IP (bottom) for  $B^+ \rightarrow J/\psi K^+$  events passing the alternate (solid red) and the standard (dashed lila) selections. Right: Same distributions for events passing only one of the selections.

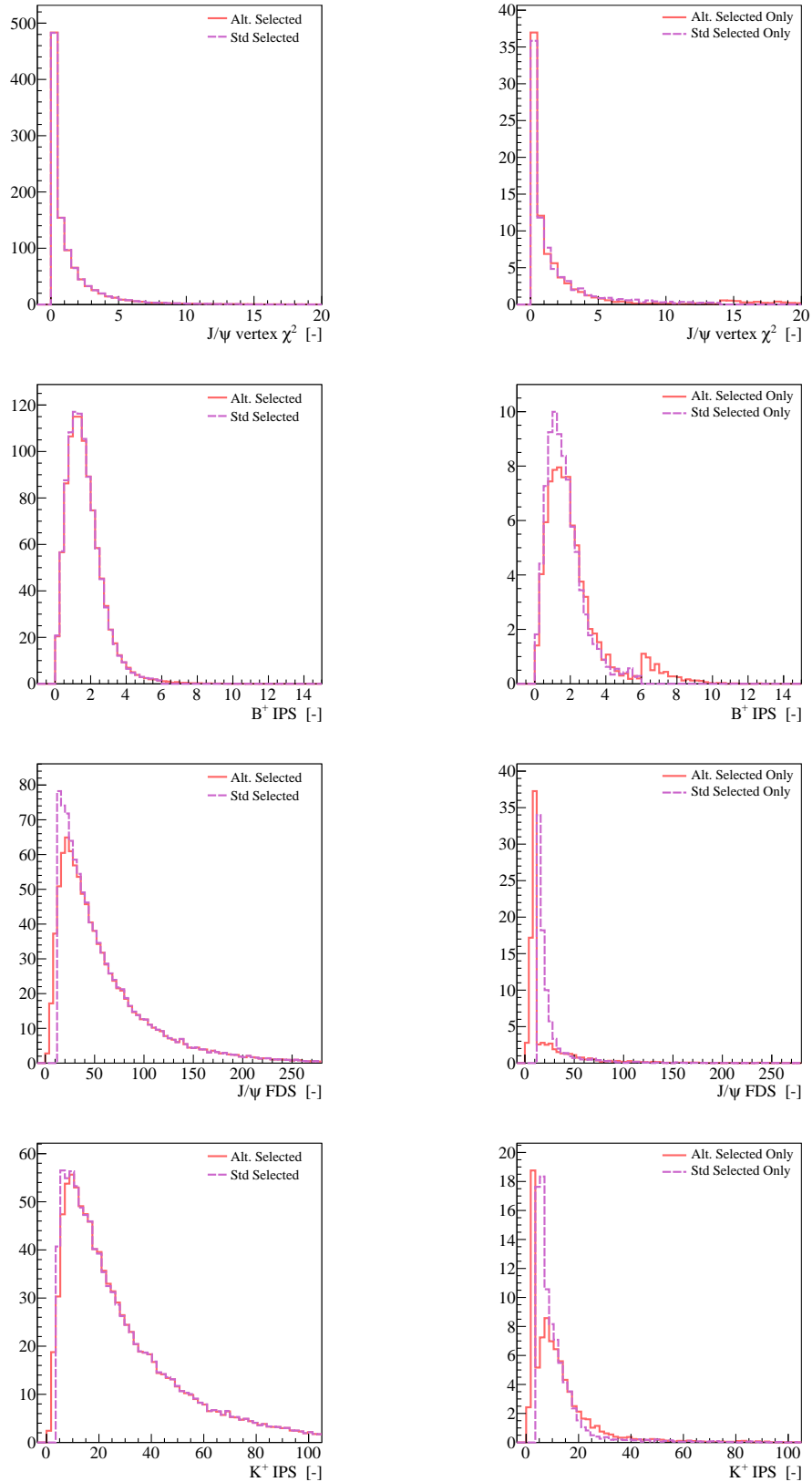


Figure B.10: Left: Distributions of the  $J/\psi$  vertex  $\chi^2$  (first row), the  $B^+$  IPS (second row), the  $J/\psi$  FDS (third row) and the  $K^+$  IPS (fourth row) for  $B^+ \rightarrow J/\psi K^+$  events passing the alternate (solid red) and the standard (dashed lila) selections. Right: Same distributions for events passing only one of the selections.

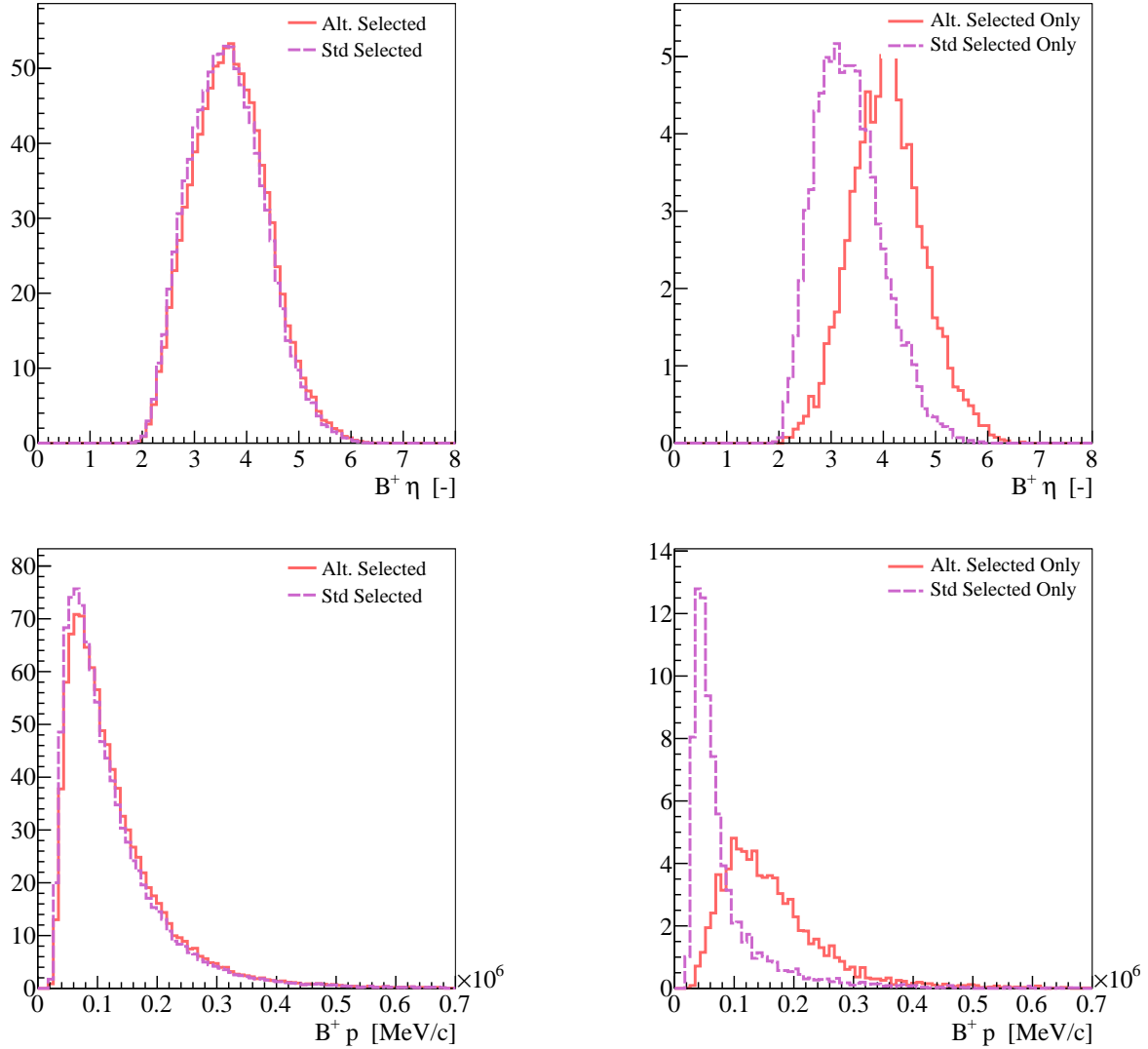


Figure B.11: Left: Distributions of the  $B^+$  pseudorapidity (top), the  $B^+$  momentum (bottom) for  $B^+ \rightarrow J/\psi K^+$  events passing the alternate (solid red) and the standard (dashed lila) selections. Right: Same distributions for events passing only one of the selections.

## Appendix C

# More on the Geometry Likelihood

This appendix consists of elements that were not discussed in the body of this document but that may be of interest for some readers. We present some further information about the GL and attempt to define the GL without the use of the muon isolations information.

### Geometry Likelihood including the muon isolations

Figure C.1 shows the two-dimensional plots of each pairs of variables used for the GL construction for the  $B_s^0 \rightarrow \mu^+ \mu^-$  signal. While the variables are gaussianly distributed and uncorrelated, as shown in Fig. 5.5, not every combinations of two variables have a two-dimensional Gaussian distribution, which means that they are not independant. Variables which contain an important part of the muon isolation information are most affected. The ongoing efforts to find an alternate definition of the isolation variable may bring some improvement. The case of the dimuon background is shown in Fig. C.2.

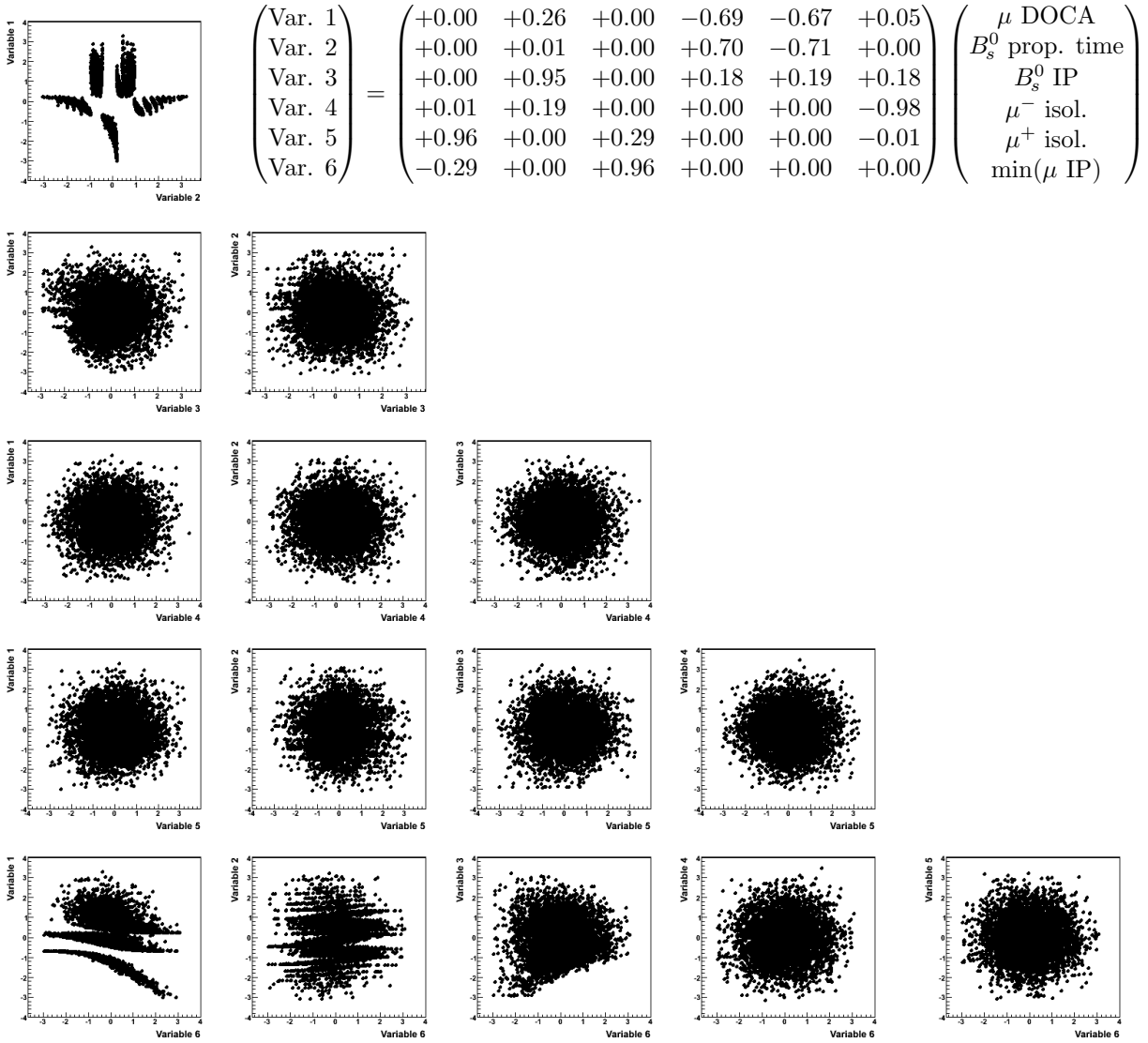


Figure C.1: Scatter plots of the distributions of the variables used to define the GL for the  $B_s^0 \rightarrow \mu^+ \mu^-$  signal. On each graph, two variables are plotted against each other. The rotation matrix, which defined the composition of the new variables (before the second gaussianisation) in terms of the normal Gaussian version of the physical input variables is given.

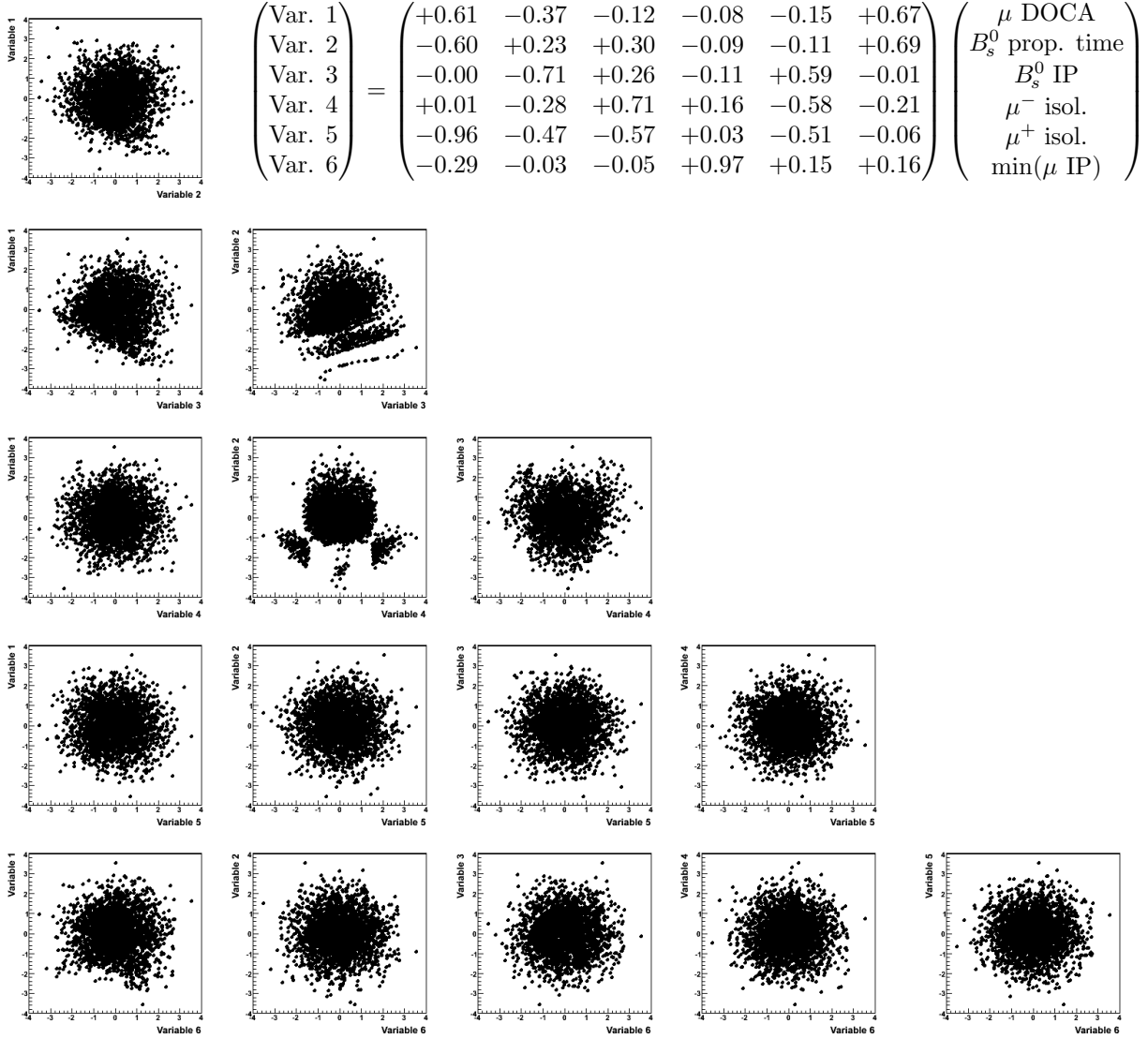
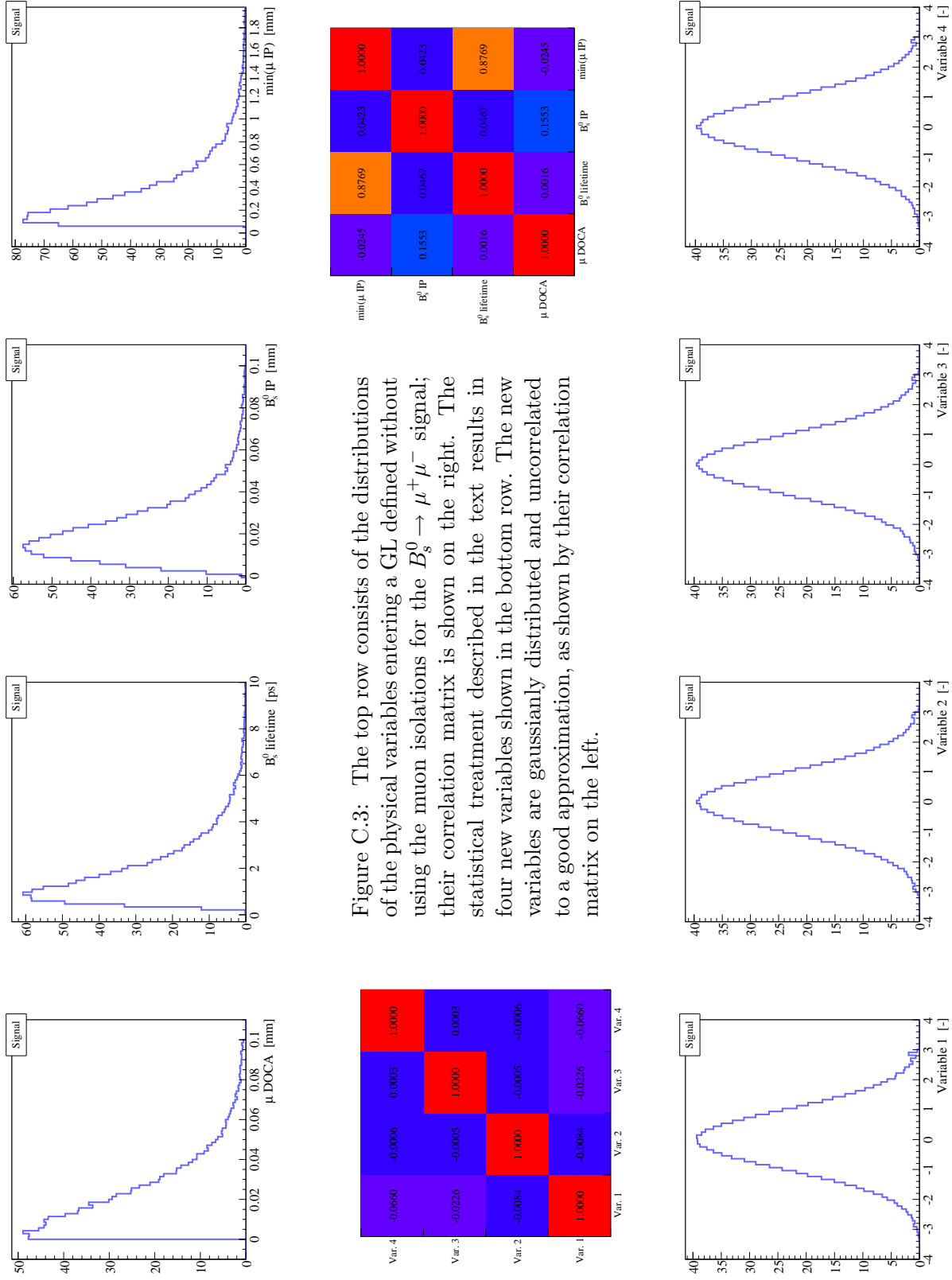


Figure C.2: Scatter plots of the distributions of the variables used to define the GL for the dimuon background. On each graph, two variables are plotted against each other. The rotation matrix, which defined the composition of the new variables (before the second gaussianisation) in terms of the normal Gaussian version of the physical input variables is given.

## Geometry Likelihood without the muon isolation information

In this section, we consider the case of a GL defined with the DOCA of the muons, the  $B_s^0$  IP, the  $B_s^0$  proper time and the smallest IP of the muons w.r.t. all PVs. The muon isolations are not used.

Figures C.3 and C.4 depict the GL input variables before and after gaussianisation and decorrelation for the  $B_s^0 \rightarrow \mu^+ \mu^-$  signal and for the dimuon background, respectively. The two-dimensional distributions of the gaussianised variables are shown in Figs C.5 and C.6, respectively.



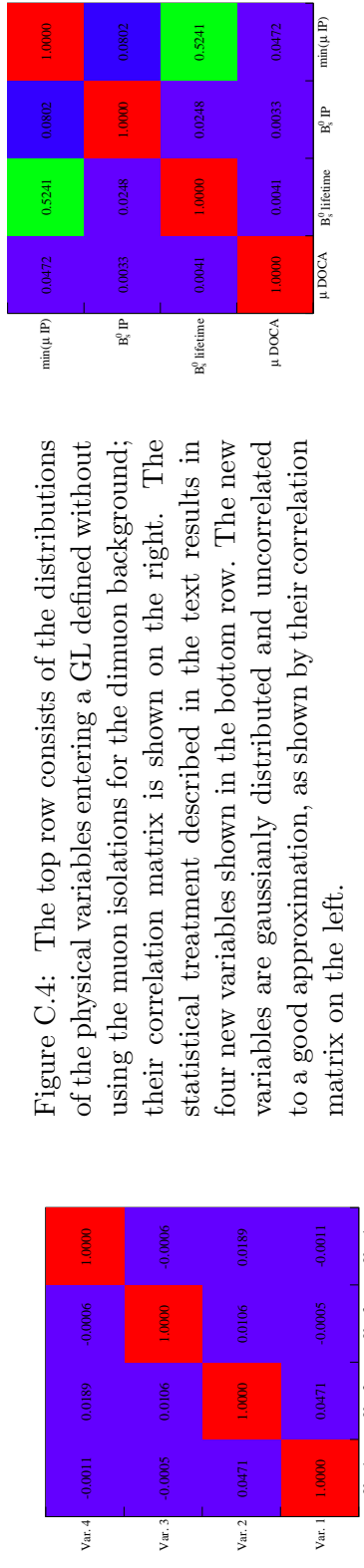
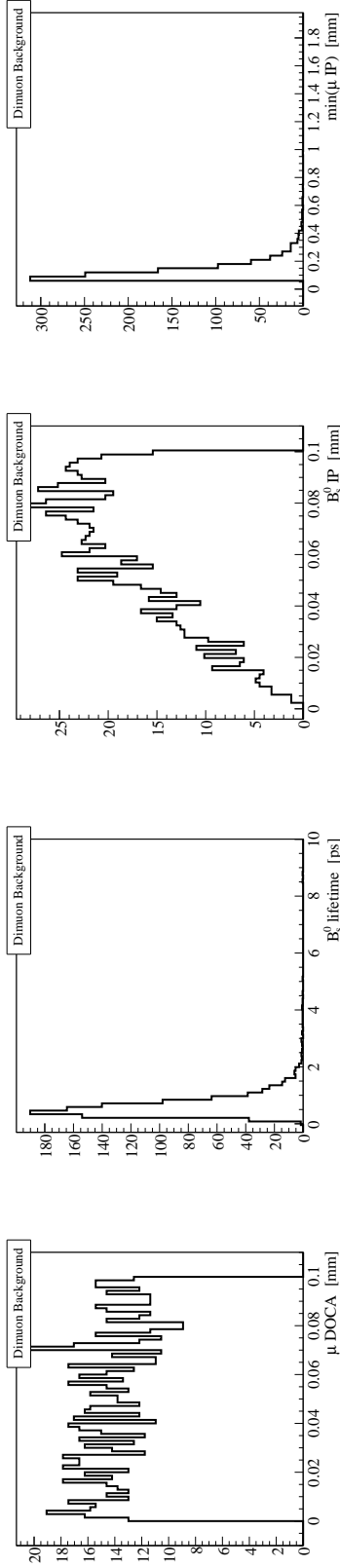
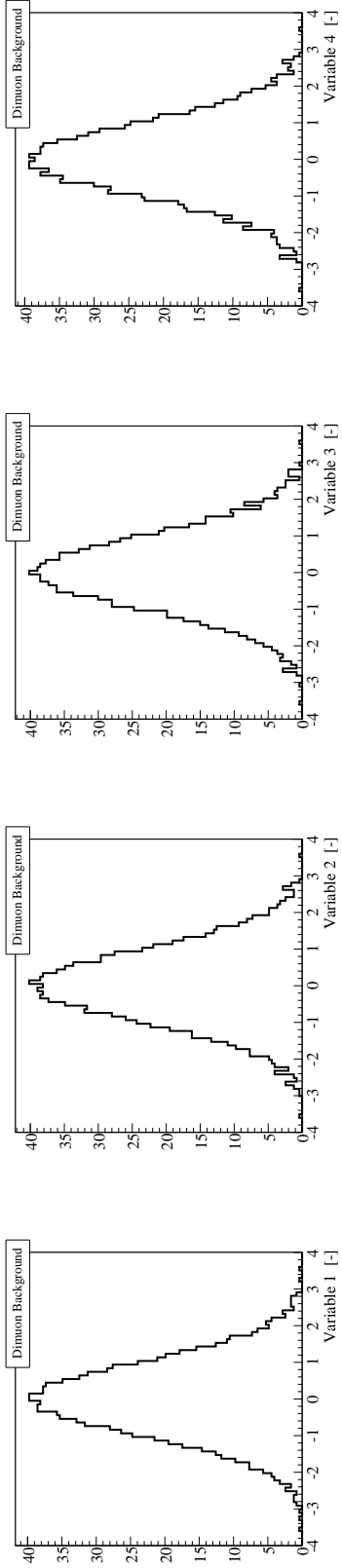


Figure C.4: The top row consists of the distributions of the physical variables entering a GL defined without using the muon isolations for the dimuon background; their correlation matrix is shown on the right. The statistical treatment described in the text results in four new variables shown in the bottom row. The new variables are gaussianly distributed and uncorrelated to a good approximation, as shown by their correlation matrix on the left.



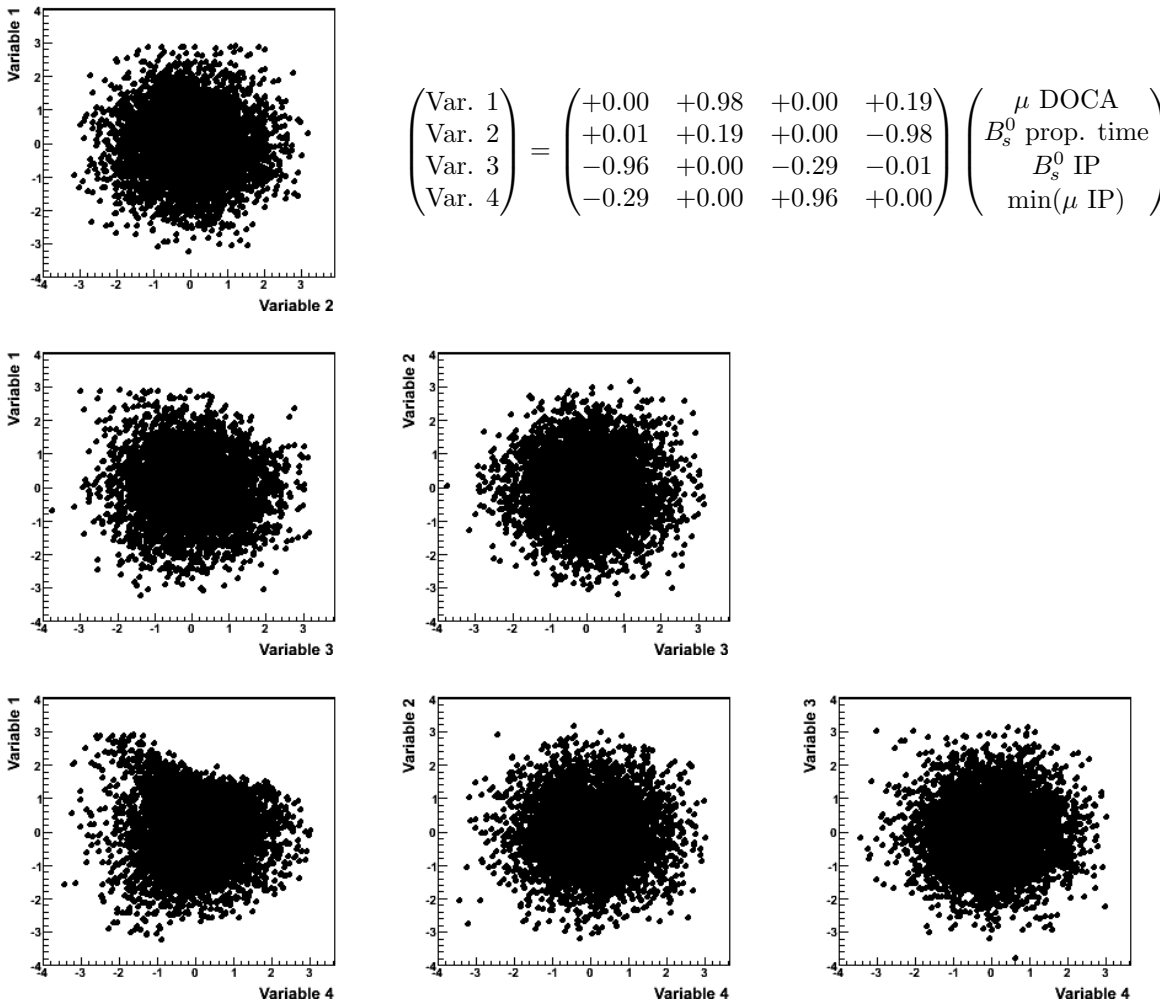


Figure C.5: Scatter plots of the distributions of the variables used to define the GL for the  $B_s^0 \rightarrow \mu^+\mu^-$  signal. In this case the muons isolations were not used in the computation of the three (gaussianisation – rotation – gaussianisation) transformations. On each graph, two variables are plotted against each other. The rotation matrix, which defined the composition of the new variables (before the second gaussianisation) in terms of the normal Gaussian version of the physical input variables is given.

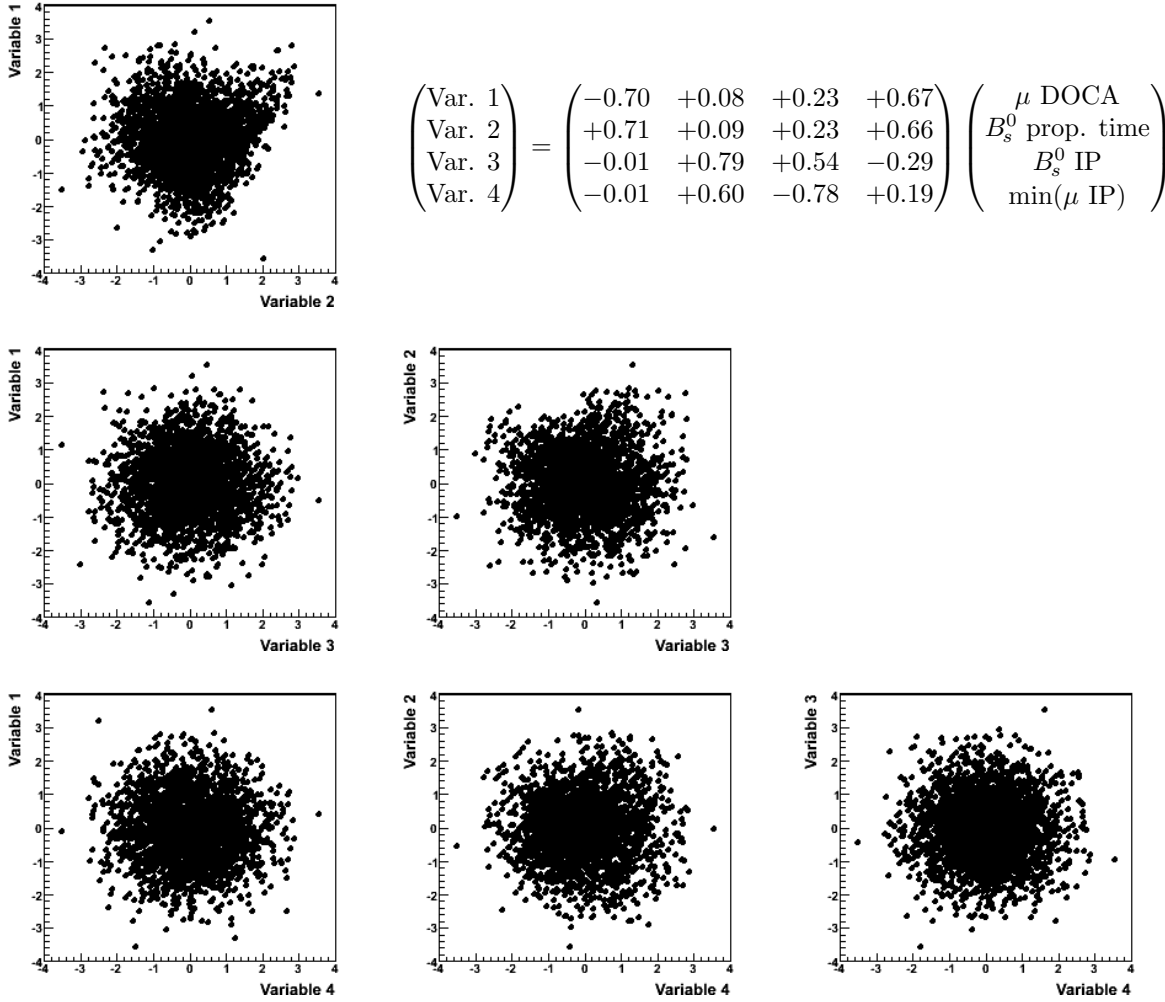


Figure C.6: Scatter plots of the distributions of the variables used to define the GL for the dimuon background. In this case the muons isolations were not used in the computation of the three (gaussianisation – rotation – gaussianisation) transformations. On each graph, two variables are plotted against each other. The rotation matrix, which defined the composition of the new variables (before the second gaussianisation) in terms of the normal Gaussian version of the physical input variables is given.

# References

- [1] W. Pauli, *Letter to Lise Meitner, Gruppe der Radioaktivien bei der Gauvereins-Tatung, Tuebingen*, 1930, PDF on CERN Document Server.
- [2] C. L. Cowan, F. Reines, F. B. Harrison, H. W. Kruse, and A. D. McGuire, *Detection of the Three Neutrino: A Confirmation*, Science **124**, 103 (1956).
- [3] D. Décamp *et al.* [ALEPH collaboration], *Determination of the Number of Light Neutrino Species*, Phys. Lett. **B231**, 519 (1989).
- [4] S. L. Glashow, *Partial-Symmetries of Weak Interactions*, Nucl. Phys. **22**, 579 (1961).
- [5] A. Salam, *Weak and Electromagnetic Interactions*, Proceedings Of The Nobel Symposium Held At Lerum, Sweden, 1968.
- [6] S. Weinberg, *A Model of Leptons*, Phys. Rev. Lett. **19**, 1264 (1967).
- [7] P. W. Higgs, *Broken Symmetries and the Masses of Gauge Bosons*, Phys. Rev. Lett. **13**, 508 (1964).
- [8] F. Englert and R. Brout, *Broken Symmetry and the Mass of Gauge Vector Mesons*, Phys. Rev. Lett. **13**, 321 (1964).
- [9] G. S. Guralnik, C. R. Hagen, and T. W. B. Kibble, *Global Conservation Laws and Massless Particles*, Phys. Rev. Lett. **13**, 585 (1964).
- [10] C. Amsler *et al.* [Particle Data Group], *Review of Particle Physics*, Phys. Lett. B **667**, 1 (2008), and 2009 partial update for the 2010 edition.
- [11] E. Leader and E. Predazzi, *An Introduction to Gauge Theories and Modern Particle Physics* (Cambridge University Press, 1996).
- [12] L. B. Okun, *Leptons and Quarks* (North-Holland, Amsterdam, 1982), Trans. from Russian.
- [13] W. N. Cottingham and D. A. Greenwood, *An Introduction to the Standard Model of Particle Physics* (Cambridge University Press, 1998).
- [14] G. L. Kane, *Modern Elementary Particle Physics* (Addison-Wesley, Redwood City, CA, 1987).
- [15] Y. Nambu, *Axial Vector Current Conservation in Weak Interactions*, Phys. Rev. Lett. **4**, 380 (1960).
- [16] G. 't Hooft and M. Veltman, *Regularization and Renormalization of Gauge Fields*, Nucl. Phys. **B44** (1972).

- [17] N. Cabibbo, *Unitary Symmetry and Leptonic Decays*, Phys. Rev. Lett. **10**, 531 (1963).
- [18] M. Kobayashi and T. Maskawa, *CP Violation in the Renormalizable Theory of Weak Interaction*, Prog. Theor. Phys. **49**, 652 (1973).
- [19] J. Charles *et al.* [CKM fitter Group], Preliminary results as of Beauty 2009, updated results and plots from [20], available at <http://ckmfitter.in2p3.fr>.
- [20] J. Charles *et al.* [CKM fitter Group], *CP Violation and the CKM Matrix: Assessing the Impact of the Asymmetric B Factories*, Eur. Phys. J. **C41**, 1 (2005) [[hep-ph/0406184](#)].
- [21] G. P. Zeller *et al.* [NuTeV collaboration], *A Precise Determination of Electroweak Parameters in Neutrino Nucleon Scattering*, Phys. Rev. Lett. **88**, 091802 (2002) [[hep-ex/0110059](#)].
- [22] G. W. Bennett *et al.* [Muon  $g - 2$  collaboration], *Final Report of the Muon E821 Anomalous Magnetic Moment Measurement at BNL*, Phys. Rev. **D73**, 072003 (2006) [[hep-ex/0602035](#)].
- [23] R. Davis, D. S. Harmer, and K. C. Hoffman, *Search for Neutrinos from the Sun*, Phys. Rev. Lett. **20**, 1205 (1968).
- [24] Y. Fukuda *et al.* [Super-Kamiokande collaboration], *Measurements of the Solar Neutrino Flux from Super-Kamiokande's First 300 Days*, Phys. Rev. Lett. **81**, 1158 (1998).
- [25] S. Fukuda *et al.* [Super-Kamiokande collaboration], *Constraints on Neutrino Oscillations Using 1258 Days of Super-Kamiokande Solar Neutrino Data*, Phys. Rev. Lett. **86**, 5656 (2001).
- [26] Q. R. Ahmad *et al.* [Sudbury Neutrino Observatory collaboration], *Measurement of the Rate of  $\nu_e + d \rightarrow p + p + e^-$  Interactions Produced by  ${}^8B$  Solar Neutrinos at the Sudbury Neutrino Observatory*, Phys. Rev. Lett. **87**, 071301 (2001).
- [27] A. G. Riess *et al.* [Supernova Search Team], *Observational Evidence from Supernovae for an Accelerating Universe and a Cosmological Constant*, Astron. J. **116**, 1009 (1998) [[astro-ph/9805201](#)].
- [28] S. Perlmutter *et al.* [Supernova Cosmology Project], *Measurements of  $\Omega$  and  $\Lambda$  from 42 High-Redshift Supernovae*, Astrophys. J. **517**, 565 (1999) [[astro-ph/9812133](#)].
- [29] D. N. Spergel *et al.* [WMAP collaboration], *Wilkinson Microwave Anisotropy Probe (WMAP) Three Year Results: Implications for Cosmology*, Astrophys. J. Suppl. **170**, 377 (2007) [[astro-ph/0603449](#)].
- [30] F. Zwicky, *Spectral Displacement of Extra Galactic Nebulae*, Helv. Phys. Acta **6**, 110 (1933).
- [31] F. Zwicky, *On the Masses of Nebulae and of Clusters of Nebulae*, Astrophys. J. **86**, 217 (1937).
- [32] M. S. Roberts and A. H. Rots, *Comparison of Rotation Curves of Different Galaxy Types*, Astronomy and Astrophysics **26**, 483 (1973).
- [33] W. L. Freedman *et al.* [HST collaboration], *Final Results from the Hubble Space Telescope Key Project to Measure the Hubble Constant*, Astrophys. J. **553**, 47 (2001) [[astro-ph/0012376](#)].

- [34] J. Dunkley *et al.* [WMAP collaboration], *Five-Year Wilkinson Microwave Anisotropy Probe (WMAP) Observations: Likelihoods and Parameters from the WMAP Data*, *Astrophys. J. Suppl.* **180**, 306 (2009) [hep-ph/0803.0586].
- [35] F. Jegerlehner and A. Nyffeler, *Muon  $g - 2$* , *Phys. Rept.* **477**, 1 (2009) [hep-ph/0902.3360].
- [36] R. Barate *et al.* [LEP Working Group for Higgs Boson Searches], *Search for the Standard Model Higgs Boson at LEP*, *Phys. Lett.* **B565**, 61 (2003) [hep-ex/0306033].
- [37] The ALEPH, CDF, DØ DELPHI, L3, OPAL, SLD collaborations, *Precision Electroweak Measurements and Constraints on the Standard Model*, (2009) [hep-ex/0911.2604].
- [38] TeVatron New Phenomena and Higgs working group [CDF and DØ collaborations], *Combined CDF and DØ Upper Limits on Standard Model Higgs Boson Production with 2.1 – 5.4  $fb^{-1}$  of Data*, (2009) [hep-ex/0911.3930].
- [39] S. P. Martin, *A Supersymmetry Primer*, (1997) [hep-ph/9709356].
- [40] S. Dimopoulos and D. W. Sutter, *The Supersymmetric Flavor Problem*, *Nucl. Phys.* **B452**, 496 (1995) [hep-ph/9504415].
- [41] H. E. Haber, *The Status of the Minimal Supersymmetric Standard Model and Beyond*, *Nucl. Phys. Proc. Suppl.* **62**, 469 (1998) [hep-ph/9709450].
- [42] P. van Nieuwenhuizen, *Supergravity*, *Phys. Rept.* **68**, 189 (1981).
- [43] A. H. Chamseddine, R. L. Arnowitt, and P. Nath, *Locally Supersymmetric Grand Unification*, *Phys. Rev. Lett.* **49**, 970 (1982).
- [44] G. F. Giudice and R. Rattazzi, *Theories with Gauge-Mediated Supersymmetry Breaking*, *Phys. Rept.* **322**, 419 (1999) [hep-ph/9801271].
- [45] T. Gherghetta, G. F. Giudice, and J. D. Wells, *Phenomenological Consequences of Supersymmetry with Anomaly-Induced Masses*, *Nucl. Phys.* **B559**, 27 (1999) [hep-ph/9904378].
- [46] T. Kaluza, *On the Problem of Unity in Physics*, *Sitzungsber. Preuss. Akad. Wiss. Berlin (Math. Phys.)* **1921**, 966 (1921).
- [47] O. Klein, *Quantum Theory and Five-Dimensional Theory of Relativity*, *Z. Phys.* **37**, 895 (1926).
- [48] A. Perez-Lorenzana, *An Introduction to Extra Dimensions*, *J. Phys. Conf. Ser.* **18**, 224 (2005) [hep-ph/0503177].
- [49] S. Mele, *Experimental Constraints on Extra Dimensions*, *Eur. Phys. J.* **C33**, 919 (2004).
- [50] S. L. Glashow, J. Iliopoulos, and L. Maiani, *Weak Interactions with Lepton-Hadron Symmetry*, *Phys. Rev. D* **2**, 1285 (1970).
- [51] J. E. Augustin *et al.*, *Discovery of a Narrow Resonance in  $e^+e^-$  Annihilation*, *Phys. Rev. Lett.* **33**, 1406 (1974).
- [52] J. J. Aubert *et al.*, *Experimental Observation of a Heavy Particle J*, *Phys. Rev. Lett.* **33**, 1404 (1974).

- [53] F. Abe *et al.*, *Observation of Top Quark Production in  $p\bar{p}$  Collisions with the Collider Detector at FermiLab*, Phys. Rev. Lett. **74**, 2626 (1995).
- [54] S. Abachi *et al.* [DØ collaboration], *Search for High Mass Top Quark Production in  $p\bar{p}$  Collisions at  $\sqrt{s} = 1.8$  TeV*, Phys. Rev. Lett. **74**, 2422 (1995) [hep-ex/9411001].
- [55] M.-O. Bettler [LHCb collaboration], *Search for New Physics in B Rare Decays at LHCb*, (2009) [hep-ex/0910.0942].
- [56] J. Wicht *et al.* [Belle collaboration], *Observation of  $B_s^0 \rightarrow \phi\gamma$  and Search for  $B_s^0 \rightarrow \gamma\gamma$  Decays at Belle*, Phys. Rev. Lett. **100**, 121801 (2008) [hep-ex/0712.2659].
- [57] R. N. Mohapatra and J. C. Pati, *Left-right Gauge Symmetry and an "Isoconjugate" Model of CP Violation*, Phys. Rev. D **11**, 566 (1975).
- [58] H. E. Haber and G. L. Kane, *The Search for Supersymmetry: Probing Physics Beyond the Standard Model*, Phys. Rept. **117**, 75 (1985).
- [59] B. Adeva *et al.* [LHCb collaboration], *Roadmap for Selected Key Measurements of LHCb*, (2009), [hep-ex/0912.4179], CERN Report LHCb-PUB-2009-029.
- [60] S. Barsuk *et al.* [LHCb collaboration], Analysis of  $B_s^0 \rightarrow \phi\gamma$  and other radiative B decays, In *Roadmap for Selected Key Measurements of LHCb* [59], [hep-ex/0912.4179], CERN Report LHCb-PUB-2009-029.
- [61] L. Shchutska, A. Golutvin, and I. Belyaev, *Study of Radiative Penguin Decays  $B^0 \rightarrow K^{*0}\gamma$  and  $B_s^0 \rightarrow \phi\gamma$  at LHCb*, CERN Report LHCb-2007-030, 2007.
- [62] L. Shchutska *et al.*, *Probing the Photon Polarization in  $B_s^0 \rightarrow \phi\gamma$  at LHCb*, CERN Report LHCb-2007-147, 2007.
- [63] J. T. Wei *et al.* [Belle collaboration], *Measurement of the Differential Branching Fraction and Forward-Backward Asymmetry for  $B^0 \rightarrow K^{(*)}\ell^+\ell^-$* , Phys. Rev. Lett. **103**, 171801 (2009) [hep-ex/0904.0770].
- [64] J. Dickens *et al.* [LHCb collaboration], Analysis of the decay  $B^0 \rightarrow K^{*0}\mu^+\mu^-$ , In *Roadmap for Selected Key Measurements of LHCb* [59], [hep-ex/0912.4179], CERN Report LHCb-PUB-2009-029.
- [65] J. Dickens, V. Gibson, C. Lazzeroni, and M. Patel, *A Study of the Sensitivity to the Forward-Backward Asymmetry in  $B_d \rightarrow K^*\mu^+\mu^-$  Decays at LHCb*, CERN Report LHCb-2007-039, 2007.
- [66] F. Jansen, N. Serra, G. Y. Smit, and N. Tuning, *Determination of the Forward-Backward Asymmetry in the Decay  $B_d \rightarrow K^*\mu^+\mu^-$  with an Unbinned Counting Analysis*, CERN Report LHCb-2009-003, 2009.
- [67] M. Beneke, T. Feldmann, and D. Seidel, *Exclusive Radiative and Electroweak  $b \rightarrow d$  and  $b \rightarrow s$  Penguin Decays at NLO*, Eur. Phys. J. **C41**, 173 (2005) [hep-ph/0412400].
- [68] A. Ali, T. Mannel, and T. Morozumi, *Forward-Backward Asymmetry of Dilepton Angular Distribution in the Decay  $b \rightarrow sl^+\ell^-$* , Physics Letters B **273**, 505 (1991).
- [69] U. Egede, T. Hurth, J. Matias, M. Ramon, and W. Reece, *New Observables in the Decay Mode  $\overline{B} \rightarrow \overline{K}^{*0}\ell^+\ell^-$* , JHEP **11**, 032 (2008) [hep-ph/0807.2589].

- [70] B. Aubert *et al.* [BABAR collaboration], *Measurements of Branching Fractions, Rate Asymmetries, and Angular Distributions in the Rare Decays  $B \rightarrow K\ell^+\ell^-$  and  $B \rightarrow K^*\ell^+\ell^-$* , Phys. Rev. **D73**, 092001 (2006) [hep-ex/0604007].
- [71] T. Aaltonen *et al.* [CDF collaboration], *Search for the Rare Decays  $B^+ \rightarrow \mu^+\mu^-K^+$ ,  $B^0 \rightarrow \mu^+\mu^-K^{*0}(892)$ , and  $B_s^0 \rightarrow \mu^+\mu^-\phi$  at CDF*, Phys. Rev. **D79**, 011104 (2009) [hep-ph/0804.3908].
- [72] D. Martínez Santos *et al.* [LHCb collaboration], *Analysis of the decay  $B_s^0 \rightarrow \mu^+\mu^-$* , In *Roadmap for Selected Key Measurements of LHCb* [59], [hep-ex/0912.4179], CERN Report LHCb-PUB-2009-029.
- [73] M.-O. Bettler [LHCb], *The LHCb Analysis for  $B_s^0 \rightarrow \mu^+\mu^-$* , (2009) [hep-ex/0908.4066].
- [74] C. T. Hill, *Topcolor Assisted Technicolor*, Phys. Lett. **B345**, 483 (1995) [hep-ph/9411426].
- [75] K. D. Lane, *A New model of Topcolor Assisted Technicolor*, Phys. Lett. **B433**, 96 (1998) [hep-ph/9805254].
- [76] W. Liu, C.-X. Yue, and H.-D. Yang, *Rare Decays  $B_s \rightarrow \ell^+\ell^-$  and  $B \rightarrow K\ell^+\ell^-$  in the Topcolor-assisted Technicolor Model*, (2009) [hep-ph/0901.3463].
- [77] K. G. Wilson, *Non-Lagrangian Models of Current Algebra*, Phys. Rev. **179**, 1499 (1969).
- [78] K. G. Wilson and W. Zimmermann, *Operator Product Expansions and Composite Field Operators in the General Framework of Quantum Field Theory*, Commun. Math. Phys. **24**, 87 (1972).
- [79] G. Buchalla, A. Buras, and M. Lautenbacher, *Weak Decays beyond Leading Logarithms*, Rev. Mod. Phys. **68**, 1125 (1996) [hep-ph/9512380].
- [80] E. Witten, *Short Distance Analysis of Weak Interactions*, Nucl. Phys. **B122**, 109 (1977).
- [81] C. Bobeth, T. Ewerth, F. Kruger, and J. Urban, *Analysis of Neutral Higgs Boson Contributions to the Decays  $\bar{B}_s \rightarrow \ell^+\ell^-$  and  $\bar{B} \rightarrow K\ell^+\ell^-$* , Phys. Rev. **D64**, 074014 (2001) [hep-ph/0104284].
- [82] T. Inami and C. S. Lim, *Effects of Superheavy Quarks and Leptons in Low-Energy Weak Processes  $K_L^0 \rightarrow \mu\bar{\mu}$ ,  $K^+ \rightarrow \pi^+\nu\bar{\nu}$  and  $K^0 \leftrightarrow \bar{K}^0$* , Prog. Theor. Phys. **65**, 297 (1981).
- [83] T. Inami and C. S. Lim, *Errata: Effects of Superheavy Quarks and Leptons in Low-Energy Weak Processes  $K_L^0 \rightarrow \mu\bar{\mu}$ ,  $K^+ \rightarrow \pi^+\nu\bar{\nu}$  and  $K^0 \leftrightarrow \bar{K}^0$* , Prog. Theor. Phys. **65**, 1772 (1981).
- [84] B. Grzadkowski and P. Krawczyk, *Higgs Particle Effects in Flavour Changing Transitions*, Z. Phys. **C18**, 43 (1983).
- [85] P. Krawczyk, *Flavour Changing Yukawa Coupling of the Standard Higgs Boson: Effects of the External Quark Masses*, Z. Phys. **C44**, 509 (1989).
- [86] G. Buchalla *et al.*, *B, D and K Decays*, Eur. Phys. J. **C57**, 309 (2008) [hep-ph/0801.1833].
- [87] A. J. Buras, *Relations Between  $\Delta M_{s,d}$  and  $B_{s,d} \rightarrow \bar{\mu}\mu$  in Models with Minimal Flavor Violation*, Phys. Lett. **B566**, 115 (2003) [hep-ph/0303060].

- [88] M. Blanke, A. Buras, D. Guadagnoli, and C. Tarantino, *Minimal Flavour Violation Waiting for Precise Measurements of  $\Delta M_s$ ,  $S_{\psi\phi}$ ,  $A_{\text{SL}}^s$ ,  $|V_{ub}|$ ,  $\gamma$  and  $B_{s,d}^0 \rightarrow \mu^+ \mu^-$* , JHEP **10**, 003 (2006) [hep-ph/0604057].
- [89] E. Gamiz, C. T. H. Davies, G. P. Lepage, J. Shigemitsu, and M. Wingate [HPQCD collaboration], *Neutral B Meson Mixing in Unquenched Lattice QCD*, Phys. Rev. **D80**, 014503 (2009) [hep-lat/0902.1815].
- [90] A. J. Buras *et al.*, *Patterns of Flavour Violation in the Presence of a Fourth Generation of Quarks and Leptons*, (2010) [hep-ph/1002.2126].
- [91] T. Aaltonen *et al.* [CDF collaboration], *Search for  $B_s^0 \rightarrow \mu^+ \mu^-$  and  $B_d^0 \rightarrow \mu^+ \mu^-$  Decays with  $2 \text{ fb}^{-1}$  of  $p\bar{p}$  Collisions*, Phys. Rev. Lett. **100**, 101802 (2008) [hep-ph/0712.1708].
- [92] T. Aaltonen *et al.* [CDF collaboration], *Search for  $B_s^0 \rightarrow \mu^+ \mu^-$  and  $B_d^0 \rightarrow \mu^+ \mu^-$  Decays in  $3.7 \text{ fb}^{-1}$  of  $p\bar{p}$  Collisions with CDF II*, Fermilab Report CDF Public note 9892, 2009.
- [93] B. Aubert *et al.* [BABAR collaboration], *A Search for the Rare Decay  $B^0 \rightarrow \tau^+ \tau^-$  at BABAR*, Phys. Rev. Lett. **96**, 241802 (2006) [hep-ex/0511015].
- [94] M. Acciarri *et al.* [L3 collaboration], *Search for Neutral B Meson Decays to Two Charged Leptons*, Phys. Lett. **B391**, 474 (1997).
- [95] J. Gunion, H. Haber, G. Kane, and S. Dawson, *The Higgs Hunter's Guide* (Addison-Wesley, Reading, MA, USA, 1990).
- [96] P. Koppenburg *et al.* [Belle collaboration], *Inclusive Measurement of the Photon Energy Spectrum in  $b \rightarrow s\gamma$  Decays*, Phys. Rev. Lett. **93**, 061803 (2004) [hep-ex/0403004].
- [97] B. Aubert *et al.* [BABAR collaboration], *Measurement of the Branching Fraction and Photon Energy Moments of  $B \rightarrow X_s \gamma$  and  $A_{CP}(B \rightarrow X_{s+d} \gamma)$* , Phys. Rev. Lett. **97**, 171803 (2006) [hep-ex/0607071].
- [98] E. Barberio *et al.* [Heavy Flavor Averaging Group], *Averages of  $b$ -Hadron Properties at the End of 2005*, (2006) [hep-ex/0603003].
- [99] E. Barberio *et al.* [Heavy Flavor Averaging Group], *Averages of  $b$ -Hadron and  $c$ -Hadron Properties at the End of 2007*, (2008) [hep-ph/0808.1297].
- [100] M. Misiak *et al.*, *The First Estimate of  $\mathcal{B}(\overline{B} \rightarrow X_s \gamma)$  at  $\mathcal{O}(\alpha_s^2)$* , Phys. Rev. Lett. **98**, 022002 (2007) [hep-ph/0609232].
- [101] H. Logan and U. Nierste,  *$B_{s,d} \rightarrow \ell^+ \ell^-$  in a Two Higgs Doublet Model*, Nucl. Phys. **B586**, 39 (2000) [hep-ph/0004139].
- [102] G. D'Ambrosio, G. F. Giudice, G. Isidori, and A. Strumia, *Minimal Flavour Violation: An Effective Field Theory Approach*, Nucl. Phys. **B645**, 155 (2002) [hep-ph/0207036].
- [103] A. J. Buras, P. Gambino, M. Gorbahn, S. Jager, and L. Silvestrini, *Universal Unitarity Triangle and Physics Beyond the Standard Model*, Phys. Lett. **B500**, 161 (2001) [hep-ph/0007085], Although anterior to the MFV modern definition, this paper introduce what is now known as the constrained MFV (CMFV).

- [104] T. Hurth, G. Isidori, J. F. Kamenik, and F. Mescia, *Constraints on New Physics in MFV models: A Model-Independent Analysis of  $\Delta F = 1$  Processes*, Nucl. Phys. **B808**, 326 (2009) [hep-ph/0807.5039].
- [105] S. Heinemeyer, X. Miao, S. Su, and G. Weiglein, *B-Physics Observables and Electroweak Precision Data in the CMSSM, mGMSB and mAMSB*, JHEP **08**, 087 (2008) [hep-ph/0805.2359].
- [106] B. Allanach, G. Hiller, D. Jones, and P. Slavich, *Flavour Violation in Anomaly Mediated Supersymmetry Breaking*, JHEP **04**, 088 (2009) [hep-ph/0902.4880].
- [107] J. R. Ellis, S. Heinemeyer, K. A. Olive, A. M. Weber, and G. Weiglein, *The Supersymmetric Parameter Space in Light of B-Physics Observables and Electroweak Precision Data*, JHEP **08**, 083 (2007) [hep-ph/0706.0652].
- [108] J. R. Ellis, K. A. Olive, Y. Santoso, and V. C. Spanos, *Gravitino Dark Matter in the CMSSM*, Phys. Lett. **B588**, 7 (2004) [hep-ph/0312262].
- [109] J. R. Ellis, K. A. Olive, and Y. Santoso, *Constraining Supersymmetry*, New J. Phys. **4**, 32 (2002) [hep-ph/0202110].
- [110] J. R. Ellis, K. A. Olive, and Y. Santoso, *The MSSM Parameter Space with Non-Universal Higgs Masses*, Phys. Lett. **B539**, 107 (2002) [hep-ph/0204192].
- [111] V. Berezinsky *et al.*, *Neutralino Dark Matter in Supersymmetric Models with Non-Universal Scalar Mass Terms*, Astropart. Phys. **5**, 1 (1996) [hep-ph/9508249].
- [112] J. Ellis, T. Hahn, S. Heinemeyer, K. A. Olive, and G. Weiglein, *WMAP-Compliant Benchmark Surfaces for MSSM Higgs Bosons*, JHEP **10**, 092 (2007) [hep-ph/0709.0098].
- [113] O. Buchmueller *et al.*, *Likelihood Functions for Supersymmetric Observables in Frequentist Analyses of the CMSSM and NUHM1*, Eur. Phys. J. **C64**, 391 (2009) [hep-ph/0907.5568].
- [114] J. R. Ellis, J. S. Lee, and A. Pilaftsis, *B-Meson Observables in the Maximally CP-Violating MSSM with Minimal Flavour Violation*, Phys. Rev. **D76**, 115011 (2007) [hep-ph/0708.2079].
- [115] A. K. Alok and S. K. Gupta,  *$B_s \rightarrow \mu^+ \mu^-$  Decay in the  $\mathcal{R}$ -Parity Violating Minimal Supergravity*, (2009) [hep-ph/0904.1878].
- [116] H. K. Dreiner, M. Kramer, and B. O'Leary, *Bounds on  $\mathcal{R}$ -Parity Violation from Leptonic and Semi-Leptonic Meson Decays*, Phys. Rev. **D75**, 114016 (2007) [hep-ph/0612278].
- [117] A. Mir, F. Tahir, and K. Ahmed, *Lepton Polarization Asymmetry in  $B \rightarrow \ell^+ \ell^-$  Decays in  $\mathcal{R}$ -Parity Violating Minimal Supersymmetric Standard Model*, Europhys. Lett. **83**, 41002 (2008) [hep-ph/0707.2268].
- [118] P. Langacker and M. Plumacher, *Flavor Changing Effects in Theories with a Heavy  $Z'$  Boson with Family Nonuniversal Couplings*, Phys. Rev. **D62**, 013006 (2000) [hep-ph/0001204].
- [119] T. G. Rizzo,  *$Z'$  Phenomenology and the LHC*, (2006) [hep-ph/0610104], SLAC-PUB-12129.

- [120] K. Cheung, C.-W. Chiang, N. G. Deshpande, and J. Jiang, *Constraints on Flavor-Changing  $Z'$  Models by  $B_s^0$  Mixing,  $Z'$  Production, and  $B_s^0 \rightarrow \mu^+ \mu^-$* , Phys. Lett. **B652**, 285 (2007) [hep-ph/0604223].
- [121] F. J. Hasert *et al.* [Gargamelle collaboration], *Observation of Neutrino-like Interactions without Muon or Electron in the Gargamelle Neutrino Experiment*, Phys. Lett. **B46**, 138 (1973).
- [122] D. Mohl, G. Petrucci, L. Thorndahl, and S. van der Meer, *Physics and Technique of Stochastic Cooling*, Phys. Rept. **58**, 73 (1980).
- [123] G. Arnison *et al.* [UA1 collaboration], *Experimental Observation of Isolated Large Transverse Energy Electrons with Associated Missing Energy at  $\sqrt{s} = 540$  GeV*, Phys. Lett. **B122**, 103 (1983).
- [124] M. Banner *et al.* [UA2 collaboration], *Observation of Single Isolated Electrons of High Transverse Momentum in Events with Missing Transverse Energy at the CERN  $p\bar{p}$  Collider*, Phys. Lett. **B122**, 476 (1983).
- [125] P. Bagnaia *et al.* [UA2 collaboration], *Evidence for  $Z^0 \rightarrow e^+ e^-$  at the CERN  $p\bar{p}$  Collider*, Phys. Lett. **B129**, 130 (1983).
- [126] *LEP Design Report Vol. 1. The LEP Injector Chain*, CERN Report LEP-83-29, 1983.
- [127] *LEP Design Report Vol. 2. The LEP Main Ring*, CERN Report LEP-84-01, 1984.
- [128] L. Evans and P. Bryant (Eds), *LHC Machine*, JINST **3**, S08001 (2008).
- [129] K. Wille, *The Physics of Particle Accelerators: An Introduction* (Oxford University Press, 2000).
- [130] E. Wilson, *An Introduction to Particle Accelerators* (Oxford University Press, 2001).
- [131] *Fermilab TeV Program, Superconducting Magnet Ring: Energy Doubler, Energy Saver, Colliding Beams*, FermiLab Report MISC-1977-01, 1977.
- [132] K. Del Signore [CDF and DØ collaborations], *The Future Collider Physics Program at FermiLab: Run II and TeV 33*, FermiLab Report CONF-98-221-E, 1998.
- [133] CERN History Highlights, available at:  
<http://public.web.cern.ch/public/en/About/History-en.html>.
- [134] M. Bajko *et al.*, *Report of the Task Force on the Incident of 19th September 2008 at the LHC*, CERN Report LHC-PROJECT-Report-1168, 2009.
- [135] J.-L. Caron, *Accelerators Chain of CERN: Operating and Approved Projects*, available at:  
<http://cdsweb.cern.ch/record/43487>.
- [136] G. Aad *et al.* [ATLAS collaboration], *The ATLAS Experiment at the LHC*, JINST **3**, S08003 (2008).
- [137] R. Adolphi *et al.* [CMS collaboration], *The CMS Experiment at the LHC*, JINST **3**, S08004 (2008).
- [138] G. Anelli *et al.* [TOTEM collaboration], *The TOTEM Experiment at the LHC*, JINST **3**, S08007 (2008).

- [139] O. Adriani *et al.* [LHCf collaboration], *The LHCf Detector at the LHC*, JINST **3**, S08006 (2008).
- [140] K. Aamodt *et al.* [ALICE collaboration], *The ALICE Experiment at the LHC*, JINST **3**, S08002 (2008).
- [141] A. Alves *et al.* [LHCb collaboration], *The LHCb Detector at the LHC*, JINST **3**, S08005 (2008).
- [142] J. Pequenao [ATLAS collaboration], *Computer Generated Image of the ATLAS Detector*, available at: <http://cdsweb.cern.ch/record/1095924>.
- [143] The CMS collaboration, *Layout of the CMS detector*, available at: <http://cdsweb.cern.ch/record/39040>.
- [144] The ALICE collaboration, *Layout of the ALICE detector*, available at: <http://cdsweb.cern.ch/record/627595>.
- [145] S. Amato *et al.* [LHCb collaboration], *LHCb Technical Proposal*, CERN Report LHCC-98-4, 1998.
- [146] S. Amato *et al.* [LHCb collaboration], *LHCb Magnet: Technical Design Report*, CERN Report LHCC-2000-007, 2000.
- [147] S. Amato *et al.* [LHCb collaboration], *LHCb Calorimeters: Technical Design Report*, CERN Report LHCC-2000-036, 2000.
- [148] S. Amato *et al.* [LHCb collaboration], *LHCb RICH: Technical Design Report*, CERN Report LHCC-2000-037, 2000.
- [149] P. R. Barbosa-Marinho *et al.* [LHCb collaboration], *LHCb Muon System: Technical Design Report*, CERN Report LHCC-2001-010, 2001.
- [150] P. R. Barbosa-Marinho *et al.* [LHCb collaboration], *LHCb Muon System: addendum to the Technical Design Report*, CERN Report LHCC-2003-002, 2003.
- [151] P. R. Barbosa-Marinho *et al.* [LHCb collaboration], *LHCb Muon System: second addendum to the Technical Design Report*, CERN Report LHCC-2005-012, 2005.
- [152] P. R. Barbosa-Marinho *et al.* [LHCb collaboration], *LHCb VELO (VERtex LOcator): Technical Design Report*, CERN Report LHCC-2001-11, 2001.
- [153] P. R. Barbosa-Marinho *et al.* [LHCb collaboration], *LHCb Outer Tracker: Technical Design Report*, CERN Report LHCC-2001-024, 2001.
- [154] P. R. Barbosa-Marinho *et al.* [LHCb collaboration], *LHCb Online System, Data Acquisition and Experiment Control: Technical Design Report*, CERN Report LHCC-2001-040, 2001.
- [155] T. Nakada, E. Aslanides, A. Smith, and W. Witzeling, *Addendum to the LHCb Online System Technical Design Report*, CERN Report LHCC-2005-039, 2005.
- [156] P. R. Barbosa-Marinho *et al.* [LHCb collaboration], *LHCb Inner Tracker: Technical Design Report*, CERN Report LHCC-2002-29, 2002.
- [157] R. Antunes-Nobrega *et al.* [LHCb collaboration], *LHCb Reoptimized Detector Design and Performance: Technical Design Report*, CERN Report LHCC-2003-030, 2003.

- [158] R. Antunes-Nobrega *et al.* [LHCb collaboration], *LHCb Trigger System: Technical Design Report*, CERN Report LHCC-2003-31, 2003.
- [159] O. Callot, *Improved Robustness of the Velo Tracking*, CERN Report LHCb-2003-017, 2003.
- [160] W. Hoogland, L. Wiggers, and N. Zaitsev, *The Use of Silicon Detectors for Fast Primary Vertex Reconstruction and Pile-Up Rejection*, CERN Report LHCb-97-016, 1998.
- [161] R. Cornat, J. Lecoq, and P. Perret, *Level-0 Decision Unit for LHCb*, CERN Report LHCb-2003-065, 2003.
- [162] P. A. Cerenkov, *Visible Luminescence of Pure Fluids Induced by  $\gamma$  Rays*, Dokl. Akad. Nauk Ser. Fiz. **2**, 451 (1934).
- [163] P. A. Aarnio *et al.* [DELPHI collaboration], *The DELPHI Detector at LEP*, Nucl. Instrum. Meth. **A303**, 233 (1991).
- [164] F. C. D. Metlica *et al.* [LHCb collaboration], *Development of Light-Weight Spherical Mirrors for RICH Detectors*, Nucl. Instrum. Meth. **A595**, 197 (2008).
- [165] M. Alemi *et al.*, *First Operation of a Hybrid Photon Detector Prototype with Electrostatic Cross-Focussing and Integrated Silicon Pixel Readout*, Nucl. Instrum. Meth. **A449**, 48 (2000).
- [166] M. Patel, M. Losasso, and T. Gys, *Magnetic Shielding Studies of the LHCb RICH Photon Detectors*, Nucl. Instrum. Meth. **A553**, 114 (2005).
- [167] S. Barsuk *et al.*, *Design and Construction of Electromagnetic Calorimeter for LHCb Experiment*, CERN Report LHCb-2000-043, 2000.
- [168] R. W. Forty and O. Schneider, *RICH Pattern Recognition*, CERN Report LHCb-98-040, 1998.
- [169] T. Sjostrand *et al.*, *High-Energy Physics Event Generation with PYTHIA 6.1*, Comput. Phys. Commun. **135**, 238 (2001) [hep-ph/0010017], see also:  
<http://projects.hepforge.org/pythia6/>.
- [170] J. Albrecht [LHCb collaboration], *The LHCb Trigger System*, Nucl. Phys. Proc. Suppl. **187**, 237 (2009).
- [171] G. Barrand *et al.*, *GAUDI - A Software Architecture and Framework for Building HEP Data Processing Applications*, Comput. Phys. Commun. **140**, 45 (2001), see also:  
<http://proj-gaudi.web.cern.ch/proj-gaudi/>.
- [172] R. Antunes-Nobrega *et al.* [LHCb collaboration], *LHCb Computing: Technical Design Report*, CERN Report LHCC-2005-019, 2005.
- [173] I. Belyaev *et al.*, *Simulation Application for the LHCb Experiment*, (2003) [physics/0306035], see also:  
<http://lhcb-release-area.web.cern.ch/LHCb-release-area/DOC/gauss/>.
- [174] D. J. Lange, *The EvtGen Particle Decay Simulation Package*, Nucl. Instrum. Meth. **A462**, 152 (2001), see also: <http://www.slac.stanford.edu/~lange/EvtGen/>.

- [175] S. Agostinelli *et al.* [GEANT4 collaboration], GEANT4: *A simulation toolkit*, Nucl. Instrum. Meth. **A506**, 250 (2003), see also: <http://geant4.web.cern.ch/geant4/>.
- [176] LHCb collaboration, The BOOLE project,  
<http://lhcb-release-area.web.cern.ch/LHCb-release-area/DOC/bole/>.
- [177] LHCb collaboration, The BRUNEL project,  
<http://lhcb-release-area.web.cern.ch/LHCb-release-area/DOC/brunel/>.
- [178] LHCb collaboration, The DAVINCI project,  
<http://lhcb-release-area.web.cern.ch/LHCb-release-area/DOC/davinci/>.
- [179] I. Belyaev *et al.*, *Python-based Physics Analysis Environment for LHCb*, CERN Report LHCb-2004-089, 2004, see also:  
<http://lhcb-comp.web.cern.ch/lhcb-comp/Analysis/Bender/index.html>.
- [180] G. van Rossum, The PYTHON programming language, <http://www.python.org/>.
- [181] LHCb collaboration, The PANORAMIX project,  
<http://lhcb-release-area.web.cern.ch/LHCb-release-area/DOC/panoramix/>.
- [182] C. Bauer *et al.*, *Test Beam Results on Inner Tracker Silicon Prototype Sensors*, CERN Report LHCb-2001-135, 2001.
- [183] M. Agari *et al.*, *Test Beam Results of Multi-Geometry Prototype Sensors for the LHCb Inner Tracker*, CERN Report LHCb-2002-058, 2002.
- [184] A. Perrin, *Contribution to the Inner Tracker Design and Penguin Sensitivity Studies for the Measurement of sin 2 beta in LHCb*, PhD thesis, EPFL, Lausanne, 2008, CERN-THESIS-2008-100.
- [185] M. Moll [RD50 collaboration], *Radiation Tolerant Semiconductor Sensors for Tracking Detectors*, Nucl. Instrum. Meth. **A565**, 202 (2006).
- [186] M.-O. Bettler *et al.*, *Assembly of the Inner Tracker Detector Boxes*, CERN Report LHCb-2008-074, 2007.
- [187] Hamamatsu Photonics K.K., <http://www.hamamatsu.com>.
- [188] B. Adeva *et al.*, *Silicon sensor probing and radiation studies for the LHCb silicon tracker*, Nucl. Instrum. Meth. **A568**, 277 (2006), CERN Report LHCb-2005-033, 2005.
- [189] S. Löchner and M. Schmelling, *The Beetle Reference Manual - Chip Version 1.3, 1.4 and 1.5*, CERN Report LHCb-2005-105, 2006.
- [190] A. Bay *et al.*, *Hybrid Design, Procurement and Testing for the LHCb Silicon Tracker*, CERN Report LHCb-2005-061, 2005.
- [191] Rhe Microsystems, <http://www.rhe.de>.
- [192] A. Vollhardt, *An Optical Readout System for the LHCb Silicon Tracker*, PhD thesis, Univ. of Zürich, Zürich, CERN-THESIS-2005-025, 2005.
- [193] D. Esperante Pereira and A. Vollhardt, *Design and development of the Control Board for the LHCb Silicon Tracker*, CERN Report LHCb-2007-153, 2008.

- [194] Composite Design, <http://www.compositedesign.ch>.
- [195] Merriam-Webster online dictionary, <http://www.merriam-webster.com>.
- [196] R. P. Bernhard *et al.*, *The LHCb Silicon Tracker*, Nucl. Instrum. Meth. **A596**, 17 (2008), CERN Report LHCb-2007-126, 2007.
- [197] G. Conti *et al.*, *Inner Tracker Survey Strategy*, CERN Report LHCb-2008-068, 2008.
- [198] L. Roy, *Detector Safety System of the Inner Tracker Detector*, CERN EDMS ID 830675.
- [199] N. (Gueissaz) Gauvin and M.-O. Bettler, *Qualification of Thermic C05 06 and Honeywell 2455R Thermostats for Use in Magnetic Fields*, CERN EDMS ID 982702.
- [200] M. Agari *et al.*, *Radiation Monitoring System for the LHCb Inner Tracker*, CERN Report LHCb-2007-062, 2007.
- [201] W. Witzeling, *LHCb Part Identification*, CERN EDMS ID 369654.
- [202] W. Witzeling, *LHCb Institutes Codes*, CERN EDMS ID 373611.
- [203] W. Witzeling, *System and Sub-system Codes*, CERN EDMS ID 373610.
- [204] M. Capeans, R. Chritin, and F. Perez, *Tightness Specifications and Test Procedure for the Final Connections of the Cooling and Active Gas Circuits of the ATLAS TRT Detector*, CERN EDMS ID 681672.
- [205] P. Vazquez Regueiro, D. Esperante Pereira, H. Voss, and L. Nicolas, *Setup for Testing LHCb Inner Tracker Modules*, 12<sup>th</sup> Workshop on Electronics for LHC and Future Experiments (LECC 2006), Valencia, p. 539, 2006.
- [206] CAEN, *Technical Information Manual Mod A1511B*.
- [207] CAEN, *SY1527 Universal Multichannel Power Supply System*.
- [208] WIENER, *MARATON Power Supply System: Technical Manual*.
- [209] G. Haefeli *et al.*, *The LHCb DAQ Interface Board TELL1*, Nucl. Instrum. Meth. **A560**, 494 (2006).
- [210] R. Jacobsson, P. König, A. Chlopik, and Z. Guzik, *The Final LHCb Readout Supervisor ODIN*, (2002), 8<sup>th</sup> Workshop on Electronics for LHC Experiments, Colmar, France.
- [211] H. Voss *et al.*, *Production, Commissioning and First Data of the LHCb Silicon Tracker*, CERN Report LHCb-2008-062, 2008.
- [212] A. Gallas *et al.*, *First Operational Experience from the LHCb Silicon Tracker*, CERN Report LHCb-CONF-2009-051, 2009.
- [213] M. Needham, *Track Reconstruction in the LHCb Inner Tracker*, CERN Report LHCb-PUB-2009-005, 2009.
- [214] L. Nicolas and M. Needham, *Alignment of the Inner Tracker Stations Using First Data*, CERN Report LHCb-PUB-2009-012, 2009.

- [215] L. Nicolas, *Alignment of the LHCb Tracking Stations and Selection of  $X(3872)$  and  $Z(4430)^\pm$  in  $pp$  Collisions at 14 TeV*, PhD thesis, EPFL, Lausanne, 2009, CERN-THESIS-2009-129.
- [216] G. Conti *et al.*, *Inner Tracker Survey Strategy*, CERN Report LHCb-2008-068, 2008.
- [217] G. Conti and F. Blanc, *IT Survey Measurements: Analysis and Implementation in the LHCb Software*, CERN Report LHCb-2008-069, 2008.
- [218] D. Martínez Santos, J.-A. Hernando, and F. Teubert, *LHCb Potential to Measure/Exclude the Branching Ratio of the Decay  $B_s^0 \rightarrow \mu^+ \mu^-$* , CERN Report LHCb-2007-033, 2007.
- [219] D. Martínez Santos,  $B_s^0 \rightarrow \mu^+ \mu^-$  in LHCb, CERN Report LHCb-2008-018, 2008.
- [220] A. Read, Modified frequentist analysis of search results (the  $cl_s$  method), CERN Yellow Report 2000-005, 2000.
- [221] A. L. Read, *Presentation of Search Results: The  $CL_s$  Technique*, J. Phys. **G28**, 2693 (2002).
- [222] T. Junk, *Confidence Level Computation for Combining Searches with Small Statistics*, Nucl. Instrum. Meth. **A434**, 435 (1999) [hep-ex/9902006].
- [223] LHCb collaboration, *Parameters of DC06 Monte Carlo Productions*, <https://twiki.cern.ch/twiki/bin/view/LHCb/SettingsDc06>.
- [224] D. Karlen, *Using Projections and Correlations to Approximate Probability Distributions*, Comput. Phys. **12**, 380 (1998).
- [225] G. Zech, *Upper Limits in Experiments with Background or Measurement Errors*, Nucl. Instrum. Meth. **A277**, 608 (1989).
- [226] M. Lamont, leader of the LHC Operation Group, <http://lhc-commissioning.web.cern.ch/lhc-commissioning>.
- [227] LHCb collaboration, *Parameters of MC09 Monte Carlo Productions*, <https://twiki.cern.ch/twiki/bin/view/LHCb/SettingsMc09>.
- [228] H. Dijkstra, H. J. Hilke, T. Nakada, and T. Ypsilantis [LHCb collaboration], *LHCb Letter of Intent*, CERN Report LHCb-95-001, 1995.
- [229] R. Louvot *et al.* [Belle collaboration], *Measurement of the Decay  $B_s^0 \rightarrow D_s^- \pi^+$  and Evidence for  $B_s^0 \rightarrow D_s^\mp K^\pm$  in  $e^+ e^-$  Annihilation at  $\sqrt{s} \approx 10.87$  GeV*, Phys. Rev. Lett. **102**, 021801 (2009) [hep-ph/0809.2526].
- [230] A. Drutskoy, *Results and Prospects for  $\Upsilon(5S)$  Running at B Factories*, (2008) [hep-ph/0807.3973].



**Curriculum Vitæ****Marc-Olivier Bettler**

Date and Place of Birth: March 6<sup>th</sup> 1980, Sierre, Switzerland.  
Nationalities: Swiss and Canadian.

**Education**

- Since 2005: Ph.D. Student in High Energy Physics at EPFL, Switzerland,  
Thesis: Construction of the Inner Tracker Detector and  
Sensitivity to the  $B_s^0 \rightarrow \mu^+ \mu^-$  Decay at LHCb,  
Thesis supervisor: Prof. Olivier Schneider.
  - > Preparation of an alternate analysis for the  $B_s^0 \rightarrow \mu^+ \mu^-$  decay search with early data at LHCb.
  - > Responsible for the development of the assembly procedure and the final assembly of the LHCb Inner Tracker Detector.
- 2004–2005: Researcher in Nuclear Physics applied to Oncology, EPFL, Switzerland, Prof. Rakesh Chawla.
- 2003–2004: Diploma in Nuclear Physics applied to Oncology, EPFL, Switzerland,  
Diploma thesis: Dwell time optimisation for brachytherapy using a new dosimetric database concept,  
Diploma supervisor: Prof. Rakesh Chawla.
- 1999–2003: Undergraduate studies in Physics,  
Ecole Polytechnique Fédérale de Lausanne (EPFL), Switzerland.
- 1994–1999: Lycée-Collège des Creusets, Sion, Switzerland.
- 1993–1994: Collège Evangélique de Bangwa, Cameroon.
- 1992–1993: Cycle d’Orientation, Crans, Switzerland.
- 1992: Collège Catholique Adiwa, Lambaréné, Gabon.